UNIVERSITÀ
DEGLI STUDI
DI BRESCIA

DOTTORATO DI RICERCA IN
INGEGNERIA CIVILE, AMBIENTALE, DELLA COOPERAZIONE
INTERNAZIONALE E DI MATEMATICA

Settore Scientifico Disciplinare: ICAR/09 – Tecnica delle Costruzioni

XXXV CICLO

STUDY ON THE STRUCTURAL BEHAVIOUR OF 3D PRINTED CONCRETE ELEMENTS MADE BY EXTRUSION PROCESS

PhD Candidate:
Lucia Licciardello

Tutor:
Prof. Giovanni Metelli

Co-Tutor:
Prof. Giovanni A. Plizzari
Dott. Adriano Reggia

SYNOPSIS

The growing interest in the use of 3D printing of concrete (3DPC) in the construction industry is strongly associated with new design capabilities aimed at creating efficient and sustainable buildings. Unlike conventional construction methods, this technology provides extensive design freedom, allowing the production of complex and variable geometries. In fact, the concrete material can maintain its shape without the use of formworks due to its rheological properties and the control of their evolution over time. Furthermore, the material use can be reduced by applying structural optimisation, a mathematical method that uses material only where it is structurally necessary.

In recent years, several digital fabrication approaches have been developed; in this thesis, attention will be focused on the extrusion process, which consists of printing through an automated print head and layer-by-layer deposition of a filament of fresh concrete. While traditional cast concrete can be considered an isotropic material, the 3D printed material, due to its layered structure, is anisotropic. Consequently, typical standards and methodologies of cast concrete are not always applicable to assess the mechanical properties of 3D printed concrete. There are many parameters that can influence the hardened properties of the printed material, such as the direction of load application with respect to the printed layers and the interlayer interval time. In this thesis, the hardened properties of the printed material, whose characterization is important as it can impact the structural behaviour of 3D printed elements, are investigated with compression and flexural tests considering different orientations of the layers with respect to the applied load. The influence of load direction on compressive strength is minimal, while the impact on flexural strength is more significant. Particular attention is given to the interlayer strength, which is studied with direct tensile test in the case of normal forces acting on the interface. Furthermore, two additional tests are proposed in the case of interfaces subjected to the shear action. The first test is a modification of the push-out test, commonly used to evaluate the shear properties of masonry elements. In particular, this test is suitable to represent a biaxial state of stress typical of a wall subjected to both a transverse shear force and a vertical compressive load. The second test is a modification of the slant shear test, which is commonly used to study the interface strength between the concrete and a repair material. In this case, the interface is subjected to a combined state of shear and compression, and it allows the mechanical properties to be studied at different inclinations of the layers with respect to the horizontal plane. In addition, the specimens tested with modified slant shear test were printed with different interlayer interval time, to study its influence on the mechanical properties. These tests enable the measurement of the cohesion and the

angle of friction and provide a methodology to determine the resistance domain of 3DPC elements.
On a large scale, although several prototype buildings have been built in recent years, only a few studies have been devoted to the structural behaviour of these elements. To this aim five full-scale walls were tested at the University of Brescia. Four walls were unreinforced and one was reinforced with vertical steel bars grouted in outer small pockets to connect the wall to the foundation. The walls were subjected to a top cyclic displacement of increasing amplitude and to a constant vertical load that simulates the load acting on a wall of a typical two-story building. The walls showed high initial stiffness, high resistance to horizontal loads, and brittle behaviour with flexural failure when the tensile strength of the material is reached. After cracking, a rocking mechanism followed. The reinforced wall had a cold joint due to the interruption of the printing process for 45 min because of overheating problems. It exhibited similar behaviour to the unreinforced wall until failure, which occurred earlier with respect to that of the unreinforced wall due to the cold joint. The failure was characterized by shear sliding along the cold joint. This highlights an inherent aspect of the 3D printing process, as cold joints are likely to occur during in-situ printing.
In addition, the possibility of enhancing the thermal insulation of the panel is discussed first by proposing an analytical and a finite element method. The models are then validated by testing a specimen subjected to a thermal gradient (between the inner and outer faces of the wall) to evaluate the thermal conductivity of the element, which resulted in compliance with the current standards.
Moreover, a numerical method is developed to predict the interface behaviour and structural performance of 3D printed concrete walls. The modified push-out test is modelled with smeared cracking and discrete cracking approaches. The 3DPC walls are modelled using a smeared cracking approach with interface elements at the base that simulate the crack opening. The finite element analysis results, both for the modified push-out test and the 3DPC walls, are in good agreement with the experimental findings.
Finally, the integration of structural and thermal design using 3DPC technology is discussed with regards to a two-story reference building.

SOMMARIO

Il crescente interesse per l'uso della stampa 3D del calcestruzzo (3DPC) nel settore delle costruzioni è fortemente associato alle nuove capacità di progettazione volte a creare edifici efficienti e sostenibili. A differenza dei metodi di costruzione tradizionali, questa tecnologia offre un'ampia libertà di progettazione ed è in grado di produrre geometrie complesse senza bisogno di utilizzare casseforme. Infatti, il calcestruzzo utilizzato durante la stampa può mantenere la sua forma senza l'uso di casseforme grazie alle sue proprietà reologiche e al controllo della loro evoluzione nel tempo. Inoltre, l'uso del materiale può essere ridotto applicando l'ottimizzazione strutturale, un metodo matematico che utilizza il materiale solo dove è strutturalmente necessario. Ciò può comportare un notevole risparmio di costi e una riduzione degli sprechi di materiale.

Negli ultimi anni sono stati sviluppati diversi approcci nell'ambito della fabbricazione digitale; in questa tesi, l'attenzione si concentra sul processo di estrusione, che consiste nella stampa e nel deposito di un filamento di calcestruzzo fresco strato per strato attraverso una testina di stampa. Mentre il calcestruzzo tradizionale può essere considerato un materiale isotropo, il materiale utilizzato per la stampa 3D, a causa della sua struttura a strati, è anisotropo. Di conseguenza, le normative generalmente utilizzate per la caratterizzazione delle proprietà meccaniche del calcestruzzo tradizionale non sono sempre utilizzabili. Sono molti i fattori che possono influenzare le proprietà del materiale stampato allo stato indurito, come la direzione di applicazione del carico rispetto agli strati stampati e l'intervallo di tempo che intercorre tra la stampa di uno strato e l'altro. In questa tesi, le proprietà del materiale stampato allo stato indurito, la cui caratterizzazione è molto importante in quanto può influenzare il comportamento sturtturale di elementi realizzati con la tecnica della stampa tridimensionale, sono state studiate con prove di compressione e flessione, considerando diversi orientamenti degli strati stampati rispetto alla direzione di carico applicato. Particolare attenzione è rivolta alla resistenza tra i layer, che viene studiata con prove di trazione diretta nel caso di forze normali che agiscono sull'interfaccia, mentre vengono proposte due prove nel caso di interfacce soggette a forze di taglio. La prima prova è una modifica della prova di push-out, comunemente utilizzata per valutare le proprietà di taglio delle strutture in muratura. In particolare, questa prova è adatta a rappresentare lo stato di sollecitazione che agisce su una parete; il provino è infatti soggetto a una forza verticale e a un carico di precompressione orizzontale che rappresentano rispettivamente i carichi verticali e orizzontali che agiscono su una parete. La seconda prova è lo shear slant test, comunemente utilizzata per studiare la resistenza dell'interfaccia tra il calcestruzzo e un materiale differente. In questo caso, l'interfaccia è sottoposta a una combinazione di azioni di taglio e compressione e

consente di studiare le proprietà meccaniche considerando diverse inclinazioni degli strati rispetto al piano di stampa orizzontale. Inoltre, questi provini sono stati stampati con diversi intervalli di tempo tra gli strati per studiarne l'influenza sulle proprietà meccaniche.
Sebbene negli ultimi anni siano stati costruiti diversi edifici con la tecnica della stampa 3D, solo pochi studi sono stati dedicati al comportamento strutturale di questi elementi. Cinque pareti sono state testate presso l'Università di Brescia. Le pareti sono state sottoposte a un carico orizzontale nel piano che simula il carico orizzontale agente su un edificio e a un carico verticale costante che simula il carico di un edificio a due piani che grava sulla parete. Le pareti testate sono quattro non armate e una armata con barre d'acciaio verticali inserite in piccole tasche ai lati della parete. Inoltre, viene discussa la possibilità di migliorare l'isolamento termico del pannello, proponendo prima un metodo analitico e un metodo agli elementi finiti, che vengono poi convalidati facendo una prova termica su un provino per valutare la conducibilità termica dell'elemento. È stato sviluppato un metodo numerico per prevedere il comportamento dell'interfaccia e le prestazioni strutturali di pareti in calcestruzzo realizzate con la tecnica della stampa tridimensionale per estrusione. Infine, l'integrazione della progettazione strutturale e termica con la tecnologia 3DCP viene discussa in relazione a un edificio a due piani.

ACKNOWLEDGMENTS

I express my gratitude to my supervisor, Professor Giovanni Plizzari, for his valuable suggestions, support and the opportunity to attend the PhD course.
I acknowledge my supervisor, Professor Giovanni Metelli, for his constant support and valuable advice, especially during the last year of my doctoral studies.
Special thanks goes to Eng. Adriano Reggia for his constant presence and help during this three years journey.
I would also like to thank Professor Walter Kaufmann, who gave me the opportunity to spend seven months of doctoral studies at ETH Zurich, and to Eng. Alejandro Giraldo-Soto for his constant support and advice during my stay. Thanks also to all my colleagues of the group of Structural Concrete and Bridge Design of ETH Zurich.
I wish to thank the technicians of the laboratory "Pietro Pisa", who kindly helped me in the experimental part of my work.
I wish to thank Italcementi and Professor Costantino Menna of the University Federico II for providing the specimens and for assistance during the printing process.
I would like to thank Professor Freek Bos and Professor Sergio Cavalaro for taking time to meticulously revise my PhD thesis. Thanks to their suggestions, this thesis has improved considerably.
I would like to thank my colleague Fabiola, Enrico, Nico, Stefano, Simone and Anthony for sharing this journey with me. Your presence and support has been essential.
I would like also to thank Luca, Anna, Giulia, Matteo, Paolo and Elisa for the time together during the last months of my doctoral studies.
I would like to thank my parents, Salvatore and Mariella, and my sister Silvia for always supporting me and my choices unconditionally.
Finally, thanks Daniele for always being by my side.

CONTENTS

STUDY ON THE STRUCTURAL BEHAVIOUR OF 3D PRINTED CONCRETE ELEMENTS MADE BY EXTRUSION PROCESS

1 INTRODUCTION

1.1 Background and motivation

3D printing of concrete (3DPC) is a modern digital fabrication method that industrialises the production of architectural and structural components. By integrating digital design and construction processes, 3DPC can offer significant economic and environmental benefits, such as reduced construction time, costs, and enhanced quality.

In contrast to conventional construction methods, this technology provides extensive design freedom and is capable of producing complex geometries without the need of formworks. In fact, architectural design is often constrained to standard geometries to reduce costs and enable the reuse of formworks. In the case of digital fabrication of concrete (DFC), on the other hand, the concrete material can maintain its shape without the use of formworks due to its rheological properties and the control of its evolution over time. Moreover, it has been highlighted the potential benefit of additive manufacturing to reduce the use of materials by applying structural optimisation, a mathematical method that uses material only where it is structurally necessary se. This can result in significant cost savings and a reduction in material waste which reduces the impact of the construction industry on the environment. The potential of 3DPC technology to reduce the environmental impact, which is significant due to the use of cement-based materials [1], is considerable: the use of recycled and artificial aggregates, supplementary cementitious materials (SCM) and alternative low-carbon cements are among the most likely approaches to reduce the impact, particularly with regard to the global warming potential (GWP) of construction materials [1]. In order to ensure a sustainable construction process, life cycle assessments (LCA) have to be performed. Some studies were conducted [2]-[3] to examine the environmental impact of digitally fabricated building components, which were compared to traditional construction. According to the results of the assessment, the impact of the digital construction process was relatively small as compared to the environmental impact of traditional construction methods.

Several digital fabrication approaches have been developed in the last few years, among which the extrusion process is one of the most common. It consists of printing through an automated print head and layer-by-layer deposition of a filament of fresh concrete. As a result, the 3D printed concrete material is anisotropic, unlike traditional concrete, which is considered isotropic. This characteristic implies that the standards used for characterizing the mechanical properties of traditional concrete may not be suitable for 3D printed concrete. Therefore, it is necessary to establish a common approach and guidelines. It is essential to verify the properties of the

printed material in both the fresh and hardened state, because they can influence the overall structural behaviour of 3D printed concrete elements.
In the fresh state, it is essential to control pumpability, extrudability and buildability to avoid buckling and plastic collapse, which are typical failure modes. To avoid collapse, it is important to determine and control the evolution over time of the properties in the fresh state, such as elastic modulus, Poisson's ratio, cohesion, angle of friction and dilatancy angle. These properties can be determined using unconfined compression tests [4–6], shear tests [7,8] and triaxial tests [7]. The hardened properties of 3D printed concrete material, as well as those in the fresh state, play an important role in influencing the structural performance of a 3D printed concrete structure. The printed material is anisotropic as it is built up from different filaments. Consequently, the role of interfaces will become increasingly important. The hardened properties are influenced by the direction of application of the load with respect to the printed layer which was investigated in [9–14] with compression and flexural test. Another important factor is the time interval between the layers which was studied under different conditions. Marchment et.al. [11], Le et al. [14], and Panda et al. [15] studied the interface subjected to tensile action, while Napolitano et al. [16] studied the interface behaviour under shear action. They all came to the conclusion that a longer interval time leads to a decrease in interface strength, commonly referred as cold joint.
Moving to the large scale, although nowadays there are many prototypes that demonstrate the great potential of the 3D printing technology, a common approach to structural engineering has not been developed yet because of the lack or research result on structural performance of 3DPC members. Consequently, there is an urgent need for new design-to-fabrication approaches, as well as testing methods and standards. Due to the different properties of the 3D printed material, the standards usually employed for the construction of traditional concrete structures are not always applicable. Ideally, in 3D printed concrete elements the reinforcement should be placed automatically to enable the digital manufacturing of the entire structural element, but nowadays most reinforcements are still placed manually. Most of the existing building prototypes uses the 3D printed concrete as a lost formwork and traditional concrete elements as load-bearing. The printing of load-bearing structures requires extensive preliminary experimental investigation to support structural design, but there are only a few examples in the literature demonstrating how 3D printed concrete structures can be evaluated for structural integrity. These include the flexural tests performed on two bridges, nowadays located in Gemert [17] and in Nijmegen [18], as well as the compression and out-plane tests conducted on the walls of the 3D printed houses in Eindhoven [20] and Beckum [19], which are the only example where the 3D printed walls are used as load bearing.
Given this background, it is evident that there is a need to establish common approaches and guidelines. The thesis took advantage of collaborations between

research institutes (University of Brescia, ETH) and industrial partners (Cybe, Italcementi, BASF and Knauf gips KG). Thanks to these collaborations, which provided valuable expertise, the thesis played a central role in the advancement of solutions for the creation of 3D concrete structural elements. The development of these solutions focused on two main aspects: the study of the material and the investigation of the structural characteristics of the elements. Throughout the process, the introduction of innovations in the material had an impact on the design of the structural elements and vice versa. As consequence, the materials initially studied underwent subsequent transformations, making any comparison between them less relevant. Therefore, the significance of this thesis is not in the comparison of the performance of the materials used, but rather in the development of test methods and the interpretation of the results, which establish fundamental principles for the structural design of 3D printed concrete elements.

1.2 Objectives and scope of the research

The aim of the thesis is the study on the structural behaviour of 3D printed concrete elements with particular focus on 3DPC walls made by extrusion process.
The main objectives of this thesis are the development of methodologies to assess the hardened properties of 3D printed materials and the structural behaviour of 3D printed concrete walls.
Experimental and numerical research studies were undertaken to address the aim of this thesis. Regarding the development of methodologies to study the hardened properties of 3D printed material, the following stages can be identified:

1. characterization of compression, flexural, tensile properties adopting tests setup commonly used for traditional concrete;
2. development of two tests methodologies to assess the shear properties of the printed material with a particular focus on the effect of the interface between the layers;
3. development of numerical analysis to predict the interlayer behaviour between the concrete layers.

Considering the assessment of the structural behaviour of 3DPC walls the following steps can be identified:

4. investigation of the main thermal, geometrical and mechanical parameters through analytical models and numerical analysis to optimize the design of 3DPC concrete walls;
5. assessment of the structural performance of the 3DPC walls with in-plane quasi-static cyclic tests;
6. development of analytical calculations and numerical analysis to predict the structural performance of 3DPC walls.

1.3 Organization of the thesis

This thesis presents the work undertaken to study the structural behaviour of 3D printed concrete walls. The program addressed in this thesis and the research objectives are reviewed in Chapter 1.

Chapter 2 focuses on the state of the art. Firstly, the main aspects regarding the rheology of the material are explained. Subsequently, the common tests that are carried out to characterize the mechanical properties of the 3D printed material both at fresh and at hardened state will be shown. In conclusion, the main existing printed prototype and the main structural tests on 3D printed concrete elements will be discussed.

Chapter 3 focuses on the characterization of the hardened properties of 3D printed concrete. Firstly, the compressive, the flexural and the tensile strength are experimentally investigated using set-up already presented in the literature. Subsequently, the attention is focused on the study of the interface strength of 3D printed concrete under shear load. Two test set-up will be proposed: the modified push-out test and the modified slant shear test. Those tests are typically used for masonry and concrete structures, respectively, but they will be adapted to the specific case study.

Chapter 4 presents the design and testing of 3DPC walls. Firstly, the main thermal, geometrical and mechanical parameters to optimize the design of 3DPC walls will be identified through numerical analysis and analytical models. To validate the model proposed, a thermal test on a 3D printed concrete walls is performed in order to calculate the thermal performance of the wall. Subsequently, in-plane quasi-static cyclic test are performed on five 3DPC walls. Four walls are unreinforced, while one wall is reinforced.

Chapter 5 presents the numerical analyses carried out to predict the interface behaviour of 3D printed concrete elements and the structural performance of 3D printed concrete walls.

Chapter 6 presents the integration of structural and thermal design of 3DCP technology which is discussed with regards to a two-story reference building.

Finally, Chapter 7 summarizes the main findings, provides conclusions, and discusses recommendations for future work.

2 LITERATURE REVIEW

This chapter presents an extensive literature review on the digital fabrication of concrete (DFC), with a focus, among different technologies, on the extrusion process. The main objective is to provide a summary of current studies and knowledge in the field and to highlight the most urgent needs. The chapter begins by describing the most common technologies and prototypes built using 3D printing concrete extrusion, with a focus on the load-bearing system. In order to gain an in depth understanding of the material and processes, the chapter also presents the main rheological properties of the printed material and the most common procedure for evaluating the material properties in the fresh state related to the stability of elements during printing. Furthermore, the main differences between 3D printed concrete and traditional concrete in the hardened state are clarified and the most common experimental procedures to investigate the hardened properties of 3D printed material are illustrated, focusing mainly on the influence of anisotropy and the effect of the time interval between layers. As the technique is still in its infancy, it comes out the need to find common approaches and guidelines. Moreover, considering large scale elements, structural tests are required to evaluate the performance of 3D printed concrete elements to be used as load-bearing structures. In the literature there is a lack of research studies on the structural behaviour of 3D printed members. A few structural tests are documented in recent research studies investigating the behaviour of beams and walls, which are described in detail in the following sections.

2.1 3D printing techniques

Several digital fabrication approaches have been developed in the last few years: 3D Concrete Printing, Contour Crafting and Particle-Bed Printing.

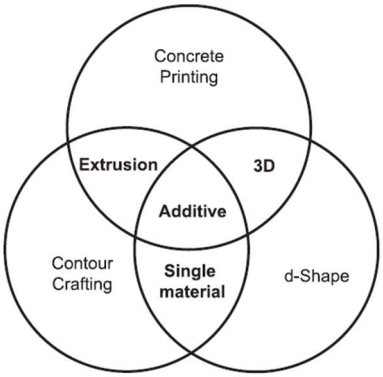

Figure 2-1: Similarities and differences in additive manufacturing [20].

The *Contour Crafting* was developed at the University of Southern California (US) which used extruded clay as permanent formwork, filling the central section with conventional cast concrete to construct a vertical wall [21–23].

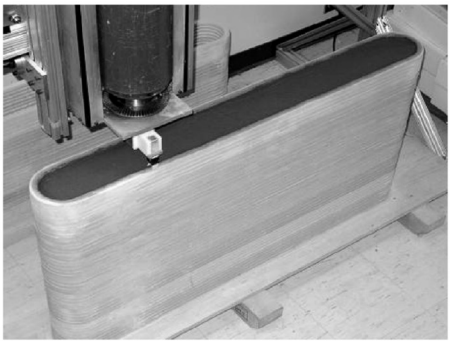

Figure 2-2: Wall sections build by contour crafting technique [21–23].

The *D-Shape* or *Particle-Bed Binding* was developed by the Italian Engineer Enrico Dini and it consists in an additive manufacturing process in which particles of material are joined using a bonding agent [24,25]. In general, the printing process consists of two repetitive steps. Firstly, a layer of dry particles is spread over the printing area with a uniform thickness of about 5 to 10 mm. Then a binding agent is deposited on the particle bed by means of a print head. This process is repeated in series until the component is complete. Once cured, the non-bonded particles are removed in a post-processing step of de-powdering.

The first example is from 2008 with the Radiolaria Pavilion. An other example is the 12 m long and 1.5 m wide footbridge, installed in Madrid by Acciona in 2017 [25,26].

(a) (b)

Figure 2-3: D-Shape case study: (a) Radiolaria Pavilion [24]; (b) the footpath bridge in Madrid by Acciona [25,26].

The *concrete printing* was developed at Loughborough University (UK) and used extrusion of cement mortar; it was developed to allow for three-dimensional freedom [27,28]. Figure 2-4a shows a free-shaped wall [27] and Figure 2-4b the double-curved panels with conformal voids manufactured at Loughborough University in 2011 [28].

(a) (b)

Figure 2-4: Concrete printing show case: (a) free-shaped wall [27]*, (b) double-curved panels printed with conformal voids* [28].

2.2 Existing examples of 3d printed concrete elements

In recent years, numerous large-scale projects have been completed around the world, demonstrating the potential of 3DPC technology. In this section, some bridges and low-rise buildings printed with the extrusion process are illustrated and explained.

The first example is a bicycle bridge built in Gemert, the Netherlands, in 2017 (as shown in Figure 2-5a). The Eindhoven University of Technology used an additive manufacturing technique based on material extrusion to build the bridge [29]. The structure consists of six horizontally printed elements that were rotated 90° after

production. The elements were bonded with epoxy resin and then prestressed with unbonded post-tensioned tendons. The tendons were fixed in traditional cast-in-place concrete blocks located at both ends of the bridge. A high-strength steel reinforcement cable is positioned through the cable reinforcement device in the bottom 10% of the layers of each of the six element. The cable acts as passive reinforcement in the transverse direction, while the prestressing tendons provide active reinforcement in the longitudinal direction of the bridge. Another example is the pedestrian bridge developed through the collaboration between the Technion Israel Institute of Technology and the Ghent University of Technology [30–32], as shown in Figure 2-5b. The beam shape was optimised using topological optimisation and it was made of multiple concrete segments post-tensioned with tendons, similar to the former bridge built in Gemert.

(a)

(b)

Figure 2-5: Case study projects: (a) Bycile bridge in Gemert (the Netherlands), (b) optimized girder (Ghent University and Israel University).

Figure 2-6a refers to the BOD office building [33] which was printed on-site with an extrusion-based additive approach by COBOD in Nordhavn, Denmark in 2017. It was the first 3D construction printing project in Europe to receive approval from a municipality. The printing process was used for building the walls, which were not considered as load-bearing, and the formworks of the eleven structural columns. The structural columns were then casted and reinforced using standard practices during concrete printing to support the roof. This allowed the structural elements to be produced according to existing codes, with the printed parts serving as permanent formwork. The roof, windows, doors, and surface finishes were installed using standard building practices.

Figure 2-6b illustrates the B-Hut printed in Illinois (USA) by the US Army Corps of Engineers [34]. The intent of the case study was to investigate the feasibility of printing standard structures with locally sourced materials, instead of building them with timber or masonry blocks. The structure consists of a reinforced concrete foundation slab that was cast in-situ. The 3D printed walls were used as permanent formwork with a hollow core that was reinforced and filled with concrete after fabrication, they were connected to the foundation and the roof by dowels bars. The roof is composed of reinforced concrete precast slabs and the walls carry the vertical loads of the roof.

Figure 2-6c shows the DFAB house in Dubendorf, Switzerland, which features two innovative construction techniques: Smart Dynamic Casting and Mesh Mould. The reinforced façade mullions (Figure 2-6c1) were manufactured using Smart Dynamic Casting [35–38], an extrusion process that shapes concrete when it is still plastic but have enough strength to support its own weight. The 15 mullions were each designed with a different shape and were 3 m high. The production time was around 8 hours in total per mullion. The Mesh Mould technology was used to produce a 12 m long and 120 mm thick double curved wall (Figure 2-6c2) at the first floor of the DFAB house [39]. A double-sided welded steel reinforcement mesh was produced on site, which was then filled with a special concrete mix that achieved sufficient compaction without flowing out the mesh, eliminating the need for formwork. The Smart Slab (Figure 2-6c3), which is the floor supported by the Mesh Mould wall, was designed as a post-tensioned structure with ribs parallel and perpendicular to the supporting Mesh Mould wall [40]. Each of the eleven prefabricated concrete segments was mounted on site using scaffolding until the activation of the post-tensioning. The ribs transversal to the Mesh Mould wall carry the main load, while the secondary ribs parallel to the wall carry post-tensioning strands used to compress the joints between the prefabricated segments. The Smart Slab is an example of a conventional concrete structure built with a digitally fabricated formwork.

Figure 2-6d shows the temporary installation of a 100m² 3d printed house that was on show in Milan in 2018 during the design week [41]. The house is composed of 30 modules printed separately and structurally connected with steel plates at top and bottom of the wall. The roof deck is composed of primary timber beams and plywood panels used as a diaphragm.

Figure 2-6e shows the first residential building in Beckum, Germany [19], which is a two-storey house with an area of 80 m² per floor, printed on site by PERI. The structure is characterised by three types of printed walls: i) non-load-bearing walls, ii) structural walls of printed lost formworks with unreinforced cast concrete, and iii) double-shell walls with a non-load-bearing outer shell and a load-bearing inner shell or 3D printed formwork filled with cast concrete. The roof of the building consists of an in-situ cast reinforced slab. The transfer of vertical loads takes place by means of walls and columns made of non-reinforced in-situ concrete (C25/30), which

guarantee the stability and stiffening of the building even without the 3D printed load-bearing elements. The geometric design of the walls and columns is provided by printed formwork that is not used for load transfer.

ApisCor [42] printed on-site a two-storey administrative building for the municipality of Dubai (Figure 2-6f) which was completed in 500 hours. The 3D printed structures served as lost formwork and were filled with reinforced concrete, which acted as a load-bearing structure.

Figure 2-6g shows the Milestone project [43], which consists of five 3D printed residential houses built in Eindhoven, the Netherlands. The designs of the houses aim to demonstrate the design freedom offered by 3D printing technology. All the houses are planned to be inhabited. The first house was completed in April 2021, it is a single-story house with an area of approximately 94 m^2. The 3D printed wall elements performed the primary load-bearing function and supported the entire roof structure. Consequently, the aim was to use less material (thinner walls) and exploit the flexibility of the form to achieve more rigid walls through curvature.

It should be noted that the projects mentioned above demonstrate the significant potential of 3D printing by extrusion. However, in most cases, the load-bearing part of the structure consists of traditional reinforced concrete elements, while the printed parts are used as lost formwork. Although 3D printing of concrete is similar to traditional concrete in many aspects, there are also several differences, such as layered structures and construction without formworks. Currently, there are challenges to be addressed, such as the evaluation of material properties, calculation input, reinforcement integration, and verification of the structural behaviour of 3D printed concrete elements. There is a need to establish standardised procedures for characterising the material properties of 3D printed concrete in both the fresh and hardened state, as well as to conduct large-scale tests to evaluate the structural behaviour of 3D-printed concrete elements so that they can be used as load-bearing structures. The following sections of this chapter will illustrate the current state of the art regarding the evaluation of the material properties of 3D printed concrete elements in the fresh state (Section 2.3) and in the hardened state (Section 2.4), as well as the few projects in the literature that study the structural performance of 3D printed concrete elements (Section 2.5).

(a)

(b)

(c 1)

(c 2)

(c 3)

(c 4)

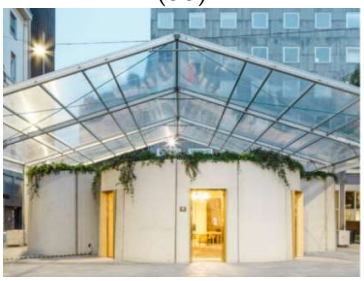

(d)

(e)

(f)

(g)

Figure 2-6: Case study projects: (a) BOD office building [33]; (b) B-Hut [34]; (c) DFAB house [35–40] ; (d) 3D Housing 05 [41]; (e) Beckum house [19] ; (f) Dubai office [42]; (g) Milestone house [43].

2.3 Fresh properties of 3d printed concrete

Within this thesis the attention is focused on the extrusion process, which is commonly characterized by 5 steps (Figure 2-7): 1) material delivery to the print head, 2) print-head process, 3) deformation of the material during deposition, 4) mechanical loading after deposition and 5) behaviour of material after deposition.
The comprehending of the processes is a prerequisite for the design and optimization of digital fabrication systems. This section begins with an overview of the rheological characteristics of the material. Following this, the most significant factors to consider during the printing process, extrusion, and deposition of the material will be addressed. Moreover, the experimental tests used to study the properties at fresh state are described.

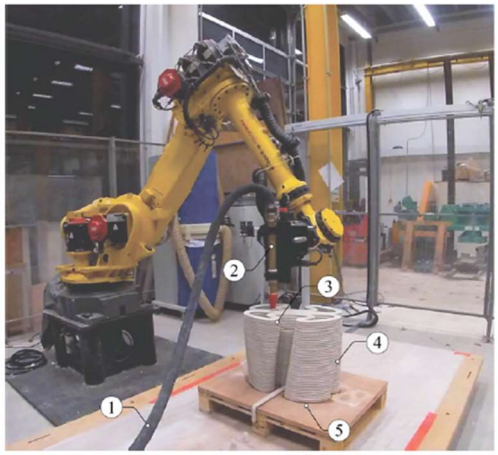

Figure 2-7: Steps of extrusion process [44].

2.3.1 Rehology of printable material

In their fresh state, cementitious materials behave as visco-plastic materials. Figure 2-8a shows their behaviour as an elastic solid under a critical stress (called yield stress τ_c), and critical shear strain γ_c, and as a viscous fluid when the stress and strain in the material exceed the critical values. Their modulus of elasticity in shear can be expressed as $G = \tau_c / \gamma_c$.
During transportation (pumping, extrusion) in extrusion-based additive manufacturing, the visco-plastic behaviour governs the flow profile, whereas elasto-plastic properties govern the shape of the deposited layer [45]. Gravity acts on the material after extrusion, and the material will flow if the gravitational forces are greater than the yield stress at the bottom layer. As further discussed, the thixotropy of these materials and their capacity to form an internal structure at rest (or during

exstrusion), is a crucial characteristic in the majority of printing applications [46]. The material has an initial critical shear strength τ_{c0}, strain γ_{c0} and an initial elastic shear modulus G_0 (Figure 2-8b). These rheological parameters change with time, and experimental results indicate that while $\tau_c(t)$ and $G(t)$ are increasing function of time, $\gamma_c(t)$ decreases with the time at rest [47,48] (Figure 2-8b).
In its initial phase, the progression of the yield stress is frequently assumed to be linear, with a structural build-up rate to be defined as A_{thix} [49–51], and it can be described as:

$$\tau_0(t) = \tau_{0,t=0} + A_{thix}t \qquad 2\text{-}1$$

With $\tau_{0,t=0}$ the shear yield stress of the material in a destructured state and t being the duration of the resting period of the material. After a linear behaviour, the evolution of the yield stress can be described by an exponential relationship [52] tending to a linear model for short time periods after material deposition:

$$\tau_0(t) = \tau_{0,t=0} + A_{thix}t_c(e^{\frac{t}{t_c}} - 1) \qquad 2\text{-}2$$

With t_c is a characteristic time over which the behaviour can be considered linear. Equation 2-2 can be used to describe the progression of the yield stress over longer periods. Increases in stiffness and strength enable the deposited material to withstand the growing forces associated with the printing progression of the structure. Taking into account the change in material properties over time, it is possible to calculate and predict the optimal printing speed to ensure the stability of the printed structure [53,54].

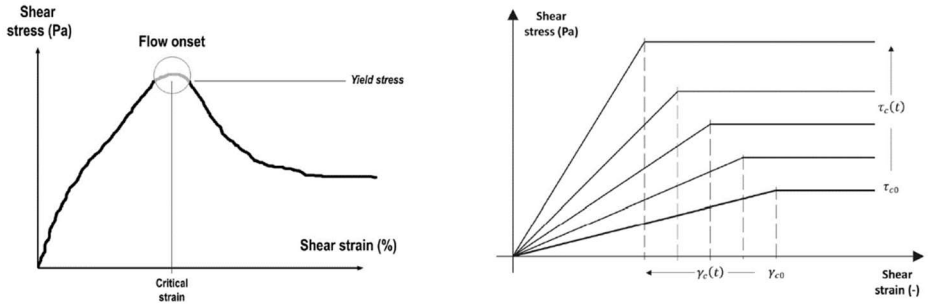

(a) (b)

Figure 2-8: a) Shear stress as a function of the shear strain, (b) shear stress vs shear strain for increasing resting time [45].

From a microstructural point of view, it has been demonstrated that the capacity of a cementitious material to display a yield stress and build up a structure at rest is due to the following mechanisms [50]:

a) Cement particles are disperse at the end of mixing (Figure 2-9a).

b) Due to colloidal attractive forces, cement particles flocculate and form a network of interacting particles that can withstand stress and have an initial elastic modulus G_0 and an initial yield stress τ_{c0} (Figure 2-9b). This phase is known as flocculation [50]. The material reorganises itself for several tens up to hundreds of seconds [50].
c) Simultaneously, at the contact point between particles hydrate nucleation occurs (Figure 2-9c). Locally, this nucleation transforms the colloidal interactions between cement particles into interactions with a higher energy level, which can be conceived roughly as solid bridges. As a consequence, the elastic modulus increases at the macroscopic scale.
d) An increase in the size or number of hydrate bridges causes a further increase in the elastic modulus and yield stress. (Figure 2-9d). This stage is known as structuration. On a microscopic scale, hydrate bonds are formed between particles as a result of a non-reversible chemical reaction.

To sum up, the transformation of a fluid into a solid-state material (structural build-up), which typically takes several hours, can be divided into reversible physical processes (flocculation induced thixotropy) and non-reversible chemical processes (hardening due to hydration/chemical reactions).

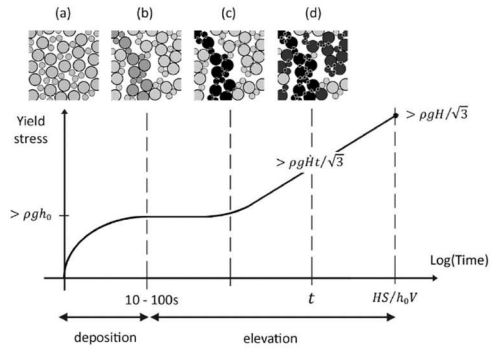

Figure 2-9: Interaction between cement particles with yield stress. H is the final height of the object, h_0 is the layer thickness, S is the contour length, V is the nozzle velocity and ρ is the printed material density [45].

Once the background on the rheology of printable material has been summarized, it is fundamental to present the rheological requirements, that are pumpability, extrudability and buildability, as presented by Le et al. [55].

2.3.2 *Pumpability*

The pumpability consists in the transport of the fresh material from the pump to the extrusion nozzle [55]. As the material has to be pumped and supplied into the robot and through the robot head, there are requirements for its initial fluidity or "pumpability" [56,57]. Therefore, it is expected that the yield stress and viscosity of the material should be as low as possible. Many factors can influence the pumpability as the technology used, the pumping distance and the pump diameter. Additionally, it is essential to regulate the printing speed and the pumping pressure.

2.3.3 *Extrudability*

The extrudability is the ability to extrude the mix through the nozzle without considerable cross-sectional deformation [55].
Three type of extrusion can be identified: the *infinite brick* (Figure 2-10a) in which the filament and the nozzle cross-section are equal. The material exits the nozzle as a stiff continuous and non-deformed filament. The deposited material is already flocculated as it was not sheared in the nozzle and already exhibit a yield stress. Its shape is entirely imposed by the nozzle cross-section.
The *free flow* deposition (Figure 2-10c) in which the material flows freely until the stress caused by the gravity equals the yield stress of the printable material. A structure and a yield stress are created until the final shape is reached. In reality the real behaviour lies in between these two approaches and it can be described as the extrusion of a sufficient stiff material through a nozzle with a geometric reduction (Figure 2-10b).

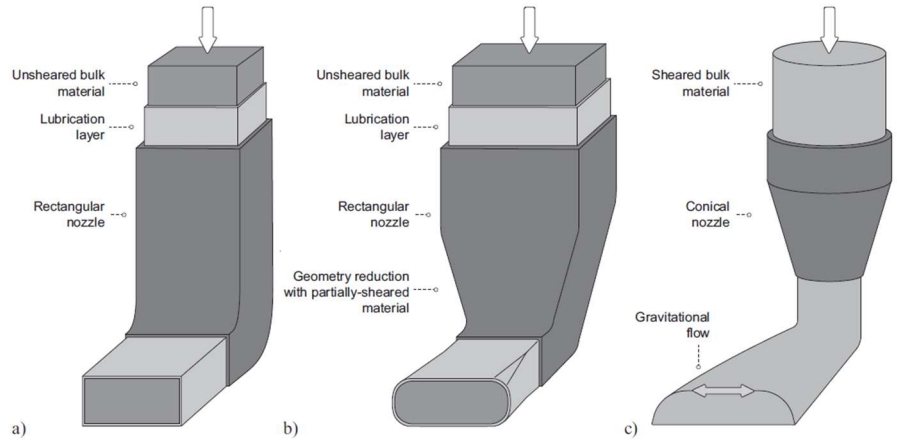

Figure 2-10: Material extrusion: (a) infinite brick strategy, (c) free flow deposition and (b) is the more realistic situation [58].

2.3.4 *Buildability*

The buildability consists in the creation of "bridges" between particles and it is the resistance of a printable mortar against collapse during printing. It refers to the ability to print a certain number of layers [55].
The absence of formwork is a common characteristic in digital fabrication processes. While this is clearly advantageous from a productivity and sustainability point of view, the possibility of collapse is more likely during the printing process, which is nearly impossible with conventional concrete casting due to the support given by the formwork. This issue is not irrelevant because the concrete does not begin to harden until sometime after deposition.
The collapse of an element during printing is caused by its bucking due to the loads acting on it. In the simplest assumption, it consists of the centred self-weight of a layer and those stacked on top of it. Consequently, as the height of an object increases, the stresses caused by gravity increase. The critical layer is the bottom one, as it is the first to be extruded and is therefore loaded by all the material subsequently deposited. However, as depicted in Figure 2-11, a several load types may also occur during the manufacturing process. They depend on both the process and the characteristics of the object's design. For instance, imperfections or oscillations in the process that lead to misalignment of subsequent layers can cause eccentricities and imperfections. Additionally, it should be noted that a print object may be subjected to kinetic stresses caused by the deposition of material in addition to static loads [59]. The studies [59] indicate that the dynamic loading is dependent on process parameters such as filament pressure, nozzle speed, filament dimensions, and layer height.

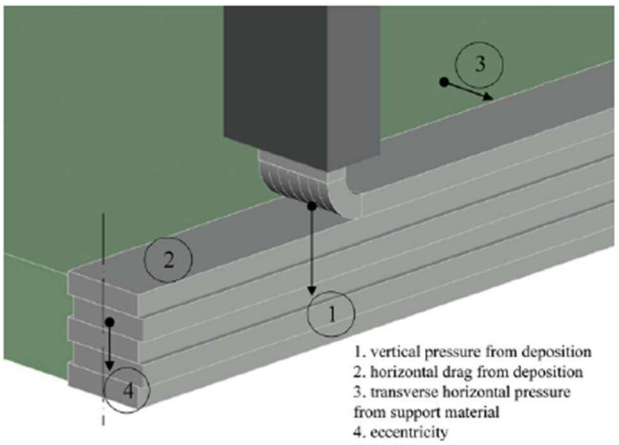

Figure 2-11: Loads acting on a wall during printing in addition to the self-weight [60].

Two different mechanisms have been identified to cause collapse in DFC based on material extrusion:

- *Plastic collapse or material failure* which occurs when the strength of the material is exceeded causing a fracture or deformation due to yielding or flow;
- *Buckling or stability failure*, is when the object loose the stability because it cannot withstand equilibrium of forces.

These mechanisms often interact, but it is generally one or the other that initiates the collapse. Which mechanism is governing depends on many factors like the material and the process characteristics, the printing speed, the size of the printed object etc.
There are many approaches in the literature to take into account the failure mode. Di Carlo et al. [5] investigated the strength and rigidity properties of a fresh print mortar using a uniaxial compression test. The experiment were reproduced in a Finite Element Model (FEM) in which a Drucker-Prager failure criterion was applied. Alternatively, Perrot et al. [53] presented a buildability approach based on the rheological yield stress τ_c of the print mortar as the material failure criterion. This model is described by:

$$\alpha_{geom}\tau_0(t) \geq \rho g h(t) \qquad 2\text{-}3$$

Where α_{geom} is a geometrical factor, $\tau_0(t)$ the time dependent yield stress of the mortar, ρ its density, g the gravitational acceleration, and $h(t)$ the time dependent object height.
The model was validated by the results of an experimental campaign.
Wangler et al. [54] adopted similar approach, but the von Mises plasticity criterion was applied, by introducing a factor $\sqrt{3}$ into the buildability equation:

$$\tau_0(t) \geq \rho g h(t)/\sqrt{3} \qquad 2\text{-}4$$

Wolfs et al. [48,61] introduced for the first time a method that considers both material and stability failure in a numerical FEM approach. Their approach involved the development of the geometrical and material properties over time. On the contrary with respect to the rheology based approach, in order to take into account both failure modes, this method requires more experimental parameters to be determined, which are function of the time, as the Young's modulus E(t), Poisson's ratio v(t), cohesion C(t), angle of friction $\phi(t)$, and dilatancy angle $\psi(t)$. These properties were obtained through uniaxial unconfined compression and shear box tests with different vertical load ratios, which allowed, in contrast to the experimental campaign implemented by di Carlo et al. [5], the determination of the full material failure envelope and thus the analysis of multi-axial stress states induced by various loads.
Suiker et al. [62,63] subsequently developed a parametric mechanistic model based on the same assumptions and experimental data as Wolfs et al. [48,61], which allows

for efficient analysis of strength and stability behaviour in wall-type structures printed (Figure 2-12).

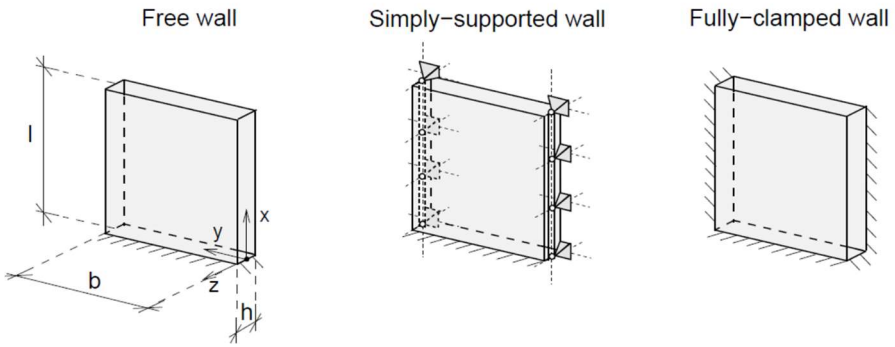

Figure 2-12: Configuration of the wall: free wall, simply clamped wall and fully clamped wall [62].

Three parameters for elastic buckling were defined:

$$\overline{l_{cr}} = \left(\frac{\rho g h}{D_0}\right)^{\frac{1}{3}} l_{cr} \qquad 2\text{-}5$$

$$\overline{b} = \left(\frac{\rho g h}{D_0}\right)^{\frac{1}{3}} b \qquad 2\text{-}6$$

$$\overline{\varepsilon_E} = \left(\frac{D_0}{\rho g h}\right)^{\frac{1}{3}} \frac{\varepsilon_E}{i} \qquad 2\text{-}7$$

Where l_{cr} is the critical buckling length, b is the length of the wall, ε is the curing rate, I is the printing velocity and D_0 is the initial bending stiffness expressed as $D_0 = \frac{E_0 h^3}{12(1-\nu^2)}$.

In addition, two parameters for plastic buckling expressed as:

$$\overline{\varepsilon_\sigma} = \frac{\varepsilon_\sigma \left|\sigma_{p,0}\right|}{\rho g i} \qquad 2\text{-}8$$

$$\overline{l_p} = \frac{\rho g l_p}{\left|\sigma_{p,0}\right|} \qquad 2\text{-}9$$

Where l_p is the length of the wall in correspondence of plastic collapse, $\sigma_{p,0}$ is the yield strength at onset of the printing process.

The failure criteria was evaluated as:

$$\frac{\overline{l_p}}{\overline{l_{cr}}} < \overline{\Lambda} \qquad \text{elastic buckling} \qquad 2\text{-}10$$

$$\frac{\overline{l_p}}{\overline{l_{cr}}} > \overline{\Lambda} \qquad \text{plastic collapse} \qquad 2\text{-}11$$

With

$$\Lambda = (\frac{h}{D_0})^{\frac{1}{3}} \frac{|\sigma_{p,0}|}{(\rho g)^{\frac{2}{3}}} \quad 2\text{-}12$$

Furthermore, Roussel proposed an alternative model [45] that accounts for both material and stability failure. Based on the research conducted by Wolfs et al. [48,61], it is anticipated that strength-based failure would be critical below a certain height, whereas buckling would become the critical failure mode above this height. The critical height H_{cr} at which stability failure is expected to occur for one linear meter slender wall subjected to its own weight can be expressed as:

$$H_c = (\frac{8EI}{\rho g A})^{\frac{1}{3}} \quad 2\text{-}13$$

$$E = \frac{3\rho g H^3}{2\delta^2} \quad 2\text{-}14$$

Where E is the elastic modulus of the material, I is the quadratic moment of inertia, A is the horizontal rectangular cross-sectional area, and δ is the width of the wall. This model was also applied by Casagrande et al. [6] and by Esposito et al. [64] to investigated how many layers can be printed during a general printing process before failure occurs.

Within this section the basic physics behind printable materials were explained. It came out that besides yield stress and viscosity also the yield stress evolution and the elastic modulus plays an important role. As consequence, the characterization technique for the fresh state properties are briefly discussed.

2.3.5 Measuring methods

The properties at fresh state are of great importance to control the processing phases in digital fabrication, (e.g. pumping and extruding). Due to the absence of confinement by traditional formwork, which characterises the majority of digital fabrication processes, the mechanical properties of fresh concrete and their development in time are of vital importance to control the structural behaviour during the fabrication process and prevent collapse. To accurately attribute the properties to a specific age and eliminate any effects from ongoing flocculation and hydration, tests on the fresh material should be conducted quickly.

2.3.5.1 Compression test

There are several studies in the literature for the assessment of the compression properties of fresh 3D printed concrete [5,6,48,53]. Compression tests can be used to determine the compressive strength, Young's modulus, and Poisson's ratio of fresh

concrete, as well as their evolution as a function of the concrete age. Based on ASTM D2166, cylindrical samples with a height-to-diameter ratio between 2.0 and 2.5 are typically used. The unconfined compressive strength is defined as the maximum stress value, the Young's modulus and Poisson's ratio are derived from the stress-strain relationship in the linear branch. However, a compression test is not suitable for testing multi-axial stress states. Figure 2-13b depicts the average relationship between stress and strain, indicating the transition from a plastic state towards a brittle failure. Figure 2-13c displays the failure modes of compressed specimens at various ages between 5 and 90 minutes after extrusion [48]. The laws of the variation of the elastic modulus and of the compressive strength with time were obtained.

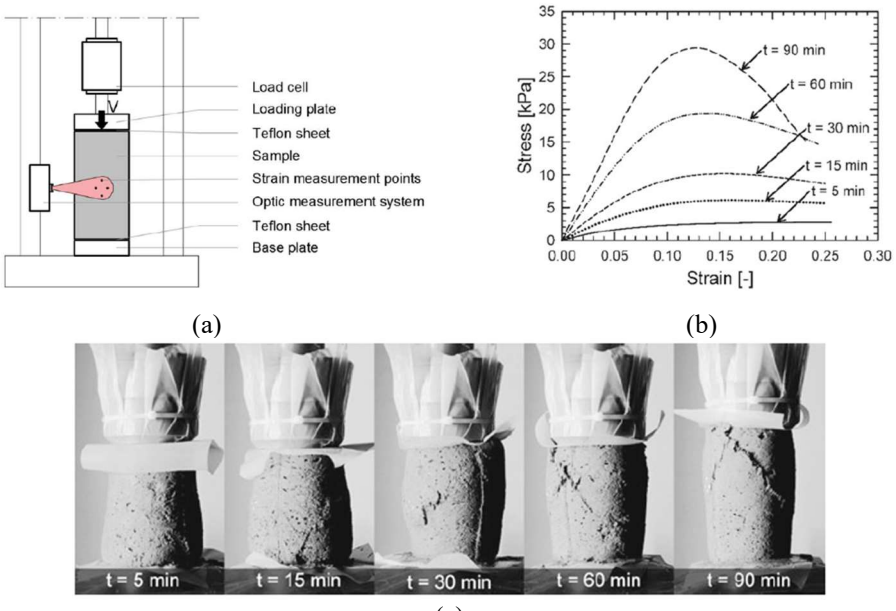

Figure 2-13: Uniaxial unconfined compression test: (a) schematic of the test; (b) average stress-strain relationship for each concrete age and (c) failure modes [48].

2.3.5.2 *Shear test*

Fresh concrete can undergo shear tests to establish a failure criterion and observe its evolution over time. There are various types of shear tests available, such as those outlined in ASTM D2166 or D6128, but they all essentially involve the horizontal displacement of a two-part specimen, typically cylindrical, as shown in Figure 2-14a. One part remains fixed while the other is horizontally displaced by an external load. Prior to shearing, a constant normal force can be applied to the specimen in the vertical direction. The maximum shear force can be used to derive the shear strength of the specimen. The stiffness properties cannot be accurately determined using this test. A failure criterion, well represented from the Mohr-Coulomb theory, can be constructed by deriving the shear strength for various vertical forces applied [8,48]. This criterion is based on two material parameters, cohesion, and angle of friction. Figure 2-14 shows the stress-strain relationship for each concrete age; similar to the compression test the material exhibit a transition from a plastic behaviour at early age to a brittle failure for older specimens. This is shown from the initial mild decrease of force for early age concrete (0 min, 15 min and 30 min) to a steep drop of force for older age concrete (60 min and 90 min).

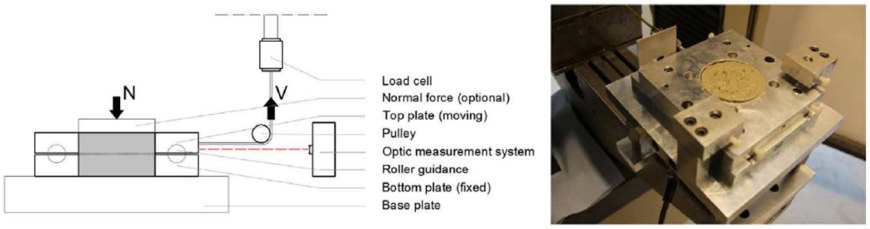

(a)

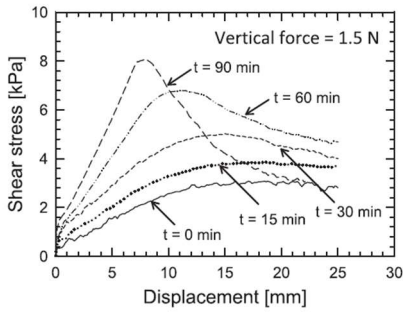

(b)

Figure 2-14: Direct shear test: (a) schematic of the test and (b) average stress strain relationship for each concrete age [48].

2.3.5.3 *Triaxial compression*

A triaxial compression test is a suitable method to obtain all the necessary properties required to define a failure criterion for fresh concrete, including those needed to assess both failure by elastic buckling and plastic collapse. According to ASTM D2850, a specimen is subjected to a constant confining pressure and then to a vertical force until failure (Figure 2-15). Like the compression test, triaxial tests are conducted on cylindrical samples with a height-to-diameter ratio between 2.0 and 2.5, which enables the induction of a shear failure plane. By measuring the specimen deformation and vertical force for various confining pressures, a failure criterion can be derived, such as the Mohr-Coulomb criterion, which has been found to be suitable for fresh concrete [61]. Therefore, experimental testing is necessary to obtain five time-dependent material properties, including cohesion C(t), angle of friction ϕ(t), dilatancy angle ψ(t), elastic modulus E(t), and poisson ratio ν(t), which are required for the structural analysis of the printed object.

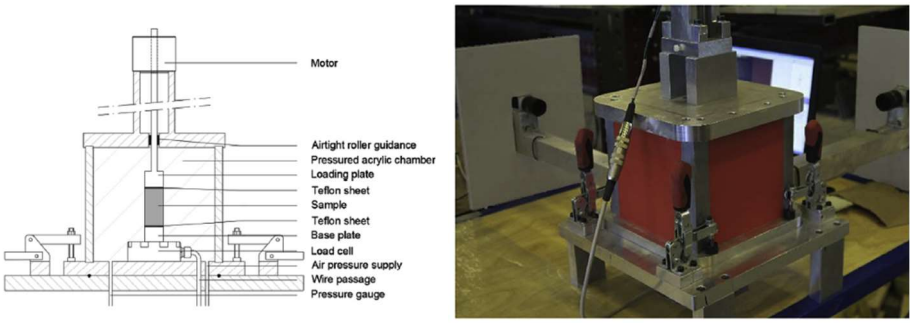

(a) (b)

Figure 2-15: Triaxial compression test setup [61].

2.3.5.4 Tensile test

Fresh concrete can undergo a tensile test to determine its tensile strength and how it develops over time [47,65]. This test involves the use of a mould with two parts that can be separated horizontally, with one part being fixed, see Figure 2-16. The force required to cause failure of the sample is used to determine the specimen's tensile strength. A round notch can be made on the specimen to induce controlled failure at the centre without introducing peak stresses.

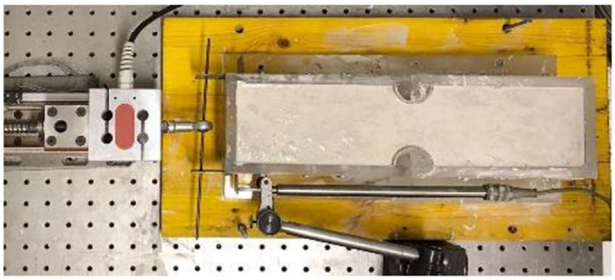

Figure 2-16: Tensile test setup [65].

2.4 Hardened properties of 3d printed concrete

The hardened properties of 3D printed concrete material, as well as the properties in the fresh state, play an important role in influencing the structural performance of a 3D printed concrete structure. Unlike traditional casting methods, in which concrete is poured and vibrated in a formwork to create a homogeneous and isotropic structural element, 3D printed concrete is anisotropic as it is built up from different layers. Consequently, the role of interfaces will become increasingly important. This section aims to explore current practices for evaluating the hardened properties of 3D printed concrete and to provide an overview of the parameters that influence the hardened properties of a printed cementitious material.

The overall strength of a printed specimen can be influenced by various parameters, such as the direction of the load with respect to the printed layer, the interlayer interval time, the print path, the speed of the print head, the height of the print nozzle, the composition of the mix (water/cement ratio, aggregate size and cement size relative to aggregates), the addition of fibres, surface preparation, the compressive strength of the weakest bond layer, the moisture content of the substrate, curing conditions, void content and reinforcement crossing the interfaces. In this chapter the attention is focused on the direction of the applied load with respect to the printed layer and the interlayer interval time. Available studies typically conduct tests in three different orthogonal directions to account for the impact of anisotropy. Various definitions have been used for these directions. Bos et al. [66] suggested to define directionality in printing as a local coordinate system (u,v,w), where u represents the direction of the print path, v is perpendicular to u within the print plane, and w is perpendicular to the print plane (refer to Figure 2-17). It should be noted that this definition is incomplete when the specimens are not uniformly sized in each orthogonal direction, such as beams rather than cubes or spheres. Therefore, Mechtcherine et al. [67] proposed an expanded definition of directionality, which is composed by two letters (u,v,w) separated by a dot with the first letter indicating the axis of a normal force (or axis of rotation for a bending load), while the second letter the longitudinal axis of the specimen. This approach results in a total of nine possible directions for non-cubic specimens. For cubic specimens, the number of directions would be reduced to the previously known three directions (see Figure 2-18).

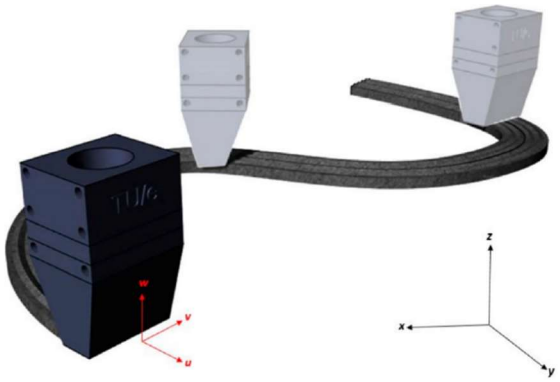

Figure 2-17: Definition of local axis system in printing proposed by [66].

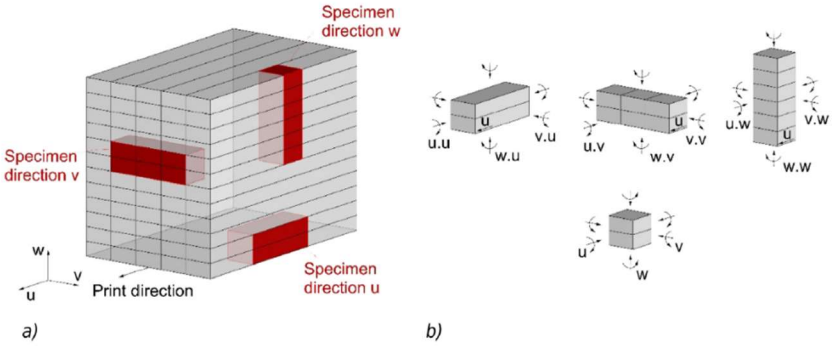

Figure 2-18: a) Definition of orientations of specimens and b) directionally of testing in relation to loading direction. The first letter indicates the axis of load, or of revolution in the case of a moment, the second indicates the specimen orientation [67].

The interlayer interval time between two successive layers in a construction process is a crucial parameter. On the one hand, the interval must be long enough to provide adequate mechanical strength to support the weight of the successive layers, but on the other hand, the time gap has to be short enough to ensure optimized bonding strength as well as building rate. Therefore, the ideal interval should be as short as possible to maintain the stability of the layer during construction (Perrot et al. [53]). Several studies [10,14,68] have shown that a longer interval leads to a decrease in interface strength, resulting in "cold joints". Cold joints occur when a critical resting time is exceeded. The critical resting time depends on material density ϱ, gravitational force g, layer height h, structural build-up A_{thix} rate and construction rate μ_p, as presented in Equation 2-15 [54].

$$t_c = \frac{\sqrt{\frac{(\rho g h)^2}{12} + (\frac{2\mu_p V}{h})^2}}{A_{thix}} \quad 2\text{-}15$$

Inadequately controlled interlayer intervals time can lead to cold joints at the interface, resulting in a decrease in the overall strength of the structure. To avoid discontinuities and minimise delays, the optimal time interval between layers must be carefully determined. New layers must be added after the previous layer has hardened sufficiently, but before it has hardened too much, and the fabrication speed must be designed accordingly.

With the increase of projects, the demand for reliable mechanical properties for use in structural calculations grows. However, as the printing process is significantly different from conventional concrete production methods, existing design codes that assume concrete homogeneity may not be fully compatible with the specific properties of printed elements. For example, test methods used in the field of repair mortars can be a source of inspiration for determining the bond strength between layers.

2.4.1 Compression test

The compressive strength of the 3D printed concrete material has been measured by means of a uniaxial compression test on cubic or cylindrical specimens, similar to traditionally cast concrete. To analyse the anisotropic behaviour and the layered structure, different loading directions with respect to the printed layers have been examined (see Figure 2-19) [10,11,14,68–72]. The materials considered within these studies were all different, with in common the use of cement as a binder and aggregates with a maximum diameter of 3 mm. The results showed that the compressive strength was slightly higher when loading according to orientation III (Figure 2-19), but the difference compared to orientation I was negligible with a maximum up to 10%. As consequence, the anisotropy resulted to have low influence on the compression properties. Other researchers have investigated other factors that may influence the compressive strength, such as the time interval between two successive layers (Nerella et al.[68] and Marchment et al.[11]). Nerella et al. [68] considered time gap of 1 minute, 10 minutes and 1 day. 1 minute is the minimum time required to print a layer, 10 minutes is the minimum time required to print a layer in large elements and 1 day represents an interruption in the construction process followed by a subsequent resumption. The decrease of the compressive strength with the time gap was around 5%. Marchment et al. [11] considered shorter time intervals of 10, 20 and 30 minutes. Also in this study a difference with the time gap of maximum 5% was observed. Therefore, the interlayer time gap was not considered to have a relevant influence on the compressive strength.

Nerella et al. [68] also studied different compositions, one with only Portland cement as binder and the other with a binder consisting of Portland cement, fly ash and micro-silica. It was reported that that the mixture containing additional cementitious materials showed superior performance with a compressive strength that was 30% higher than the material with only cement as binder. Furthermore, Panda et al. [10] used a glass fibre reinforced geopolymer mortar to investigated the influence of the fibre length and percentage in the mixture. The fibres resulted to slightly reduced the compressive strength of the mortar, probably because they were parallel to the loading direction and acted as voids depending on the ability of the matrix to accommodate them. A difference of about 20% between the mixture that contained 0.25% fibres and the one that contained 1% was observed.

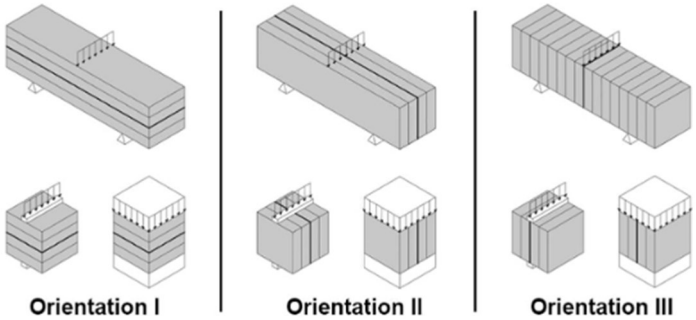

Figure 2-19: Printed layer orientation in flexural and compression tests [69].

2.4.2 *Direct tensile test*

The direct tensile test is also commonly called pull-off test (ASTM D7234-05) and it allows to evaluate the bond strength in tension of the interface. The specimens used for the characterization could have different geometries (Figure 2-20).

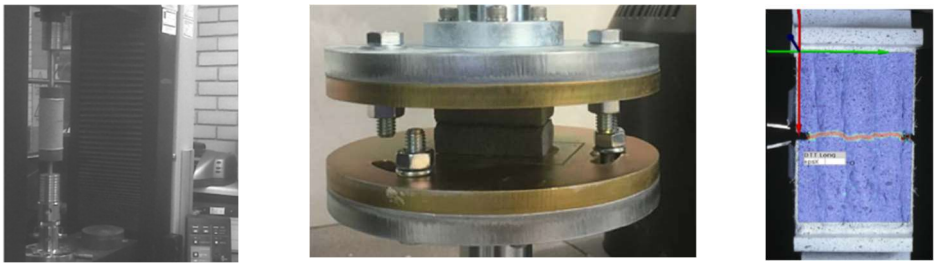

Figure 2-20: Different direct tensile test setup [14,15,72].

Many studies [11,14,15] have investigated the effect of the interlayer interval time on the interlayer bond strength considering orientation I (see Figure 2-19) with the load acting perpendicularly to the layers. Interlayer interval time between 0 min and 7

days have been investigated. Panda et al. [15] and Le et al. [14] found out that without cold joint the measured tensile strength was between 1.6 and 2.5 MPa, but it sharply decreased with a time interval of 15 min down to values around 0.7÷0.8 MPa, see Figure 2-21a. It was observed that up to a time interval of 30 min a reduction of the tensile strength of 50% was observed with respect to that of control specimens with 0 s interval time. After 30 min the decreasing becomes more gradual and some studies showed that the tensile strength was 0.7 MPa after 7 days [14]. Marchment et al. [11] considered a time gap of 10 min, 20 min and 30 min and the tensile strength was around 0.6 MPa. No substantial difference was found between these interval time. Van den Heever [72] conducted also a tensile test to measure the tensile strength according to orientation III (see Figure 2-19), which resulted to be 50% lower than that measured in orientation I.

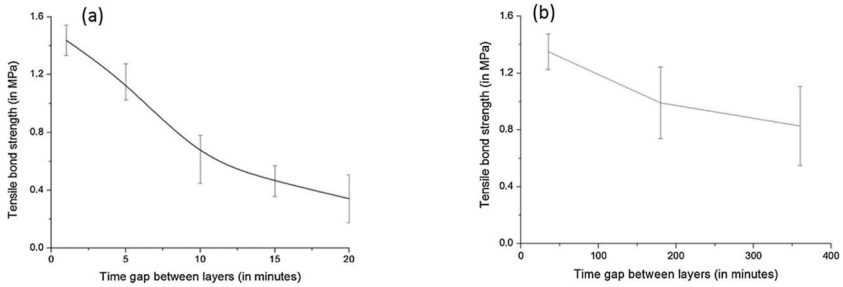

Figure 2-21: Effect of the time gap [15].

The specimens with a short time interval between the layers failed in the material, while the ones with a longer time gap failed at the interface (Figure 2-22).

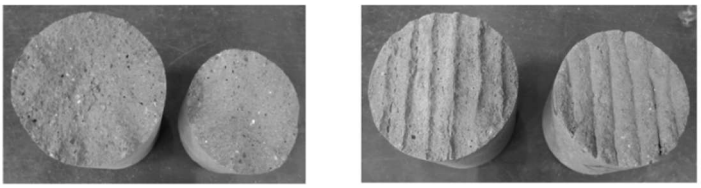

Figure 2-22: Failure mode [14].

2.4.3 *Flexural test*

The flexural strength can be measured through 3-point bending test on prismatic specimens (Figure 2-23), similar to mortar specimens.

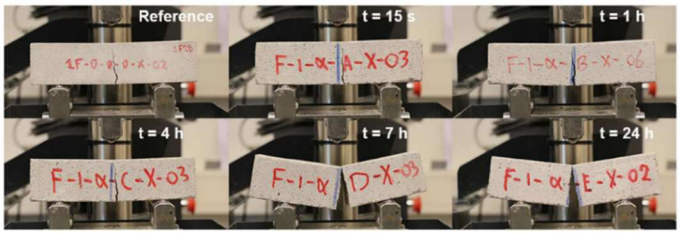

Figure 2-23: Flexural test setup [69].

Different test directions (see Figure 2-19) were considered to investigate the anisotropic behaviour [10,11,14,68–72]. The studies have indicated that the orientation of the applied load with respect to the printed layer has a greater impact on the flexural strength than on the compressive strength. Orientation I showed a higher flexural strength than orientation III in most studies, because in orientation I the maximum tensile stress acts parallel to the printed layer, while in orientation III tensile stresses act perpendicularly to the interfaces between layers , making the strength strongly dependent on the bond strength between adjacent layers. On average, the difference in strength between the different directions varies from 20% to 25%, with the exception of studies [14]-[70] where a greater dispersion was observed. Nerella et al. [68], Marchment et al. [11] and Wolfs et al. [69] conducted studies on the impact of the interval time gap between successive layers. In Nerella et al. [68], opposite to what was found for the compressive strength, it was observed that a long time interval (1 day) affected the flexural strength with a reduction around 20%. Marchment et al. [11] and Wolfs et al. [69] also confirmed this trend with a difference of flexural strength between the different directions of 25% and 16%, respectively. Furthermore, Nerella et al. [68] studied the effect of two different mixtures on flexural strength. The mixture with only cement as binder showed a higher flexural strength than the mixture with cement, fly ash and micro-silica as binder. However, the second concrete showed better resistance at the interface. Indeed, considering the material with just cement as binder a reduction in flexural strength of 91.9% (between a time gap of 2 min and 1 day) was registered, while with the second material only 23.1%. The formation of cold joints can be significantly reduced even over long time intervals by carefully selecting the material composition. Panda et al. [10] examined the impact of the addition of glass fibre with different length (3 mm, 6 mm and 8 mm) and different fibre content (0.25%, 0.50%, 0.75% and 1%) on flexural strength. While no significant influence on compressive strength was observed, an increase in flexural strength was noted with the addition

of fibres, both by increasing the length (increase of the flexural strength of about 13%) and the percentage of fibres (increase of the flexural strength up to 30%).

2.4.4 *Shear test*

Two tests have been identified in the literature to assess the interface strength under shear load. One of these tests, proposed by Napolitano et al. [16], is a modified version of the punch-through shear test. The test involves the induction of a sliding fracture along two identified surfaces. However, due to constraints related to the printing process, some modifications were made to the original setup and specimen geometry. The concrete test specimens consisted of seven layers, with the three middle layers positioned under the upper load plate and the two outer layers in contact with the lower supports (as shown in Figure 2-24). One steel corner 5 mm thick was placed on each side of the specimen as side supports, attached to the support plates with M6 screws. The dimensions and details of the set-up are shown in Figure 2-24.

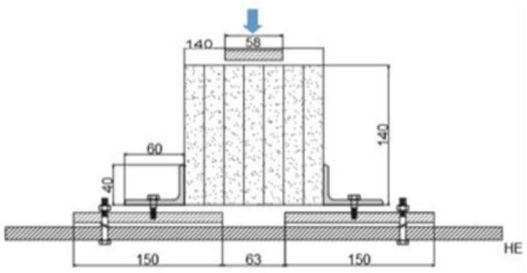

Figure 2-24: Shear test set-up [16].

In order to carry out the experimental tests, prismatic specimens were tested and compared with cast prismatic specimens. Three different groups of specimens were printed, each with a different interlayer interval time (100 s, 200 s, and 30 min). The results indicated that an increase in the interlayer interval time had an impact on the bond strength between layers. Even with a short time interval, the shear strength of the specimen was found to be 45% lower than the shear strength obtained from the shear test on the plain concrete elements. It is worth noting that regardless of the interval time, all specimens failed at the interface (Figure 2-25).

Figure 2-25: Failure mode [16].

Van der Heveer [73] proposes a direct shear test to evaluate the shear properties using cylindrical specimens. Different direction of load application with respect to the printed layers were considered (Figure 2-26). The sample testing configurations are presented in Figure 2-26. The shear apparatus is shown in *Figure 2-27*. This test allowed to define the failure criterion, well represented by the Mohr-Coulomb criteria. From the linear regression of the results, the coefficient of friction resulted almost equal to 45° in all the directions.

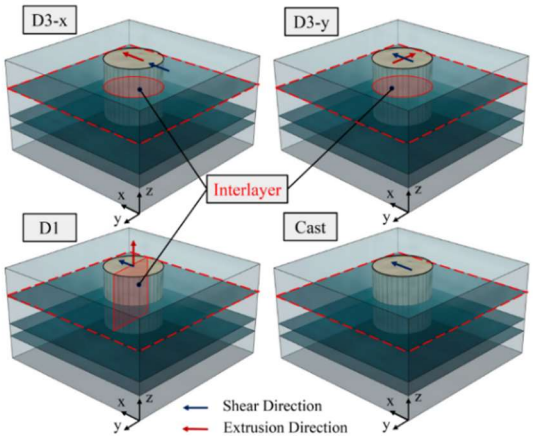

Figure 2-26: Sample configurations assessed through direct shear test. The blue arrow indicates the shearing direction, while the red arrow the printing direction [73].

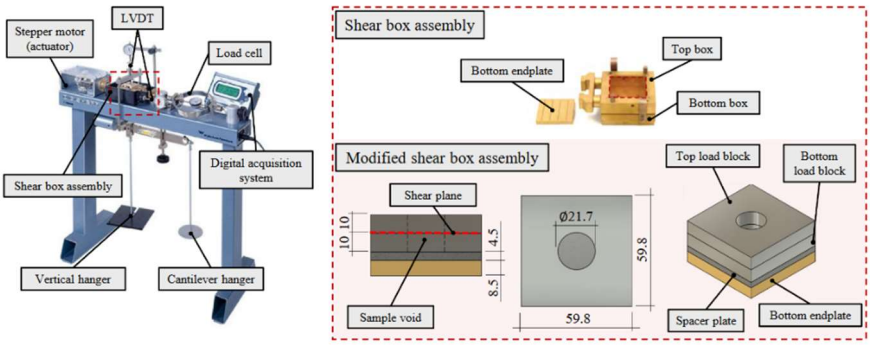

Figure 2-27: Direct shear test apparatus [73].

2.5 *Structural test of 3d printed concrete elements*

Digital fabrication using concrete technologies allows for greater design freedom and both architectural and structural aspects may benefit from the advantages of this technology. This new method of construction has the potential to create complex geometries. Since it is a relatively new technique, a common approach to conceive and design 3DPC elements has not already developed. In recent years, there has been a surprising increase in the number of large-scale 3DFC projects (see Section 2.2), which highlights the urgent need for new design-to-fabrication approaches, as well as testing methods and regulations. There are several challenges associated with the structural engineering of DFC, including unknown material properties, input structural design calculations, design aspects, minimum reinforcement requirements, and code compliance. (Figure 2-28).

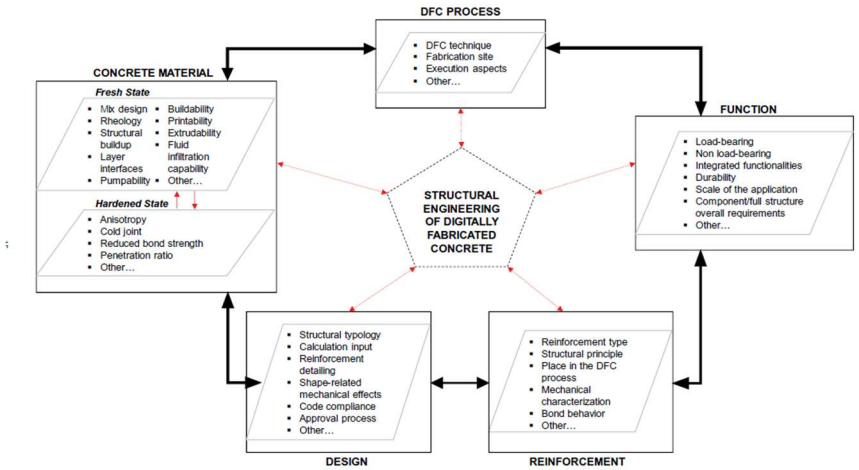

Figure 2-28: Aspects for the structural engineering of DFC structures [74].

To perform a structural calculation, different types of input are required. Typically, structural verification consists of comparing the calculated structural response with the limit values of this response. Geometrical, material and structural data are used as inputs to calculate the response. However, due to the novelty of DFC technology and its specific characteristics discussed in the previous sections, there is a lack of results and data on material properties, structural performance and geometric features of 3DPC members. Although some suppliers provide product data obtained through studies of the mechanical behaviour of their printable mortars, the data is often incomplete (relevant data for design purposes are missing). Moreover, they are quantitatively limited and obtained with experimental test-up or and methodologies which are not fully detailed and accepted by the scientific community.

Empirical relationships obtained from testing on structural elements are commonly used to gather structural data for traditional concrete. However, it is important to note that the processes involved in the manufacturing of DFC can vary significantly between each project, making it difficult to obtain universally validated empirical relations. This aspect is in contrast to the manufacturing method of conventional reinforced concrete, which is essentially the same everywhere. Finally, a structural analysis of DFC may also be hindered by a lack of geometrical data, which is due to the adjustment of the printed layer during the process [20].

Considering large scale projects with DFC, in addition to the abovementioned characteristics, the freedom of shape brings to complex geometries. As consequence, the design approaches used for traditional concrete are not always suitable. When dealing with concrete structures, a key problem is that concrete materials do not possess sufficient tensile capacity and ductility and are therefore mainly implemented in combination with tensile reinforcement. However, the reinforcement concepts and principles used in conventional concrete construction are generally not applicable to DFC. Each case requires a unique solution strategy. Consequently, in order to facilitate the application of digitally fabricated concrete structures, the fundamental concepts of reinforcement technology, dimensioning and detailing needs to be modified. It is important to note that reinforcement is not only required to gain high flexural and shear strength. A significant part of the reinforcement in real structures is the so-called 'minimum reinforcement', which performs one or more of the following functions: (i) avoid brittle fracture at cracks, (ii) ensure sufficiently ductile behaviour to allow redistribution of stresses and (iii) limit deformations and crack widths.

Conventional reinforcement can be classified as internal or external, metallic or non-metallic, passive or active. In traditionally built structures, passive internal reinforcement with deformed steel bars with a yield strength of approximately 450-500 MPa is the most commonly used combination. This type of reinforcement is cheap, ductile, and easy to place on site. The ribs or indentations on the deformed bars usually provide a sufficient bond with the concrete to transfer the force of the bars to the concrete. Pre-stressed (active) reinforcement is mainly used for precast elements, large span structures and bridges. It is either pre-tensioned (tensioned before casting of the concrete around it) or post-tensioned (stressed against the hardened concrete). Post-tensioned reinforcement can be external (outside the concrete cross-section) or internal (in channels within the concrete). In the case of internal post-tensioning, the reinforcement can be unbonded or bonded by grouting the channels. In recent years, the use of fibres in addition to or instead of conventional reinforcement has become widespread. However, compared to conventional reinforced concrete, fibre-reinforced concrete has limitations in terms of strength and ductility. To achieve strain hardening in cement-based fibre-reinforced materials,

single fibre types and lengths, such as steel or polymer fibres, as well as hybrid fibre blends with short and long deformed fibres, have been successfully used.
Ideally, in DFC the reinforcement should be positioned automatically to enable the digital manufacturing of the entire structural element, but nowadays most reinforcements are still placed manually. This is admissible in the current early age of digital fabrication. Considering the extrusion process, the most common reinforcing strategies are [75,76]:

- *External reinforcement*: the main focus of external reinforcement is to create reinforced concrete elements using digital fabrication of concrete technology without interfering with the reinforcement during the production process. This approach makes it possible to produce structural elements with complex shapes, low weight and optimized shape. The idea behind this approach is to divide a reinforced concrete element into 'segments', which are printed separately using a concrete-specific digital fabrication technology. In a second step, these segments are assembled with a steel reinforcement system to create the final structural element. The concrete segments can be optimised with voids to save material while still ensuring the required mechanical performance. In addition, segments can be provided with functional voids to accommodate sensors and tendons. For example, at the Federico II University in Naples, Italy, a beam was printed with two post installed separate external layers of steel reinforcement on both side of the concrete element and connected with orthogonal threaded rods [77], see Figure 2-29a. Other examples consist in the application of post-tensioned rods. The free-form concrete bench (Figure 2-29b), digitally fabricated using Concrete Printing [27]. The bench had a footprint of 2.0 m by 0.9 m and a height of 0.8 m and included a series of conduits through the full height of the bench for the placement of 8 mm diameter reinforcement bars. These bars were post-tensioned and grouted to achieve a predetermined compressive stress state in the structure [27]. The pedestrian and bicycle bridge developed at the Eindhoven University of Technology (TU/e) is another example that follows the same structural design principle. The bridge consists of six segments which after printing were rotated of 90°, positioned next to each other and connected by post-tensioned prestressing tendons anchored in conventional plaster blocks.
- *Placement of the reinforcement between the concrete layers*: the placement of the reinforcement occurs during the printing process. Reinforcement such as steel bars or textile reinforcement can be placed in between two layers, providing reinforcement in the printing direction only (Figure 2-29c) [78–80]. Additionally, there are ongoing studies to explore the reinforcement of concrete layers by inserting nails, screws and steel bars through a predefined number of fresh printed layers (Figure 2-29d). The aim is to provide

reinforcement also across the concrete layers. For example, Perrot et al. [81] used 30 mm long nails with a diameter of 1.8 mm with various orientations i.e. vertical, inclined and crossed positions with respect to the printed concrete layers. Marchment and Sanjayan [82] introduced a technique involving the insertion of a 7 mm diameter deformed steel bar through several freshly printed layers. Hass and Bos [83,84] presented a method that combines translational and rotational movements to insert screws into fresh concrete.

- *Cable in the concrete filament:* during the printing, a flexible reinforcement cable is directly embedded into the extruded layer (Figure 2-29e). This approach allows the reinforcement of the elements in the printing direction, even for complex shapes. However, it can be challenging to ensure a proper anchorage of the cables when working with smooth high strength cables [85].
- *Fibre reinforced concrete*: during the printing process, short fibres are suitable to be pumped into the concrete matrix, providing tensile and post-crack bonding capabilities through cracks. This approach can lead to a strong alignment of the fibres in the printing direction, which could increase the effectiveness of the fibre reinforcement. Some studies, such as those carried out by Hambach and Volkmer [86], who added 3–6mm basalt, glass and carbon fibres to a printable mixture, Panda et al. [10], who compared glass fibres of different lengths (3, 6 and 8 mm) and different volume percentages, Bos et al. [87] who investigated the effect of the inclusion of short and straight steel fibres, and Arunothayan et al. [88] who investigated a ultra-high performance fibre-reinforced concrete reinforced with 13 mm long steel fibres reported a significant increase in flexural tensile strength as well as an effect of fibre orientation in the direction of filament flow. Some studies [89–95] have also reported the development of a 3D printable strain-hardening cementitious composites (SHCC) reinforced with short polymeric fibres, such as polyvinyl alcohol (PVA) and high density polyethylene (HDPE) fibres, which exhibits high tensile strength and tensile strain capacity.
- *Reinforcement inside 3D printed concrete formworks*: In some projects (as discussed in section 2.2), a different approach has been adopted, in which 3D-printed concrete is used as a lost formwork for traditional reinforced concrete (Figure 2-29f). In this case, the printed concrete does not contribute to the structural strength and the reinforcement is placed passively during the production process. This approach involves the use of conventional steel elements for reinforcement, a simpler method than the previously described technologies. Placing by hand and repeatedly horizontal and vertical reinforcing steel rebar seems to be one of the easiest solution able to create a regular reinforcing scheme in structural elements with a standard geometry [96].

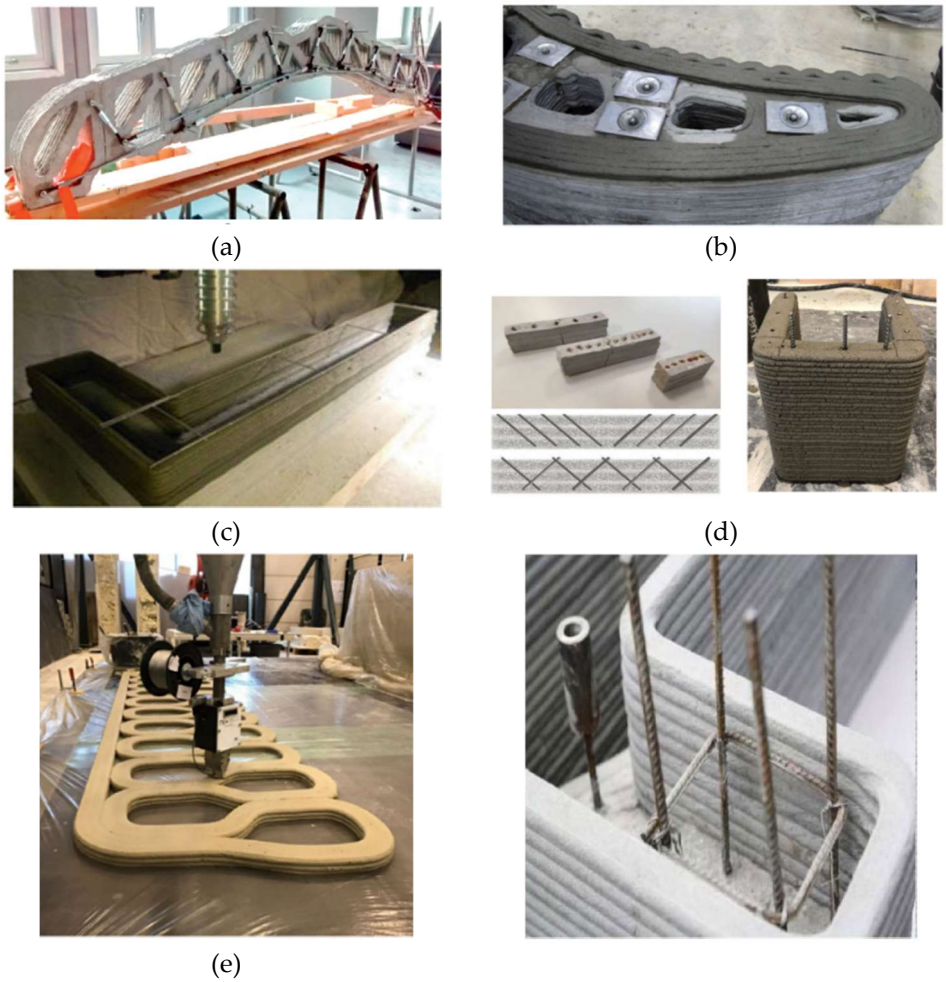

Figure 2-29: Reinforcement strategies for extrusion based additive manufacturing: (a) and (b) external reinforcement [77], [27] ; (c) reinforcement between the concrete layers [78]; (d) reinforcement using penetration (left [81] right [82]); (e) cable between the layers [85]; (f) reinforcement inside 3D printed concrete formworks [96].

The printing of load-bearing structures is conceived as a completely new structural system (in terms of concrete material, element geometry, reinforcement) and requires extensive preliminary experimental investigation to support structural design at all stages. However, there are only a few examples in the existing literature that demonstrate how 3D-printed concrete structures can be evaluated for structural integrity. Most of these examples refer to beams or walls, some of them will be briefly described.

2.5.1 Structural test on beams

A bridge, which is located in Gemert, has been printed using the print facility of the Eindhoven University of Technology (TU/e) [97].
The bridge has a span of 6.5 m and a width of 3.5 m. It consists of printed concrete elements, rotated 90° after printing and then pressed together by post-tensioned tendons placed in the openings of the printed elements. The components were prestressed to overcome the lack of bending moment resistance of unreinforced concrete. No additional passive reinforcement is required in the longitudinal direction. A high-strength steel reinforcement cable is positioned through the cable reinforcement device in the bottom 10% of the layers of each element. The cable provides passive reinforcement in the transverse direction, while the prestressing tendons provide active reinforcement in the longitudinal direction of the bridge. The bridge was composed of a total of six elements, each with a height of approximately 1 m. The height of each element was limited for transport and handling requirements. To apply the prestressing 16 Dywidag tendons were used. However, as this method of constructing a concrete bridge was new, a 1:2 scale model was created and tested to ensure its structural integrity. The bridge was subjected to a load-controlled four-point bending test (Figure 2-30b) and the crack occurred between the loading points running vertically along the interface between two layers which indicated bending-induced damage, a desired failure mechanism as it is more ductile than shear failure. Compared to the required minimum capacity of 170 kN, the first signs of damage to the bridge occurred at a much higher load capacity (>240 kN). In addition, an in-situ test was conducted, as illustrated in Figure 2-30c.

(a)

(b)

(c)

Figure 2-30: Bicycle bridge in Gemert: (a) photos of the bridge, (b) flexural test in the laboratory, and (c) in situ test [97].

With reference to [18], a project aimed to examine the difficulties associated with the implementation of 3DPC technology in a large-scale structure, specifically a cycle-pedestrian bridge located in Nijmegen covering a total distance of 29 meters. The design of the bridge (illustrated in Figure 2-31) was developed by Witteveen+Bos, while TU Eindhoven was responsible for researching the printing process and conducting structural tests. Like the 3D-printed concrete bridge built in Gemert, the structural principle of this bridge involves the assembly of several printed elements with prestressing tendons. As a result, there is no need for passive reinforcement along the bridge span, as the level of prestressing was selected to ensure that only compressive stresses due to bending moments remain active in each section. The 29 m long bridge span is divided into five simply supported sections, each of which has a span of between 4.5 and 6.5 metres (Figure 2-31a). The five beams were further subdivided into smaller elements to meet production and logistical constraints.
In contrast to the previous bridge design, the geometry of each element is unique, as it was designed for a custom-made double-curved bridge. The width of each element is 3500 mm and the height varies between 700 and 1200 mm, as shown in Figure 2-31a. During the assembly phase, these elements are glued together. The anchor

blocks are supported by four pairs of columns along the bridge span and two traditional abutments at the ends of the bridge, as shown in Figure 2-31a. The columns are made of reinforced concrete and are cast in 3D printed lost formwork. These columns are fixed to a pile foundation and, from a structural engineering perspective, can be treated as conventional reinforced concrete columns. Consequently, they are excluded from structural testing. To evaluate the structural performance of the 3D printed bridge, a 1:1 experimental test program was conducted using a single 3D printed and pre-stressed girder (Figure 2-31b). The beam had a total length of 5875 mm and was subjected to a four-point bending test, with the distance between the load and support points varying in two configurations, to validate the bridge resistance towards both bending moment and shear stresses. The experimental program concluded that the mock-up of the bridge performed well and had sufficient structural capacity. The beam was able to resist without failure a bending resistance of two times the ULS load and a shear resistance of three times the ULS load, at this point the test was stopped even though no visible cracks were observed but the risk of a sudden release of energy was to high. The tests also confirmed that the serviceability limit state (SLS) requirements were met, as the deflections in both configurations were minimal. In addition, an in-situ test was conducted by placing water tanks on each girder (Figure 2-31c). In this case, the bridge was not loaded to failure, but only with a load that provided sufficient information on its safety without causing any damage.

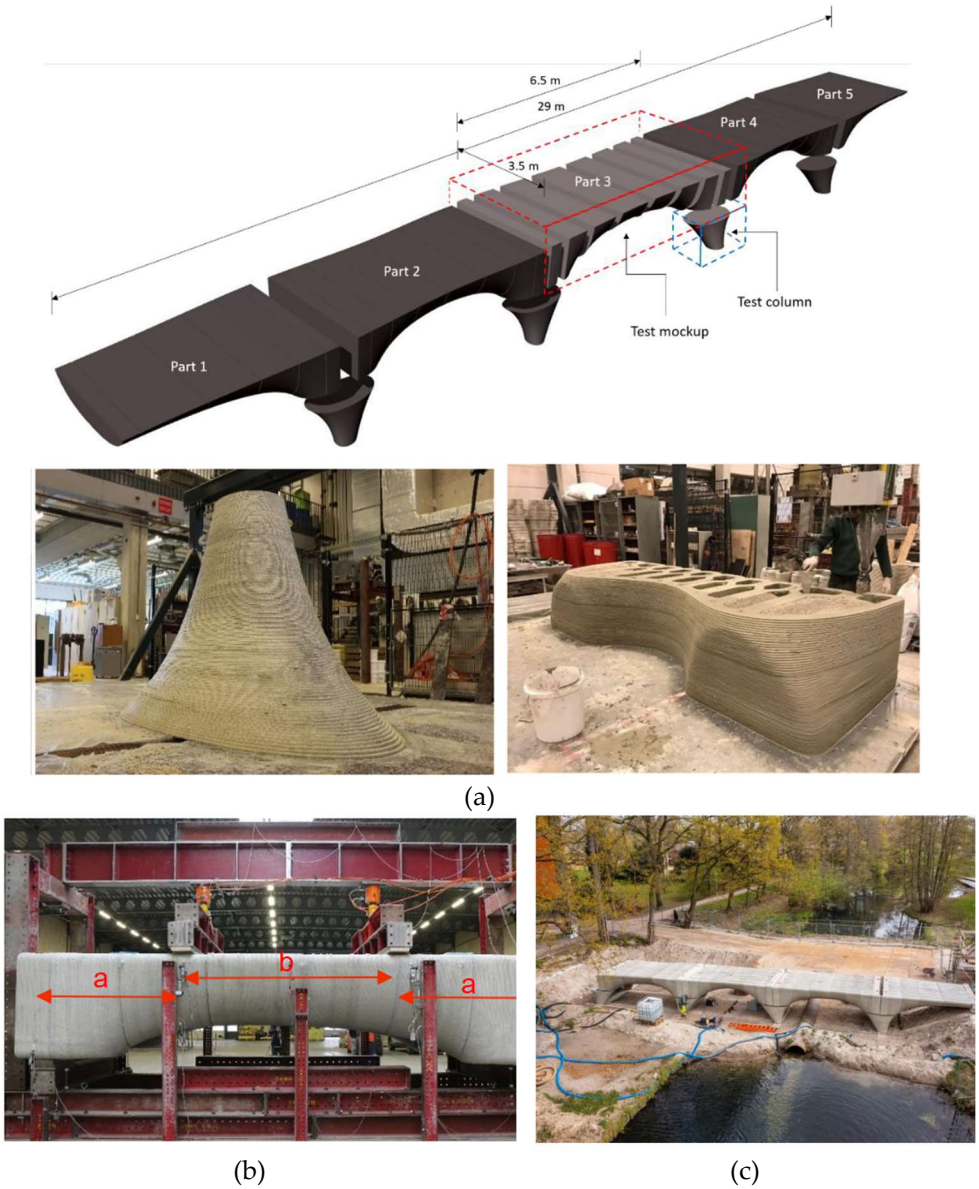

Figure 2-31: Bridge in Nijmegen: (a) Detail of the column and of the girder segment; (b) set-up and (c) assembly [18].

Other studies on the structural behaviour of 3D printed concrete beams can be found in the literature [77,98,99]. Figure 2-32a illustrates a large-scale test performed on a trussed -beam developed at the University of Federico II of Naples [77]. The beam was subjected to a three-point bending test, and was 3 m long, 0.45 m high and 0.20 m wide. The beam was divided into five segments, each was designed using topological optimisation to reduce the use of material and ensure adequate mechanical

performance against internal forces acting on the segments. The holes were designed for the anchoring of the longitudinal reinforcement system or for the installation of the external shear reinforcement system. The segments and reinforcement system were designed to provide the final element with a continuous concrete top chord to resist compressive forces, a steel bottom chord to balance the top compressive stresses and resist tensile forces, and diagonal concrete compression struts and opposite diagonal steel struts to resist shear forces. The initial flexural stiffness of the printed reinforced concrete beam is comparable to that of an equivalent reinforced concrete beam. However, the overall non-linear flexural behaviour is influenced by local failure mechanisms, such as shear damage at the interfaces between adjacent concrete segments and failure of the steel-concrete anchorage. These damage mechanisms cause large overall deflections and limit the performance of the printed beams. Although the beams exhibit large deflections, no steel yielding was observed in the external reinforcement system. Further research is needed to address these critical issues. However, the authors point out that the basic idea presented in this study could introduce a new and rational use of additive manufacturing technologies in structural engineering. This idea allows the production of complex shapes, topological optimisation, reduction of concrete volume and mass, elimination of complex formwork systems, and ease of transport and installation.

Figure 2-32b shows experiments conducted by Kinomura et al. [98] on a bridge structure consisting of 44 distinct segments with varying complex shapes, individually printed and subsequently combined in a compression-loaded structure by means of a pre-stressed external reinforcement. The overall dimensions of the structure are 6.0 m in length, 1.2 m in width and 1.0 m in height. Furthermore, Figure 2-32c shows a beam test conducted by Gebhard et al. [99], in which the structural performance of the beam was evaluated by means of a six-point bending test. With the formation of multiple bending cracks, then a sudden brittle failure and a shear crack formed. After inspection of the T-beam web, it was discovered that the main reinforcement was not adequately surrounded by concrete (Figure 2-32c). As consequence, shear forces could not be transferred to the stirrups but were merely carried by the unreinforced printed mortar.

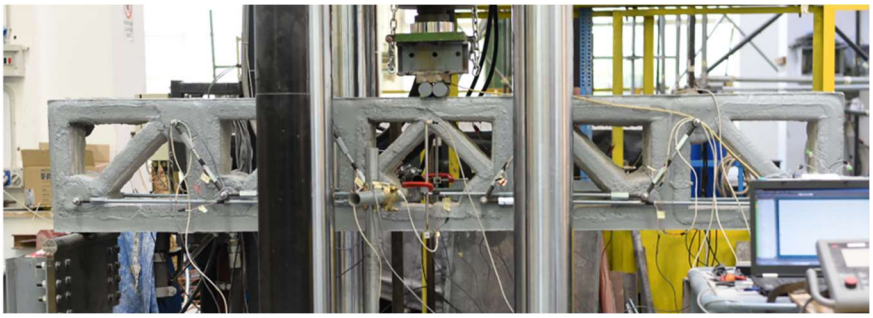

(a)

(b)

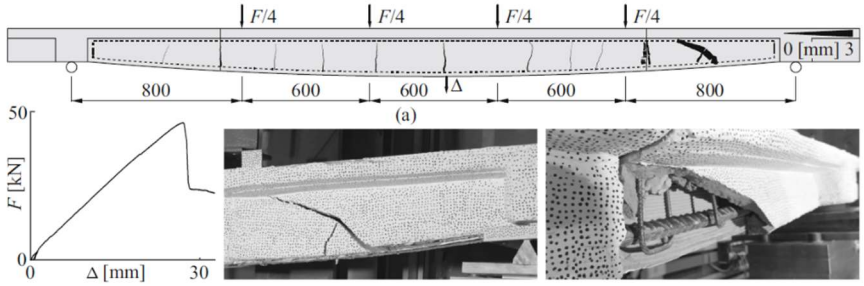

(c)

Figure 2-32: 3 point bending test set-up. Example of structural test on DFC beams: (a) test of a 3D printed truss [77], (b) test of a beam obtained with topology optimization [98] and (c) test on a beam with integrated reinforcement [99].

2.5.2 *Structural test on walls*

The introduction of 3D printed concrete walls as part of the main force resisting structure required additional structural testing to obtain approval. The main design principle involved the use of 3D printed concrete technology to create a new structural element that made efficient use of materials, reducing the amount through topological optimization, and exploited the freedom of form. Several studies have been conducted in the literature to evaluate the structural behaviour of 3DPC walls.

Van der Putten et al. [100] conducted two different series of tests, one of which involved the testing under compressive load of two different wall types, one structural and one insulated (Figure 2-33a), both with a specimen height of 66 cm, as illustrated in Figure 2-33b. In the second series of tests, two alternative methods of reinforcing the window lintel were tested, including the integration of reinforcing bars (Ø 10 mm) above the window opening in the first test configuration and the integration of a small reinforcing mesh in the second alternative (Figure 2-33c). Both types of reinforcement were integrated manually during printing. Bos et al. [101] conducted several tests to evaluate the structural performance of 3DPC walls under different conditions. These walls were to be used in a student house project in Nyborg, Denmark. The wall shown in Figure 2-33d was 2.5 m high, 85.5 cm wide and 40 cm thick, with the inner and outer faces joined by tie rods with hinge connections to distribute horizontal loads (as shown in Figure 2-33d). The two leafs can be loaded in bending by the wind or a collision, they are slender and can be subjected to buckling when subjected to compression load and subsequent failure due to flexural tensile stresses. Considering the possible load cases, three type of tests were performed: a compression/buckling test, a bending test and an impact test. The vertical flexural test was conducted as a 3-point bending test with the load acting horizontally (Figure 2-33e). Both wall faces were able to withstand the design load without collapsing, so the design was considered safe for these loading conditions. The compression test was conducted once on each face of the test element, with the outer face loaded in the first test and the inner face loaded in the second test, as illustrated Figure 2-33f. Although the Euler buckling load of each individual sheet was above 200 kN, the possibility of buckling due to eccentricity could not be completely excluded. It is unlikely that compression would be the dominant load case, since a damaged element could easily carry six times the design load. To assess the resistance of the 1.33 m high element to localised dynamic loads and its susceptibility to damage, a pendulum impact test was conducted (Figure 2-33g), which is not typically required for single-storey building walls. The test was performed using a configuration derived from EN 12600, with the element standing on a base plate and supported back to the steel frame by two horizontal timber beams at the bottom and the top of the element. The element and impact body were positioned so that the impact occurred at half the height. EN 12600 requires three consecutive drop heights and the element was subjected to impacts from each height several times. No significant damage was observed after multiple impacts from heights of 190 mm and 450 mm, but increasing damage was observed with each impact from a height of 1200 mm. Despite this, the behaviour of the printed wall element was considered safe for its intended use.

The walls used in the Milestone project's [43] houses underwent large-scale mock-up testing at TU/e. Each wall element was 3D printed at a 1:1 scale to test stability during printing and was subjected to in- and out-of-plane loading to validate its structural

performance (Figure 2-33h). The Beckum House [19] employed 3DPC using a combination of cast and printed concrete as loadbearing. The project involved testing large-scale wall elements, including impact and flexural strength tests on load-bearing and non-load-bearing walls (Figure 2-33i). Approval for the project was obtained based on existing standards for concrete and masonry construction and required monitoring of the materials and execution of design details during construction, as well as long-term monitoring. The approval was also granted for the 3D-printing mortar used in combination with the 3D-printed wall types and the 3D printer used in the project.

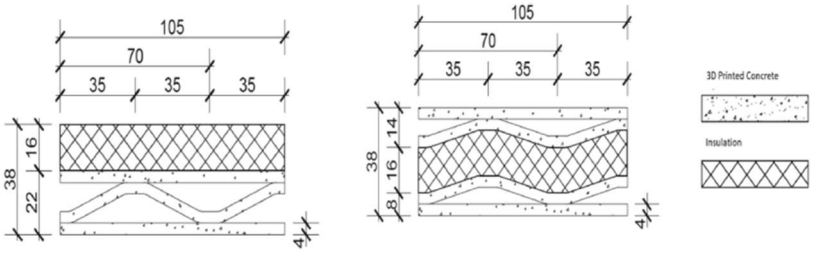

(a)

(b)

(c)

(d)

(e)

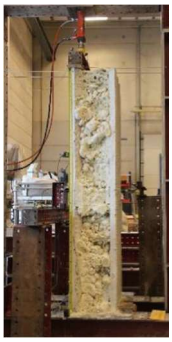

(f)

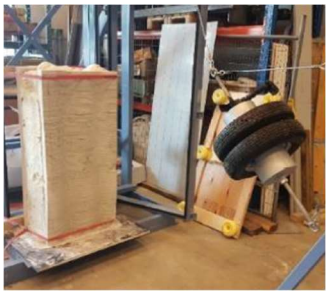

(g)

(h)

(i)

Figure 2-33: Structural test on 3D printed concrete walls:[43] (a)-(c) compression test [100]; (d)-(g) Nyborg house: flexural, compression and impact test [101]; (h) Milestone project [43] and (i) Beckum house [43].

2.6 summary

This chapter presented a summary of the digital fabriaction of concrete focusing on the extrusion process. Unlike traditional concrete, which is cast using formwork, the 3D printed material, due to its rheological properties, is able to sustain its own weight during the printing process. As consequence, 3D printed elements are composed of multiple layers, making the printed material anisotropic, while traditional concrete is isotropic. Consequently, the interfaces between the layers play an important role in the overall structural behaviour of 3D printed concrete elements. Currently, to assess the material properties of the 3D printed concrete, tests used for traditional concrete and mortar are employed and adapted to the specific case study. It comes out the strong need to find and establish common approaches to evaluate the mechanical properties of 3D printed materials. On a larger scale, given the novelty of this technique, a standardized design approach has not yet been developed. There is an urgent need to establish standards and tests to assess the structural behaviour of 3DPC elements to allow their use as load-bearing components. In fact, nowadays although there are many examples demonstrating the great potential of this technique, in most cases the 3D printed elements serve as temporary formwork, while the structural role is given to traditional concrete elements. Another widely studied aspect is the integration of reinforcement in structures created by 3D printing technique. However, the concepts and principles of reinforcement used in conventional concrete construction are generally not applicable to DFC. Each case requires a unique solution strategy. It is important to find solutions that enable the reinforcement to be integrated into 3D printed elements efficiently.

3 MECHANICAL CHARACTERISATION OF THE HARDENED PROPERTIES OF 3D PRINTED CONCRETE

3.1 Introduction

The 3D printing of concrete is an innovative technique that offers a new construction method whose effectiveness depends on the concrete properties both at fresh and hardened state. Therefore, this chapter focuses on the printed concrete properties at hardened state and their influence on the overall structural behaviour.

The 3D printed concrete is an anisotropic material, as the concrete elements consist of several extruded layers. As consequence, the interfaces between layers play an important role as they may affect the structural performance of the 3D printed concrete elements. Many studies have been conducted to investigate the anisotropy [10–12,14,68–71,102] and it is evident that the properties depend on the direction of the applied load with respect to the printed layers. Many parameters could influence the anisotropy: a) the printing process which is affected by the printing path and the print head speed [70]; b) the nozzle shape, since circular nozzles may create voids which can reduce the concrete strength; thus, rectangular nozzles have to be preferred [66,71]; c) the surface preparation [14,103]; d) the moisture content of the substrate [104]; e) the curing condition [14]; f) early age shrinkage [105] and g) the interlayer time interval which has to be high enough to ensure adequate strength to sustain the weight of subsequent layers and also short enough to optimize the bonding strength. Long interval time, named as "cold-joint", may cause a reduction of the interface strength and of the overall structure [68,69,106].

There are currently no established standards or codes to regulate the tests that evaluate the hardened properties of 3D printed concrete. Therefore, it is necessary to do research in order to establish some common approaches. The purpose of this chapter is to provide a methodology to assess the hardened properties of 3D printed concrete. Due to the anisotropic nature of 3D printed concrete, standard tests used for conventional concrete are often not suitable and need to be adapted. The standards for repair material can serve as a good reference. Firstly, the compression, flexural, and tensile (this is the case of an interface subjected to normal force) properties are estimated using setup configurations that are already present in the literature. Subsequently, particular attention is given to the investigation on the effect of interface between adjacent printed layers on the shear strength of 3D printed elements. Two test set-up are proposed. The first test configuration is referred to as modified push-out shear test, which is adapted from the test used for masonry structures to evaluate the initial shear strength. The second test, named as modified

slant shear test, which is commonly used to study the properties between cast concrete and a repair material, was developed in collaboration with ETH Zurich [107].

3.1.1 Materials

In this chapter three different materials are employed named as:

- Material type 1 is the 3D printed mortar developed by Cybe for architectural, structural, industrial and design 3D printed concrete applications;
- Material type 2 is the i.tech 3D printing NF developed by Italcementi and Heidelberg;
- Material type 3 is a material for 3D printing application developed at ETH Zurich at the Chair of Physical Chemistry and Building Materials in collaboration with Knauf Gips KG and BASF.

The properties listed in Table 3-1 and *Table 3-2* refers to material type 1 and the ones listed in Table 3-3 and Table 3-4 refers to material type 2. These properties are provided by the producers and are contained in the technical datasheets.

Property	Symbol	Unit	Days	Value
Compressive strength	f_{cm}	N/mm²	After 5h	20
			After 1d	25
			After 7d	30
			After 28d	40
Tensile/Bond strength	f_{ctm}	N/mm²	-	2.4
Flexural strength	$f_{ctm,fl}$	N/mm²	After 5h	4
			After 1d	4
			After 7d	5
			After 28d	6
Density	ϱ	kg/m³	-	2100-2200
Elastic modulus	E_{cm}	N/mm²	-	26000-28000
Thermal conductivity	λ	W/mK	-	0.979

Table 3-1: Hardened properties of material type 1 contained in the technical datasheet[1].

Property	Unit	Value
Grain	mm	0-3
Setting time	min	3-5
Load bearing	min	> 60
Application temperature	°	5 - 30
Flow	mm	160
Air void content	%	5.3

Table 3-2: Fresh state properties of material type 1 contained in the technical datasheet[1].

[1] https://lybrary.cybe.eu/wp-content/uploads/2021/01/2020.01.08-Datasheet-Mortar.pdf

Property	Symbol	Unit	Days	Value
Compressive strength	f_{cm}	N/mm²	After 1d	≥ 10
			After 7d	≥ 35
			After 28d	≥ 48
Flexural strength	$f_{ctm,fl}$	N/mm²	After 1d	≥ 2
			After 7d	≥ 5
			After 28d	≥ 7
Desity	ϱ	kg/m³	-	1950 ± 50
Elastic modulus	E_{cm}	N/mm²	-	≥ 20000
Thermal conductivity	λ	W/mK	-	0.963

Table 3-3: Hardened properties of material type 2 contained in the technical datasheet[2].

Property	Unit	Value
Grain	mm	0 - 2
Density	kg/m³	2150 ± 50
Water content	%	16 - 17
Setting time	min	150-200
Workability	min	20
Application temperature	°	5 - 30
Flow	mm	135 ± 5

Table 3-4: Fresh state properties of material type 2 contained in the technical datasheet.

The commercial material type 3 was developed at ETH Zurich at the Chair of Physical Chemistry and Building Materials in collaboration with Knauf Gips KG and BASF. The composition of the material cannot be disclosed and only few information are available: the mixture consisted of quartz sand, limestone filler, cement (CEM I 52.5R), fine ground gypsum, superplasticiser, stabiliser and water. The maximum aggregate size of the mortar is 1.2 mm.

[2] https://www.italcementi.it/sites/default/files/assets/document/e8/9f/tech_data_sheet_i.tech_3d_n_ita.pdf

3.1.2 Research significance

The aim of this chapter is to provide methodologies to assess the mechanical properties of 3D printed concrete in the hardened state with particular attention on their influence on the structural performance of 3D printed concrete elements. As mentioned in Chapter 1, the material has undergone subsequent changes that make the comparison between the results less relevant.
The attention will be mainly focused on:

- the layer orientation: the relationship between the application of the load with respect to different layer orientation will be discussed;
- the layer adhesion under shear loads: 3D printed concrete elements could be subjected both to bending moment and shear action. Thus, it is of importance to understand how the interfaces behave when subjected to combinations of internal actions.
- Effect of the cold joint on the interlayer strength: as previously mentioned one of the main parameter that affect the interlayer adhesion is the interval time gap. If the interval time gap is too long, the adhesion between the layers may be weakened thus jeopardizing the overall behaviour of the 3D printed element.

Table 3-5 summarizes the tests that were performed to assess the hardened properties of 3D printed concrete materials.

Test	Manufacturer	Compression				Flexural				Direct tension			Elastic modulus			Modified push-out test		Modified slant shear test
Direction		C	I	II	III	C	I	II	III	I	II	III	I	II	III	c	III	-
Material 1	Cybe	no	yes	yes	yes	no	yes	yes	yes	no	no	yes	no	no	yes	no	yes	no
Material 2	Italcementi	yes	yes	no	yes	yes	yes	no	yes	no	no	yes	no	no	yes	yes	yes	no
Material 3	ETH	yes	no	no	no	yes	no	no	no	no	no	no	no	no	no	no	no	yes

Table 3-5: Overview of the experimental test conducted.

3.2 Specimens preparation

The 3DCP specimens were printed and cured in laboratory with constant environmental conditions: temperature equal to 20±2°C and humidity of 80±5%. The specimens were printed through a 6-axis robotic arm connected to a digital system through which the tri-dimensional printing path was programmed. The print head of the system was equipped with a circular nozzle with a diameter of 40 mm and 28 mm considering specimens printed using material type 1 and material type 2, respectively. The printing speed rate was set to 250±25 mm/s. The dry compound was mixed with water in a pump-mixer which provided a concrete flow rate consistent with the printing speed, width and thickness of the fresh concrete filament. The specimens were cut by wet-sawing from a companion specimen of the wall; an example is shown in Figure 3-1.

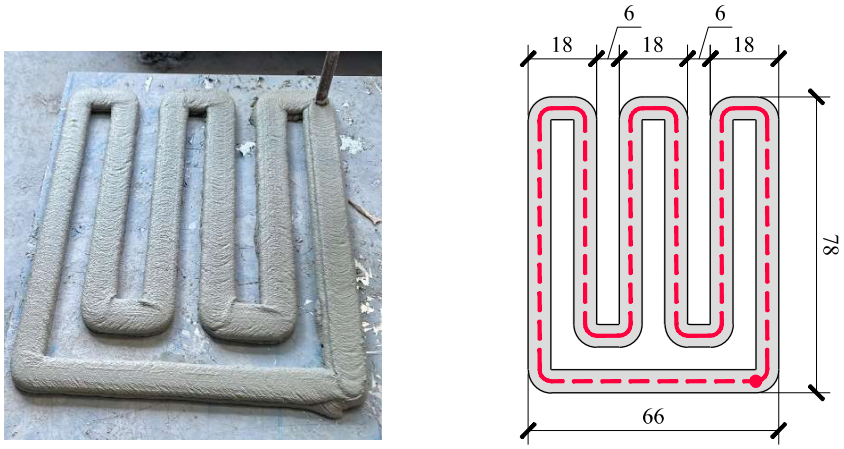

Figure 3-1: Companion specimen of the wall: plan view with measures. Measures in centimetres.

3.3 Specimens' orientation

The anisotropy of the 3D printed concrete requires specific attention as the testing direction with respect to the printed layers could influence the material properties. Available studies proposes different definitions of directionality (see Section 2.4). Bos et al. [66] defined directionality in printing as a local coordinate system (u,v,w), where *u* represents the printing direction (see Figure 2-17). Mechtcherine et al. [67] proposed an expanded definition of directionality, which is composed by two letters (u,v,w) separated by a dot with the first letter indicating the axis of a normal force, while the second letter the longitudinal axis of the specimen (see Figure 2-18). This approach results in a total of nine possible directions for non-cubic specimens. Available studies [10,11,14,68–72] generally perform tests in three orthogonal directions to capture anisotropic effect considering different directions of application of the load with respect to the printed layers (see Figure 2-19).
The common aspect among the definitions of directionality is their dependence on both the printing direction and the direction of force application on the specimen. This approach encounters difficulties in defining complex stress states, such as those found in structural elements where normal and tangential stresses act simultaneously. To address this issue, a more general definition of directionality is introduced, no longer based on the direction of the external force (or bending moment) applied to the specimen but based on the position of the sections on which the stresses act. A local coordinate system (u,v,w) is defined, where *u* represents the printing direction, *v* is perpendicular to the printing direction in the printing plane *uv* and *w* is perpendicular to the printing plane *uv*. Three different angles are defined, as illustrated in Figure 3-2:

- α is the inclination with respect to the printing plane in the *uw* plane;
- β is the inclination with respect to the printing plane in the *vw* plane;
- γ is the inclination with respect to the printing direction in the *uv* printing plane.

Not all possible directions are relevant to the purpose of the tests; three main cases can be identified, as shown in Figure 3-3:

- Orientation (0°,0°,0°) refers to specimens with inclination of the layers $\alpha = 0°$ with respect to the printing plane in the plane *uw*. This case is similar to orientation I [69] (see Figure 2-19).
- Orientation (0°,90°,0°) refers to specimens with inclination of the layers $\beta = 90°$ with respect to the printing plane in the plane *vw.* This case is similar to orientation II [69] (see Figure 2-19).

- Orientation (90°,0°,0°) refers to specimens with inclination of the layers α = 90° with respect to the printing plane in the plane *uw*. This case is similar to orientation III [69] (see Figure 2-19).

Figure 3-3 illustrates the material tests described in this chapter to evaluate the hardened properties of 3D printed concrete, considering the direction of stresses rather than of the forces (see Figure 2-19) with respect to the printed layers. Figure 3-3a refers to the flexural tensile test, Figure 3-3b to the shear slant test, the direct tensile test and to the compression test and Figure 3-3c to the push-out test. In Figure 3-3 the red arrow indicates the printing direction, in blue and pink the distribution of forces and the distribution of stresses are represented, respectively. As an example, $f_{ctm,fl,(0°,0°,0°)}$ is the flexural tensile strength measured on specimens with an inclination of the layers α = 0° and stresses parallel to the printing plane; $\tau_{max,(90°,0°,0°)}$ is the shear strength measured on specimens with an inclination of the layers α = 0° and stresses perpendicular to the printing plane.

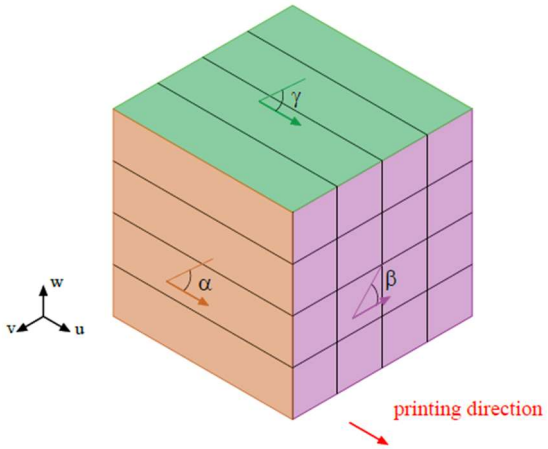

Figure 3-2: Definition of the local axis system and inclinations.

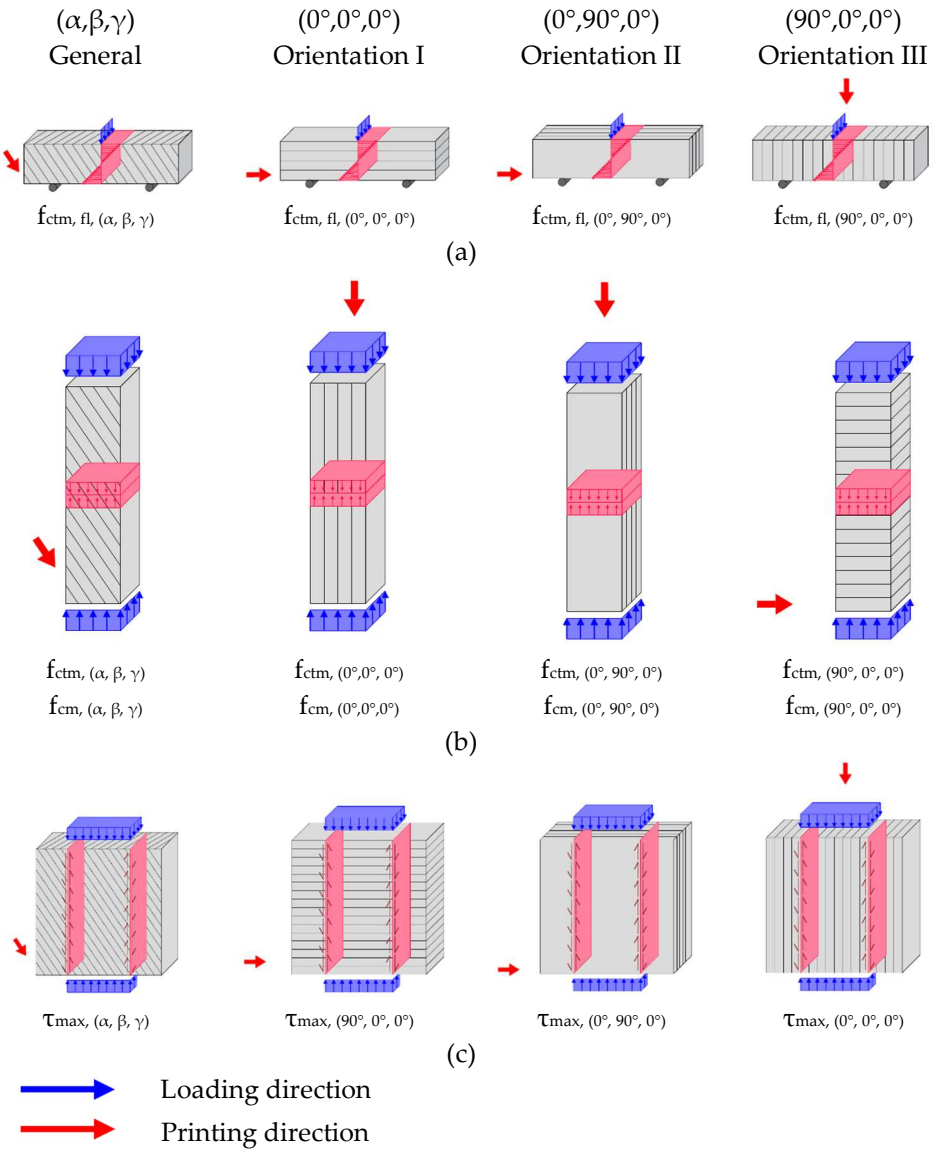

Figure 3-3: Material properties of the 3D printed material at hardened state according to the different orientations: (a) flexural tensile strength; (b) tensile strength and compressive strength; (c) shear strength.

3.4 Accuracy of the specimens

Due to the printing process, the cross-section of the printed specimens has significant irregularities with bulging sides, as shown in *Figure 3-4*a. Depending on the type of test performed, the concrete waves may or may not contribute to the resistance of the specimens. As consequence, three different resisting area are defined:

- A_{max} (in red in *Figure 3-4*b) calculated considering the nominal dimensions of the specimens; it results in an overestimation the effective resisting cross-sectional area of the specimens;

  $$A_{max} = h * t \quad (3\text{-}1)$$

  Where h and t are the nominal height and thickness of the specimen.
- A_{min} correspond to the resisting cross-sectional area of the specimens excluding the contribution of the concrete waves (in green in *Figure 3-4*c);

  $$A_{min} = h * t_{min} \quad (3\text{-}2)$$

  Where h is the effective height of the specimen and t_{min} is the minimum thickness, which is estimated between 75% and 80% of the nominal thickness t of the specimen (see *Figure 3-4*c). It has to be noted that the cross-section of the 3DPC specimen in *Figure 3-4* serves as a reference; the cross-section of other tested specimens (see 8) was considered and the minimum thickness t_{min} resulted in the same range.
- A_{mean} is the average between the two previous areas and it considers the contribution of the waves (in orange in *Figure 3-4*d). The mean thickness t_{mean} is estimated between 87% and 90% of the effective thickness t of the specimens (see *Figure 3-4*d). In 8 this approximation with reference to other 3DPC cross-sections is shown.

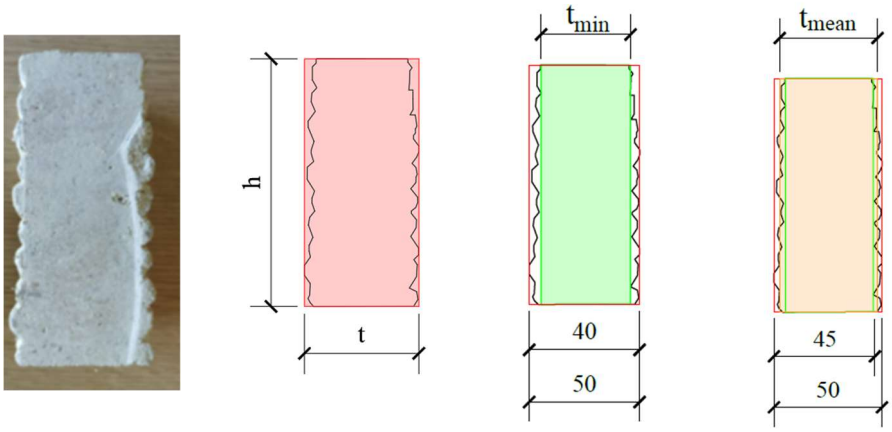

Figure 3-4: Accuracy of the 3D printed specimens: (a) typical cross-section of 3D printed concrete specimens; (b) maximum area A_{max}; (c) minimum area A_{min} and (d) mean area A_{mean}.

3.5 Compressive strength

3.5.1 Literature review

Extensive of research has been conducted to assess the compressive properties of 3D printed concrete. Many researchers determined the compressive strength by means of uniaxial compressive strength on cubic specimens [10–12,14,68–71]. The compressive properties were studied considering the anisotropy of the material and the influence of the application of the load with respect to different layers orientations [10–12,14,68–71], as shown in Figure 3-5 (the red arrow indicates the printing direction).

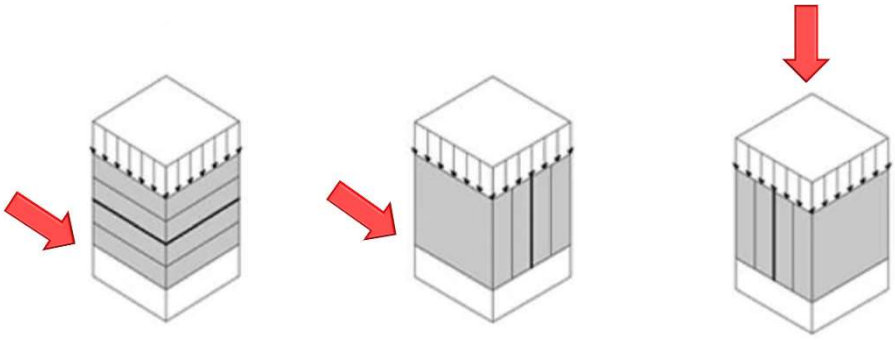

Orientation I Orientation II Orientation III

Figure 3-5: Printed layer orientations in compression tests [69].

Based on the test results, it was found that the direction of application of the load does not affect the compressive strength. In fact, the difference between the compressive strength measured according to orientation I and orientation III is considered in most of the cases negligible [11,12,14,68–70]. Other studies have investigated the effect of time gap between the layers on the compressive strength, revealing that longer interlayer intervals result in slightly decreased compressive strength [11,68,69]. Thus, the interlayer time gap was not considered to have a relevant influence. To ensure a strong bond between layers, it is recommended to keep the interlayer interval time as short as possible. Research has indicated that material properties can vary up to 24 hours [68,69], but further studies have suggested that interlayer intervals between 10 and 30 minutes should not negatively impact the bond strength [11,102].

3.5.2 *Specimen geometry and test set-up*

The specimens for the characterisation of the compressive strength were obtained from the flexural test specimens (see Section 3.6), as shown in Figure 3-6a. The specimens had a nominal height equal to h = 40 mm, a nominal thickness t = 40 mm and a nominal width w = 40 mm. Table 3-6 and Table 3-7 shows the effective height h, thickness t and width w of the printed specimens for material type 1 and material type 2, respectively. The values of the minimum thickness t_{min} and mean thickness t_{mean} are also indicated, which are estimated as the 80% and 90% of the effective thickness, respectively. Considering Orientation III, the resisting area A_{min} excludes the surface waves that do not contribute to the compressive concrete strength (Figure 3-6b and c), while Orientation I and II consider all the area A_{mean} as resistant (Figure 3-6b and c).

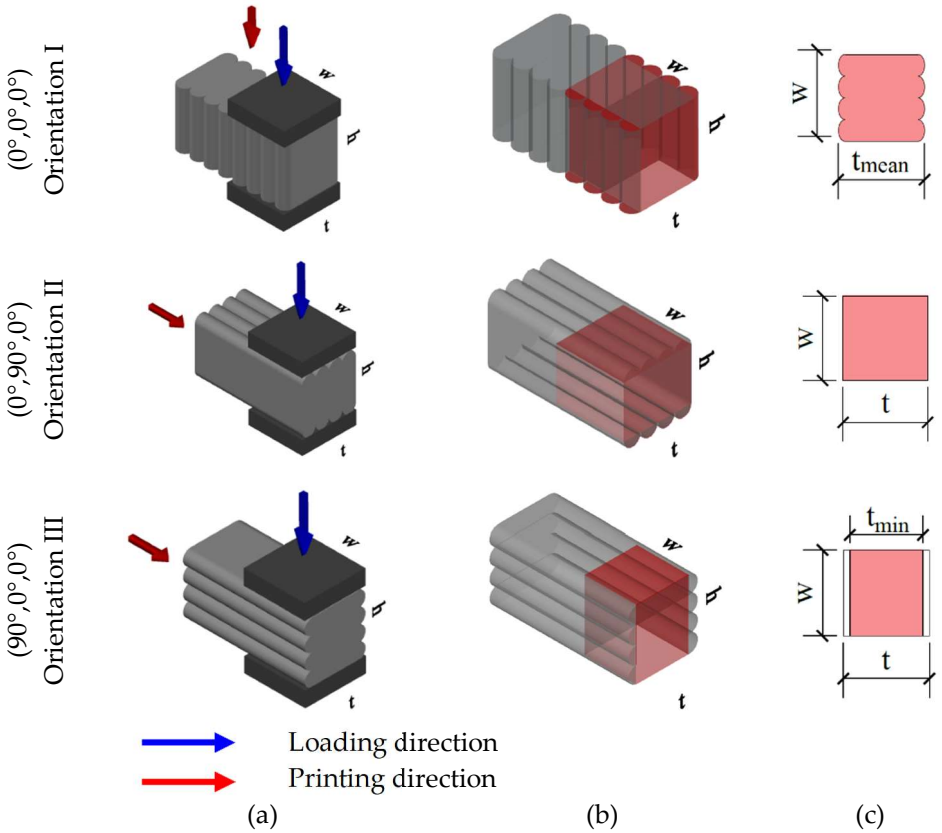

Figure 3-6: Compression test: (a) specimens geometry; (b) and (c) loading area.

(0°,0°,0°) Orientation I

Material	Nomenclature	t	h	w	t_{mean}	A_{mean}
1	3D-C-I-A	39.9	34.6	40	35.9	1436
1	3D-C-I-B	40.9	36.7	40	36.8	1472
1	3D-C-I-C	40.5	36.9	40	36.5	1458
1	3D-C-I-D	38.7	37.2	40	34.8	1393
1	3D-C-I-E	39.4	34.6	40	35.5	1418
1	3D-C-I-F	38.5	37.6	40	34.7	1386
1	3D-C-I-G	39.6	37.1	40	35.6	1426
1	3D-C-I-H	41.9	34.1	40	37.7	1508
1	3D-C-I-I	37.8	33.7	40	34.0	1360
1	3D-C-I-L	39.1	39.2	40	35.2	1407
1	3D-C-I-M	39.8	36.3	40	35.8	1432
1	3D-C-I-N	41.9	35.8	40	37.7	1508
1	3D-C-I-O	39.3	32.7	40	35.4	1414

(0°,90°,0°) Orientation II

Material	Nomenclature	t	h	w	t	A_{mean}
1	3D-C-II-A	40.4	37.2	40	40.4	1616
1	3D-C-II-B	41.1	34.4	40	41.1	1644
1	3D-C-II-C	40.1	35.3	40	40.1	1604
1	3D-C-II-D	40.3	36.7	40	40.3	1612
1	3D-C-II-E	41.7	37.1	40	41.7	1668
1	3D-C-II-F	42.4	33.4	40	42.4	1696
1	3D-C-II-G	40.8	39.2	40	40.8	1632
1	3D-C-II-H	35.3	37.1	40	35.3	1412
1	3D-C-II-I	36.0	37.0	40	36.0	1440
1	3D-C-II-L	38.4	37.2	40	38.4	1536
1	3D-C-II-M	39.2	35.6	40	39.2	1568
1	3D-C-II-N	38.2	37.4	40	38.2	1528
1	3D-C-II-O	34.2	36.3	40	34.2	1368

(90°,0°,0°) Orientation III

Material	Nomenclature	t	h	w	t_{min}	A_{min}
1	3D-C-III-A	43.3	34.7	40	34.6	1385
1	3D-C-III-B	43.9	34.9	40	35.1	1404
1	3D-C-III-C	43.9	45.3	40	35.1	1404
1	3D-C-III-D	43.6	38.8	40	34.9	1576
1	3D-C-III-E	44.8	35.6	40	35.8	1432
1	3D-C-III-F	43.5	36.2	40	34.8	1392
1	3D-C-III-G	43.6	37.0	40	34.9	1396
1	3D-C-III-I	38.1	41.9	40	30.5	1220
1	3D-C-III-M	43.4	39.3	40	34.7	1388
1	3D-C-III-N	40.3	36.5	40	32.2	1288
1	3D-C-III-P	42.3	37.4	40	33.8	1352
1	3D-C-III-Q	38.2	43.2	40	30.6	1224
1	3D-C-III-R	40.4	34.6	40	32.3	1292

Table 3-6: Effective dimensions of 3D printed specimens with material type 1 used for the compression test.

	Material	Nomenclature	t	h	w	t_{mean}	A_{mean}
(0°,0°,0°) Orientation I	2	3D-C-I-A	68.1	56.2	40	40.0	1600
	2	3D-C-I-B	66.8	56.3	40	40.0	1600
	2	3D-C-I-C	68.5	57.3	40	40.0	1600
	2	3D-C-I-D	50.4	40.3	40	45.4	1814
	2	3D-C-I-E	40.0	32	40	36.0	1440
	2	3D-C-I-F	40.0	32	40	36.0	1440
	2	3D-C-I-G	44.3	35.4	40	39.9	1594
	2	3D-C-I-H	44.4	35.5	40	39.9	1598
	2	3D-C-I-I	45.6	36.4	40	41.0	1640
	2	3D-C-I-L	43.4	34.7	40	39.0	1562
	2	3D-C-I-M	43.9	35.1	40	39.5	1581
	2	3D-C-I-N	39.6	31.6	40	35.6	1424
	2	3D-C-I-O	40.9	32.7	40	36.8	1473
	2	3D-C-I-P	46.0	36.8	40	41.4	1656
	2	3D-C-I-Q	41.3	33.1	40	37.2	1488
	2	3D-C-I-R	45.4	36.3	40	40.8	1634
	2	3D-C-I-S	43.7	35	40	39.3	1574
	2	3D-C-I-T	40.4	32.3	40	36.3	1453
	Material	**Nomenclature**	t	h	w	t_{min}	A_{min}
(90°,0°,0°) Orientation III	2	3D-C-III-A	61.0	40.1	40	40.0	1600
	2	3D-C-III-B	63.0	39.8	40	40.0	1600
	2	3D-C-III-C	66.0	39.1	40	40.0	1600
	2	3D-C-III-D	40.0	39.4	40	32.0	1280
	2	3D-C-III-E	40.0	33.9	40	32.0	1280
	2	3D-C-III-F	40.0	39.6	40	32.0	1280
	2	3D-C-III-G	40.7	36.3	40	32.6	1303
	2	3D-C-III-H	43.4	39.6	40	34.7	1389
	2	3D-C-III-I	43.4	31.8	40	34.7	1387
	2	3D-C-III-L	39.6	39.4	40	31.7	1267
	2	3D-C-III-M	41.1	41.9	40	32.8	1314
	2	3D-C-III-N	40.1	40.9	40	32.1	1284
	2	3D-C-III-O	40.4	40.6	40	32.3	1294
	2	3D-C-III-P	41.2	40.7	40	32.9	1317
	2	3D-C-III-Q	42.1	40.4	40	33.6	1346
	2	3D-C-III-R	44.7	40.4	40	35.8	1431
	2	3D-C-III-S	40.7	41.1	40	32.5	1302
	2	3D-C-III-T	44.6	31.8	40	35.6	1427

Table 3-7: Effective dimensions of 3D printed specimens with material type 2 used for the compression test.

The compression test was performed considering three different orientations (see Figure 3-6a). Tests on cast specimens were also performed for reference purposes, which were considered to be directionally independent. The vertical load was applied on the top part of the specimen by a servo-controlled hydraulic jack with a maximum capacity of 100 kN. The test was conducted in displacement control with a velocity of 0.05 mm/min. The specimen was inserted between two steel plates with

dimensions 40x40 mm (see Figure 3-7). The compressive strength (f_{cm}) was calculated as:

$$f_{cm} = \frac{F_{max}}{A} \quad 3\text{-}3$$

where:

F_{max} is the maximum force reached during the test; and

A is the loaded area of the specimen (see *Table 3-6* and Table 3-7) indicated in red in Figure 3-6b and c.

Figure 3-7: Compression test: set-up.

3.5.3 Results

Table 3-8 and Table 3-10 show the compressive strength results obtained from the 3DPC specimens for material type 1 and material type 2, respectively. The tables includes information on the type of material, loaded area A, nomenclature ID, maximum force F_{max} and maximum compressive strength f_{cm} achieved during the test. Table 3-9 and Table 3-11 show the results of the compressive strength obtained from cast specimens for material type 2 and type 3, respectively. For material type 1 the results on cast specimens refers to the technical datasheet as reported in Table 3-1. It has to be noted that no layered specimens are provided for material type 3 because the study carried out in collaboration with ETH Zurich was not intended to investigate the compressive strength according to different orientations [107].

	Orientation I (0°,0°,0°)				Orientation II (0°,90°,0°)				Orientation III (90°,0°,0°)			
Material	**ID**	F_{max}	A_{mean}	$f_{cm,(0°,0°,0°)}$	**ID**	F_{max}	A_{mean}	$f_{cm,(0°,90°,0°)}$	**ID**	F_{max}	A_{min}	$f_{cm,(90°,0°,0°)}$
[-]	**[-]**	**[kN]**	**[mm²]**	**[MPa]**	**[-]**	**[kN]**	**[mm²]**	**[MPa]**	**[-]**	**[kN]**	**[mm²]**	**[MPa]**
1	3D-C-I-A1	86.6	1436	60.3	3D-C-II-A1	110.6	1616	64.8	3D-C-III-A1	124.5	1385	89.9
1	3D-C-I-A2	102.1	1436.4	71.1	3D-C-II-A2	72.6	1616	44.9	3D-C-III-A2	127.8	1385	92.3
1	3D-C-I-B1	103.4	1472.4	70.2	3D-C-II-B1	85.0	1644	51.7	3D-C-III-B1	118.1	1404	84.1
1	3D-C-I-B2	98.1	1472.4	66.6	3D-C-II-B2	41.8	1644	25.5	3D-C-III-B2	100.6	1404	71.6
1	3D-C-I-C1	108.6	1458	74.5	3D-C-II-C1	83.7	1604	52.2	3D-C-III-C1	97.3	1404	69.3
1	3D-C-I-C2	95.2	1458	65.3	3D-C-II-C2	59.8	1604	37.3	3D-C-III-C2	-	1404	-
1	3D-C-I-D1	94.2	1393.2	67.6	3D-C-II-D1	65.3	1612	40.5	3D-C-III-D1	86.9	1576	62.2
1	3D-C-I-D2	118.7	1393.2	85.2	3D-C-II-D2	41.4	1612	25.8	3D-C-III-D2	95.8	1576	68.8
1	3D-C-I-E1	121.3	1418.4	85.6	3D-C-II-E1	44.0	1668	26.4	3D-C-III-E1	105.0	1432	73.3
1	3D-C-I-E2	118.2	1418.4	83.4	3D-C-II-E2	107.5	1668	64.5	3D-C-III-E2	118.9	1432	83
1	3D-C-I-F1	103.4	1386	74.6	3D-C-II-F1	-	1696	-	3D-C-III-F1	104.8	1392	75.3
1	3D-C-I-F2	95.0	1386	68.6	3D-C-II-F2	-	1696	-	3D-C-III-F2	106.1	1392	76.2
1	3D-C-I-G1	92.3	1425.6	64.7	3D-C-II-G1	39.7	1632	24.3	3D-C-III-G1	105.8	1396	75.7
1	3D-C-I-G2	113.1	1425.6	79.3	3D-C-II-G2	46.2	1632	28.4	3D-C-III-G2	102.7	1396	73.8
1	3D-C-I-H1	104.6	1508.4	69.3	3D-C-II-H1	85.1	1412	60.3	3D-C-III-H1	91.0	1220	75.1
1	3D-C-I-H2	124.5	1508.4	82.3	3D-C-II-H2	111.7	1412	79.1	3D-C-III-H2	-	1220	-
1	3D-C-I-I1	104.6	1360.8	77.0	3D-C-II-I1	59.7	1440	41.5	3D-C-III-I1	105.4	1388	75.9
1	3D-C-I-I2	116.2	1360.8	85.4	3D-C-II-I2	98.6	1440	68.4	3D-C-III-I2	93.8	1388	73.4
1	3D-C-I-L1	107.5	1407.6	76.4	3D-C-II-L1	70.9	1536	46.1	3D-C-III-L1	102.9	1288	79.8
1	3D-C-I-L2	93.0	1407.6	66.0	3D-C-II-L2	71.4	1536	46.4	3D-C-III-L2	99.0	1288	76.9
1	3D-C-I-M1	116.8	1432.8	81.5	3D-C-II-M1	86.7	1568	55.3	3D-C-III-M1	96.3	1352	71.2
1	3D-C-I-M2	113.3	1432.8	79.0	3D-C-II-M2	52.5	1586	33.5	3D-C-III-M2	77.1	1352	57
1	3D-C-I-N1	102.1	1508.4	67.7	3D-C-II-N1	95.4	1528	62.4	3D-C-III-N1	-	1224	-
1	3D-C-I-N2	103.4	1508.4	68.5	3D-C-II-N2	82.9	1528	54.2	3D-C-III-N2	-	1224	-
1	3D-C-I-O1	103.2	1414.8	72.9	3D-C-II-O1	109.9	1368	80.4	3D-C-III-O1	89.4	1292	69.2
1	3D-C-I-O2	115.5	1414.8	81.6	3D-C-II-O2	116.5	1368	85.2	3D-C-III-O2	94.2	1292	72.9
Average				**74.03**				**50.10**				**74.85**
St.dev				**7.45**				**12.03**				**4.32**
C.o.V				**10.1%**				**24.0%**				**5.77%**

Table 3-8: Material type 1 - Compressive strength of 3DPC specimens. Codification: production (3D = printed specimens) – type of load applied (C = compression) - Orientation (I-II-III) - a letter (from A to O) referring to the printed specimen - specimen number.

Cast										
		7 days			14 days			28 days		
Material	**A**	**Id**	**F_{max}**	**$f_{cm,cast}$**	**Id**	**F_{max}**	**$f_{cm,cast}$**	**Id**	**F_{max}**	**$f_{cm,cast}$**
[-]	**[mm²]**	**[-]**	**[kN]**	**[MPa]**	**[-]**	**[kN]**	**[MPa]**	**[-]**	**[kN]**	**[MPa]**
2	1600	C-7-A1	50.43	31.52	C-14-A-1	54.36	33.98	C-28-A-1	59.68	37.30
2	1600	C-7-A2	53.07	33.17	C-14-A-2	60.75	37.97	C-28-A-2	56.64	35.40
2	1600	C-7-B1	50.31	31.44	C-14-B-1	59.20	37.00	C-28-B-1	68.50	42.81
2	1600	C-7-B2	52.90	33.06	C-14-B-2	62.13	38.83	C-28-B-2	68.85	43.03
2	1600	C-7-C1	50.10	31.31	C-14-C-1	61.43	38.39	C-28-C-1	58.08	36.30
2	1600	C-7-C2	53.14	33.21	C-14-C-2	54.42	34.01	C-28-C-2	63.38	39.61
2	1600	C-7-D1	54.49	34.06	C-14-D-1	57.15	35.72	C-28-D-1	57.23	35.77
2	1600	C-7-D2	52.00	32.50	C-14-D-2	58.70	36.69	C-28-D-2	59.53	37.21
2	1600	C-7-E1	54.03	33.77	C-14-E-1	59.09	36.93	C-28-E-1	61.60	38.50
2	1600	C-7-E2	52.00	32.50	C-14-E-2	59.29	37.06	C-28-E-2	56.15	35.09
2	1600	C-7-F1	54.86	34.29	C-14-F-1	53.82	33.64	C-28-F-1	62.78	39.24
2	1600	C-7-F2	49.00	30.63	C-14-F-2	63.58	39.74	C-28-F-2	58.64	36.65
2	1600	C-7-G1	50.18	31.36	C-14-G-1	50.45	31.53	C-28-G-1	66.50	41.56
2	1600	C-7-G2	51.94	32.46	C-14-G-2	54.44	34.03	C-28-G-2	60.80	38.00
2	1600	C-7-H1	51.57	32.23	C-14-H-1	51.67	32.29	C-28-H-1	60.52	37.83
2	1600	C-7-H2	53.09	33.18	C-14-H-2	58.88	36.80	C-28-H-2	65.91	41.19
2	1600	C-7-I1	53.33	33.33	C-14-I-1	58.26	36.41	C-28-I-1	55.51	34.69
2	1600	C-7-I2	49.48	30.93	C-14-I-2	61.13	38.21	C-28-I-2	57.97	36.23
Average				**32.50**			**36.07**			**38.13**
St.dev				**1.10**			**2.33**			**2.61**
C.o.V				**3.38%**			**6.45%**			**6.84%**

Table 3-9: Material type 2 - Compressive strength of cast specimens. Codification: production (Cast = C) - concrete age (7,14 or 28 days) – a letter (from A to I which refers to the cast specimens) – number of the specimen.

	Orientation I (0°,0°,0°)				Orientation III (90°,0°,0°)			
Mat	**Id**	**F_{max}**	**A_{mean}**	**$f_{cm,(0°,0°,0°)}$**	**Id**	**F_{max}**	**A_{min}**	**$f_{cm\ (90°,0°,0°)}$**
[-]	**[-]**	**[kN]**	**[mm²]**	**[MPa]**	**[-]**	**[kN]**	**[mm²]**	**[MPa]**
2	3D-C-I-A1	99.22	1600	62.01	3D-C-III-A1	65.73	1600	41.08
2	3D-C-I-A2	96.11	1600	60.07	3D-C-III-A2	64.58	1600	40.36
2	3D-C-I-B1	62.15	1600	38.84	3D-C-III-B1	85.87	1600	53.67
2	3D-C-I-B2	99.70	1600	62.31	3D-C-III-B2	79.54	1600	49.71
2	3D-C-I-C1	108.8	1600	67.97	3D-C-III-C1	43.83	1600	27.39
2	3D-C-I-C2	85.76	1600	53.60	3D-C-III-C2	56.46	1600	35.29
2	3D-C-I-D1	99.93	1814	55.09	3D-C-III-D1	93.68	1280	73.19
2	3D-C-I-D2	98.48	1814	54.29	3D-C-III-D2	98.98	1280	77.33
2	3D-C-I-E1	105.7	1440	73.42	3D-C-III-E1	94.98	1280	74.20
2	3D-C-I-E2	79.05	1440	54.90	3D-C-III-E2	89.15	1280	69.65
2	3D-C-I-F1	89.76	1440	62.33	3D-C-III-F1	74.89	1280	58.51
2	3D-C-I-F2	81.94	1440	56.90	3D-C-III-F2	76.37	1280	59.66
2	3D-C-I-G1	98.51	1594	61.80	3D-C-III-G1	104.0	1303	79.83
2	3D-C-I-G2	62.37	1594	39.13	3D-C-III-G2	103.7	1303	79.62
2	3D-C-I-H1	84.59	1598	52.95	3D-C-III-H1	81.53	1389	58.69
2	3D-C-I-H2	93.21	1598	58.34	3D-C-III-H2	79.09	1389	56.94
2	3D-C-I-I1	87.01	1640	53.06	3D-C-III-I1	75.17	1387	54.19
2	3D-C-I-I2	83.61	1640	50.99	3D-C-III-I2	68.89	1387	49.66
2	3D-C-I-L1	80.95	1562	51.84	3D-C-III-L1	64.21	1267	50.67
2	3D-C-I-L2	78.13	1562	50.03	3D-C-III-L2	65.03	1267	51.32
2	3D-C-I-M1	93.36	1581	59.06	3D-C-III-M1	59.47	1314	45.26
2	3D-C-I-M2	77.02	1581	48.72	3D-C-III-M2	58.73	1314	44.70
2	3D-C-I-N1	97.74	1424	68.65	3D-C-III-N1	77.89	1284	60.67
2	3D-C-I-N2	72.92	1424	51.22	3D-C-III-N2	69.42	1284	54.07
2	3D-C-I-O1	89.65	1473	60.87	3D-C-III-O1	70.03	1294	54.13
2	3D-C-I-O2	56.39	1473	38.29	3D-C-III-O2	64.68	1294	49.99
2	3D-C-I-P1	106.1	1656	64.08	3D-C-III-P1	101.2	1317	76.88
2	3D-C-I-P2	101.2	1656	61.15	3D-C-III-P2	80.63	1317	61.23
2	3D-C-I-Q1	94.03	1488	63.21	3D-C-III-Q1	85.07	1346	63.19
2	3D-C-I-Q2	101.2	1488	68.02	3D-C-III-Q2	85.71	1346	63.67
2	3D-C-I-R1	93.38	1634	57.16	3D-C-III-R1	96.38	1431	67.36
2	3D-C-I-R2	98.01	1634	59.99	3D-C-III-R2	59.36	1431	41.49
2	3D-C-I-S1	88.83	1574	56.44	3D-C-III-S1	93.33	1302	71.68
2	3D-C-I-S2	109.6	1574	69.66	3D-C-III-S2	73.83	1302	56.70
2	3D-C-I-T1	56.87	1453	39.13	3D-C-III-T1	96.23	1427	67.46
2	3D-C-I-T2	99.32	1453	68.34	3D-C-III-T2	80.89	1427	56.70
Average				**57.05**				**57.67**
St.dev				**6.88**				**9.99**
C.o.V				**12.1%**				**17.3%**

Table 3-10: Material type 2 - Compressive strength of 3DPC specimens. Codification: production (3D = printed specimens) – type of load applied (C = compression) - orientation (I-II-III) - a letter (from A to T) referring to the printed specimen - specimen number.

Cast										
		7 days			14 days			28 days		
Material	**A**	**Id**	**F_{max}**	**$f_{cm,cast}$**	**Id**	**F_{max}**	**$f_{cm,cast}$**	**Id**	**F_{max}**	**$f_{cm,cast}$**
[-]	**[mm²]**	**[-]**	**[kN]**	**[MPa]**	**[-]**	**[kN]**	**[MPa]**	**[-]**	**[kN]**	**[MPa]**
3	1600	C-7-A-1	76.6	47.9	C-14-A-1	106.5	66.6	C-28-A-1	101.0	64.6
3	1600	C-7-A-2	74.3	46.4	C-14-A-2	101.5	63.4	C-28-A-2	98.6	63.1
3	1600	C-7-B-1	58.4	58.4	C-14-B-1	100.7	62.9	C-28-B-1	107.3	67.1
3	1600	C-7-B-2	55.8	55.8	C-14-B-2	105.1	65.7	C-28-B-2	104.1	65.1
3	1600	C-7-C-1	57.9	57.9	C-14-C-1	98.8	62.8	C-28-C-1	110.9	69.3
3	1600	C-7-C-2	58.8	58.8	C-14-C-2	95.3	60.5	C-28-C-2	108.6	67.9
Average				**57.7**			**63.7**			**66.2**
St.dev				**1.16**			**1.84**			**1.52**
C.o.V				**0.02**			**0.03**			**0.02**

Table 3-11: Material type 3 - Compressive strength of 3DPC specimens. Codification: production (Cast = C) - concrete age (7,14 or 28 days) – a letter (from A to C refers to the cast specimens) – number of the specimen.

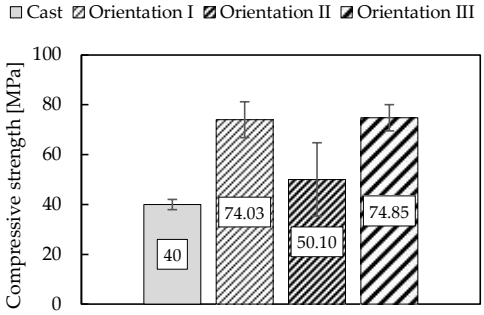

(a)

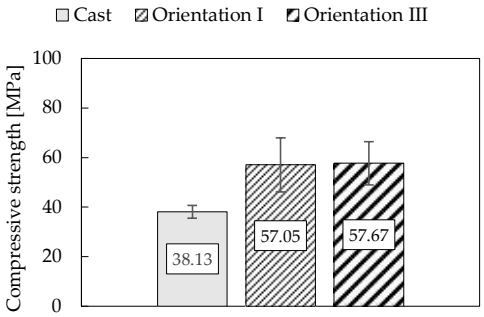

(b)

Figure 3-8: Compressive strength f_{cm} of 3DPC specimens with respect to different orientations: (a) Material type 1 (the result on cast specimen refers to the technical datasheet) and (b) Material type 2.

3.5.4 Discussion

In this section the results obtained from the compression tests on 3D printed concrete to estimate the compressive strength are discussed. The compressive strength of specimens printed with material type 1 resulted to be 74.03 MPa, 50.1 MPa and 74.8 MPa for orientation I, orientation II and orientation III, respectively. The compressive strength of specimens printed with material type 2 resulted to be 57.05 MPa and 57.67 MPa for orientation I and III, respectively. The values of the compressive strength resulted 33% and 34% higher considering orientation I and orientation III respectively compared to cast specimens, which have a compressive strength equal to 38.13 MPa measured at 28 days. The obtained results are in line with the literature: the difference between the compressive strength obtained from Orientation I and Orientation III is negligible [11,12,14,68–70].

3.6 Tensile strength

3.6.1 Literature review

The flexural strength of concrete is commonly measured with three point bending test [10–12,14,68–71,102]. As for the compressive strength, to take into account the anisotropy of 3D printed concrete different orientations were considered [10–12,14,68–71,102] (Figure 3-9). It should be pointed out that while in orientation I the tensile stresses are parallel to the interlayer surface, in orientation III, the tensile stresses act perpendicularly to the interlayer surface. The former case may represent the typical behaviour of a 3D printed beam, the latter case may highlight the state of stress at the base of a shear wall subjected to a lateral load.

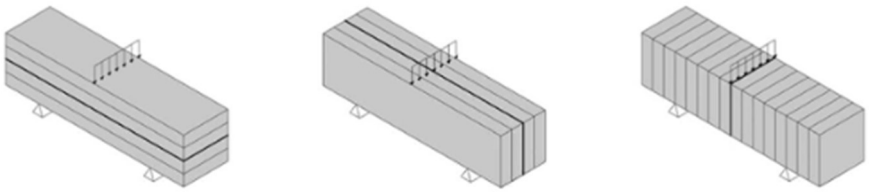

Orientation I Orientation II Orientation III

Figure 3-9: Printed layers orientation in flexural tests [69].

As previously mentioned, the strength of the interlayer is crucial in determining the overall structural performance. When the bonding strength is low, it can lead to the formation of a cold joint, which can cause a reduction in mechanical strength. To measure the interface strength in the case of normal forces acting on the interface, the pull-off test is commonly used. In [11,12,14,102,108] the tensile strength was measured in various loading directions (as shown in Figure 3-10), and the direction identified as D3, with the load applied in the perpendicular direction to the layers, was found to be the weakest (that is equivalent to the previous defined as orientation I).

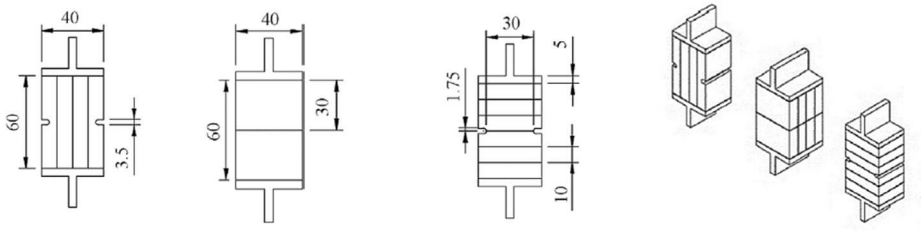

D1 D2 D3

Figure 3-10: Printed layers orientation in direct tensile tests [12].

3.6.2 Specimen geometry and test set-up

3.6.2.1 Three-point bending test

The specimens for the characterization of flexural strength had nominal dimensions 160x40x40 mm (Figure 3-11a).

Table 3-12 and Table 3-13 show the effective height h, thickness t and length l of the printed specimens for material type 1 and material type 2, respectively. The values of the minimum thickness t_{min} and mean thickness t_{mean} are also indicated, which are estimated as the 80% and 90% of the effective thickness, respectively. The cross-section of the specimens that contributes to the flexural tensile strength $f_{ctm,fl}$ is indicated in red in Figure 3-11b and c. Considering Orientation I and II, the cross-sectional area A_{mean} of the specimen was considered as fully resistant, while considering Orientation III the resisting area A_{min} excludes the surface waves that did not contribute to the flexural tensile strength (Figure 3-11b and c).

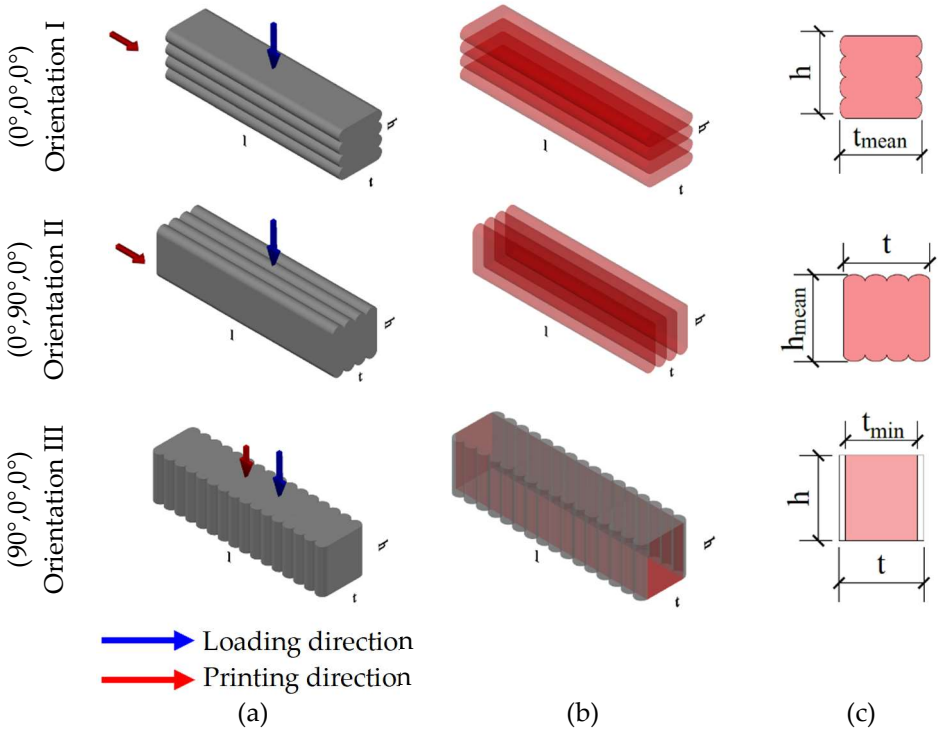

Figure 3-11: Flexural tests: (a) specimens geometry; (b) and (c) loading area.

	Material	Nomenclature	t	h	l	t_{mean}	A_{mean}
(0°,0°,0°) Orientation I	1	3D-C-I-A	43.3	34.7	158.7	39.0	1352
	1	3D-C-I-B	43.9	34.9	159.0	39.5	1379
	1	3D-C-I-C	43.9	45.3	159.0	39.5	1790
	1	3D-C-I-D	43.6	38.8	158.9	39.2	1523
	1	3D-C-I-E	44.8	35.6	159.4	40.3	1435
	1	3D-C-I-F	43.5	36.2	158.6	39.2	1417
	1	3D-C-I-G	43.6	37.0	158.6	39.2	1452
	1	3D-C-I-H	38.1	41.9	156.3	34.3	1437
	1	3D-C-I-I	43.4	39.3	158.5	39.1	1535
	1	3D-C-I-L	40.3	36.5	155.7	36.3	1324
	1	3D-C-I-M	42.3	37.4	159.2	38.1	1424
	1	3D-C-I-N	38.2	43.2	153.9	34.4	1485
	1	3D-C-I-O	40.4	34.6	155.2	36.4	1258
	Material	**Nomenclature**	t	h	l	h_{mean}	A_{mean}
(0°,90°,0°) Orientation II	1	3D-C-II-A	40.4	37.2	154.8	33.5	1353
	1	3D-C-II-B	41.1	34.4	156.4	31.0	1272
	1	3D-C-II-C	40.1	35.3	156.0	31.8	1274
	1	3D-C-II-D	40.3	36.7	155.7	33.0	1331
	1	3D-C-II-E	41.7	37.1	156.2	33.4	1392
	1	3D-C-II-F	42.4	33.4	159.1	30.1	1275
	1	3D-C-II-G	40.8	39.2	158.4	35.3	1439
	1	3D-C-II-H	35.3	37.1	159.1	33.4	1179
	1	3D-C-II-I	36.0	37.0	159.1	33.3	1199
	1	3D-C-II-L	38.4	37.2	155.4	33.5	1286
	1	3D-C-II-M	39.2	35.6	154.3	32.0	1256
	1	3D-C-II-N	38.2	37.4	155.4	33.7	1286
	1	3D-C-II-O	34.2	36.3	154.2	32.7	1117
	Material	**Nomenclature**	t	h	l	t_{min}	A_{min}
(90°,0°,0°) Orientation III	1	3D-C-III-A	39.9	34.6	153.7	31.9	1104
	1	3D-C-III-B	40.9	36.7	152.3	32.7	1201
	1	3D-C-III-C	40.5	36.9	152.9	32.4	1196
	1	3D-C-III-D	38.7	37.2	154.7	31.0	1152
	1	3D-C-III-E	39.4	34.6	151.6	31.5	1091
	1	3D-C-III-F	38.5	37.6	154.7	30.8	1158
	1	3D-C-III-G	39.6	37.1	154.4	31.7	1174
	1	3D-C-III-I	41.9	34.1	163.7	33.5	1143
	1	3D-C-III-M	37.8	33.7	151.1	30.2	1019
	1	3D-C-III-N	39.1	39.2	149.7	31.3	1226
	1	3D-C-III-P	39.8	36.3	166.3	31.8	1156
	1	3D-C-III-Q	41.9	35.8	154.6	33.5	1200
	1	3D-C-III-R	39.3	32.7	154.7	31.4	1028

Table 3-12: Effective dimensions of 3D printed specimens with material type 1 used for the flexural tensile test.

	Material	Nomenclature	t	h	l	t_{mean}	A_{mean}
(0°, 0°, 0°) Orientation I	2	3D-C-I-A	61.0	40.1	160.6	59.4	2382
	2	3D-C-I-B	63.0	39.8	160.4	59.4	2364
	2	3D-C-I-C	66.0	39.1	160.5	63.9	2498
	2	3D-C-I-D	40.0	39.4	160	36.0	1419
	2	3D-C-I-E	40.0	33.9	160	36.0	1219
	2	3D-C-I-F	40.0	39.6	160	36.0	1426
	2	3D-C-I-G	40.7	36.3	160	36.6	1331
	2	3D-C-I-H	43.4	39.6	160	39.1	1548
	2	3D-C-I-I	43.4	31.8	160	39.0	1239
	2	3D-C-I-L	39.6	39.4	160	35.6	1402
	2	3D-C-I-M	41.1	41.9	160	37.0	1548
	2	3D-C-I-N	40.1	40.9	160	36.1	1478
	2	3D-C-I-O	40.4	40.6	160	36.4	1477
	2	3D-C-I-P	41.2	40.7	160	37.0	1507
	2	3D-C-I-Q	42.1	40.4	160	37.9	1528
	2	3D-C-I-R	44.7	40.4	160	40.2	1624
	2	3D-C-I-S	40.7	41.1	160	36.6	1505
	2	3D-C-I-T	44.6	31.8	160	40.1	1274
	Material	**Nomenclature**	t	h	l	t_{min}	A_{min}
(90°,0°,0°) Orientation III	2	3D-C-III-A	70.3	40	164.0	56.2	2250
	2	3D-C-III-B	70.4	36.4	160.0	56.3	2050
	2	3D-C-III-C	71.6	35.6	162.0	57.3	2039
	2	3D-C-III-D	50.4	44.4	160.0	40.3	1625
	2	3D-C-III-E	40.0	34.0	160.0	32.0	1024
	2	3D-C-III-F	40.0	34.0	160.0	32.0	1024
	2	3D-C-III-G	44.3	38.3	160.0	35.4	1255
	2	3D-C-III-H	44.4	38.4	160.0	35.5	1261
	2	3D-C-III-I	45.6	39.6	160.0	36.4	1328
	2	3D-C-III-L	43.4	37.4	160.0	34.7	1204
	2	3D-C-III-M	43.9	37.9	160.0	35.1	1234
	2	3D-C-III-N	39.6	33.6	160.0	31.6	1001
	2	3D-C-III-O	40.9	34.9	160.0	32.7	1071
	2	3D-C-III-P	46.0	40.0	160.0	36.8	1354
	2	3D-C-III-Q	41.3	35.3	160.0	33.1	1093
	2	3D-C-III-R	45.4	39.4	160.0	36.3	1318
	2	3D-C-III-S	43.7	37.7	160.0	35.0	1223
	2	3D-C-III-T	40.4	34.4	160.0	32.3	1043

Table 3-13: Effective dimensions of 3D printed specimens with material type 2 used for the flexural tensile test.

The tests were performed considering three different orientations (see Figure 3-11a). Tests on cast specimens were also performed for reference purposes, which were considered to be directionally independent. The flexural strength was determined by three-point bending test, according to the standard used for mortar EN 1015-11:2019 [109], which is taken as reference. The set-up is composed by two steel bearing rollers and a third roller is centrally placed on top of the sample to apply the load (see Figure 3-12). The vertical load was applied on the top part of the specimen by a servo-

controlled hydraulic jack with a maximum capacity of 100 kN. The test was conducted in displacement control with a velocity of 0.05 mm/min. The flexural tensile strength ($f_{ctm,fl}$) was calculated as:

$$f_{ctm,fl} = \frac{M_{max} y}{J} = \frac{3}{2} \frac{F_{max} d}{t h^2} \quad 3\text{-}4$$

where:
M_{max} is the maximum bending moment reached during the test;
J is the moment of inertia;
y is the depth of the neutral axis;
F_{max} is the maximum force reached during the test;
d is the distance between the axis of the support rollers in mm (see Figure 3-12);
t is the width of the specimen in millimetres;
h is the depth of the specimen in millimetres.

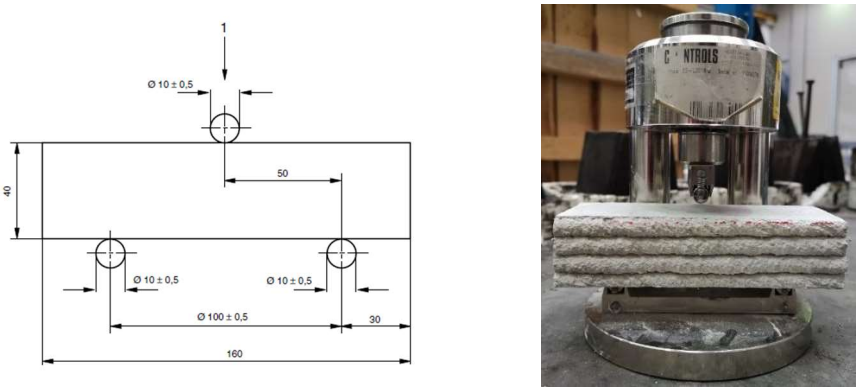

Figure 3-12: Flexural test set-up.

3.6.2.2 *Direct tensile test*

Specimens for the characterization of direct tensile strength had nominal dimensions 120x60x60 mm. Table 3-14 and *Table 3-15* shows the effective height *h*, thickness *t* and width *w* of the printed specimens for material type 1 and material type 2, respectively. The minimum thickness t_{min} is also reported and it is estimated as the 80% of the effective thickness.

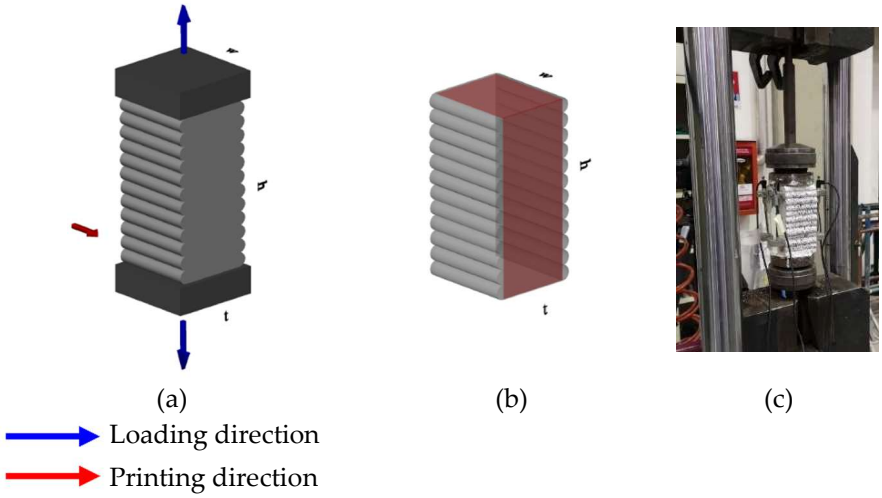

Figure 3-13: Direct tensile test: (a) specimen; (b) loading area and (c) test set-up.

	Material	Nomenclature	*t*	*h*	*w*	t_{min}	A_{min}
(90°,0°,0°) Orientation III	1	3D-T-A	36.0	165	36	28.8	1037
	1	3D-T-B	37.5	163	36	30.0	1080
	1	3D-T-C	51.3	169	35	41.0	1435
	1	3D-T-D	39.1	160	35.5	31.3	1112
	1	3D-T-E	48.7	149.7	48.8	38.9	1870
	1	3D-T-F	43.2	148.5	53.6	34.6	1852
	1	3D-T-G	40.9	152.6	35.5	32.7	1153

Table 3-14: Effective dimensions of 3D printed specimens with material type 1 used for the direct tensile test.

	Material	Nomenclature	*t*	*h*	*w*	t_{min}	A_{min}
(90°,0°,0°) Orientation III	2	3D-T-A	71.2	125	65	57	3705
	2	3D-T-B	68.7	119	64	55	3520
	2	3D-T-C	68.7	124	66	55	3630
	2	3D-T-D	67.5	125	65	54	3510
	2	3D-T-E	71.2	122	64	57	3648
	2	3D-T-F	67.5	123	65	54	3510
	2	3D-T-G	67.5	121	62	54	3348

Table 3-15: Effective dimensions of 3D printed specimens with material type 2 used for the direct tensile test.

The tests were conducted considering orientation III (see Figure 3-13), with the stresses direction perpendicular to the printed concrete layers. The vertical load was applied on the top part of the specimen by a servo-controlled hydraulic jack with a maximum capacity of 100 kN. The test was carried out in displacement control with a velocity of 0.001 mm/min. The steel plates were glued to the specimen and connected to the testing machine (see Figure 3-13). Longitudinal deformation of the specimen was monitored with small linear voltage displacement transducers (LVDTs) with 2 mm stroke, which were placed in couple on two opposite side of the specimen. On the other two sides the digital image correlation was applied.
The tensile strength f_{ctm} was calculated as:

$$f_{ctm} = \frac{F_{max}}{A_{min}} \qquad 3\text{-}5$$

where:
F_{max} is the maximum force reached during the test; and
A_{min} is the loaded area excluding the concrete waves that do not contribute to the tensile strength.

3.6.3 Results

3.6.3.1 Three-point bending test

Table 3-16 and Table 3-18 shows the flexural tensile strength results obtained from 3DPC specimens for material type 1 and material type 2 respectively. The tables includes information on the type of material, loaded area A, nomenclature ID, maximum force F_{max} and maximum flexural strength $f_{cmt,fl}$ achieved during the test. Table 3-17 and Table 3-19 shows the results of the flexural tensile strength obtained from cast specimens for material type 2 and type 3, respectively. For material type 1 the results on cast specimens refers to the technical datasheet as reported in Table 3-1. No layered specimens are provided for material type 3 (study carried out in collaboration with ETH Zurich [107]) because the goal of the research was not to study the flexural strength according to different orientations.

	Orientation I (0°, 0°,0°)					Orientation II (0°, 90°,0°)					Orientation III (90°, 0°,0°)				
Material	ID	F_{max}	M_{max}	t_{mean}	$f_{ctm,(0°,0°,0°)}$	ID	F_{max}	M_{max}	t_{mean}	$f_{ctm,(0°,90°,0°)}$	ID	F_{max}	M_{max}	t_{mean}	$f_{ctm,(90°,0°,0°)}$
[-]	[-]	[kN]	[kNm]	[mm]	[MPa]	[-]	[kN]	[kNm]	[mm]	[MPa]	[-]	[kN]	[kNm]	[mm]	[MPa]
1	3D-T-I-A	1.43	0.036	39	4.57	3D-T-II-A	2.12	0.053	40.4	4.82	3D-T-III-A	2.04	0.051	31.9	8.01
1	3D-T-I-B	1.67	0.042	39.5	5.21	3D-T-II-B	2.73	0.068	41.1	5.90	3D-T-III-B	1.79	0.045	32.7	6.09
1	3D-T-I-C	2.50	0.063	39.5	4.63	3D-T-II-C	2.33	0.058	40.1	5.42	3D-T-III-C	2.33	0.058	32.4	7.92
1	3D-T-I-D	2.19	0.068	39.2	6.93	3D-T-II-D	3.13	0.078	40.3	7.17	3D-T-III-D	2.26	0.057	31.0	7.91
1	3D-T-I-E	1.52	0.038	40.3	4.46	3D-T-II-E	3.15	0.079	41.7	6.52	3D-T-III-E	2.32	0.058	31.5	9.22
1	3D-T-I-F	2.73	0.055	39.2	6.40	3D-T-II-F	2.28	0.057	42.4	4.49	3D-T-III-F	1.86	0.047	30.8	6.41
1	3D-T-I-G	2.14	0.054	39.2	5.98	3D-T-II-G	3.35	0.084	40.8	7.40	3D-T-III-G	2.05	0.051	31.7	7.07
1	3D-T-I-H	0.70	0.018	34.3	1.74	3D-T-II-H	2.73	0.068	35.3	9.31	3D-T-III-H	2.37	0.059	33.5	9.12
1	3D-T-I-I	1.93	0.048	39.1	4.80	3D-T-II-I	3.02	0.076	36.0	9.71	3D-T-III-I	0.94	0.024	30.2	4.11
1	3D-T-I-L	1.55	0.039	36.3	4.81	3D-T-II-L	2.63	0.066	38.4	6.97	3D-T-III-L	2.26	0.057	31.3	7.05
1	3D-T-I-M	2.25	0.056	38.1	6.34	3D-T-II-M	2.34	0.059	39.2	5.83	3D-T-III-M	2.41	0.060	31.8	8.62
1	3D-T-I-N	1.54	0.039	34.4	3.60	3D-T-II-N	2.46	0.062	38.2	6.62	3D-T-III-N	1.66	0.042	33.5	5.80
1	3D-T-I-O	1.12	0.031	36.4	4.24	3D-T-II-O	1.43	0.036	34.2	5.36	3D-T-III-O	1.37	0.034	31.4	6.11
Average					**5.00**					**6.58**					**7.19**
St.dev					**0.89**					**1.57**					**0.98**
C.o.V					**17.9%**					**23.9%**					**13.6%**

Table 3-16: Material type 1 - flexural tensile strength of 3DPC specimens. Codification: production (3D = printed specimens) – type of load applied (T = tension) - orientation (I-II-III) - a letter (from A to R) referring to the printed specimen.

	Cast 7 days						Cast 14 days					
Material	**ID**	**F_{max}**	**M_{max}**	**t_{mean}**	**$f_{ctm,cast}$**	**ID**	**F_{max}**	**M_{max}**	**t_{mean}**	**$f_{ctm,cast}$**	**ID**	**F_{max}**	**M_{max}**	**t_{mean}**	**$f_{ctm,cast}$**
[-]	**[-]**	**[kN]**	**[kNm]**	**[mm]**	**[MPa]**	**[-]**	**[kN]**	**[kNm]**	**[mm]**	**[MPa]**	**[-]**	**[kN]**	**[kNm]**	**[mm]**	**[MPa]**
2	C-7-A	2.58	0.065	40.0	6.05	C-14-A	2.16	0.054	40.0	5.06	C-28-A	2.57	0.064	40.0	6.02
2	C-7-B	2.47	0.062	40.0	5.79	C-14-B	2.64	0.066	40.0	6.19	C-28-B	2.67	0.067	40.0	6.26
2	C-7-C	2.37	0.059	40.0	5.55	C-14-C	2.58	0.065	40.0	6.05	C-28-C	2.48	0.062	40.0	5.81
2	C-7-D	2.58	0.065	40.0	6.05	C-14-D	2.38	0.060	40.0	5.58	C-28-D	2.34	0.059	40.0	5.48
2	C-7-E	2.35	0.059	40.0	5.51	C-14-E	2.42	0.061	40.0	5.67	C-28-E	2.78	0.070	40.0	6.52
2	C-7-F	2.54	0.064	40.0	5.95	C-14-F	2.11	0.053	40.0	4.95	C-28-F	2.45	0.061	40.0	5.74
2	C-7-G	2.62	0.066	40.0	6.14	C-14-G	2.44	0.061	40.0	5.72	C-28-G	2.63	0.066	40.0	6.16
2	C-7-H	2.59	0.065	40.0	6.07	C-14-H	2.55	0.064	40.0	5.98	C-28-H	2.87	0.072	40.0	6.73
2	C-7-I	2.55	0.064	40.0	5.98	C-14-I	2.33	0.058	40.0	5.46	C-28-I	3.27	0.082	40.0	7.66
Average					**5.90**										**6.27**
St.dev					**0.23**										**0.65**
C.o.V					**3.9%**										**10.4%**

Table 3-17: Material type 2 -flexural tensile strength of cast specimens. Codification: production (Cast = C) - concrete age (7,14 or 28 days) – a letter (from A to I which refers to the cast specimens).

	Orientation I (0°,0°,0°)					Orientation III (90°,0°,0°)				
Mat	**Id**	**F_{max}**	**M_{max}**	**t_{mean}**	**$f_{ctm,fl,(0°,0°,0°)}$**	**Id**	**F_{max}**	**M_{max}**	**t_{min}**	**$f_{ctm,fl,(90°,0°,0°)}$**
[-]	**[-]**	**[kN]**	**[kNm]**	**[mm]**	**[MPa]**	**[-]**	**[kN]**	**[kNm]**	**[mm]**	**[MPa]**
2	3D-T-I-A	3.97	0.099	59.4	6.23	3D-T-IIIA	6.02	0.151	56.2	10.04
2	3D-T-I-B	4.41	0.110	59.4	7.03	3D-T-III-B	5.43	0.136	56.3	10.92
2	3D-T-I-C	4.78	0.120	63.9	7.34	3D-T-III-C	4.99	0.125	57.3	10.31
2	3D-T-I-D	3.2	0.080	36.0	8.58	3D-T-III-D	2.38	0.060	40.3	5.37
2	3D-T-I-E	2.83	0.071	36.0	10.29	3D-T-III-E	2.29	0.057	32.0	6.91
2	3D-T-I-F	4.07	0.102	36.0	10.81	3D-T-III-F	2.64	0.066	32.0	7.29
2	3D-T-I-G	3.5	0.088	36.6	10.87	3D-T-III-G	2.93	0.073	35.4	8.07
2	3D-T-I-H	5.66	0.142	39.1	13.85	3D-T-IIIH	2.84	0.071	35.5	9.52
2	3D-T-I-I	2.81	0.070	39.0	10.71	3D-T-III-I	1.30	0.033	36.4	3.41
2	3D-T-I-L	2.05	0.051	35.6	5.57	3D-T-III-L	1.35	0.034	34.7	3.51
2	3D-T-I-M	3.33	0.083	37.0	7.70	3D-T-IIIM	2.26	0.057	35.1	6.48
2	3D-T-I-N	3.4	0.085	36.1	8.43	3D-T-IIIN	1.96	0.049	31.6	6.08
2	3D-T-I-O	2.94	0.074	36.4	7.35	3D-T-IIIO	1.99	0.050	32.7	5.94
2	3D-T-I-P	2.92	0.073	37.0	7.14	3D-T-III-P	1.55	0.039	36.8	4.11
2	3D-T-I-Q	2.23	0.056	37.9	5.42	3D-T-IIIQ	1.24	0.031	33.1	3.66
2	3D-T-I-R	2.2	0.055	40.2	5.04	3D-T-III-R	1.55	0.039	36.3	4.02
2	3D-T-I-S	2.64	0.066	36.6	6.40	3D-T-III-S	1.67	0.042	35.0	4.18
2	3D-T-I-T	1.84	0.046	40.1	6.82	3D-T-III-T	1.71	0.043	32.3	5.17
Average		**3.27**			**6.85**		**2.56**			**5.58**
St.dev		**1.01**			**1.51**		**1.45**			**2.50**
C.o.V		**31%**			**22.11%**		**56%**			**44.7%**

Table 3-18: Material type 2 -flexural tensile strength of 3DPC specimens. Codification: production (3D = printed specimens) – type of load applied (T = tension) - orientation of the printed layers with respect to the load (I-II-III) - a letter (from A to T) referring to the printed specimen - specimen number.

	Cast 7 days					Cast 14 days					Cast 28 days				
Material	**ID**	**F_{max}**	**M_{max}**	**t_{mean}**	**$f_{ctm,cast}$**	**ID**	**F_{max}**	**M_{max}**	**t_{mean}**	**$f_{ctm,cast}$**	**ID**	**F_{max}**	**M_{max}**	**t_{mean}**	**$f_{ctm,cast}$**
[-]	**[-]**	**[kN]**	**[kNm]**	**[mm]**	**[MPa]**	**[-]**	**[kN]**	**[kNm]**	**[mm]**	**[MPa]**	**[-]**	**[kN]**	**[kNm]**	**[mm]**	**[MPa]**
2	C-7-A	3.7	0.093	40.4	8.5	C-14-A	3.9	0.098	40.5	9	C-28-A	5.3	0.133	39.1	12.6
2	C-7-B	4.2	0.105	40.0	10.1	C-14-B	5.1	0.128	40.5	11.4	C-28-B	5.5	0.138	40.9	12.4
2	C-7-C	4.4	0.110	40.1	10.1	C-14-C	4.9	0.123	39.4	11.7	C-28-C	5.7	0.143	40.2	13.2
Average					**9.5**					**10.7**					**12.7**
St.dev					**0.89**					**1.47**					**0.41**
C.o.V					**9,3%**					**13.7%**					**3.2%**

Table 3-19: Material type 3 - flexural tensile strength of 3DPC specimens. Codification: production (Cast = C) - concrete age (7,14 or 28 days) – a letter (from A to C which refers to the cast specimens).

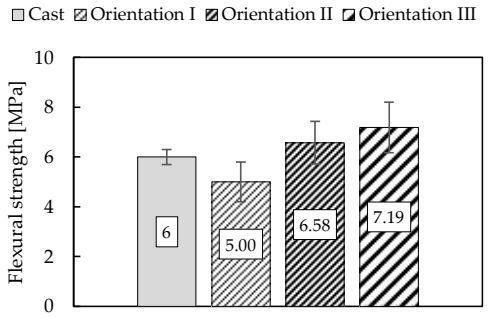

(a)

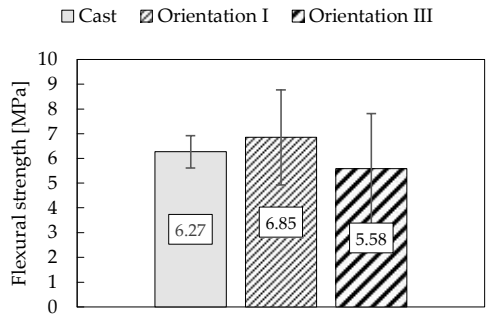

(b)

Figure 3-14: Flexural tensile strength $f_{cmt,fl}$ of 3DPC specimens with respect to different orientations: (a) Material type 1 and (b) Material type 2.

3.6.3.2 Direct tensile test

Within this section the results of the tensile strength obtained from the direct tensile test are reported. Table 3-20 and Table 3-21 summarize the results obtained from the direct tensile test for material type 1 and material type 2, respectively. It came out that the direct tensile strength resulted equal to 3.4 MPa and 2.8 MPa for material type 1 and material type 2, respectively. Figure 3-15a and Figure 3-15b shows the tensile strength versus the vertical strain measured both with the LVDTs and the digital image correlation for material type 1 and material type 2, respectively. Figure 3-16 shows the failure mode of a specimen subjected to direct tensile test, the behaviour is brittle and as consequence it was not possible to record the post-peak phase after the crack occurred (see Figure 3-15).

Orientation III (90°,0°,0°)				
Material	**Id**	**Fmax**	**A_{min}**	**$f_{ctm,(90°,0°,0°)}$**
[-]	**[-]**	**[kN]**	**[mm²]**	**[MPa]**
1	3D-T-A	4.53	1037	4.37
1	3D-T-B	5.54	1080	5.13
1	3D-T-C	4.81	1435	3.35
1	3D-T-D	4.04	1112	3.63
1	3D-T-E	4.56	1870	2.44
1	3D-T-F	5.01	1852	2.70
1	3D-T-G	3.12	1153	2.71
Average				**3.43**
St.dev				**1.25**
C.o.V				**0.36**

Table 3-20: Material type 1 - tensile strength of 3DPC specimens.

Orientation III (90°,0°,0°)				
Material	**Id**	**Fmax**	**A_{min}**	**$f_{ctm,(90°,0°,0°)}$**
[-]	**[-]**	**[kN]**	**[mm²]**	**[MPa]**
2	3D-T-A	8.86	3705	2.39
2	3D-T-B	10.71	3520	3.04
2	3D-T-C	9.31	3630	2.56
2	3D-T-D	9.46	3510	2.69
2	3D-T-E	12.29	3648	3.36
2	3D-T-F	11.17	3510	3.18
2	3D-T-G	9.97	3348	2.97
Average				**2.88**
St.dev				**0.35**
C.o.V				**0.12**

Table 3-21: Material type 2 - tensile strength of 3DPC specimens.

Regarding material type 3, the tensile strength of the concrete matrix f_{ctm} is estimated as suggested by Eurocode 2 [110] using the following equations:

$$f_{ctm,fl} = max[(1.6 - h/1000)f_{ctm}; f_{ctm}] \quad 3\text{-}6$$

$$f_{ctm} = min\left\{\frac{f_{ctm,fl}}{(1.6 - \frac{h}{1000})}; f_{ctm,fl}\right\} \quad 3\text{-}7$$

Where h is the specimen depth (40 mm) and $f_{ctm,fl}$ is the flexural tensile strength of material type 3 (see Table 3-19). Table 3-22 reports a summary of the estimated tensile strength.

Concrete age	$f_{ctm,fl}$ (1)	f_{cm} (1)	f_{ctm} (2)	f_{cm}/f_{ctm}
	MPa	MPa	MPa	-
7 days	10.1	57.7	6.47	8.9
14 days	10.7	63.7	6.86	9.3
28 days	12.7	66.2	8.14	8.1

(1) According to EN 1015-11:1999 [111]
(2) According to Eurocode 2 [113]

Table 3-22: Material type 3 - estimated tensile strength of 3DPC specimens.

The tensile strength f_{ctm} of material type 3 resulted equal to 6.47 MPa, 6.86 MPa and 8.14 MPa considering specimens tested at 7, 14 and 28 days, respectively. The ratio between the compressive strength f_{cm} and the tensile strength f_{ctm} (f_{cm}/f_{ctm}) is about 10.

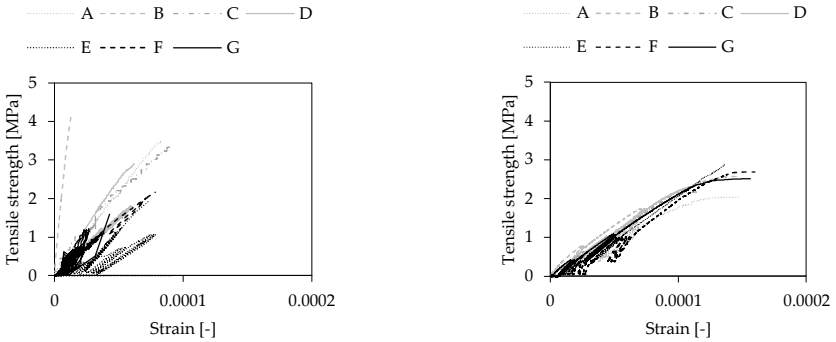

(a) (b)

Figure 3-15: Stress-strain behaviour of 3D printed concrete specimen from direct tensile test: (a) material type 1 and (b) material type 2.

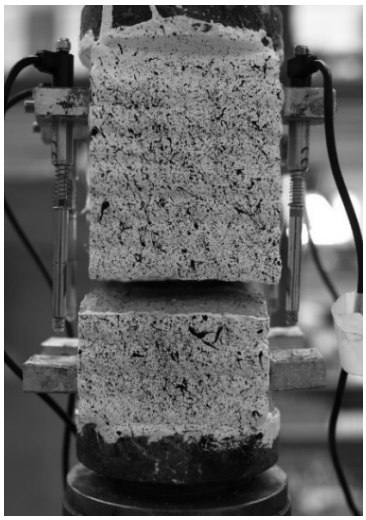

Figure 3-16: Direct tensile test: failure mode.

3.6.4 Discussion

This section presents two testing methods used to determine the tensile strength of 3D printed concrete. The flexural test provides a quick and simple estimation of the flexural tensile strength, but it cannot measure other properties and may overestimate the tensile strength. In contrast, the direct tensile test offers a more accurate estimation of the tensile strength, and it allows for the measurement of the strain field and calculation of the elastic modulus (see section 3.8). For material type 1, the flexural strength for orientations I, II, and III was 5.00 MPa, 6.58 MPa, and 7.19 MPa, respectively, which is in contrast with the literature where orientation I typically has a higher flexural strength than orientation III. The specimens were cut from a companion specimen and this discrepancy could be due to local defects of the specimens, e.g microcracks, shrinkage, weak bond between layers etc. The flexural tensile strength of cast specimens (according to technical datasheet see Table3-1) with material type 1 at 28 days resulted equal to 6 MPa, which is 17% higher and 16% lower than 3DPC specimens considering orientation I and orientation III; it resulted 9% lower than 3DPC specimens considering orientation II, respectively. For material type 2, the flexural strength was 6.85 MPa and 5.58 MPa for orientations I and III, respectively, which is instead in agreement with the literature [10–12,14,68–71,102]. The values of the flexural strength resulted 9% higher considering orientation I and 13% lower considering orientation III compared to cast specimens, which have a flexural strength equal to 6.27 MPa measured at 28 days. The direct tensile strength for material types 1 and 2 was 3.4 MPa and 2.8 MPa, respectively.

3.7 Shear strength

3.7.1 Literature review

The behaviour of 3D printed concrete structures could be significantly affected by the interfaces, which could be subjected to different stress conditions, including bending, pure shear, tension and shear, compression and shear.
Various test methods can be used to estimate the strength of the interfaces (see Figure 3-17); the test results could be influenced by several factors such as the specimen size, the test setup and the loading rate. In section 3.6, the direct tensile test to determine the interlayer strength under tensile forces was discussed (Figure 3-17b). This section focuses instead on the evaluation of the tests set-up to determine the interlayer bond strength under shear loads.

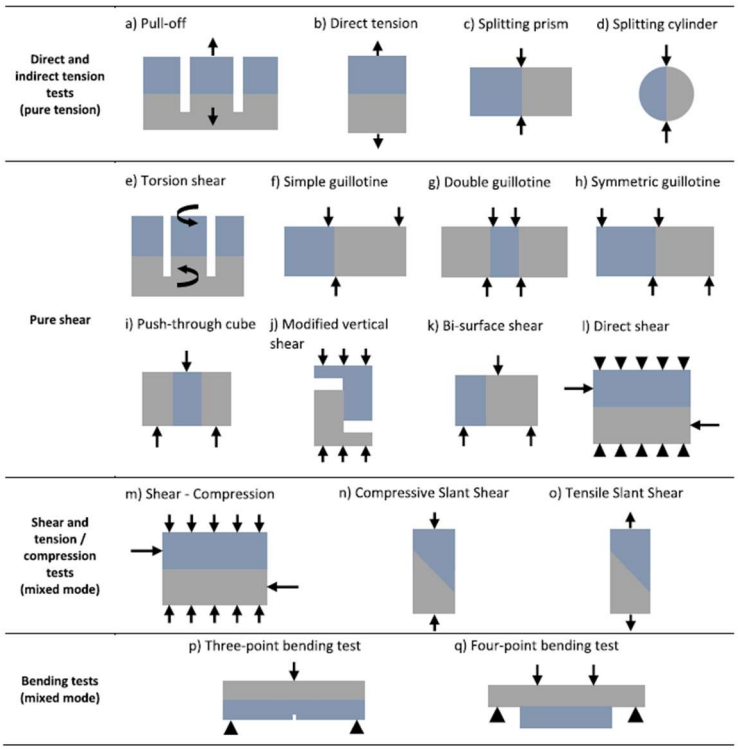

Figure 3-17: Test methods to determine interface bond strength [114].

Common shear test configurations works similarly to the guillotine, where steel supports apply shear loads at the joint line (Figure 3-17 f-h). In these tests, the greatest stress concentrations occur along the edges of the specimen in contact with the steel support. The specimen fails when the stresses in these small regions of the concrete

exceed the shear strength, giving a local strength value instead of a global average one.

Conventional direct shear test involves the application of two parallel loads in opposite directions on both sides of the specimen interface bond (Figure 3-17l). However, the main limitation of this test is the tendency to induce a bending moment along with the shear force. This aspect prevents accurate replication of pure shear conditions and consequently affects the reliability of the results obtained. To address this issue, alternative methods, such as push-out (Figure 3-17i), L-shape (Figure 3-17j) and bi-surface (Figure 3-17k) tests, are used to evaluate the bond between concrete interfaces. These techniques aim to mitigate the impact of eccentric loading generated between interfaces.

Momayez et al. [115] investigated the bi-surface shear test (Figure 3-17k) applying a three-point bending load on 150 mm cubes. Three point loads are applied such that they produce a state of shear stress on the repaired interface. The test variables included specimen size, maximum aggregate size of repair materials, type of repair material, interface roughness, and age at loading.

Giraldo-Soto et al. [116] conducted a study to examine the impact of different experimental configurations on shear transfer capacity in steel fiber reinforced concrete (SFRC). Two established configurations were explored: the push-out and the L-shaped test configuration. In the case of the L-shaped test configuration, no distinct factors were identified that could significantly affect the shear transfer capacity. On the other hand, push-out tests, which was conducted without the application of precompression, was clearly influenced by the arch effect, which led to compression of the shear plane and a reduction in crack opening. Consequently, this configuration showed a tendency to overestimate the shear capacity. The experimental shear capacities observed by the authors in the push-out tests were 6% higher than those obtained in the L-type tests, mainly due to localized failure occurring at the bearing surfaces. However, due to the presence of the arch effect, it becomes necessary to introduce additional modifications to the push-out shear test to prevent such failures. One potential modification involves the introduction of additional supports at the ends of the specimen for the application of the precompression [117]. As the applied loads increase, the crack extends toward the top side of the specimen until the maximum or peak load is reached. This behaviour leads to secondary effects, characterized by limited bending occurring before the ultimate shear stress is reached at the interface. As consequence, unwanted compressive stresses occur in the upper section of the shear interface. As a result, the current test setup reduce the arch effect but is not able to produce the desired result of pure shear failure.

Guan [118]and Javidmeh [119] used the L-shear test to overcome the shortcomings of the direct shear test. However, a concentration of stresses is noted in the corner of

the component during load application. Excessive concentration of stresses can cause the failure of the specimen.

Comparing the three different shear tests, it is evident that each has advantages and limitations. In the case of direct shear test, the load application is straightforward; however, a bending moment could arise along with shear action. On the other hand in the L-type shear test, the specimen corner could be subject to fracture due to stress concentration. Finally, the push-out test could be subjected to limited bending, but effectively minimizes the stress concentration.

The slant shear test (Figure 3-17n) is the most popular combined shear-compression test involving the compression testing of a cylinder or prism with an interface angle of 30°. Momayez et al. [120] examined the bond strength of specimens constructed with different repair materials using different test methods. It was demonstrated that the bond strength is significantly influenced by the chosen test method. Specifically, the shear slant test recorded a shear strength measurement four times greater than the strength estimated through bi-surface shear test. Furthermore, Zanotti et al. [121] compared the shear slant test (Figure 3-17n) and the push-out test (Figure 3-17i). The concrete substrate was a normal strength concrete and the repair materials consisted of normal and high strength concrete, with and without fibre reinforcement. In the slant shear test, the normal strength repair material showed interfacial bond failure, while high strength concrete predominantly failed under compression. On the contrary, all specimens exhibited clear bond failure in push-out test. The test results indicate that the shear strength measured through the push-out test is considerably lower than that measured through the slant shear test. In fact, the slant shear test measures bond strength under a combination of compression and shear. The compressive stresses in this test generate higher interlock and friction forces that increment the shear failure load. Furthermore, depending on the compressive strength of the substrate and overlay, and on the inclination of the interface plane, this test results in either adhesive interface debonding or crushing of the weaker concrete layer (substrate or overlay).

It is difficult to recommend a universal test method for all bond strength applications. Therefore, the recommended approach is to use a combination of different test methods to comprehensively assess bond strength. The predominant loading conditions specific to a given structure have to be identified to determine the most appropriate test method to be used. Within the scope of this study, the push-out test was chosen because it easily allows the simulation of the conditions of vertical and horizontal loads acting on a wall and the specimens are more easily printable compared to L-shaped specimens. The slant shear test was chosen because it allows the estimation of shear parameters by varying the inclination of the printed layers with respect the horizontal printing plane.

3.7.2 Specimen geometry and test set-up

3.7.2.1 Modified push-out test

To evaluate the interlayer shear strength of 3D printed concrete walls under constant vertical and horizontal load, modified push-out tests were conducted on small-scale specimens. UNI EN 1052-3 [122], which is used for the assessment of the initial shear strength of masonry structures, was used as a reference and modified accordingly to the needs of the present study on 3D printed elements. As consequence, throughout the text the nomenclature modified push-out test will be used. As shown in Figure 3-18, the specimens were cut with the layers in the direction parallel to the printing direction from companion specimen without printing defects (cold joints).

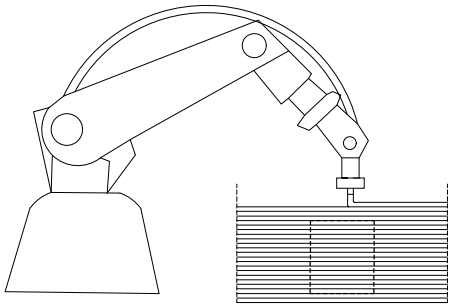

Figure 3-18: Specimens used for the characterization of the interlayer shear strength: orientation of the layers with respect to the printing direction.

Two series of tests were carried out with material type 1 and material type 2, respectively. In the case of material type 1, the specimens was 14 cm high, 14 cm long, and 4 cm thick, with each printed layer 2 cm high, resulting in a total of 7 layers (Figure 3-19a). The dimensions of the specimens used by Napolitano et al. in [16] were taken as a reference. Considering material type 2, the specimens had a height of 12 cm, a length of 16 cm and a thickness of 6 cm (Figure 3-19b). Each layer was 1 cm thick for a total of 16 layers. The push-out tests were performed also on cast specimens with material type 2. In section 3.7.3.1.2 the reason of the two different geometries will be explained.

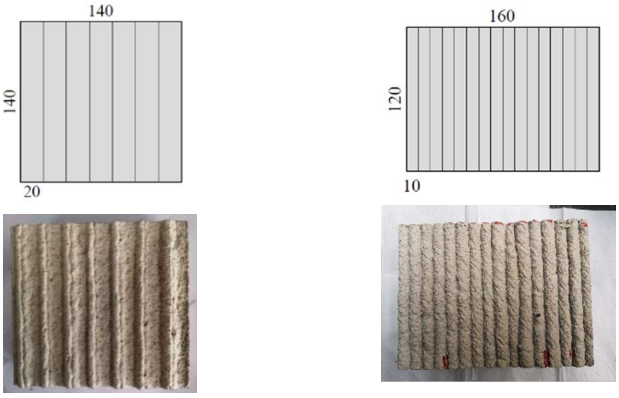

(a) (b)

Figure 3-19: Specimens used for the modified push-out test: (a) material type 1 and (b) material type 2.

The test simulates the constant vertical load (precompression σ) and the horizontal force (vertical force F) applied on a wall, as shown in Figure 3-20. The tests were carried out under two conditions: (a) without normal stress (Figure 3-20a) and (b) with normal stress applied (Figure 3-20b). The first condition represents the case of the wall subjected only to horizontal load without vertical load applied (Figure 3-20a). The second situation investigates the influence of vertical load with different intensities, as shown in (Figure 3-20b). Different levels of normal stress, which represent the load at the base of the building, were investigated. With regards to Material type 1, four level of precompression were considered: 0 MPa, 2 MPa, 4 MPa, and 6 MPa. Considering material type 2, five level of precompression were considered equal to 0 MPa, 1 MPa, 2 MPa, 4 MPa, and 6 MPa. For each level of precompression three specimens were tested for a total of 12 and 15 specimens for material type 1 and material type 2, respectively. In addition, 15 specimens cast with material type 2 were tested, three for each level of precompression.

(a) (b)

Figure 3-20: Tested specimen: (a) without normal stress, (b) with normal stress.

Figure 3-21 shows the test set-up used to assess the interlayer shear strength of 3D printed concrete walls through the modified push-out test. The specimen was rotated by 90° with respect to the printing position. The vertical load, which simulates the horizontal load applied on the wall, was applied on the top part of the specimen by a servo-controlled hydraulic jack with a maximum capacity of 500 kN. The test was performed in displacement control with a velocity of 0.05 mm/min. At the bottom of the specimen, there were two supports to counteract the applied vertical load. In this way, the central layers were forced to slide with respect to the outer portion of the specimen and the cracks occurred on two identified vertical surfaces, indicated in red in Figure 3-20. The normal stress, which simulates the vertical load carried by a wall in a building, was applied in the direction perpendicular to the printed layers by using a system of conical disc springs and two M10 threaded rods. The springs were CB - DIN 2093 60x20.4x2, arranged in series, as shown in Figure 3-21c, to take advantage of a longer stroke with the same load applied. The normal stress was kept constant during the test and measured by two load cells.

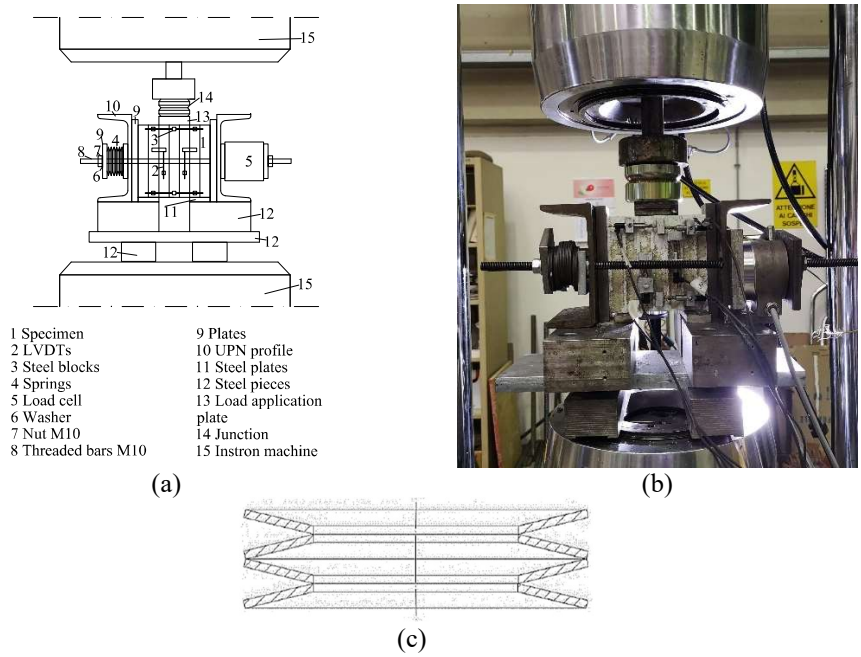

Figure 3-21: (a)&(b)Shear test set-up; (c) conical disc springs.

The specimen was instrumented on one side with two vertical and four horizontal LVDTs (linear variable displacement transducer) to measure the relative vertical displacement between the layers (LVDT 1 and LVDT 2) and the crack opening (Figure 3-22a), respectively; on the other side, with Digital Image Correlation (DIC) which was used to detect the onset and propagation of the cracks (Figure 3-22b).

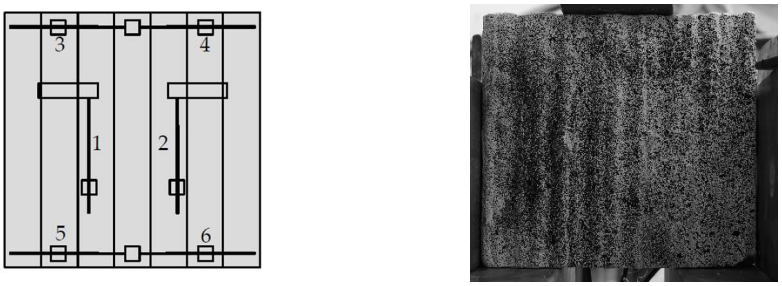

(a) (b)

Figure 3-22: Instrumentation of the specimen: (a) LVDTs; (b) digital image correlation.

3.7.2.2 Modified slant shear test

The modified slant shear test (MSST) was used to determine the 3D printed concrete strength because it allows to consider the anisotropy generated by the printed concrete layers and to calculate the shear parameters by varying the layer inclination with respect to the horizontal reference. EN 12615 [123], which is used to estimate the shear properties between cast concrete and a repair material, was used as a reference and modified accordingly to the needs of the present study on 3D printed elements. This research is the results of a joint project between the group of Concrete Structures and Bridge Design at ETH Zurich (Professor Walter Kaufmann) and of Structural Engineering at the University of Brescia (Professor Giovanni Plizzari) [107]. The specimens for MSST were extracted from 3D printed concrete walls having a thickness of 100 mm and variable height and length (Figure 3-23a) printed using material type 3. The specimens were printed using an ABB robotic arm, a hopper feeds a mixer with a drymix, which continuously mixes water to feed wet mortar into a pump. The mortar is pumped to a printhead on the ABB arm, where it is actively mixed with the accelerator via a motor driven impeller. The robot speed can reach up to 160 mm/min with a diameter of the extruder chosen equal to 25 mm. Detailed information on the printing setup can be found in [124,125]. The thickness of the printed layer varies depending on the specific object to be printed, which may consist of a single layer or several parallel vertical joint elements/walls. The printing of joint elements/walls could create voids in the 3DPC elements which could have a significant impact on the loadbearing capacity. In some cases, the choice of a smaller extruder radius facilitates the optimisation of complex geometries; moreover, it enables the printing of hollow holes for reinforcement purposes, (e.g. bespoken columns and White Tower [124–126]). A single printed concrete layer was formed by a 25 mm wide and 7 mm thick print-path. According to EN 12615 [123], the thickness of the specimen for the MSST has to be 100 mm, therefore, the 100 mm wall thickness was made of four parallel vertical joint elements/walls created by the print-paths

(Figure 3-23b). In addition, a printed concrete layer with reduced bonding, named cold joint (cold-joint-30), was introduced in the middle of the 3D printed concrete specimens stopping the printing around 30 min when approximately half the height of the specimen was reached (Figure 3-23c). The surface of the cold joint was smooth and not subjected to any treatment. The reason for introducing a cold joint was to consider a certain tolerance of possible interruption during the production of 3D printed concrete elements.

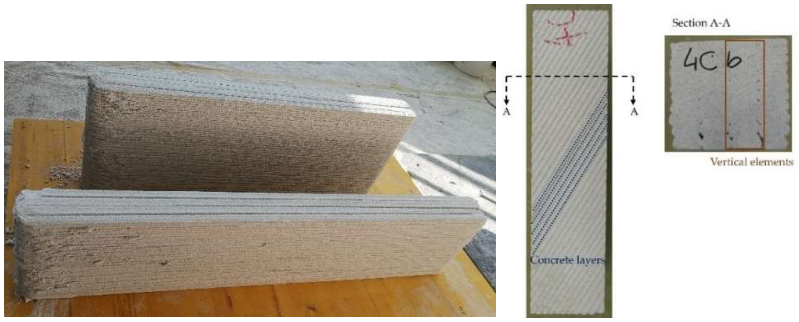

(a) (b)

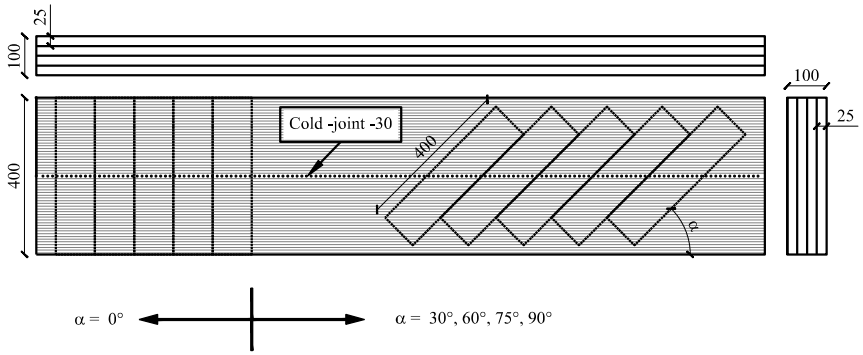

(c)

Figure 3-23: 3D printed concrete walls with cold-joint: (a) companion specimen, (b) 3DPC specimen and (c) cold joint position.

The samples used in this study were 400 mm high, 100 mm wide and 100 mm in thick. The effective dimensions of the specimens varied from 398 mm to 405 mm (C.o.V 0.93%), from 96 mm to 106 mm (C.o.V 4.9%) and from 106 mm to 119 mm (C.o.V 5.5%) considering the height, the width and the thickness, respectively. The specimens were printed and cured in laboratory environment with a temperature of 20° and a humidity of 45% and had different concrete layer inclinations with respect to the horizontal printing plane (α = 0°, 30°, 60°, 75° and 90°, see Figure 3-24). Each specimen had an untreated cold joint in the middle due to a time gap of 30 minutes.

A total of 45 prisms were tested in five series of experiments (according to the different layers inclinations) to assess the impact of interlayer inclination on the mechanical properties of 3DPC elements. Each series consisted of three groups of specimens that were tested at 7, 14, and 28 days after printing.

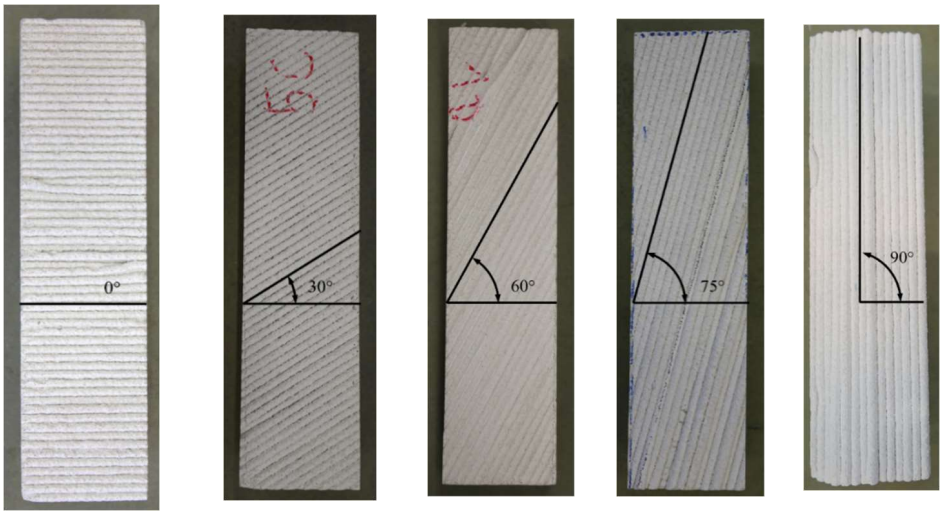

Figure 3-24: 3D printed concrete specimens with different concrete layer inclinations to the horizontal plane: a) 0°, b) 30°, c) 60°, d) 75° and e) 90°.

The Modified Slant Shear Test setup for 3D printed concrete is illustrated in Figure 3-25. This test involved the compression of 3D printed concrete prisms of size 400x100x100 mm^3 with different inclinations of the concrete layers with respect to the horizontal reference. A servo hydraulic Universal Testing Machine with a maximum capacity of 1600 kN was used to conduct the tests. The 3D printed concrete specimens were positioned vertically and subjected to compression, with the force applied in displacement control at a rate of 0.2 mm/min. The specimen was instrumented only with digital image correlation (DIC) to detect the onset and propagation of the cracks and to measure the strain field.

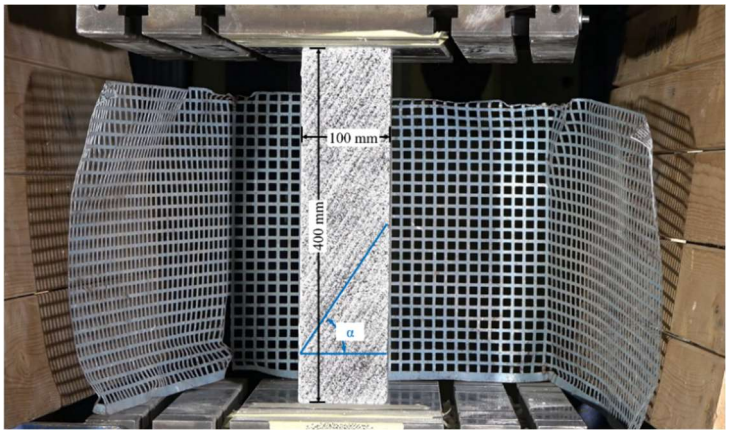

Figure 3-25: Test setup of the Modified Slant Shear Test for 3D printed concrete.

3.7.3 Test results

3.7.3.1 Modified push-out test

3.7.3.1.1 Material type 1

The shear strength τ_{max} was calculated for each specimen as follow:

$$\tau_{max} = \frac{F_{max}}{2A_{min}} \quad 3\text{-}8$$

Where F_{max} is the maximum load reached during the test and A_{min} is the minimum area of the specimen parallel to the printed layers neglecting the concrete waves that do not contribute to shear strength of the specimen. Table 3-23 shows the effective height h, thickness t and length l of the printed specimens for material type 1 and material type 2, respectively. The minimum thickness t_{min} is also reported and it is estimated as the 80% of the effective thickness.

	Material	Nomenclature	t	h	l	t_{min}	A_{min}
(90°,0°,0°) Orientation III	1	3D-S-A	55.6	136	150	44.5	6052
	1	3D-S-B	54.2	130	150	43.4	5642
	1	3D-S-C	55.7	142	140	44.6	6333
	1	3D-S-D	56.5	154	138	45.2	6961
	1	3D-S-E	56.3	124	137	45.0	5580
	1	3D-S-F	54.5	161	155	43.6	7020
	1	3D-S-G	57.5	123	134	46.0	5662
	1	3D-S-H	53.8	134	154	43.0	5762
	1	3D-S-I	50.4	155	164	40.3	6247
	1	3D-S-L	53.8	158	157	43.0	6794
	1	3D-S-M	50.0	135	140	40.0	5400
	1	3D-S-N	50.0	135	140	40.0	5400

	Material	Nomenclature	t	h	l	t_{min}	A_{min}
(90°,0°,0°) Orientation III	2	3D-S-A	67	123	155	57	6593
	2	3D-S-B	67	119	160	57	6378
	2	3D-S-C	65	122	158	55.3	6344
	2	3D-S-D	66	121	161	56	6389
	2	3D-S-E	67	119	158	57	6378
	2	3D-S-F	68	120	163	58	6528
	2	3D-S-G	66	119	159	56	6257
	2	3D-S-H	65	121	157	55.3	6292
	2	3D-S-I	67	118	158	57	6324
	2	3D-S-L	67	120	162	57	6432
	2	3D-S-M	66	122	159	56	6442
	2	3D-S-N	67	121	159	57	6486
	2	3D-S-O	43	132	169	37	4541
	2	3D-S-P	45	131	168	38	4716
	2	3D-S-Q	45	129	174	38	4438

Table 3-23: Effective dimensions of 3D printed specimens with material type 1 and material type 2 used for modified push-out test.

Table 3-24 shows the results of the modified push out test conducted using material type 1. The precompression force F_n, the critical force F_{cr} (when the first crack occurs) and the maximum force F_{max} reached during the test are reported. It has to be observed that by increasing the level of precompression the shear strength also increases, with average values of 5.83 MPa, 11.93 MPa, 10.63 MPa and 18.06 MPa for the specimen with lateral precompression equal to 0 MPa, 2 MPa, 4 MPa, and 6 MPa, respectively. Figure 3-26 shows the shear stress versus the relative vertical displacement of the tested specimen with different level of precompression applied.

Material	ID	F_n	F_{cr}	F_{max}	A_{min}	σ_n	τ_{cr}	$\tau_{max,(0°,0°,0°)}$	Failure
[-]	[-]	[kN]	[kN]	[kN]	[mm²]	[MPa]	[MPa]	[MPa]	[-]
1	3D-S-A	0	35.8	52.8	6052	0.0	2.6	4.4	IF
1	3D-S-B	0	53.1	69.9	5642	0.0	4.7	6.2	IF
1	3D-S-C	0	50.4	87.8	6333	0.0	4.0	6.9	IF
1	3D-S-D	11.2	35.6	204.6	6961	2	2.6	14.7	IF
1	3D-S-E	11.2	-	92.9	5580	2	-	8.3	IF
1	3D-S-F	11.2	126.4	180.3	7020	2	9.0	12.8	MF
1	3D-S-G	22.4	76.5	98.5	5662	4	6.8	8.7	IF
1	3D-S-H	22.4	124.7	157.3	5762	4	10.8	13.6	IF
1	3D-S-I	22.4	87.6	119.7	6247	4	7.0	9.6	CF
1	3D-S-L	33.6	120.9	229.5	6794	6	8.9	16.9	CF
1	3D-S-M	33.6	86.7	211.1	5400	6	8.0	19.5	MF
1	3D-S-N	33.6	36.1	193.0	5400	6	3.3	17.8	MF

Table 3-24: Summary of the results of the modified push-out test conducted on specimens printed with material type 1.

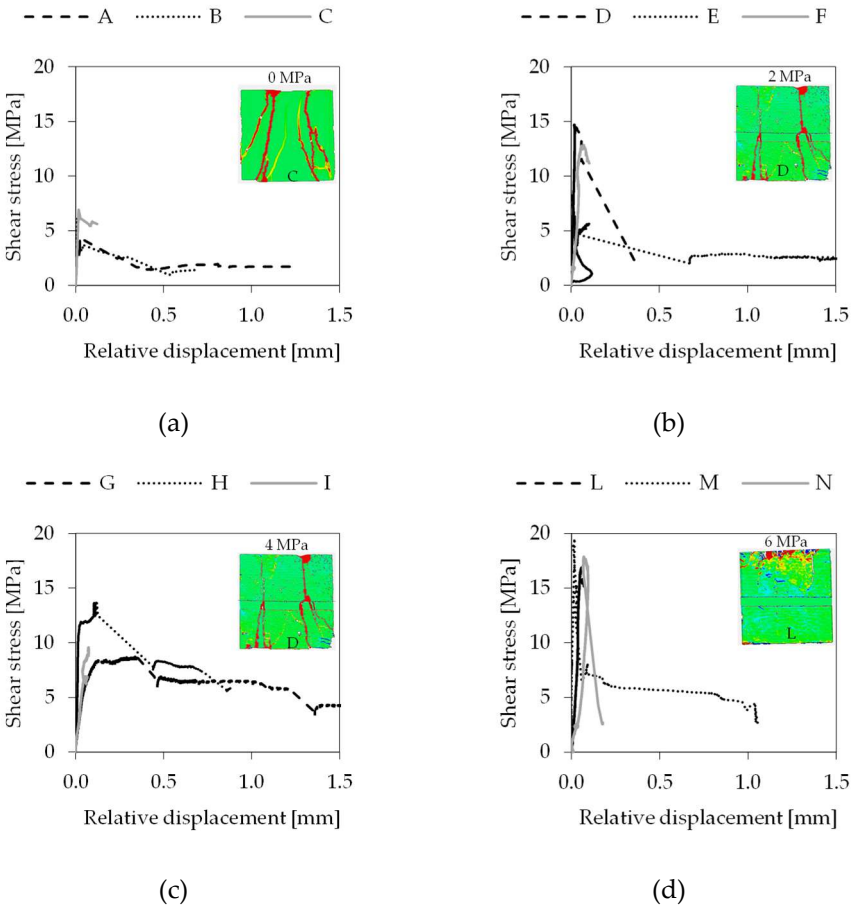

Figure 3-26: Shear stress-relative vertical displacement of the 3DPC specimens subjected to modified push-out test (material type 1) for the different level of precompression: (a) 0 MPa, (b) 2 MPa, (c) 4Mpa, and (d) 6 MPa.

Figure 3-27 shows the relationship between the shear strength and the relative vertical displacement between the layers of three selected specimens. The general behaviour of the specimens resulted to be very brittle. The behaviour of the specimens under shear action can be summarized in three main phases:

- **Pre-cracking phase**: Up to point A, the specimens exhibit linear behaviour, meaning that an increase in load results in a proportional increase in deformation.
- **Cracking phase:** A non-linear phase developed between point A and point B, indicating the onset of the cracking process. At point A the first crack occurred and at point B, which corresponds to the maximum load applied during the test, a critical crack appeared (Figure 3-28).
- **Post-fracture phase:** Distinct behaviours were observed due to different failure mechanisms. The dotted black curve depicted in Figure 3-27 corresponds to a specimen with no lateral compression (specimen C) which exhibited a concrete layer interface failure (named IF in Table 3-24) and it was possible to record the post-peak phase (Figure 3-28a). At peak load, the specimen failed on one of the two identified surfaces, and during the post-peak phase, the other critical surface remained undamaged until it failed, ending the test. The grey curve in Figure 3-27 represents a specimen with 6 MPa lateral stress applied (specimen L), which exhibited a concrete matrix failure (Figure 3-28b). In this case, the shear strength was high, the failure occurred before as concrete matrix failure under the point load rather than as concrete layer interface failure. It can be demonstrated that under the point load the compressive stress was higher (around 85 MPa) than the compressive strength of the material (equal to 75 MPa as shown in Table 3-8). Consequently, the post-peak phase could not be recorded because the test stopped almost immediately after the maximum load was reached, which does not necessarily correspond to the maximum shear strength. Due to the high level of normal stress applied, the geometry of the specimen used for the test was no longer representative and requires modification of the test set-up accordingly (see section 3.7.3.1.2). The black curve in Figure 3-27 illustrates the behaviour of a specimen with 2 MPa lateral stress applied (specimen F), exhibiting a mixed failure (named MF in Table 3-24) between concrete matrix and concrete layer interface failure (Figure 3-28c). In this case, the behaviour of the curve is similar to the specimens that exhibited a concrete matrix failure. This is evident also from the strains in Figure 3-28c where shear cracks are present, but the critical ones that brought to failure were those related to concrete matrix failure. Finally, it should be noted that by increasing the normal stress, the failure mode changes from concrete layer interface failure to concrete matrix failure.

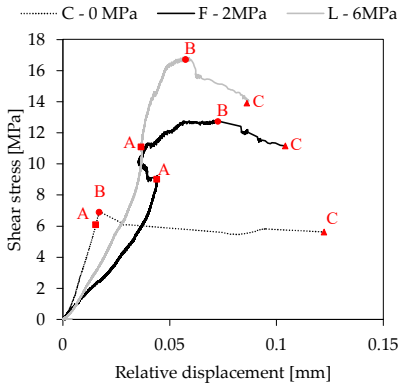

Figure 3-27: Shear stress versus relative vertical displacement of three selected specimens subjected to different levels of lateral stress.

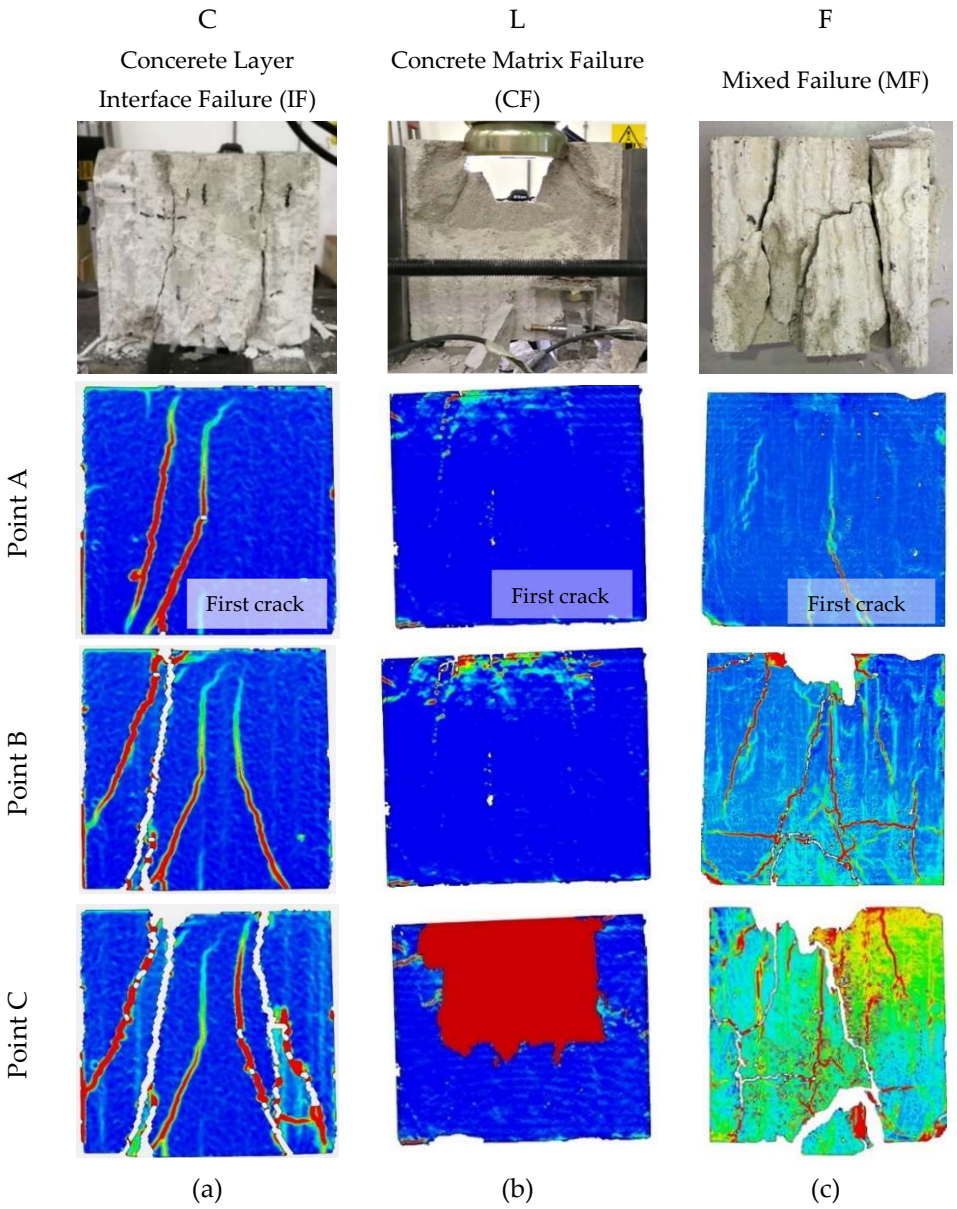

Figure 3-28: Crack pattern of the tested specimen: (a) concrete layer interface failure, (b) concrete matrix failure, and (c) mixed failure.

3.7.3.1.2 Material type 2

The second series of modified push-out test was performed with material type 2. The geometry of the specimen was modified expanding the area under the loading point (red area in Figure 3-29) to promote concrete layer interface failure rather than concrete matrix failure when a high level of precompression is applied. To this aim, preliminary tests with different geometry of the loaded area were performed (see APPENDIX C). In order to have a compressive stress under the load point higher than the shear stress on the vertical surfaces (light blue area in Figure 3-29), the height (h) of the specimen can be calculated as follows:

$$f_{cm} * \frac{l}{2} * t > 2\tau * h * t \qquad 3\text{-}9$$

$$h < l * \frac{f_{cm}}{4\tau} \qquad 3\text{-}10$$

Where f_{cm} is the compressive strength of the material (Table 3-10) and τ is the shear strength. As shown in Figure 3-29, l is the length, h the height and t the thickness of the specimen. The length of the specimen was selected based on the layer thickness w, so that the load applied (F) to the central part is equally distributed between the two external portions ($F/2$). As shown in Figure 3-19b, being the thickness of the layer equal to 1 cm the length of the specimen was chosen equal to 16 cm, so that the central part of the specimen was 8 cm long, while each of the lateral parts were 4 cm long. The height of the specimen was chosen equal to 12 cm according to equation 3-10 (assuming a compressive strength equal to 58 MPa and a maximum shear stress of 12 MPa).

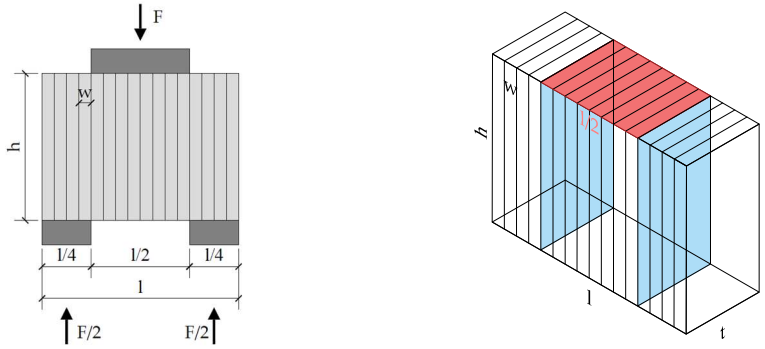

Figure 3-29: Geometry of the specimens for the modified push-out using material type 2.

Table 3-25 and Table 3-26 show the results of the modified push-out test performed on cast and printed specimens with material type 2, respectively. It has to be observed that increasing the level of precompression the shear strength also increases. Considering cast specimens, the average shear strength values are 4.9 MPa, 7.5 MPa, 9.7 MPa, 10.8 MPa and 11.6 MPa for specimens with lateral precompression

of 0 MPa, 1 MPa, 2 MPa, 4 MPa, and 6 MPa, respectively. Considering the printed specimens, the average shear strength values are 6.2 MPa, 7.5 MPa, 9.6 MPa, 11.2 MPa and 13.4 MPa for specimens with lateral precompression of 0 MPa, 1 MPa, 2 MPa, 4 MPa, and 6 MPa, respectively (the shear strength versus lateral precompression graph will be shown in section 3.7.4). Figure 3-30 and Figure 3-31 show the shear stress versus relative vertical displacement for cast and printed specimens with different level of precompression applied.

Material	ID	F_n	F_{cr}	F_{max}	A_{min}	σ_n	τ_{cr}	$\tau_{max,(0°,0°,0°)}$	Failure mode
[-]	[-]	[kN]	[kN]	[kN]	[mm²]	[MPa]	[MPa]	[MPa]	[-]
2	C-S-A	0	77.1	79.7	7170	0	5.2	5.6	IF
2	C-S-B	0	30.4	56.1	7200	0	2.0	3.9	IF
2	C-S-C	0	61.7	73.1	7200	0	4.2	5.1	IF
2	C-S-D	7.2	84.9	112.2	7381	1	5.8	7.6	IF
2	C-S-E	7.2	99.0	105.7	7320	1	6.8	7.2	IF
2	C-S-F	7.2	100.5	113.5	7140	1	7.0	7.9	IF
2	C-S-G	14.4	103.9	154.9	7259	2	7.2	10.7	IF
2	C-S-H	14.4	93.5	144.0	7259	2	6.4	9.9	IF
2	C-S-I	14.4	96.7	127.7	7502	2	6.4	8.5	IF
2	C-S-L	28.8	136.4	166.2	7316	4	9.3	11.4	IF
2	C-S-M	28.8	98.8	137.0	7378	4	6.7	9.4	IF
2	C-S-N	28.8	162.6	174.2	7378	4	11.0	11.8	IF
2	C-S-O	43.2	153.3	164.2	7140	6	10.4	11.5	IF
2	C-S-P	43.2	45.5	171.4	7200	6	3.1	11.9	IF
2	C-S-Q	43.2	143.4	169.1	7140	6	9.95	11.8	IF

Table 3-25: Summary of the results of the modified push-out conducted on cast specimens with material type 2

Material	ID	F_n	F_{cr}	F_{max}	A_{min}	σ_n	τ_{cr}	$\tau_{max,(0°,0°,0°)}$	Failure mode
[-]	[-]	[kN]	[kN]	[kN]	[mm²]	[MPa]	[MPa]	[MPa]	[-]
2	3D-S-A	0	67.4	107.2	7011	0	4.80	7.63	IF
2	3D-S-B	0	32.5	59	6783	0	2.39	4.34	IF
2	3D-S-C	0	68.1	90.7	6710	0	5.07	6.76	IF
2	3D-S-D	7.2	41.0	95.1	6776	1	3.03	7.00	IF
2	3D-S-E	7.2	106.2	137.8	6783	1	7.83	10.15	IF
2	3D-S-F	7.2	68.1	73.5	6960	1	4.89	5.28	IF
2	3D-S-G	14.4	101.9	108.3	6636	2	7.68	8.15	IF
2	3D-S-H	14.4	107.5	138.1	6686	2	8.04	10.32	IF
2	3D-S-I	14.4	91.6	139.8	6698	2	6.84	10.42	IF
2	3D-S-L	28.8	148.4	161.0	6840	4	10.85	11.75	IF
2	3D-S-M	28.8	95.9	142.6	6832	4	7.02	10.43	IF
2	3D-S-N	28.8	50.4	159.0	6897	4	3.65	11.51	IF
2	3D-S-O	31.2	129.0	138.9	4884	6	13.20	14.21	IF
2	3D-S-P	31.2	118.6	126.3	4978	6	11.91	12.66	IF
2	3D-S-Q	31.2	125.6	130.8	4902	6	12.81	13.32	IF

Table 3-26: Summary of the results of the modified push-out conducted on specimens printed with material type 2.

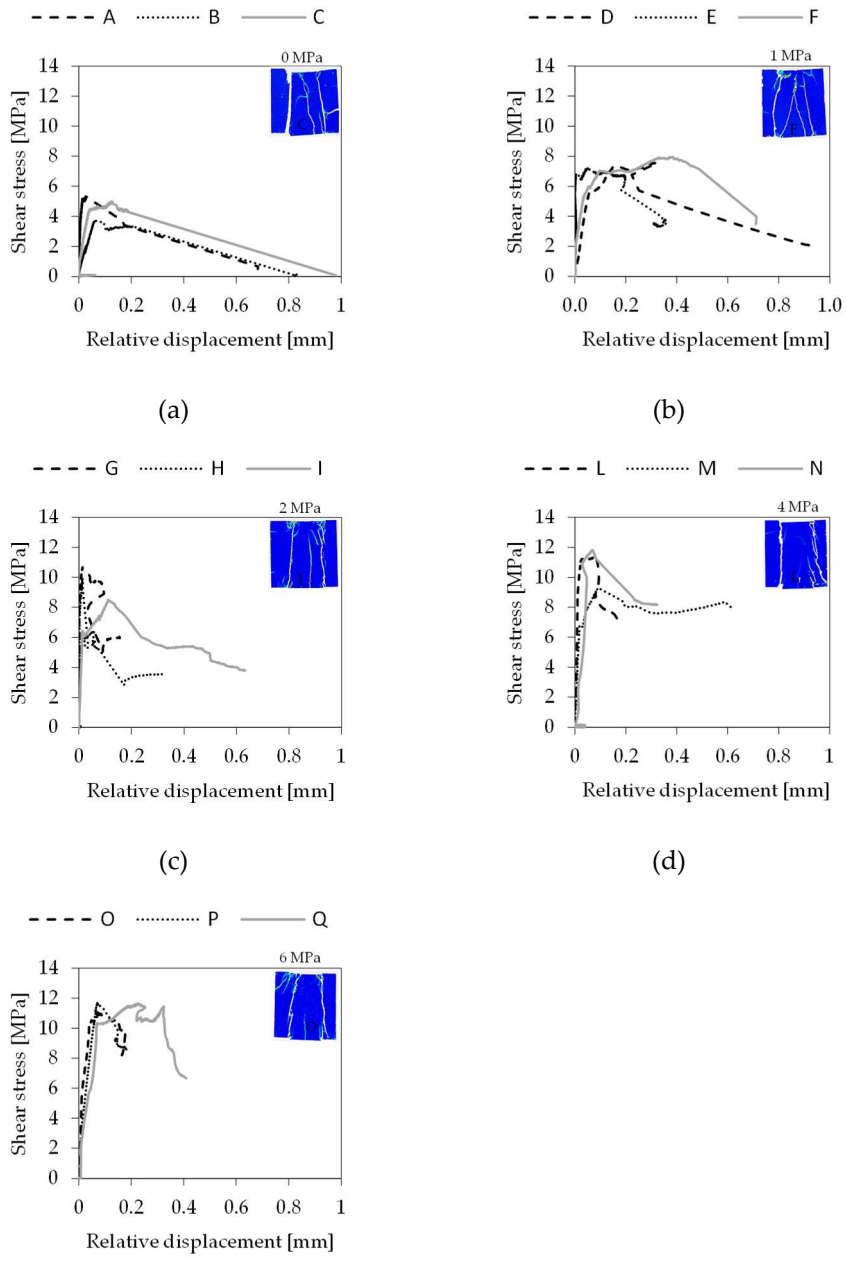

Figure 3-30: Shear stress-relative vertical displacement of cast specimens subjected to modified push-out test (material type 2) for the different level of precompression: (a) 0 MPa, (b) 1 MPa, (c) 2 MPa, (d) 4 MPa, and (e) 6 MPa.

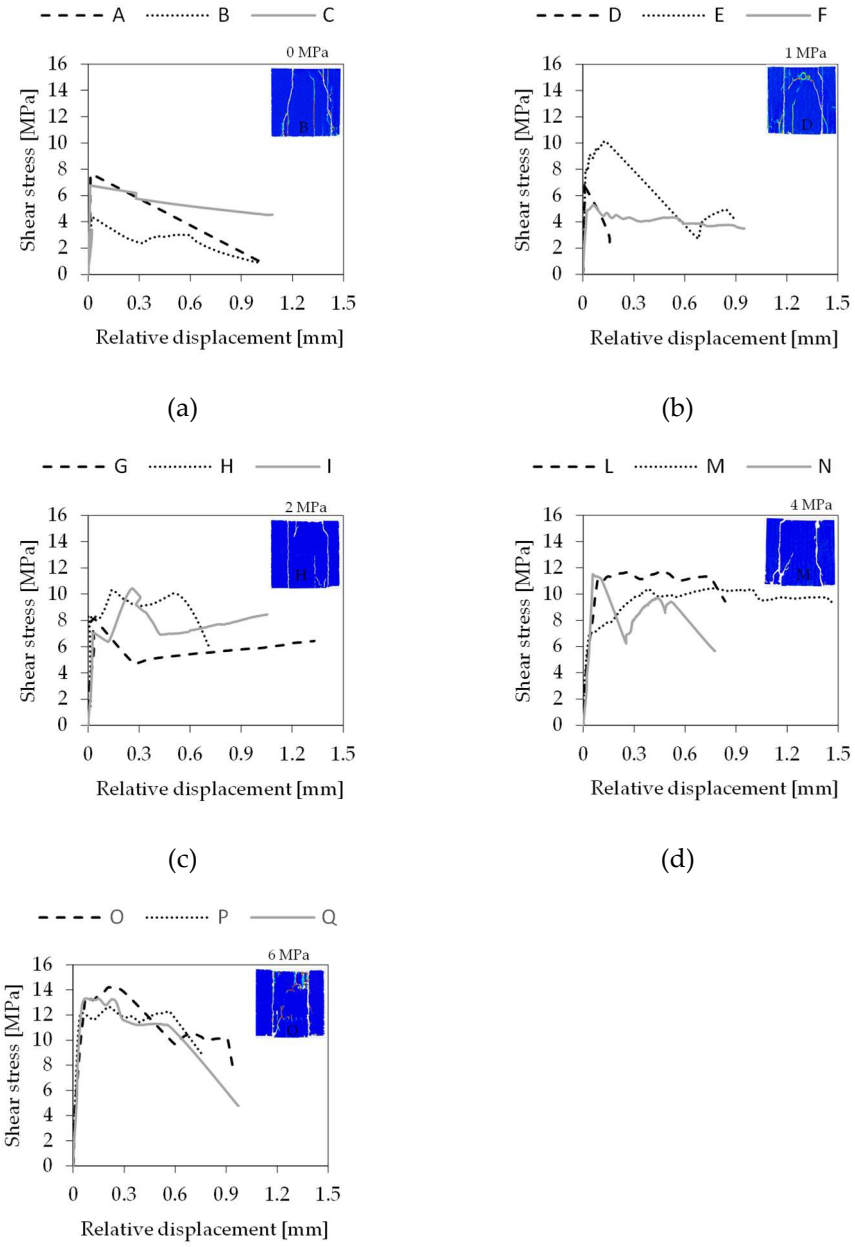

Figure 3-31: Shear stress-relative vertical displacement of the 3DPC concrete specimens subjected to modified push-out test (material type 2) for the different level of precompression: (a) 0 MPa, (b) 1 MPa, (c) 2 MPa, (d) 4 MPa, and (e) 6 MPa.

Figure 3-32 shows the relationship between the shear stress and the relative vertical displacement of a cast (C-S-I) and printed (3D-S-I) specimen, respectively. The general behaviour of all the specimens resulted to be similar since they all exhibited concrete layer interface failure (named as IF in Table 3-26). The behaviour of the specimens under shear action can be summarized in three main phases:

- **Pre-cracking phase**: Up to point A, the specimens exhibit linear behaviour, meaning that an increase in load results in a proportional increase in deformation (Figure 3-33A).
- **Cracking phase:** A non-linear phase developed between point A and point B, indicating the onset of the cracking process. At point B, which corresponds to the maximum load applied during the test, a critical crack appeared (Figure 3-33B).
- **Post-fracture phase:** all the specimen exhibited a concrete layer interface failure mechanism and thus it was possible to record the post-peak phase. At peak load (point B), the specimen failed by shear along one of the two sliding vertical surfaces, and during the post-peak phase, the other critical surface remained undamaged until it failed (point C), (Figure 3-33C).

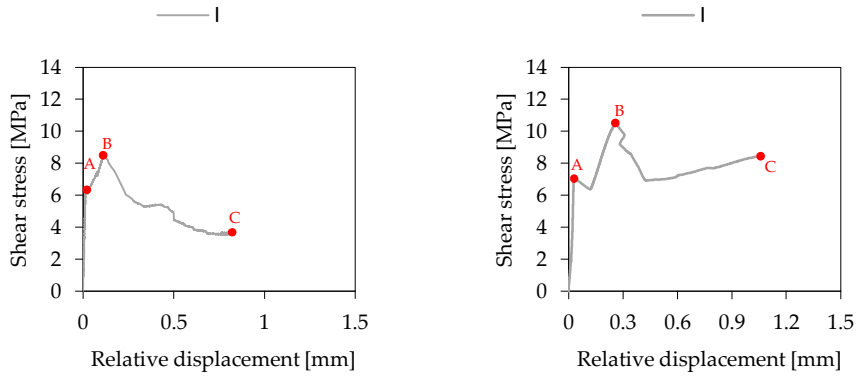

(a) (b)

Figure 3-32: Shear stress versus relative vertical displacement of a representative (a) cast and (b) printed specimen.

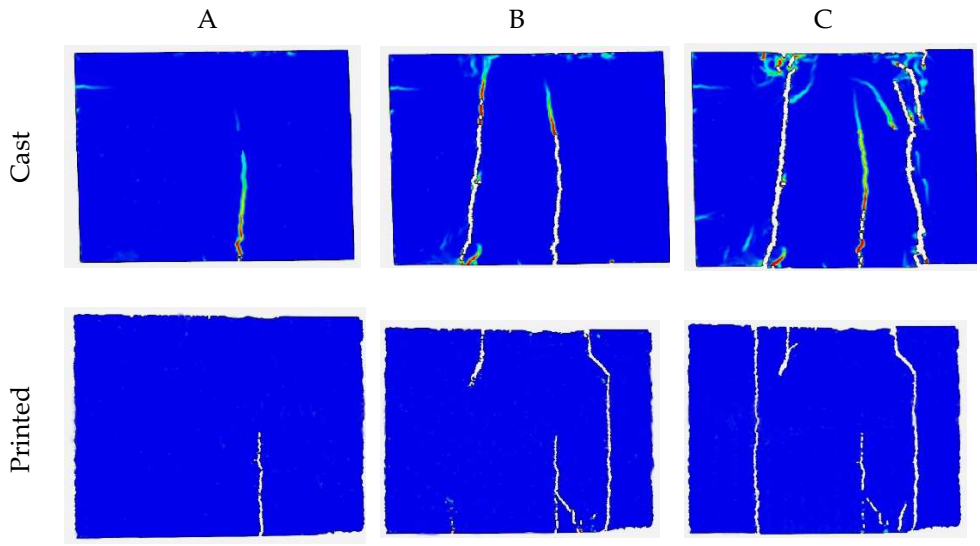

Figure 3-33: Concrete layer interface failure of the tested specimens.

3.7.3.2 Modified slant shear test

The results obtained from the slant shear test are discussed in terms of σ_v that is the vertical stresses on a horizontal plane, σ_n and τ_m that are the normal and shear stresses acting on the inclined interface section between 3D printed concrete layers (inclined planes of angle α to the horizontal plane), see Figure 3-34.

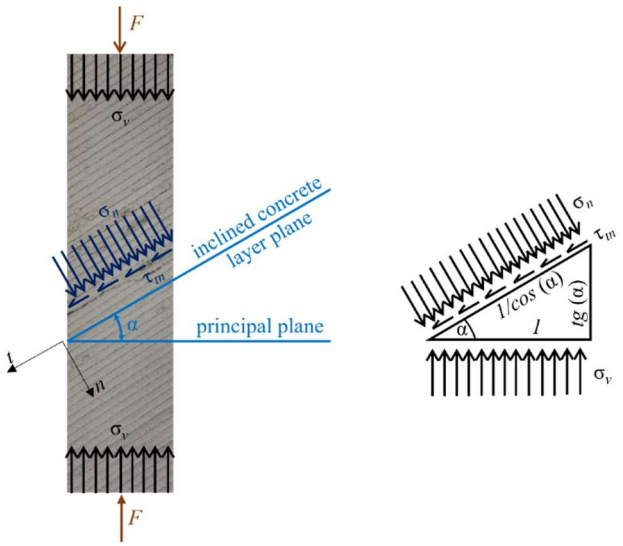

Figure 3-34: Uniaxial stress state.

The stresses were calculated by the following equations:

$$\sigma_v = \frac{F}{A_{H,eff}} \quad \rightarrow \quad for\ \alpha = 0° \ldots 75° \qquad 3\text{-}11$$

$$\sigma_v = \frac{F}{A_{H,90,eff}} \quad \rightarrow \quad for\ \alpha = 90°$$

$$\sigma_n = \sigma_v\, cos^2\alpha \qquad 3\text{-}12$$

$$\tau_n = \sigma_v\, sin\,\alpha\, cos\,\alpha \qquad 3\text{-}13$$

The effective horizontal areas, $A_{H,eff}$ and $A_{H,90,eff,}$ were determined using equations 3-14 or 3-15 based on the inclinations of the concrete layers. Figure 3-35 illustrates the horizontal and inclined cross-sections of the tested specimens, with concrete layer inclinations ranging from 0° to 75° (Figure 3-35a) and vertical concrete layer inclinations with α = 90° (see Figure 3-35b). The 3DPC specimens had wavy surfaces on their two external faces due to the printed concrete layers (Figure 3-35), and internal voids were present between the print-paths, resulting in three vertical wavy interfaces formed by the contact of two wavy surfaces (Figure 3-35a and b).

Therefore, the concrete strength was estimated by considering a reduced or effective cross-sectional area of each specimen (grey shaded area in Figure 3-35), accounting for the fact that the internal voids and all surface waves do not contribute to the strength (white areas in Section 1 and Section 2 of Figure 3-35). The wave radius was variable due to printing imperfection, but an average wave radius of 7 mm, which is equal to the thickness of the printed concrete layers, was used in a simplified approach. Two effective cross-sectional areas were distinguished: (i) the effective horizontal area $A_{H,eff}$, perpendicular to the applied vertical force F (Section 1-1), and (ii) the effective slanting area $A_{n,eff}$, corresponding to the cross-sections contained in the inclined interface planes *n* (Section 2-2), as shown in the Figure 3-35a.

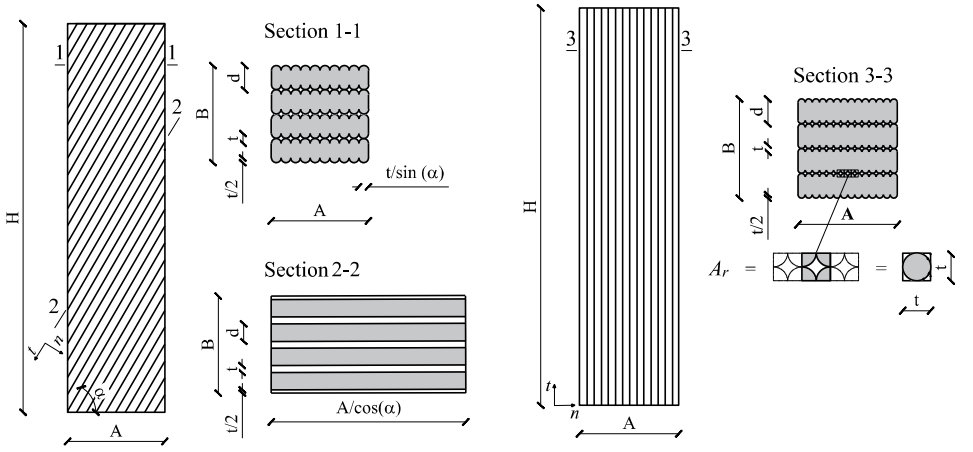

Figure 3-35: Sections in horizontal and inclined planes and geometric parameters to calculate the effective areas ($A_{H,eff}$ and $A_{n,eff}$) of the specimens. (a) α = 0°, 30°, 60° and 75°; (b) α = 90°.

The effective horizontal area $A_{H,eff}$ and the effective slanting area $A_{n,eff}$ for the specimens with concrete layer inclinations α = 0°…75° were calculated by:

$$A_{H,eff} = A \cdot B \cdot \left(1 - \frac{t}{d}\right)$$

$$A_{n,eff} = A \cdot B \cdot \left(\frac{1}{cos\alpha} - \frac{t}{d}\right) \qquad 3\text{-}14$$

Where *A* and *B* are the measured dimensions of the cross-section, *t* is the thickness and d the width of the concrete layer, and α is the concrete layer inclination to the horizontal plane.

The effective horizontal area $A_{H,90,eff}$ (Section 3-3) for the specimens with a vertical concrete layer inclination (α = 90°) is calculated by:

$$A_{r,tot} = \frac{A}{t} \cdot \frac{B}{d} \cdot \left(t^2 - \frac{\pi t^2}{4} \right) = A \cdot B \cdot \frac{(4-\pi)}{4} \frac{t}{d}$$

$$A_{H,90,eff} = A \cdot B - A_{r,tot} = A \cdot B \cdot \left[1 - \frac{(4-\pi)}{4} \frac{t}{d} \right] \quad 3\text{-}15$$

Where $A_{r,tot}$ is the total area of the voids between the four parallel vertical layers created by the print-paths (Figure 3-35b).

The average stresses in the horizontal and inclined planes ($\sigma_{v,m}$, $\sigma_{n,m}$, and $\tau_{tn,m}$) for the maximum compression force (F_{max}) achieved in the Modified Slant Shear Tests are listed in Table 3-27. The average stresses were obtained from the three tested specimens of each series for a given concrete layer inclination and each concrete age, excluding those with no representative results. Two different failure modes were observed depending on the layer inclination of the tested specimen: i) concrete matrix failure for specimens with concrete layer inclinations of 0°, 30° and 90° (Figure 3-36 a, b, and e) and ii) concrete layer interface failure, which occurred in the cold-joint only for the specimens with concrete layer inclinations of 60° (Figure 3-36c) and 75° (Figure 3-36d). The maximum mean normal stress $\sigma_{v,m}$ ranged from 55 MPa to 65 MPa, 60 MPa to 85 MPa, and 53 MPa to 78 MPa at 7, 14, and 28 days after printing, respectively. It was observed that the 3D printed concrete specimens reached their full strength at a concrete age equal to 14 days. At 28 days, the 3D printed concrete strength was slightly lower than that of the specimens tested at 14 days, and about 80% of the maximum strength was already reached at 7 days. The lower strength of the specimens tested at 28 days compared to those tested at 14 days was attributed to imperfections and irregularities in the cuts and printing patterns of the specimens, which were generally greater than those in the specimens tested at other concrete ages. The presence of printing imperfections had a negative impact on the bearing capacity of specimens with horizontal concrete layers (α = 0°). Despite attempts to address the issue by grinding the surfaces of the specimens, stress concentration still occurred in some vertical layers. Consequently, there was a significant reduction in strength (approximately 10%, 20%, and 30% at 7, 14, and 28 days, respectively) when compared to specimens with α = 30°, which failed due to crushing of the concrete matrix without the influence of the concrete layer interfaces. Similarly, specimens with vertical concrete layers (α = 90°) exhibited noticeably lower strength (approximately 15%, 30%, and 25% at 7, 14, and 28 days, respectively) than those with α = 30°. In this case, concrete matrix failure was accompanied by debonding of the printed concrete layers and vertical layers due to specimen dilatation. The maximum stresses σ_n and τ_n are particularly relevant for specimens with α = 60° and 75°, which mostly failed due to the concrete layer interface, as the strength parameters (the friction angle and the cohesion) used to define the Coulomb failure criterion were obtained from those specimens. Figure 3-37 shows the vertical stress σ_v versus the

vertical strain of specimens tested with MSST at 28 days. It should be noted that these curves are only available for specimens tested at 28 days, because the digital image correlation was applied only at this concrete age. The specimens exhibit a linear behaviour until the peak, when a sudden drop of the curve is observed due to the brittle failure.

α [°]	Codification -	Days -	Failure	Fmax [kN]	$\sigma_{v,m,(\alpha,\beta,\gamma)}$ [MPa]	$\sigma_{n,m,(\alpha,\beta,\gamma)}$ [MPa]	$\tau_{n,m,(\alpha,\beta,\gamma)}$ [MPa]
	P-00-0.5-N-07	7 days	Concrete matrix	462.86	-57.66	-57.66	-
0	P-00-0.5-N-14	14 days	Concrete matrix	543.24	-68.49	-68.49	-
	P-00-0.5-N-28	28 days	Concrete matrix	412.64	-53.47	-53.47	-
	P-30-0.5-N-07	7 days	Concrete matrix	528.03	-65.66	-49.24	28.43
30	P-30-0.5-N-14	14 days	Concrete matrix	681.22	-85.78	-64.34	37.14
	P-30-0.5-N-28	28 days	Concrete matrix	621.97	-78.99	-59.24	34.2
	P-60-0.5-N-07	7 days	Concrete layer interface	469.76	-58.52	-14.63	25.34
60	P-60-0.5-N-14	14 days	Concrete layer interface	633.33	-77.86	-19.46	33.7
	P-60-0.5-N-28	28 days	Concrete layer interface	510.15	-64.16	-16.04	27.78
	P-75-0.5-N-07	7 days	Concrete layer interface	443.88	-56.25	-3.77	14.06
75	P-75-0.5-N-14	14 days	Concrete layer interface	584.63	-73.52	-4.92	18.38
	P-75-0.5-N-28	28 days	Concrete layer interface	496.89	-62.27	-4.17	15.57
	P-90-0.5-N-07	7 days	Concrete matrix	640.33	-55	-	-
90	P-90-0.5-N-14	14 days	Concrete matrix	647.12	-59.36	-	-
	P-90-0.5-N-28	28 days	Concrete matrix	665.4	-59.29	-	-

Table 3-27: Modified Slant Shear Test results: F_{max} maximum force, mean normal stresses $\sigma_{v,m}$ in the horizontal plane, mean normal stress $\sigma_{n,m}$ and shear stresses $\tau_{tn,m}$ in the interfaces between the concrete layers.

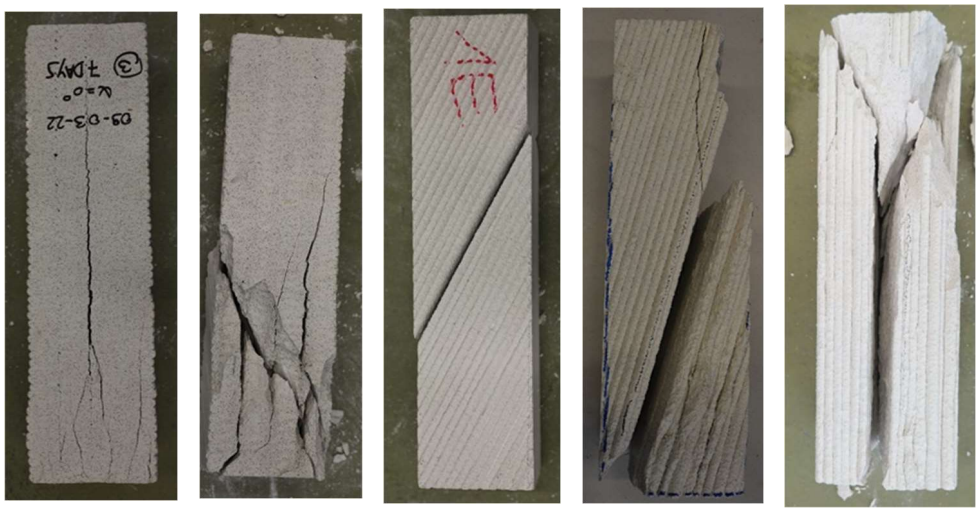

(a) (b) (c) (d) (e)

Figure 3-36: Failure mode: a) 0°, b) 30°, c) 60°, d) 75° and e) 90°.

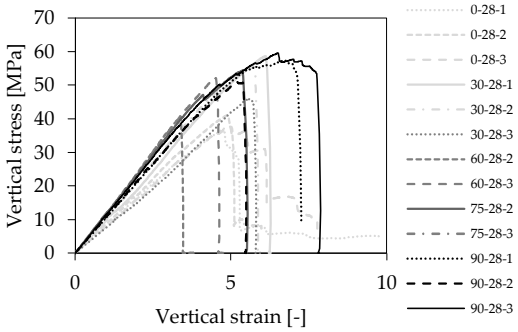

Figure 3-37: Vertical stress σ_v versus vertical strain of the specimens tested with the modified slant shear test at 28 days.

3.7.4 Discussion of the failure criteria

Within this section the different failure criteria obtained from the modified push-out and the modified shear slant test are discussed.
The failure envelope of specimens subjected to the modified push-out test, which exhibited concrete layer interface failure, is represented (or modelled) by the Coulomb failure criterion, which is determined by linear regression of the experimental data (Figure 3-38a). It can be represented as:

$$|\tau| = c - \sigma \cdot \tan(\varphi) \qquad 3\text{-}16$$

Where c is the cohesion and φ is the angle of friction.

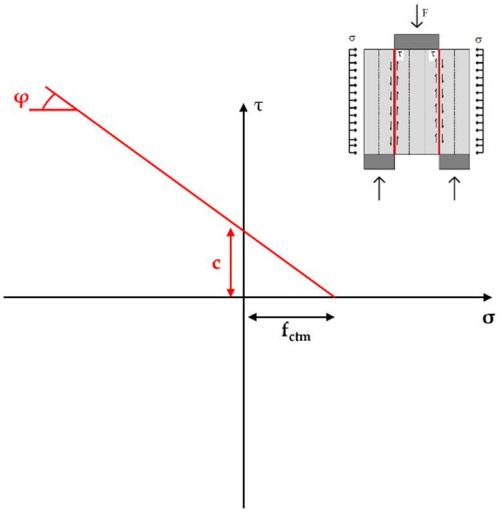

Figure 3-38: Coulomb failure criteria.

The use of the Modified Coulomb yield condition, which is a special case of Mohr's envelope complementing Coulomb's failure criterion by a tension cut-off accounting for the limited tensile strength of concrete ($\sigma<f_{ct}$), is a well-established approach for conducting limit analysis of cast concrete [127], as shown in Figure 3-39a and b. However, when comparing 3D printed concrete with cast concrete, it should be noted that 3DPC exhibits anisotropy due to the layer-by-layer printing process, which can result in interfaces behaving differently than the concrete matrix. Nevertheless, the limit analysis for 3D printed concrete can still be performed using a similar method as that for cast concrete taking into account the presence of layer interface.

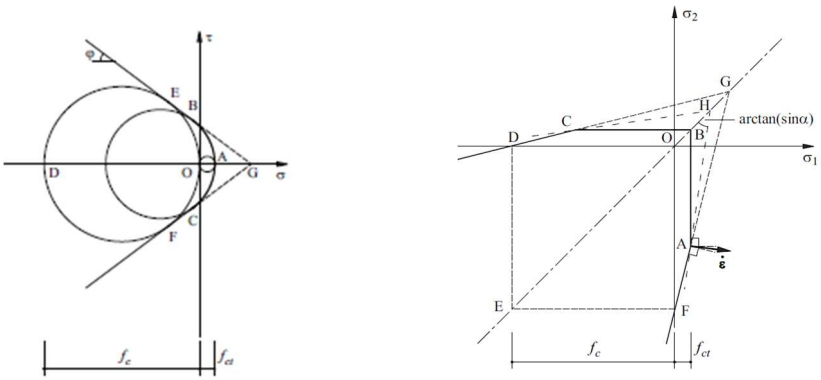

(a) (b)

Figure 3-39: Modified Coulomb yield condition: (a) stress plane and (b) coplanar stress or strain state [127].

Considering the modified slant shear test, the specimens exhibited two different type of failure i) concrete matrix failure and ii) concrete layer interface failure. A failure criterion defined as general Mohr's envelope is employed to represent the failure envelope (Figure 3-40). The general Mohr's envelope for 3DPC is defined in the following by integrating the modified Coulomb yield condition of the concrete matrix with a Coulomb failure criterion of the layer joints, using appropriate values for the angle of friction φ_i and the cohesion c_i depending on the joint type and treatment (φ_c and c_c refer to the angle of friction and cohesion of the concrete matrix). The shaded area represents the resistance domain that is limited by Mohr's envelopes and the Coulomb failure criterion (described by equation 3-16). The Mohr's circles are represented by:

$$\left(\sigma + \frac{f_c}{2}\right)^2 + \tau^2 = \frac{f_c}{4}^2$$

$$\left[\sigma + \left(f_{ct} - \frac{c_c - f_{ct}\tan\varphi_c}{\tan\left(\frac{\pi}{4} - \frac{\varphi_c}{2}\right)}\right)\right]^2 + \tau^2 = \left(\frac{c_c - f_{ct}\tan\varphi_c}{\tan\left(\frac{\pi}{4} - \frac{\varphi_c}{2}\right)}\right)^2 \quad 3\text{-}17$$

The modified Coulomb yield condition of the concrete matrix is cut off by the Coulomb failure criterion of the layer joints. Both curves intersect in Points A and B, which identify the critical angles α_{crA} and α_{crB} defining the limits between the two failure modes, i.e. concrete matrix and concrete layer interface failure. Therefore, concrete layer interface failure will occur in a MSST for layer joint inclinations in the critical range $\alpha_{crA} < \alpha < \alpha_{crB}$, while concrete matrix failures are expected for flatter ($\alpha < \alpha_{crA}$) as well as steeper ($\alpha > \alpha_{crB}$) layer interface inclinations, see Figure 3-40. In the latter cases, the compressive strength f_c of the concrete matrix will be reached in uniaxial compression (such as in the MSST). On the other hand, for layer inclinations in the critical range $\alpha_{crA} < \alpha < \alpha_{crB}$, a reduced peak compressive stress will be attained, as the layer interface fails at a uniaxial compressive stress smaller than f_c.

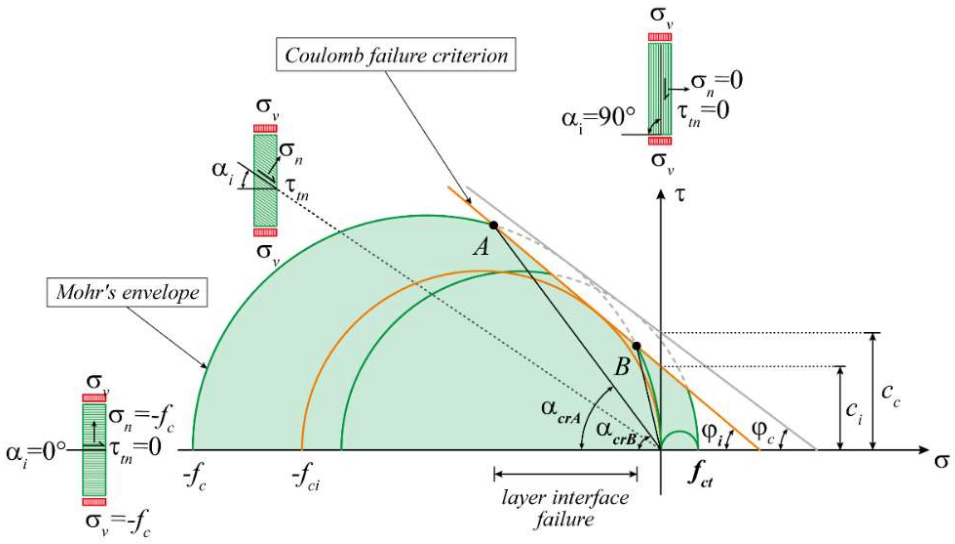

Figure 3-40: General Mohr's envelope for 3D printed concrete.

3.7.4.1 Modified push-out test

Figure 3-41 shows the results of the modified push-out in terms of shear strength versus pre-compression stress for 3D printed concrete specimens. Figure 3-41a refers to material type 1; from the linear regression of the data an angle of friction φ of 60° and a cohesion *c* of 6.02 MPa were obtained. It has to be observed that the specimens that exhibited concrete matrix failure were excluded from the linear regression of the data. Figure 3-41b concerns to material type 2 and an angle of friction φ equal to 54° and a *c* cohesion of 5.95 MPa were obtained. The angle of friction and the cohesion of cast specimens with material type 2 are similar to the value obtained from printed specimens, which resulted equal to 51° and 5.60 MPa, respectively. All the specimens showed concrete layer interface failure and were included in the linear regression analysis.

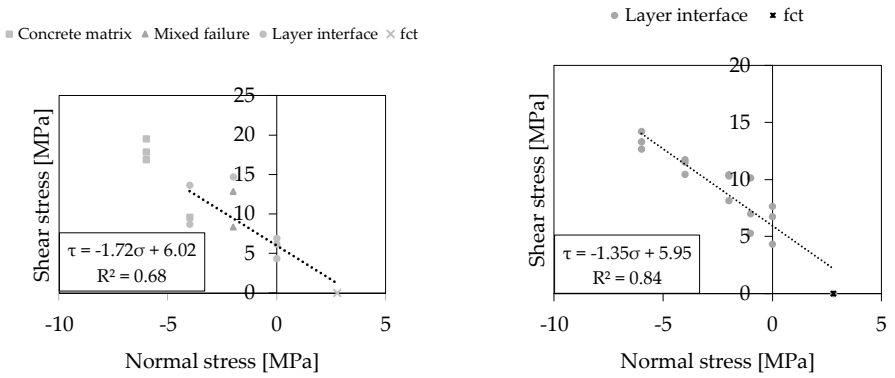

(a) (b)

Figure 3-41: Shear stress versus precompression stress for 3D printed concrete specimen: (a) material type 1 and (b) material type 2.

3.7.4.2 Modified slant shear test

Figure 3-42 shows the general Mohr's envelope of 3D printed concrete obtained from the Modified Slant Shear Test. The resistance domain is defined by the modified Coulomb yield condition and the Coulomb failure criterion from the averages of all the experimental results, on the basis that two failure modes may occur depending on the concrete layer inclination α (concrete matrix failure and concrete layer interface failure). The modified Coulomb yield condition is obtained from i) the average of the peak compressive stresses ($\sigma_v = f_c$) in the specimens that have failed by the concrete matrix (α = 0°, 30° and 90°), ii) the angle of friction and iii) the tensile strength of the concrete matrix f_{ct}, which is estimated as $f_{ct} = f_{cm}/10$ based on the results from the three-point bending tests (see Table 3-22).

The Coulomb failure criterion (see Figure 3-42) is experimentally derived from the limit stress state (σ_n and τ_{tn}) in the layer interface of the specimens failed by the concrete layer interface (α = 60° and 75°). The cohesion of the concrete matrix c_c is calculated from the experimental results by assuming that the angle of friction of the matrix correspond to that of the layer interfaces $\varphi_c = \varphi_i$.

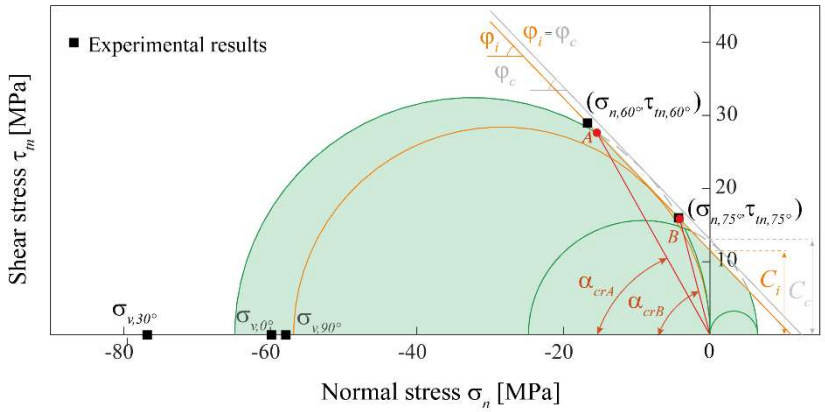

Figure 3-42: 3D printed concrete resistance domain (specimens printed with material type 3).

Table 3-28 summaries the resulting parameters that define the general Mohr's envelopes of the 3DPC plotted in Figure 3-42; note that f_{ci} is the (fictitious) uniaxial compressive strength for cohesive layer joints ($c_i > 0$) in arbitrary directions (if the layer joint orientation has not been defined yet, the 3DPC can be modelled conservatively as an isotropic material with a reduced compressive strength f_{ci}), obtained from the Mohr's circle which is tangent to the Coulomb failure criterion of the layer joints (see Figure 3-40) and is calculated as:

$$f_{ci} = \frac{2\, c_i\, cos\, \varphi_i}{1 - sin\, \varphi_i} \qquad 3\text{-}18$$

The critical angles α_{crA} and α_{crB}, identified by Point A and Pont B (Figure 3-42), are approximately 60° and 75°. The angle of friction φ_i of the concrete layer interface is relatively high, approximately 46°, similar to the value obtained by other researchers for the concrete matrix of 3DPC [128,129]. On the other hand, while the cohesion c_i of the concrete layer interfaces was about 10% smaller than the cohesion of the concrete matrix c_c at the same age (obtained with $\varphi_c = \varphi_i$). Due to this lower cohesion, the layer interfaces cause a slight anisotropy in the strength of 3DPC.

f_c	f_{ci}	$f_{ct} = f_c/10$	c_i	c_c	$\varphi_c = \varphi_i$	α_{crA}	α_{crB}
[MPa]	[MPa]	[MPa]	[MPa]	[MPa]	[°]	[°]	[°]
63.9	55.5	6.49	11.54	13.0	46.1	60.8	75.4

Table 3-28: Experimental parameters of the 3DPC resistance domain shown in Figure 3-42. Parameters are obtained from the average values of the results.

As all layer interface failures occurred along the Cold joint-30 (30 min time gap), it can be concluded that the regular layer joints had a higher strength than the cold joints; the latter caused the layer interface failures in the specimens with $\alpha = 60°$ and 75° (*Figure 3-36* c and d), hence the corresponding reduction of the peak compressive stress by about 10% to 20% compared to the specimens with $\alpha = 30°$ (matrix failure).

3.7.5 Discussion

Within this section the investigation of the interface strength subjected to shear action was carried out by conducting modified push-out and modified slant shear test. The modified slant shear test is easier to conduct and allows the estimation of shear properties at various concrete layer inclinations, but it is not possible to measure the relative displacement between two printed layers, since it cannot be establish where the failure will occur. The modified push-out test provided more accurate results than the modified slant shear test, which provided considerable scatter in the results. While the modified slant shear test showed some specimens with concrete matrix failure, the modified push-out test specimens exhibited only concrete layer interface failure. The angle of friction was found to be 60° 54° and 46° and the cohesion was 6.02 MPa, 5.95 MPa and 11.5 MPa for material type 1 (modified push-out test), material type 2 (modified push-out test) and material type 3 (modified slant shear test), respectively. Modified push-out test were also conducted on cast specimens with material type 2; an angle of friction of 51° and a cohesion of 5.60 MPa were obtained. These values are similar to those obtained by other researchers [8,73]; in fact, values of the angle of friction ranging between 45°and 55° were found for both cast and layered concrete. Based on the test results, it can be concluded that the cohesion and the angle of friction were not influenced by the test typology and the presence of a cold joint, which is a reasonable assumption for a short time gap of approximately 30 minutes. A relationship between the two type of tests could not be derived since the specimens subjected to modified push-out and modified slant shear test were printed using different materials.

3.8 Elastic modulus

3.8.1 Specimen geometry and test set-up

The elastic modulus in compression was calculated with specimens with dimensions of 120x60x60 mm. The tests were performed considering orientation III, with the stresses direction perpendicular to the layers of the printed concrete (see Figure 3-43a). The vertical load was applied on the top part of the specimen by a servo-controlled hydraulic jack with a maximum capacity of 500 kN. The test was conducted in displacement control with a velocity of 0.001 mm/min. The specimen was positioned between two steel plates (as shown in Figure 3-43b), and the longitudinal deformation was measured using linear voltage displacement transducers (LVDTs) with a stroke of 2 mm placed on two opposite sides of the specimen. The elastic modulus in tension was calculated using the same specimens and set-up used for the estimation of the tensile strength (see Figure 3-13).
The elastic modulus was calculated by performing a cyclic test composed by two cycles, each cycle made by three repetitions, according to UNI EN 12390-13:2013 [130] (see Figure 3-44). The standard refers to the elastic modulus in compression, but it was adapted to elastic modulus in tension.
The elastic modulus, both in tension and compression, was calculated as:

$$E_{cm} = \frac{\sigma}{\varepsilon} \qquad 3\text{-}19$$

where:

σ is the stress given by the force divided by the area; and
ε is the strain given by the average of all the LVDTs.

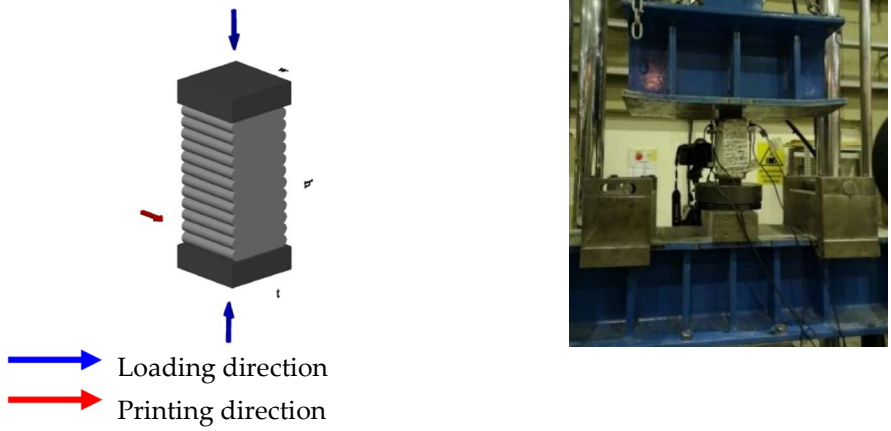

Figure 3-43: Elastic modulus in compression: (a) specimens geometry, (b) test set-up.

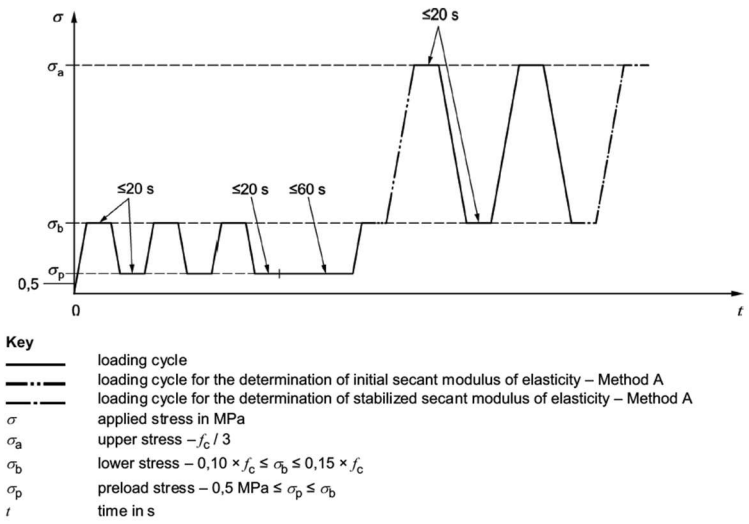

Figure 3-44: Elastic modulus test. Loading protocol [130].

3.8.2 Results

Table 3-29, Table 3-30 and Table 3-31 show the results of the elastic modulus for material type 1, material type 2 and material type 3, respectively. The elastic modulus resulted around 31 GPa for material type 1, 37 GPa for material type 2 and 27 GPa for material type 3.

	Compression		Tension	
Material	**ID**	**E**	**ID**	**E**
		MPa		**MPa**
1	3D-C-A	33534	3D-T-A	-
1	3D-C-B	41265	3D-T-B	42413
1	3D-C-C	36341	3D-T-C	34480
1	3D-C-D	32832	3D-T-D	32832
1	3D-C-E	19936	3D-T-E	23458
1	3D-C-F	20692	3D-T-F	23009
1	3D-C-G	30213	3D-T-G	33084
1	3D-C-H	37313	3D-T-H	-
1	3D-C-I	29592	3D-T-I	-
1	3D-C-L	37923	3D-T-L	-
Average		**31964**		**31546**
St.dev.		**7098**		**7335**
C.o.V		**22%**		**23%**

Table 3-29: Material type 1 – Elastic modulus of 3D printed concrete specimens.

	Compression		Tension	
Material	**ID**	**E**	**ID**	**E**
		MPa		**MPa**
2	3D-C-A	26662	3D-T-A	-
2	3D-C-B	34465	3D-T-B	37689
2	3D-C-C	32683	3D-T-C	-
2	3D-C-D	34989	3D-T-D	40987
2	3D-C-E	39465	3D-T-E	34785
2	3D-C-F	41250	3D-T-F	30825
2	3D-C-G	38924	3D-T-G	34687
Average		**35491**		**34966**
St.dev.		**5532**		**3791**
C.o.V		**16%**		**11%**

Table 3-30: Material type 2 – Elastic modulus of 3D printed concrete specimens.

		Compression
Material	**ID**	**E**
		MPa
3	0-28-1	24654
3	0-28-2	26126
3	0-28-3	23819
3	30-28-1	25291
3	30-28-2	23000
3	30-28-3	19379
3	60-28-3	32721
3	75-28-2	28912
3	90-28-1	35823
3	90-28-2	27128
3	90-28-3	27889
Average		**26795**
St.dev.		**4560**
C.o.V		**17%**

Table 3-31: Material type 3 – Elastic modulus of 3D printed concrete specimens.

3.9 Main outcomes

This chapter presents various test methods for evaluating the hardened properties of the 3D printed materials. These tests, commonly used to determine the mechanical properties of concrete or masonry structures, are customized for the specific case study. The evaluation of compressive strength and flexural tensile strength involves the use of tests typically used to evaluate the mortar properties. The focus was then on the effect of the interface between layers. Initially, the case of the interface subjected to tensile forces was examined and a setup was introduced to evaluate the tensile strength of the material. Subsequently, the attention was on to the interface subjected to shear, and two test setups were proposed: the modified push-out test and the modified slant shear test. The modified push-out test reproduces the constant vertical load and the horizontal force applied to a wall and it is commonly used to evaluate the shear properties of masonry structures. On the other hand, the modified slant shear test allows the shear properties at the interface to be determined by changing the inclinations of the layers with respect to the horizontal reference. This test is widely used to evaluate shear properties between concrete and a repair material. The 3D printed material generally exhibits high compressive strength and the influence of the loading direction is minimal. Moreover, the 3D printed material exhibits high flexural tensile and tensile strength, which are instead affected a lot by the loading direction. The interfaces could potentially be a weak point in presence of cold joints; otherwise they show significant strength. In fact, the shear properties of the printed material resulted similar to the ones obtained from cast specimens, meaning that the presence of interfaces (in absence of cold joints) does not affect the shear properties. Finally, the inclination of the layer affect the failure mode, which could either occur at the interface or in the concrete matrix. Table 3-32 reports a summary of the material properties measured.

Property	Manufacturer	f_{cm}				$f_{ctm,fl}$				f_{ctm}	E		τ_o		c	
Direction		cast	I	II	III	Cast	I	II	III	III	III		cast	III	cast	III
											Comp.	Tens				
		[MPa]	[MPa]	[MPa]	[MPa]	[MPa]	[MPa]	[MPa]	[MPa]	[MPa]	[MPa]	[MPa]	[MPa]	[MPa]	[°]	[°]
Material 1	Cybe	-	74.03	50.10	74.85	-	5.00	6.58	7.19	3.43	31964	31546	-	6.02	-	60
Material 2	Italcementi	38.13	57.05	-	57.67	6.27	6.85	-	5.58	2.88	35491	34966	5.60	5.95	51	54
Material 3	ETH	66.2	-	-	-	12.7		-	-	-	26795	-	-	11.53	-	46

Table 3-32: Summary of the mechanical properties of the 3D printed material.

4 STRUCTURAL PERFORMANCE OF 3D PRINTED CONCRETE WALLS

4.1 Introduction

With the continuous improvement of the concrete characteristics and printing technologies, many construction companies have started to print prototype buildings. Two options for 3DPC buildings have emerged: on-site or off-site construction. On-site printing involves the creation of structures in an open environment, while off-site printing involves the production of prefabricated elements in a controlled environment that can then be later assembled on-site. Projects that have used concrete extrusion for on-site printing include the prototype house in Milan (2018) [131] and the two-storey residential building in Beckum (2021) [19,132].

Those examples demonstrate the considerable potential of concrete extrusion; however, the structural performance of 3DPC concrete elements has not been widely discussed. A limited number of experimental tests have been conducted to evaluate the structural behaviour of beams, walls or other elements made with concrete extrusion (see Chapter 2). For example, the bicycle bridge in Gemert, the Netherlands, with a span of 6.5 m and a width of 3.5 m, underwent bending tests (destructive) in the TU Eindhoven laboratory and in-situ tests (non-destructive) after completion [101]. Moreover, the pedestrian bridge designed by Kinomura et al. [98], which was conceived by means of topological optimisation was verified by FEM analysis and an in-situ load test. In addition, a 3D printed concrete beam was subjected to a three-point bending test at the University of Naples [77]. Van Der Putten et al. also conducted bending tests on lintels made with concrete extrusion to evaluate the structural performance using two different types of reinforcement: bars and fibres [100]. Bos et al. conducted large-scale testing on 3D printed concrete walls for the Nyborg Pavilion [101], including compression and vertical flexure tests.

In order to provide additional insight in the study of the structural behaviour of 3D printed concrete elements made by extrusion process, this chapter focuses on the study of the structural behaviour of five full-scale 3D printed concrete walls subjected to in-plane quasi-static horizontal cyclic load and constant vertical load. The experimental results are evaluated in terms of capacity and damage pattern, with a focus on lateral load-drift response, the crack pattern development, the lateral stiffness variation and energy dissipation during the cycles.

4.2 Experimental programme on 3DPC walls

Thanks to a joint research project between the University of Brescia, Italcementi and Heidelberg Cement, five full-scale 3D printed concrete walls were tested. The walls were subjected to an in-plane quasi-static horizontal cyclic load and constant vertical load in order to study the behaviour of a wall under lateral loading (such as wind or seismic action) [133–139]. In this section the design process and the geometry of the specimens will be described. Three out of five walls belonged to the 3D printed house in Milan and thus printed using material type 1. The other two walls were printed with material type 2, which is the same concrete material used for the house printed in Beckum (Germany) [19,132].

4.2.1 3DPC walls printed with material type 1

The 3DPC house in Milan (2018) was printed using material type 1 [131]. *Figure 4-1* shows the front and the plan view of the house. The three 3D printed walls tested at the University of Brescia were taken from the outer portion of the building. They are red-coloured in *Figure 4-1*, and they are labeled by 21, 22 and 23A, respectively.

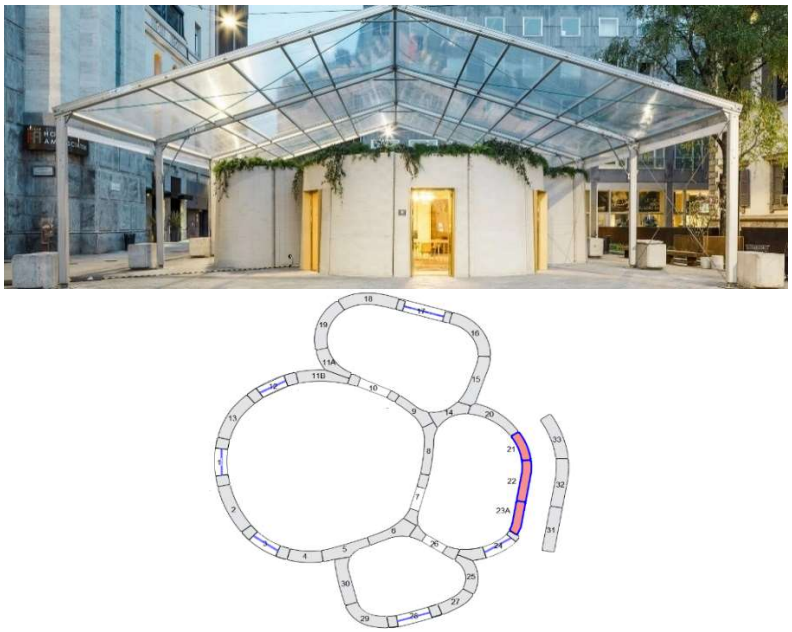

Figure 4-1: 3D printed house in Milan (2018): a) front view and b) plan view with the indication of the three 3D printed walls tested at the University of Brescia.

The tested 3D printed concrete walls had dimensions of 1.17x1.65x0.33 m, 1.27x1.65x0.33 m and 1.66x2.25x0.33 m, as shown in Figure 4-2a. Figure 4-2b shows a simplified cross-section of the walls. The walls were made of 3D printed extruded concrete (material type 1) and did not contain any reinforcement. The width of the extruded filament was 40 mm and the height was 20 mm.

The walls had a rectangular cross-section with cavities. The external layers of 3D printed concrete were connected by inner perpendicular diaphragms which serves to avoid elastic instability of the outer layers during the printing phase. The cross-section was constant throughout the height of the wall. The main geometrical properties of the wall are listed in Table 4-1.

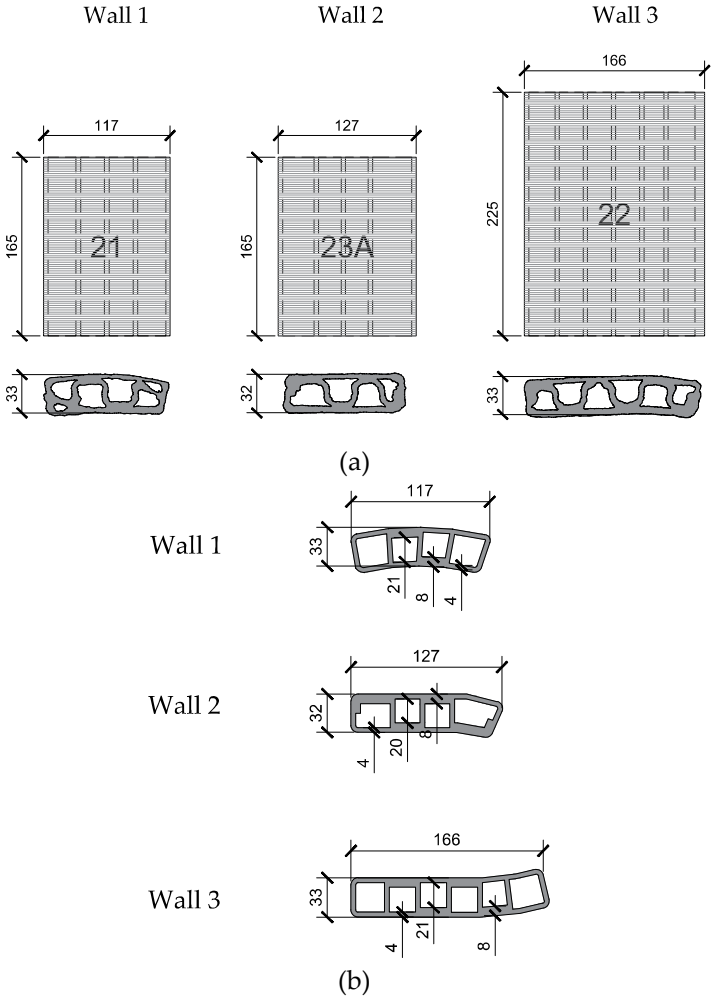

Figure 4-2: (a) Size and shape of the 3D printed concrete walls, (b) cross-sections with dimensions.

ID	l_x	l_y	l_z	A	J_{yy}	J_{xx}	n	w	t	Test
[-]	[cm]	[cm]	[cm]	[cm^2]	[cm^4]	[cm^4]	[-]	[cm]	[cm]	[-]
Wall 1	117	33	165	2186	2467026	295532	4	4	2	Test 1
Wall 2	127	32	165	2220	2661562	321561	4	4	2	Test 2
Wall 3	166	33	225	3256	7857173	459880	6	4	2	Test 3

Table 4-1: Geometrical properties: Geometrical properties: dimension of the specimen (l_x, l_y, l_z), area of the cross-section (A), moments of inertia of the cross section (J_{yy}, J_{xx}), number of cavities (n), width (w), and thickness (t) of the filament.

The walls were connected to a reinforced concrete foundation with stirrups having a diameter of 10 mm, which link the foundation to a 20 cm depth normal strength concrete corbel poured within the cavities. Figure 4-3 and Figure 4-4 show the connection of the three 3D printed concrete walls with the reinforced concrete foundation.

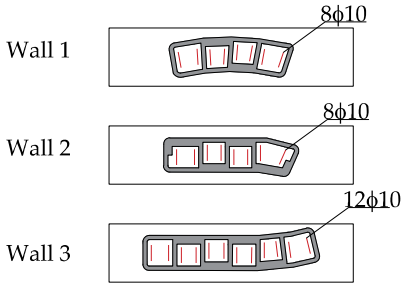

Figure 4-3: Section at the base of the 3D printed walls.

In addition three main cross-section can be identified in the wall, as shown in Figure 4-4 (wall 3 is taken as an example, but for the others wall the cross-sections are similar): cross section 1-1 shows the connection of the wall to the foundation; section 2-2 represent the typical cross-section of the wall; cross section 3-3 represents the upper 20 cm portion of the wall, that was filled with normal strength concrete to create a RC corbel to apply the horizontal and the vertical load during the test. Figure 4-5 shows a detail of a 3DPC wall and of the connection between the wall and the foundation.

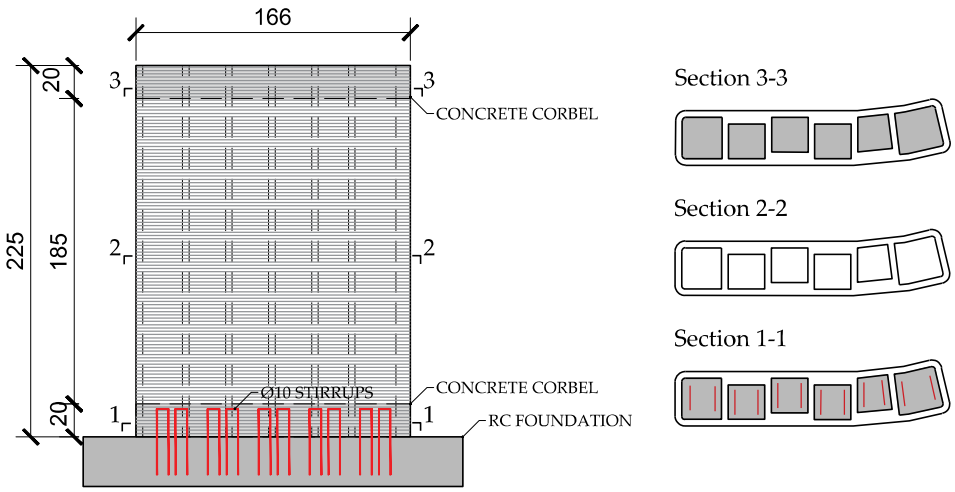

Figure 4-4: Side view and cross-section view of the 3D printed concrete walls (wall 3).

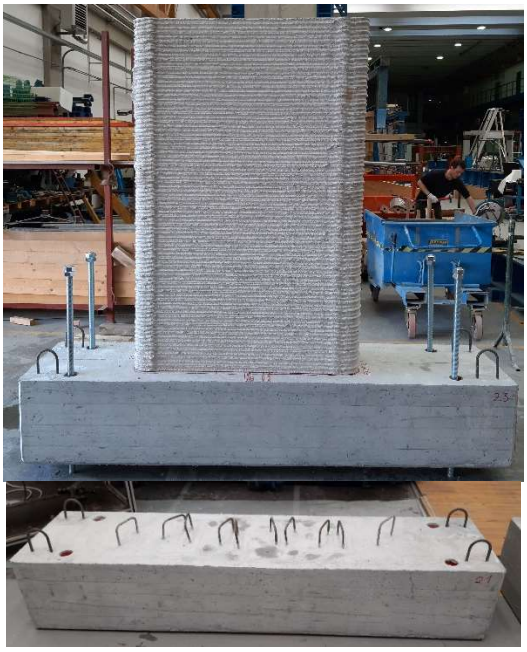

Figure 4-5: Detail of the foundation of the wall and of the connection between the wall and the foundation.

4.2.2 3DPC walls printed with material type 2

This section outlines the design process and the identification of thermal, geometrical, and mechanical parameters of the two walls printed with material type 2. The walls had a height of 3 m, a length of 3 m and a thickness of 55 cm and could be employed for the construction of low-rise building up to three stories. Figure 4-6 shows a reference building that could be taken as an example.

Figure 4-6: Reference building.

4.2.2.1 Thermal performance

The design of the 3DPC walls includes the thermal efficiency of the wall, as the goal was to create 3DPC walls with good structural and thermal performances. The climatic conditions were fixed, as the reference building was located in Milan, Northern Italy.

The design of the walls complied with the current regulation [140], which set a maximum value of the thermal transmittance for vertical walls equal to 0.26 W/m^{2}K. The following climate conditions were supposed: temperature of the external environment of 0°C; temperature of the internal environment of 20°C. The materials used for the calculation were 3D printable concrete and cellulose fibre flakes as insulating material which was derived from newspaper. The insulating material was inserted in the cavities of the 3DPC walls. Details on the properties are given in *Table 4-2*.

Property	Symbol	Unit	Values
Convective air resistance of the internal environment [141]	$R_{cv,i}$	[m^{2}k/W]	0.13
Convective air resistance of the external environment [141]	$R_{cv,e}$	[m^{2}k/W]	0.04
Thermal conductivity of the concrete	k_e	[W/mK]	0.963
Thermal conductivity of the cellulose fibre	k_i	[W/mK]	0.038

Table 4-2: Thermal properties of the materials considered in the analytical and in the finite element calculations.

An analytical model was developed using the method of equivalent resistances to the heat fluxes, the thickness of the cavity and the inclination of the internal diaphragms were varied as they were identified as the most influential parameters on thermal efficiency [142]. A finite element analysis was also performed to verify the results obtained from the analytical model.

The starting point was the investigation of the thermal performance of the walls belonging to the 3DPC house in Milan [131] (section 4.2.1), which had rectangular cross section and were composed by two external layers and perpendicular internal diaphragms (Figure 4-2). Figure 4-7 shows the heat fluxes configuration and the equivalent resistances scheme which were used for the analytical model.

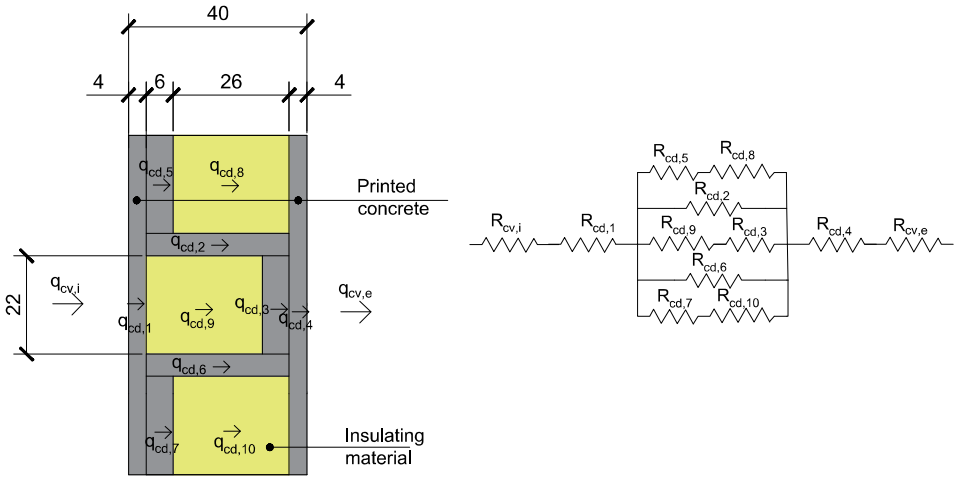

(a) (b)

Figure 4-7: Analytical model for the estimation of the thermal transmittance of 3D printed concrete walls: (a) heat fluxes configuration; (b) equivalent resistance scheme.

The thermal transmittance U is calculated as $U = 1/R_{tot}$, where R_{tot} is the total equivalent resistance which can be calculated analytically as:

$$R_{tot} = R_{cv,i} + R_{cd,1} + R_{mid} + R_{cd,4} + R_{cv,e} \quad 4\text{-}1$$

$$R_{mid} = \frac{1}{\frac{1}{R_{cd,5} + R_{cd,8}} + \frac{1}{R_{cd,2}} + \frac{1}{R_{cd,9} + R_{cd,3}} + \frac{1}{R_{cd,6}} + \frac{1}{R_{cd,7} + R_{cd,10}}} \quad 4\text{-}2$$

where $R_{cd,i}$ is the conductive resistance calculated as $R_i = l_i/(k_i \cdot A_i)$, where l_i is the length crossed by the heat flux, k_i is the thermal conductivity of the considered material and A_i is the area perpendicular to the heat flux. A detailed description of the analytical

method can be found in APPENDIX D. The analytical calculation provides a thermal transmittance value of 0.52 W/m²K.
Applying the same boundary conditions, a finite element analysis was conducted with the software THERM [143], which is able to model two-dimensional heat transfer. The calculated thermal transmittance was 0.56 W/m²K. Figure 4-8a shows the temperature variation and Figure 4-8b the heat flow. It can be observed that the diaphragms perpendicular to the external concrete layers are the elements responsible of the major heat loss of the wall section (Figure 4-8b). However, the diaphragms are necessary to avoid instability and control the buildability during the printing process (see Section 4.2.2.2).

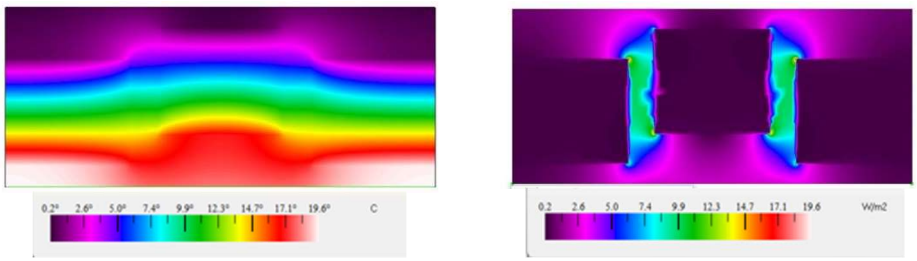

(a) (b)

Figure 4-8: Finite element model for the estimation of the thermal transmittance of 3D printed concrete walls: (a) temperature gradient and (b) heat flow.

To reduce the heat loss caused by the perpendicular diaphragms, it was decided to use inclined diaphragms, which is also a common geometry [144–147]. The examined cross-section consisted of two 3D printed concrete outer layers and inclined inner diaphragms (Figure 4-9a). A parametric study using the analytical method (Figure 4-9b) was conducted by varying the inner diaphragm inclination, the cavity thickness and the thermal transmittance. The study reveals a decrease in thermal transmittance *U* with the inclination of the diaphragms. The domain shown in Figure 4-9c was obtained by setting the thermal transmittance values between 0.15 W/m²K and 0.30 W/m²K. The designer can select the thickness of the cavity for a given inclination of the inner diaphragms and a given thermal transmittance. In this study, the chosen configuration, which corresponds to the red point in Figure 4-9c, has a thermal transmittance of 0.15 W/m²K, an internal diaphragm inclination of 37° and a cavity thickness of 55 cm. This choice was taken in order to guarantee an integer number of internal diaphragms if a 3 m long wall is considered.
Therefore, the analytical calculation gave a thermal transmittance value of 0.15 W/m²K for a cavity thickness of 55 cm. To confirm the results, a finite element analysis was conducted with the software THERM, which gave a thermal transmittance of 0.18 W/m²K, thus confirming the analytical results. Figure 4-10a shows the temperature variation and Figure 4-10b the heat flow. Although this

configuration exhibited a satisfactory thermal performance, below the limit prescribed by the standard [140], thermal bridges persisted at the intersection point of the diaphragms (Figure 4-10b). Moreover, with this configuration the problem of thermal bridges in a real building could arise at the intersection between walls, floors and foundations. To avoid this problem, the configuration was modified adding an external insulation layer, as shown in Figure 4-11a.

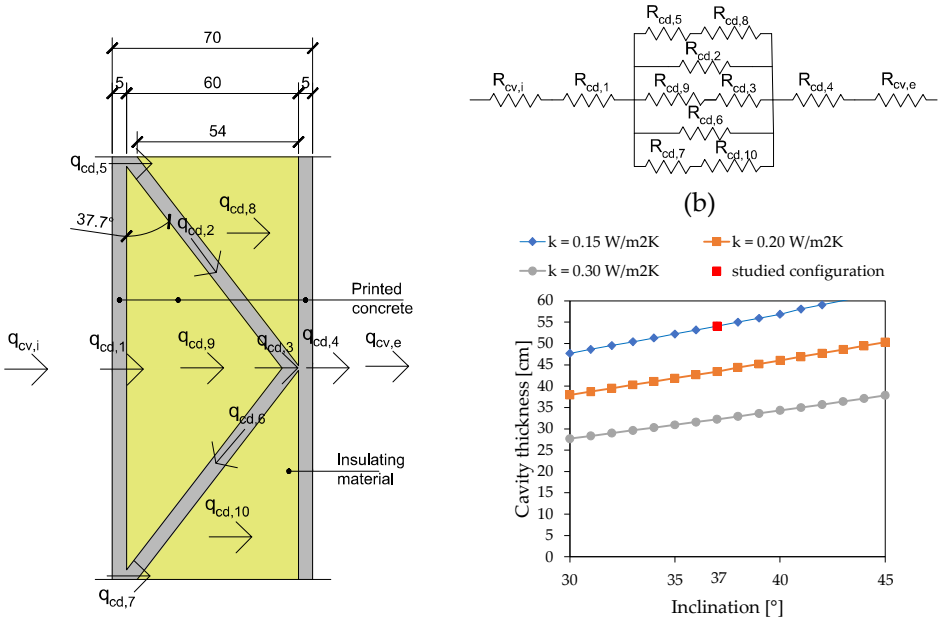

Figure 4-9: Analytical model for the estimation of the thermal transmittance of 3D printed concrete walls: (a) heat fluxes configuration; (b) equivalent resistance scheme; (c) thermal transmittance as a function of cavity thickness and diaphragm inclination.

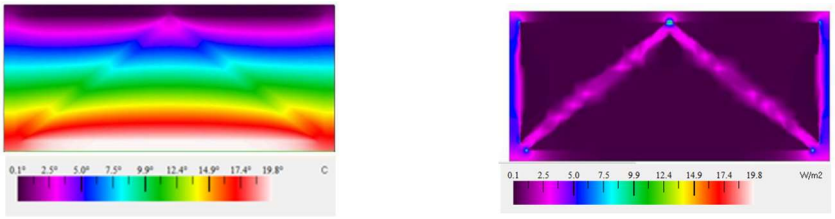

Figure 4-10: Finite element model for the estimation of the thermal transmittance of 3D printed concrete walls: (a) temperature gradient and (b) heat flow.

By means of the same analytical calculation (Figure 4-11b,c), thermal transmittance resulted equal to 0.18 W/m²K. The value obtained from the finite element analysis was equal to 0.17 W/m²K (Figure 4-12a and b).

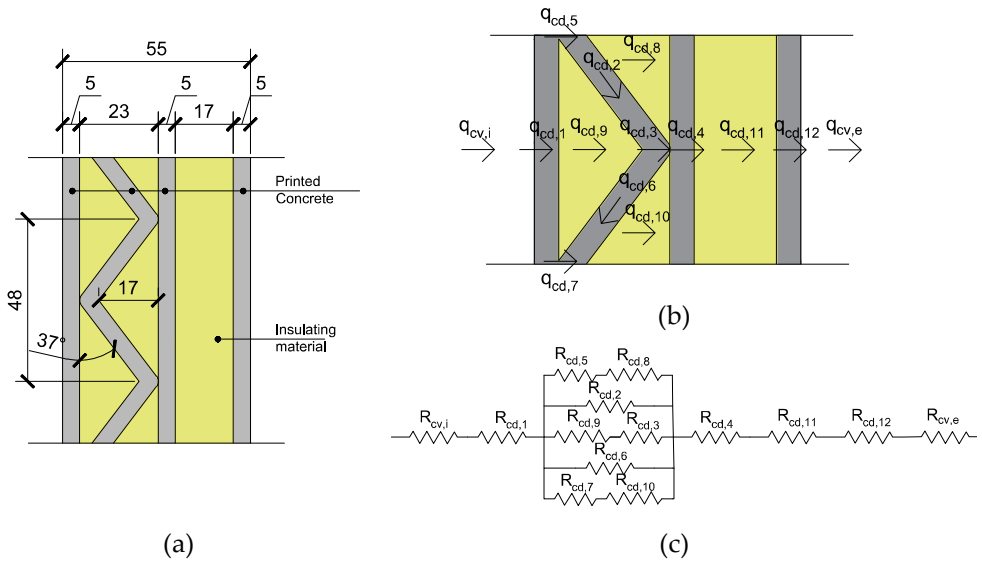

Figure 4-11: Analytical model for the estimation of the thermal transmittance of 3D printed concrete walls: (a) geometry, (b) heat fluxes configuration; (c) equivalent resistance scheme.

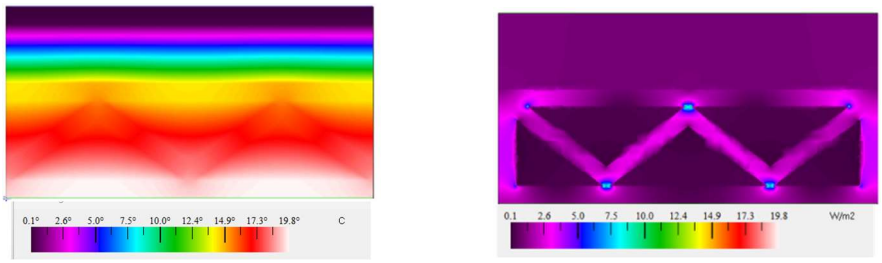

Figure 4-12: Finite element model for the estimation of the thermal transmittance of 3D printed concrete walls: (a) temperature gradient and (b) heat flow.

4.2.2.2 *Buildability*

The path of the robotic arm was developed as a closed loop (Figure 4-13). Two configurations were designed: 1) an unreinforced 3D printed concrete wall (Figure 4-13a) and 2) a reinforced 3D printed concrete wall with vertical steel bars embedded into small grouted pockets (Figure 4-13b). Both solutions are characterized by the internal part with inclined diaphragms with structural function to withstand vertical and horizontal loads (in pink in Figure 4-13) and an external concrete layer with just thermal and aesthetic function (in blue in Figure 4-13). All the cavities could be filled with insulating material to guarantee a good thermal performance of the printed wall.

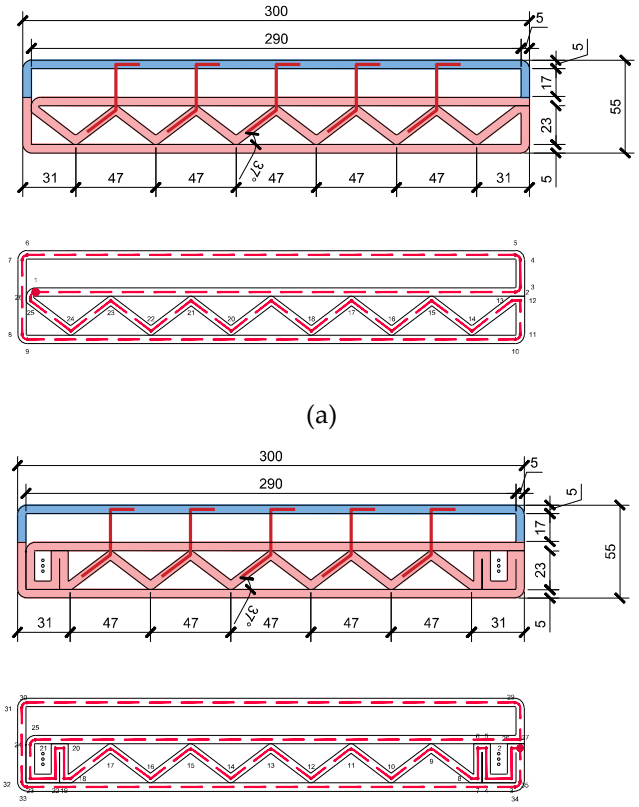

(a)

(b)

Figure 4-13: 3D printed concrete wall: (a) unreinforced configuration and (b) reinforced configuration.

To prevent the buckling of the thin outer concrete layer during the printing process, deformed steel (B450C) bars (in red in Figure 4-13) with a diameter of 6 mm were used to connect the outer concrete layer to the inner layer, which is stabilized by the inclined diaphragms. The spacing of the connectors in the horizontal direction was due to geometrical constraint (47 cm), while the vertical spacing was evaluated by means of a series of elastic phase analysis on a simplified model simulating the printing process. The analysis took into account factors such as the variation of the self-weight (resulting from the progressive deposition of the layers), the evolution of the mechanical properties of the concrete over time (resulting in the variation of the elastic modulus) and the variations of the constraint conditions (resulting from the manual positioning of the steel connectors at different heights). A general-purpose FE structural analysis software was used to perform this analysis [148].

To conduct the analysis, a wall section between two adjacent diaphragms was modelled, with a thickness of 5 cm, a width of 47 cm (orange area Figure 4-14a) and a variable height of up to 3 m. Considering a printing speed of 250 mm/s and the results of Esposito et al. in [64] on the increase in the elastic modulus of concrete over time after deposition, the value of the elastic modulus for each layer was calculated (Figure 4-14b). The analysis was conducted by placing steel connectors at a spacing of 42 cm.

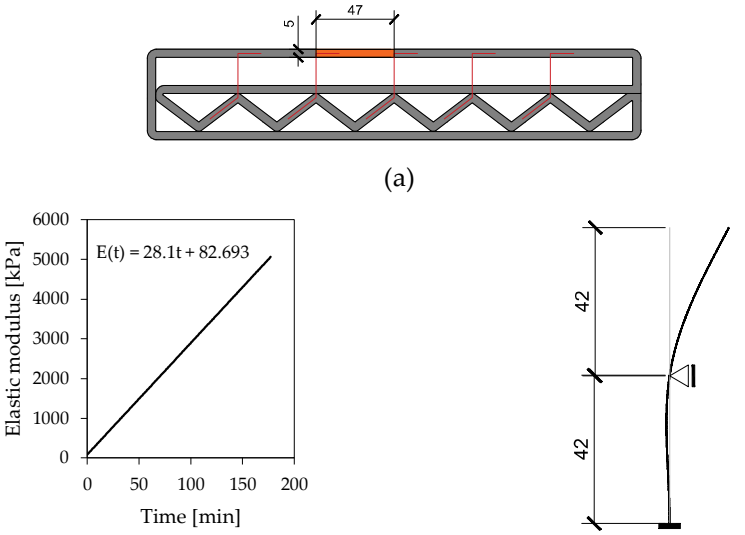

Figure 4-14: Buckling analysis: (a) portion of the wall considered, (b) evolution of the elastic modulus with time and (c) elastic buckling of the wall.

It was observed that with this spacing the buckling did not occur. Table 4-3 shows the buckling load factor (α), which is a scalar value that multiplied by the self-weight of a structure would cause buckling. It was observed that the most critical situation occurs during the printing of the first 56 layers (up to 84 cm), which has the lowest load factor.

Phase [-]	Printed layers [-]	Maximum height [cm]	Time [min]	Buckling load factor [-]
1	1-56	84	50	32.5
2	1-84	126	75	30.9
3	1-112	168	100	30.6
4	1-140	210	125	30.6
5	1-168	252	150	30.6
6	1-200	300	178	24.8

Table 4-3: Values of the load factors.

During the printing process, the connectors were positioned manually by stopping the robotic arm for a few seconds. It was essential to ensure adequate adhesion between the connectors and the printed concrete. Ribbed steel connectors were used for their advantages: high deformation capacity, low cost and good adhesion to concrete. However, they have some disadvantages, such as high thermal conductivity and corrosion potential. To overcome these problems, stainless steel bars or non-metallic reinforcements, such as FRP bars, could alternatively be used to avoid corrosion and reduce thermal conductivity [149]

4.2.2.3 Specimen preparation

The 3DCP walls were printed in a controlled laboratory environment at University Federico II (Napoli, Italy) with a temperature of 20±2°C and a relative humidity of 80±5%. A 6-axis robotic arm path was used to print the wall. A 28 mm diameter circular nozzle was connected to the print head of the digital system. The printing speed was set at 250±25 mm/s and a pump-mixer was used to mix the dry compound with water to provide a constant flow rate of concrete depending on the printing speed, width and thickness of the filament. The steel connectors were positioned manually during the printing process and any interruption in the printing process, lasting less than 120 seconds, had no impact on the structural integrity of the wall. Figure 4-15 shows the wall during the printing process.

Figure 4-15: Picture of the 3D printed concrete wall during the printing process.

4.2.2.4 Geometry of the specimens

In the previous section the main thermal, geometrical and mechanical parameters for the design of 3D printed concrete walls were identified considering a full-scale wall with a height of 3 m, a length of 3 m and a thickness of 55 cm. However, in line with the maximum dimensions allowable by the available setup and to facilitate the transport operation the printed walls were 2.10 m high, 2.10 m long and 38.5 cm

thick, as shown in Figure 4-16. The walls were made of 3D printed extruded concrete (material type 2); the first wall was unreinforced while the second wall was reinforced with vertical bars embedded in pockets placed within the outer cavities of the wall Figure 4-16b. The filling material was a cement-based grout with a maximum diameter of the aggregates of 5 mm. In the second specimen three steel ribbed bars with a diameter of 16 mm in each pocket were arranged to develop an ultimate resisting moment 1.5 times greater than the cracking moment given by the test on the unreinforced wall (see section 4.5.2 for details of the calculation). The width of the extruded filament was 35 mm and the thickness was 11 mm.
The walls had a rectangular cross-section with cavities, which was constant with the height of the wall. The main geometrical properties of the wall are given in Table 4-4.

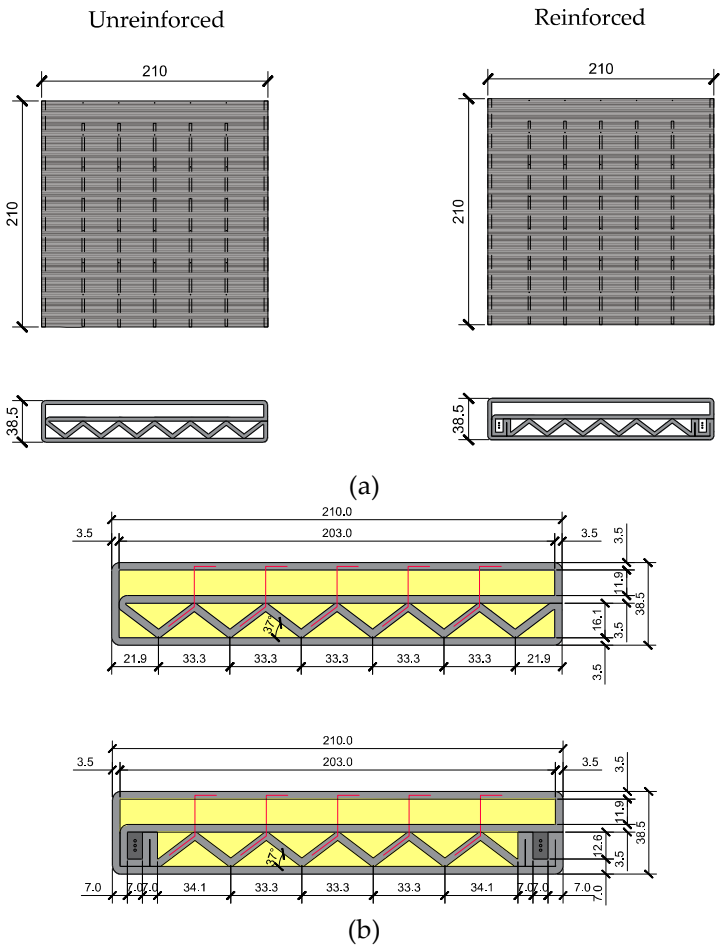

Figure 4-16: (a) Size and shape of the 3D printed concrete walls and (b) cross-sections with dimensions.

ID [-]	l_x [cm]	l_y [cm]	l_z [cm]	A [cm²]	J_{yy} [cm⁴]	J_{xx} [cm⁴]	n [-]	w [cm]	t [cm]	Test [-]
Unreinforced	210	38.5	210	3269	9733382	32825	14	3.5	1.1	Test 1
Reinforced	210	38.5	210	3506	13206186	63876	14	3.5	1.1	Test 2

Table 4-4: Geometrical properties: dimension of the specimen (lx, ly, lz), area of the cross-section (A), moments of inertia of the cross section (J_{yy}, J_{xx}), number of cavities (n), width (w), and thickness (t) of the filament.

The structural part of the walls (in pink in Figure 4-13) was connected to a reinforced concrete foundation with stirrups with a diameter of 12 mm which link the foundation to a 20 cm depth normal strength concrete corbel poured within the cavities. The external cavity (in blue in Figure 4-13), designed for thermal purposes, was not connected to the foundation and was supported by a 4 cm layer insulating material (polystyrene), as shown in Figure 4-19a. Figure 4-17 shows the connection of the two 3D printed concrete walls with the reinforced concrete foundation.

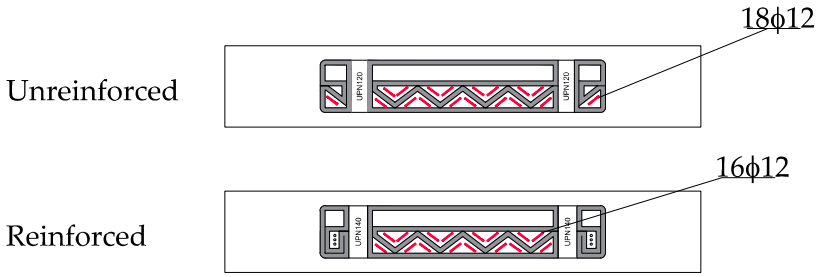

Figure 4-17: Connection of the 3D printed walls with the reinforced concrete foundations.

In addition three main cross-section can be identified in the wall, as shown in Figure 4-18: cross-section 1-1 shows the connection of the structural part of the wall to the RC foundation; section 2-2 represent the typical cross-section of the wall; cross-section 3-3 represents the upper 20 cm portion of the wall, that was filled with normal strength concrete to create a RC corbel to apply the horizontal and the vertical load during the test (it reproduces the connection of the wall to a RC slab).
As mentioned in the previous section, the wall is made by a part with internal inclined diaphragms which has a structural function and an additional external concrete layer with just a thermal and aesthetic function. To avoid buckling during the printing process, the outer concrete layer was connected to the internal portion of the wall by means of steel connectors (in red Figure 4-18). The buckling analysis presented in section 4.2.2.2 was performed also for the wall with reduced dimensions. Steel connectors with a diameter of 6 mm and a spacing of about 30 cm are needed to avoid the buckling of the 3DPC external layers (Figure 4-18). Figure 4-19 shows the detail of the connection of the wall to the foundation, of the printed cross-section and the two 3DPC walls.

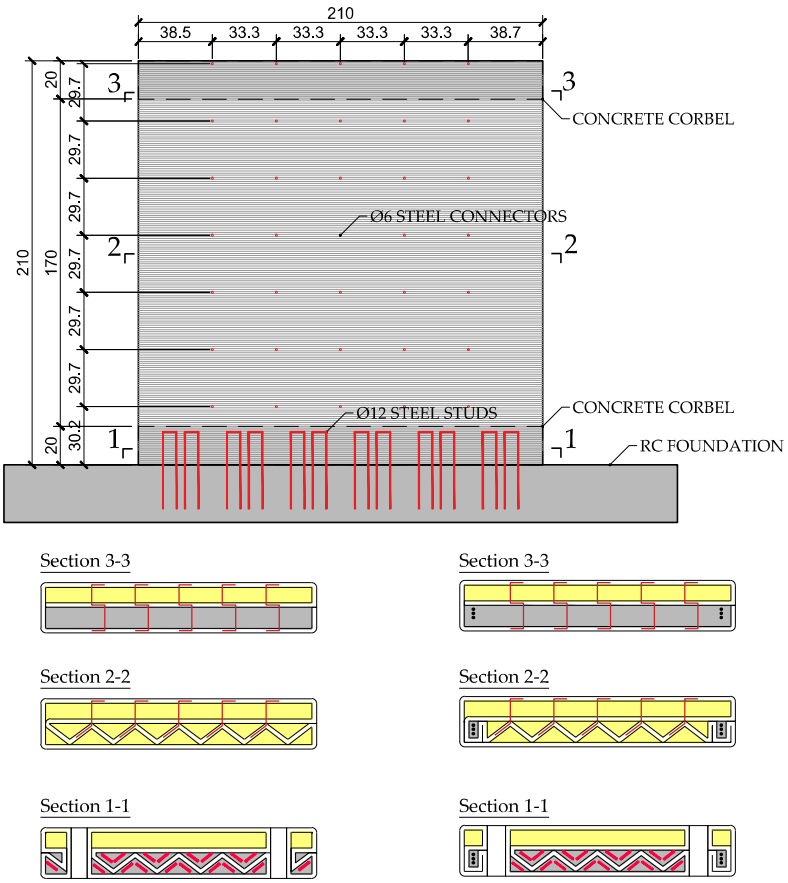

Figure 4-18: Side view and cross-section view of the 3D printed concrete walls.

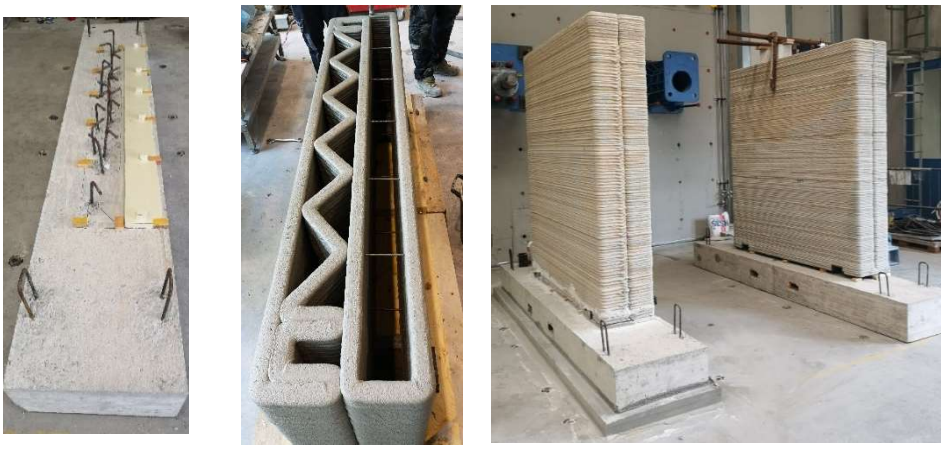

(a) (b) (c)

Figure 4-19: 3DPC wall: (a) reinforced concrete foundation, (b) cross-section of the wall, (c) printed walls.

4.3 Test setup

4.3.1 Calculation of the vertical load applied

With reference to the building in Figure 4-6, the plan view of the house could be as shown in Figure 4-20.

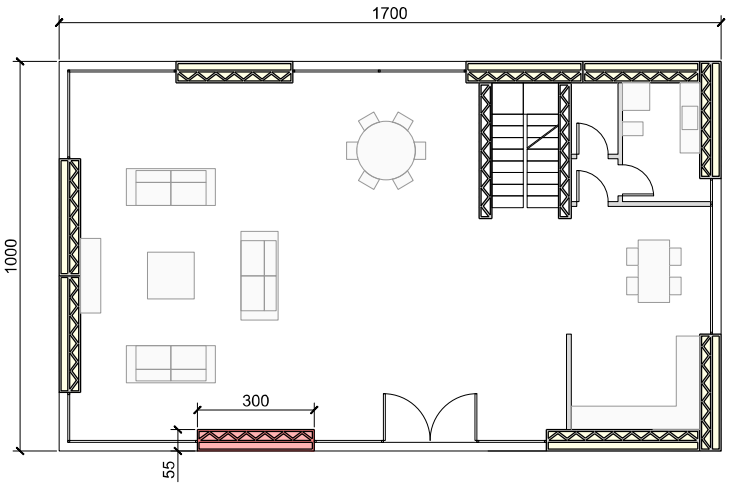

Figure 4-20: Reference building: plan view of the ground floor.

The resisting shear wall considered is highlighted in red in Figure 4-20. The wall has a height of 3 m, a length of 3 m and a thickness of 55 cm. To estimate the vertical load acting on the wall, the following loads were assumed (details of the type of roof and floor considered are reported in APPENDIX E):

- floor: G_1= 4.20 kN/m²; G_2= 3.00 kN/m²; Q= 2 kN/m²;
- roof: G_1= 4.20 kN/m²; G_2= 2.30 kN/m²; Q= 1.20 kN/m²).

All the walls of the house are assumed to be modular 3DPC walls with dimensions 3x3x0.55 m and a weight of 20 kN. The walls were in total 11. By assuming a tributary area of the 3DPC wall about 20 m², the vertical load resulted to be about 390 kN.
As shown in Table 4-4 the cross-section area of a wall 2.10 m high and 2.10 m long is 3269 cm². As consequence, the cross section area of the wall which is 3 m high and 3 m long is calculated as:

$$A^{100\%} = A^{70\%} * 0.7^2 = 6671 \text{ cm}^2 \quad \text{4-3}$$

And the load acting on the wall scaled at 70% is calculated as:

$$N^{70\%} = \frac{N^{100\%}}{A^{100\%}} * A^{70\%} = \frac{390\ kN}{6671\ cm^2} 3269\ cm^2 = 192\ kN \quad \text{4-4}$$

4.3.2 *In-plane cyclic test*

In-plane quasi-static cyclic loading test were conducted at the University of Brescia laboratory to evaluate the structural performance of 3D printed concrete modular walls, as shown in Figure 4-21.

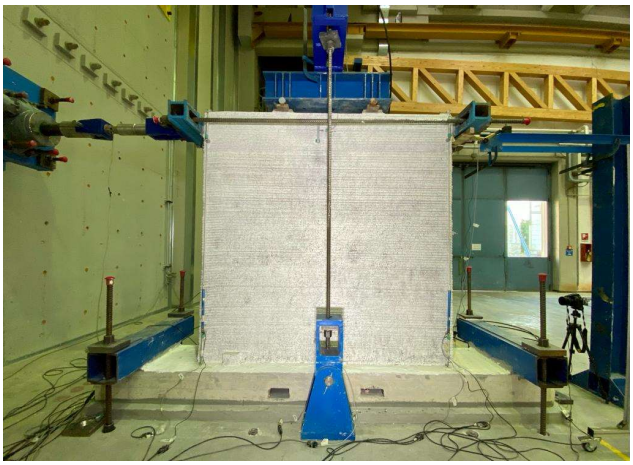

Figure 4-21: 3D printed concrete wall: experimental test.

It should be pointed out that the set-up used for the tests was the same for all the 3D printed concrete walls; in the following sections, for sake of simplicity, all the drawings and pictures refers to the unreinforced wall printed with material type 2.
To simulate the load of a typical two-storey building, a vertical load of 200 kN was applied on the wall during the test. It has to be observed that a vertical load of 150 kN was applied on wall 1 and wall 2 due to their smaller dimensions. For this purpose, a system consisting of two hydraulic jacks, a transverse beam (UPN300 S235) and a longitudinal beam (HEB240 S235), which distributed the load on two points at ¼ and ¾ of the side of the wall, was used. To counteract the vertical load, two high-strength steel bars (Dywidag 32 WR) were hinged to the laboratory floor. The vertical load was recorded by two load cells situated between the hydraulic jacks and the steel beam at the top, which was monitored and kept constant during the test. The horizontal load was applied using an electromechanical jack with a maximum capacity of 500 kN. The loading system consisted of two steel beams (S235) placed at the ends of the top corbel and two high-strength steel bars (Dywidag 32 WR) connecting the two beams. A hinged beam was placed between the electromechanical jack and the horizontal loading system. Horizontal displacements of increasing amplitude were alternately applied in both directions. The cyclic horizontal load was measured by a load cell located between the electromechanical jack and the specimen on the hinged beam. A detailed description of the test setup is provided in Figure 4-22.

The positive load direction has been defined when the wall was pushed away from the reacting wall (from left to right in Figure 4-22, called push direction throughout the section).

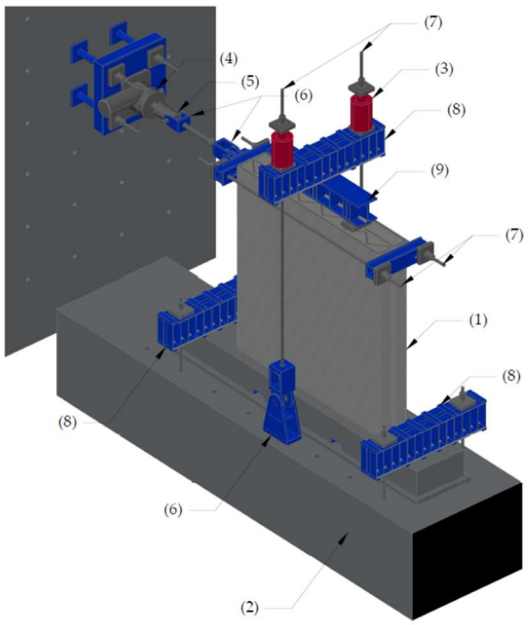

(1) 3DPC wall
(2) RC basement
(3) Hydraulic jacks (vertical loading)
(4) Electro-mechanic jack (horizontal loading)
(5) Load cell
(6) Hinge
(7) Post-tensioning rods
(8) UPN 300 S235
(9) HEB 240 S235

Figure 4-22: Detail of the test set-up.

Figure 4-23 and Table 4-5 show the loading protocol for the walls printed with material type 1 (section 4.2.1) and *Figure 4-24* and Table 4-6 show the adopted loading protocol for the walls printed with material type 2 (section 4.2.2). The loading protocol consists in bidirectional cycles at different drift limits; three fully reversed cycles were applied at each drift ratio.
The loading protocol was derived with reference to the ACI guideline 374.2R-13 [150], which serves as a reference for testing reinforced concrete structural elements under slowly applied simulated seismic loads. The loading protocol suggested by the

guideline, which involves only one cycle at half of the yielding drift, was modified to include a greater number of cycles before failure. This modification was necessary due to the absence of reinforcement in the walls, and the cracking load was used as a benchmark. Three different loading rates were implemented, resulting in each drift series lasting between 30 minutes and 60 minutes. Specifically, the chosen loading rates were 0.005 mm/s for drifts between 0.05‰ and 0.2‰, 0.01 mm/s for drifts between 0.4‰ and 1.6‰, and 0.025 mm/s for drifts beyond that range.

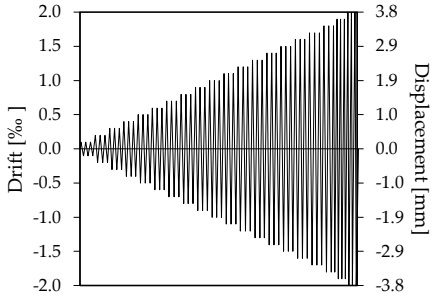

Figure 4-23: Loading protocol for structural testing of walls printed with material 1: wall 3.

Wall 1	Drift limits	[‰]	±0.1	±0.2	±0.3	±0.4	±0.5	±0.6	±0.7	±0.8	±0.9	±1.0
	n. of cycles	[-]	3	3	3	3	3	3	3	3	3	3
	Drift limits	[‰]	±1.1	±1.2	±1.3	±1.4	±1.5	±1.6	±1.7	±1.8		
	n. of cycles	[-]	3	3	3	3	3	3	3	3		
Wall 2	Drift limits	[‰]	±0.1	±0.2	±0.3	±0.4	±0.5	±1.0	±1.5			
	n. of cycles	[-]	3	3	3	3	3	3	3			
Wall 3	Drift limits	[‰]	±0.1	±0.2	±0.3	±0.4	±0.5	±0.6	±0.7	±0.8	±0.9	±1.0
	n. of cycles	[-]	3	3	3	3	3	3	3	3	3	3
	Drift limits	[‰]	±1.1	±1.2	±1.3							
	n. of cycles	[-]	3	3	3							

Table 4-5: Loading protocol for structural testing of walls printed with material 1.

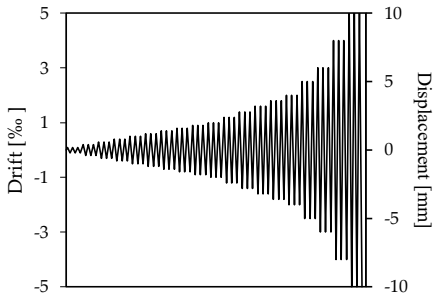

Figure 4-24: Loading protocol for structural testing of walls printed with material 2: unreinforced wall.

Unreinforced	Drift limits	[‰]	±0.1	±0.2	±0.4	±0.6	±0.8	±1.0	±1.2	±1.4	±1.6	±1.8	±2.0	±3.0	±4.0	±5.0
	n. of cycles	[-]	3	3	3	3	3	3	3	3	3	3	3	3	3	3
Reinforced	Drift limits	[‰]	±0.25	±0.5	±0.75	±1.0	±1.25	±1.5	±1.75	±2.0						
	n. of cycles	[-]	3	3	3	3	3	3	3	3						

Table 4-6: Loading protocol for structural testing of walls printed with material 2.

4.4 Instrumentation

Figure 4-25 to Figure 4-27 show the instrumentation of the in-plane test of the walls printed with material 1. The horizontal displacement was measured with sensors TD1 and TD2 with a stroke of 2 mm and 10 mm, respectively. Sensor BD1 was used to measure possible sliding of the RC foundation. The development of flexural cracking was monitored with vertical sensors (VD1, VD2, VD3, VD4, VD5, VD6). The development of shear cracking was monitored at the base of the wall (HD1, HD2, HD3, HD4, HD5 ,HD6) with wall 2 and wall 3 and along diagonals (D1 and D2) with wall 1. In order to measure the formation of shear cracks, either horizontal sliding or diagonal cracking, the digital image correlation (DIC) technique was adopted (indicated as a dotted surface).

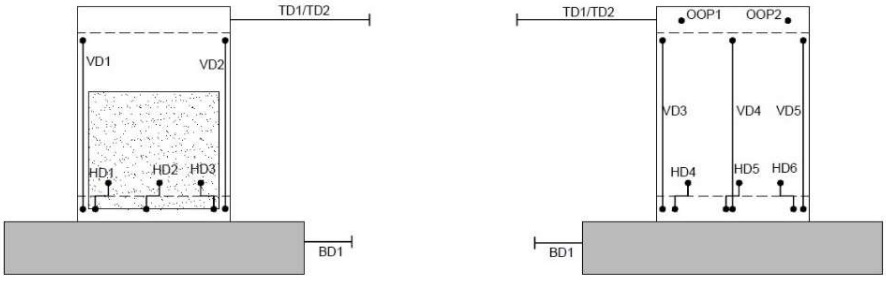

Figure 4-25: Measurement devices used in wall 1 (printed with material type 1).

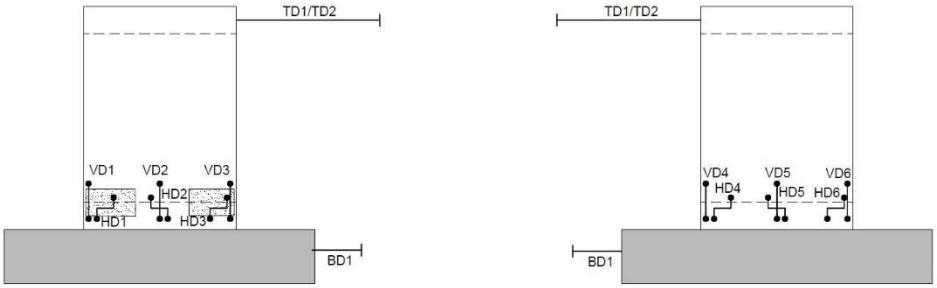

Figure 4-26: Measurement devices used in wall 2 (printed with material type 1).

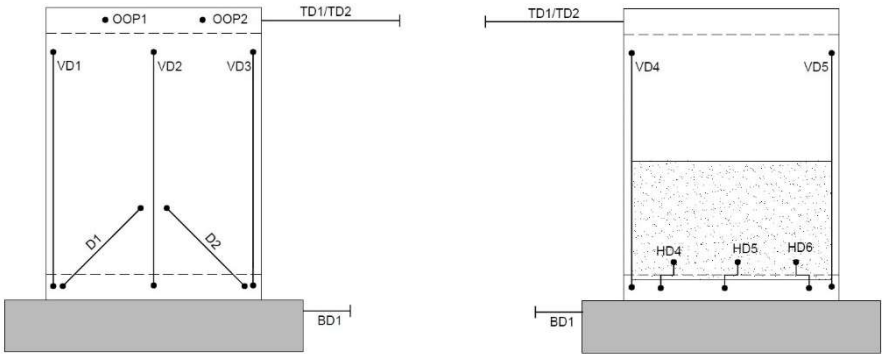

Figure 4-27: Measurement devices used in wall 3 (printed with material type 1).

Figure 4-28 shows the instrumentation scheme for the unreinforced and the reinforced wall made with material 2. The horizontal displacement was measured with sensors TD1, TD2 and TD3 with a stroke of 2 mm, 10 mm and 20 mm, respectively. Sensor BD1 was used to measure possible sliding of the RC foundation. The development of flexural cracking was monitored on the base of the wall (VD1-VD4-VD7-VD8). The development of shear cracking was monitored at the base of the wall (HD1-HD2-HD4). Sensors VD2-VD3-VD5-VD6 were used to catch other possible cracks in the wall. Moreover, two out-of-plane sensors OOP1 and OOP2 were installed. Finally, two sensors BR1 and BR2 were installed at the grout layer below the RC foundation to detect any rotations. In order to measure the formation of shear cracks, either horizontal sliding or diagonal cracking, the digital image correlation (DIC) technique was adopted on the whole surface of the wall (indicated as a dotted surface).

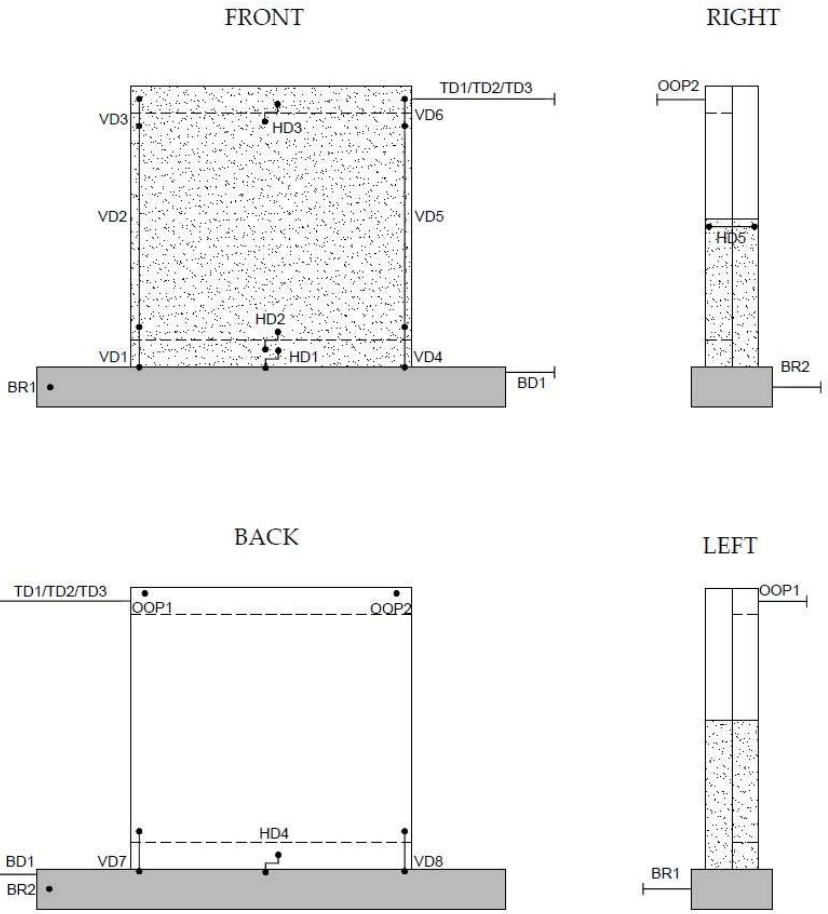

Figure 4-28: Measurement devices used in the unreinforced and reinforced wall (printed with material type 2).

4.5 Experimental results

In this section the test results will be presented. The predicted results will be shown and then the experimental ones will be presented in terms of force versus displacement behaviour, crack pattern, stiffness degradation and energy dissipation.

4.5.1 Test results

The structural response of the walls is described in terms of force versus net horizontal displacement and crack pattern. The net horizontal displacement is calculated by subtracting from the horizontal displacement, measured with sensors TD1, possible sliding of the RC foundation, measured with sensors BD1 (see section 4.4). In order to gain a deeper understanding of this behaviour, the force-displacement curve is subdivided into three main sections: i) the initial phase prior to cracking, (ii) the point at which the first crack appears, and (iii) the point at which the collapse occurred. Moreover, the performance of the structure is also described by the variation of the in-plane stiffness and energy dissipation capacity (ξ_{eq}) over repeated cycles of increasing amplitude. The secant stiffness is obtained by dividing the lateral load (F_{Dmax}) by the peak displacement (d_{Dmax}) reached during each cycle. To calculate the equivalent viscous damping coefficient (ξ_{eq}) for the energy dissipation capacity, Eq. 4-5 is employed. This equation considers the total energy dissipated (W_d), which is comprised of the areas enclosed in the single hysteretic loop and the elastic energy stored in the sample at the peak displacement within the same loop (W_e) [151].

$$\xi_{eq} = \frac{W_d}{2\pi(|W_e^+| + |W_e^-|)} \qquad 4\text{-}5$$

Section 4.5.1.1 and section 4.5.1.2 show the results of the 3DPC walls printed using material type 1 and material type 2, respectively.

4.5.1.1 3DPC walls printed with material type 1

4.5.1.1.1 Wall 1

The maximum recorded horizontal load was 118.20 kN (at a lateral displacement d = 1.189 mm) and -121.80 kN (at a lateral displacement d = -1.2 mm) for the positive and negative loading direction, respectively.
Figure 4-29 shows the initial phase of the test. The wall exhibited a high initial stiffness of about 290 kN/mm. The wall showed a bilinear elastic behaviour up to a drift of 0.9‰ (d = 1.078 mm) and a horizontal load of 118.05 kN.

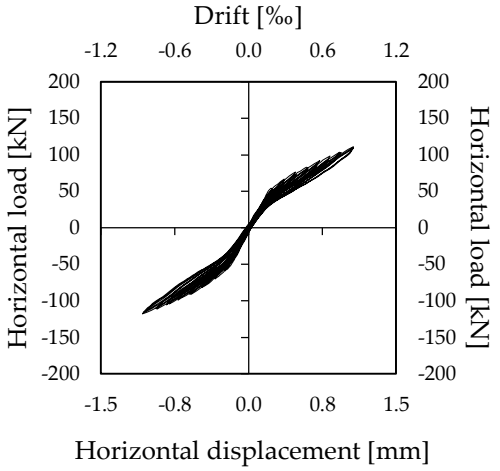

Figure 4-29: Horizontal force versus horizontal displacement of wall 1 during the pre-cracking phase.

The wall exhibited a brittle failure at the base of the wall due to the formation of a crack during the pull phase at drift of 1.0‰ (d = -1.2 mm) and a load of -121.8 kN, as shown in Figure 4-30. The first crack is indicated in red in Figure 4-32, it started at layer n.23 having a distance of 16 cm from the bottom corbel. The crack started in the outer concrete fibres and then rapidly spread towards the inner portion of the section running parallel to the printed layer interface. Approaching the innermost part of the cross-section, it moved downwards through several layers.

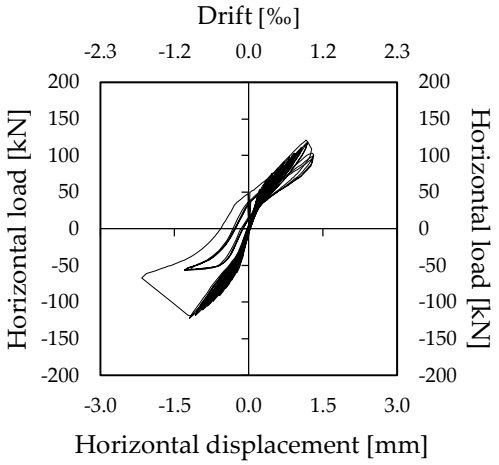

Figure 4-30: Horizontal force versus horizontal displacement of wall 1 up to the formation of the first crack.

Figure 4-31 shows the wall behaviour in term of applied load vs. lateral displacement up to the wall collapse phase with the occurrence of the second crack during the push phase at the base of the wall at a drift of 1.80‰ (d = 2.236 mm) and a load of 83.56 kN. The second crack is indicated in blue in Figure 4-32, it developed similarly from the opposite end of the cross-section and met the one created in the previous cycles.

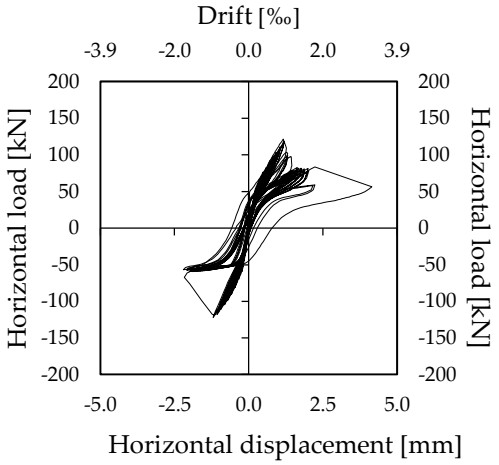

Figure 4-31: Horizontal force versus horizontal displacement of wall 1 up collapse.

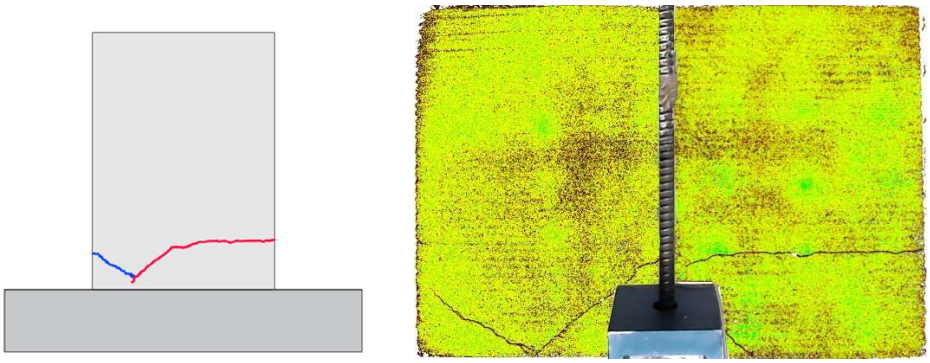

Figure 4-32: Crack pattern detected with the digital image correlation.

The test was stopped at a drift of 1.80‰ when the load was equal to 58.80 kN (d = 2.226 mm) and to -56.77 kN (d = -2.206 mm) for the positive and negative loading direction, respectively. Figure 4-33 shows the envelope curve.

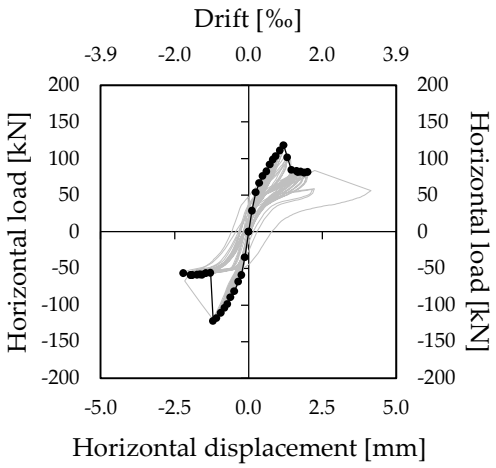

Figure 4-33: Horizontal force versus horizontal displacement: wall 1.

The performance of the structure is also described by the decrease of the in-plane stiffness (Figure 4-34) and energy dissipation capacity ξ_{eq} (Figure 4-35) over repeated cycles of increasing amplitude. Initially, the average stiffness during the first cycle (with a 0.1‰ drift) was 290 kN/mm. At the appearance of the first crack at 1.0‰ drift, the secant stiffness was 101.5 kN/mm and 99.41 kN/mm for the pull and push phase, respectively. Subsequently, the secant stiffness decreased, reaching a value of 26.42 kN/mm at 1.80‰ drift when the second crack occurred and the test was stopped.

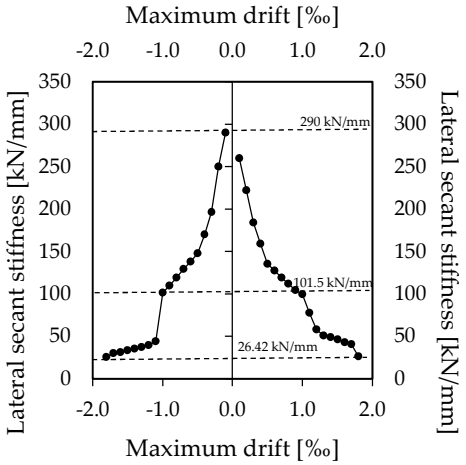

Figure 4-34: Evolution of the secant stiffness curve: wall 1.

After the first load cycles, the equivalent viscous damping coefficient (ξ_{eq}) was equal to 3.9% at 0.1‰ drift showing an overall stable behaviour until a drift of 0.9‰. However, at 1.0‰ drift, the damping coefficient increased to 8.3% due to the occurrence of flexural failure. In the following cycles, a stable trend was observed, until the occurrence of the collapse with a value of 15.2% at 1.8‰ drift.

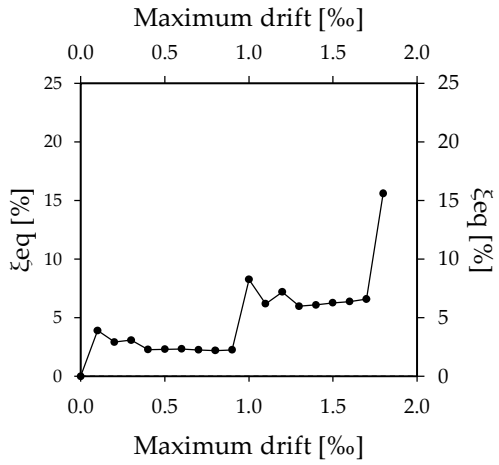

Figure 4-35: Evolution of the viscous damping coefficient: wall 1.

4.5.1.1.2 Wall 2

The maximum recorded horizontal load was 139.03 kN (at a lateral displacement d = 1.417 mm) and -81.37 kN (at a lateral displacement d = -0.520 mm) for the positive and negative loading direction, respectively.
Figure 4-36 shows the initial phase of the test. The wall exhibited a high initial stiffness of 295 kN/mm. The wall showed a bilinear elastic behaviour up to a drift of 0.4‰ (d = 0.475 mm) and a horizontal load of 80.72 kN.

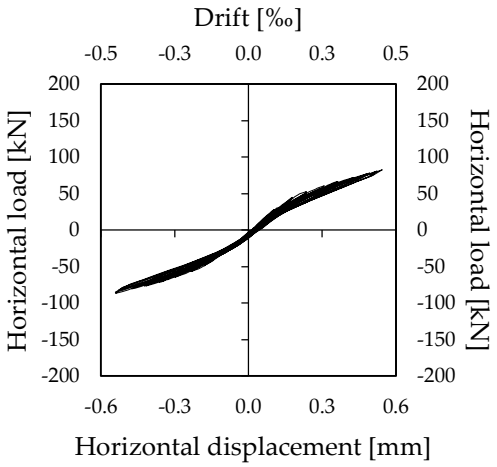

Figure 4-36: Horizontal force versus horizontal displacement of wall 2 during the pre-cracking phase.

When the maximum flexural strength was reached, the wall exhibited a brittle failure at the base of the wall. The first crack occurred during the pull phase at drift of 0.5‰ (d = -0.520 mm) and a load of -81.30 kN (Figure 4-37). The first crack is indicated in red in Figure 4-39, it started at layer n.21 at a distance of 12 cm from the bottom corbel. The crack started in the outer concrete fibres and then spread towards the inner portion of the section parallel to the printed layer interface. Approaching the innermost part of the cross-section, it moved downwards crossing several lower layers.

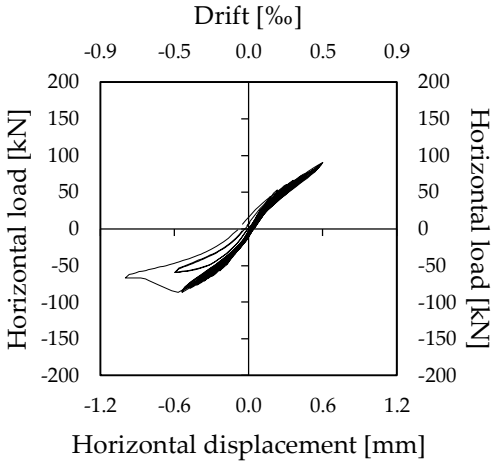

Figure 4-37: Horizontal force versus horizontal displacement of wall 2 up to the formation of the first crack.

Figure 4-38 shows the wall behaviour in term of applied load vs. lateral displacement up to the wall collapse phase with the occurrence of the second crack during the push phase at the base of the wall at a drift of 1.50‰ (d = 1.417 mm) and a load of 139.03 kN. The second crack is indicated in blue in Figure 4-39, it developed similarly from the opposite end of the cross-section and met the one created in the previous cycles.

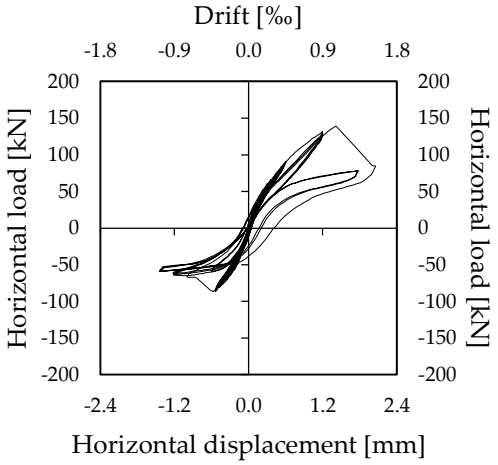

Figure 4-38: Horizontal force versus horizontal displacement of wall 2 up to collapse.

It has to be observed that it was not possible to detect the crack propagation with the digital image correlation because it was applied on a small portion of the wall which did not covered the damage zone.

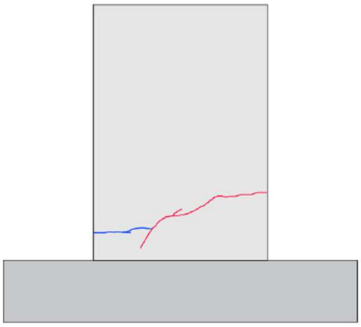

Figure 4-39: Crack pattern.

The test was stopped at a drift of 1.50‰ when the load was equal to 78.86 kN (d = 1.783 mm) and to -58.86 kN (d = -1.437 mm) for the positive and negative loading direction, respectively. Figure 4-40 shows the envelope curve.

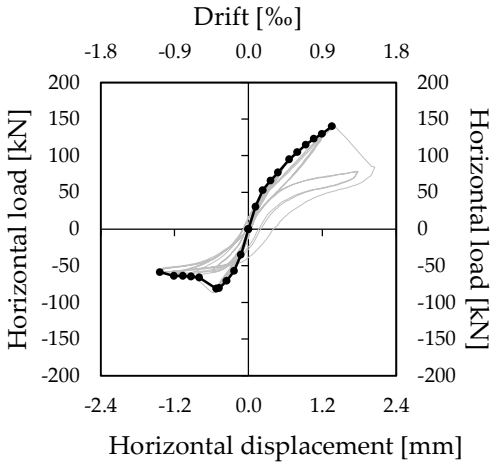

Figure 4-40: Horizontal force versus horizontal displacement: wall 2.

The performance of the structure is also described by the decrease of the in-plane stiffness (Figure 4-41) and energy dissipation capacity ξ_{eq} (Figure 4-42) over repeated cycles of increasing amplitude. Initially, the average stiffness during the first cycle (with a 0.1‰ drift) was 295.38 kN/mm. At the appearance of the first crack at 0.5‰ drift, the secant stiffness was 156.35 kN/mm and 142.86 kN/mm for the pull and push phase, respectively. Subsequently, the secant stiffness decreased, reaching a value of

102.94 kN/mm at 1.50‰ drift when the second crack occurred (as shown in Figure 4-41) and the test was stopped.

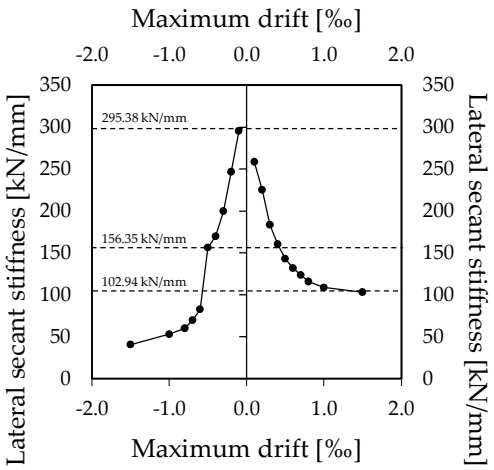

Figure 4-41: Evolution of the secant stiffness curve: wall 2.

After the first load cycles, the equivalent viscous damping coefficient (ξ_{eq}) varied from 1.4% at 0.1‰ drift to 1.7% at 0.4‰ drift, displaying an overall stable behaviour. However, at 0.5‰ drift, the damping coefficient increased to 5% due to the occurrence of flexural failure. In the following cycles, a stable trend was observed, until the occurrence of the collapse with a value of 10.5% at 1.5‰ drift.

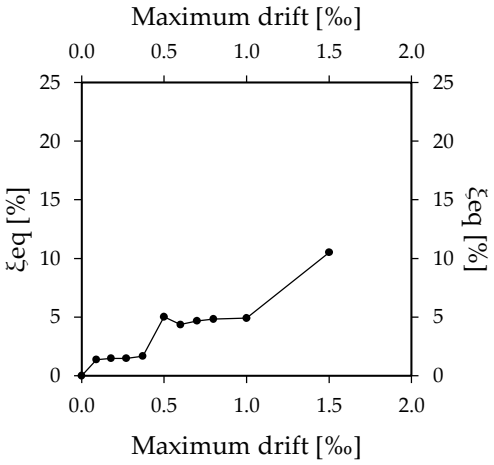

Figure 4-42: Evolution of the viscous damping coefficient: wall 2.

4.5.1.1.3 Wall 3

The maximum recorded horizontal load was 188.78 kN (at a lateral displacement d = 2.068 mm) and -166.19 kN (at a lateral displacement d = -1.090 mm) for the positive and negative loading direction, respectively.
Figure 4-43 shows the initial phase of the test. The wall exhibited a high initial stiffness of 330 kN/mm. The wall showed a bilinear elastic behaviour up to a drift of 0.6‰ (d = 0.952 mm) and a horizontal load of 151.67 kN.

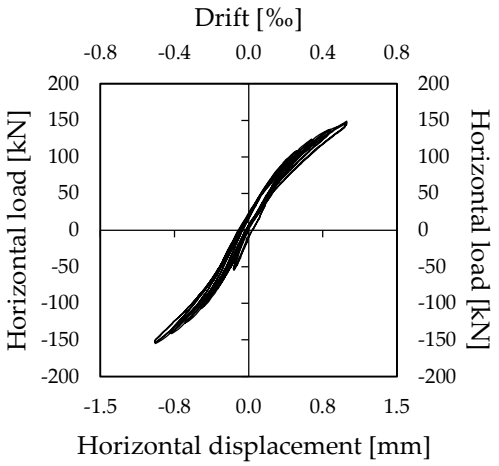

Figure 4-43: Horizontal force versus horizontal displacement of wall 3 during pre-cracking phase.

When the maximum flexural strength was reached, the wall exhibited a brittle failure at the base of the wall. Figure 4-44 shows the wall behaviour in term of applied load vs. lateral displacement up to the formation of the first crack during the pull phase at drift of 0.7‰ (d = -1.09 mm) and a load of 166.19 kN. The first crack is indicated in red in Figure 4-46, it started at layer 22, 14 cm away from the bottom corbel, and progressed horizontally within a layer of concrete from the outermost part of the cross-section. As it approached the innermost part of the cross-section, it gradually moved downwards through several layers.

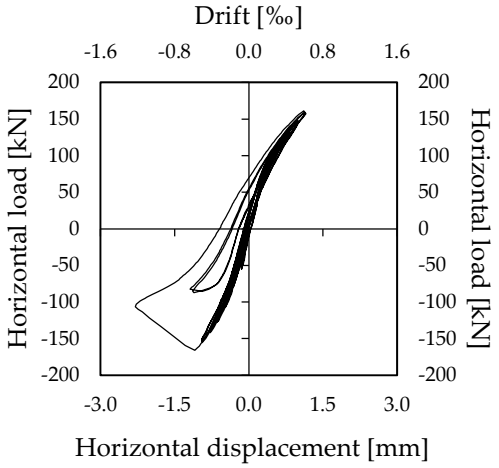

Figure 4-44: Horizontal force versus horizontal displacement of wall 3 up to the formation of the first crack.

Figure 4-45 shows the wall behaviour in term of applied load vs. lateral displacement up to the wall collapse phase with the occurrence of the second crack during the push phase at the base of the wall at a drift of 1.20‰ (d = 1.961 mm) and a load of 188.78 kN. The second crack is indicated in blue in Figure 4-46, it developed similarly from the opposite end of the cross-section and met the one created in the previous cycles.

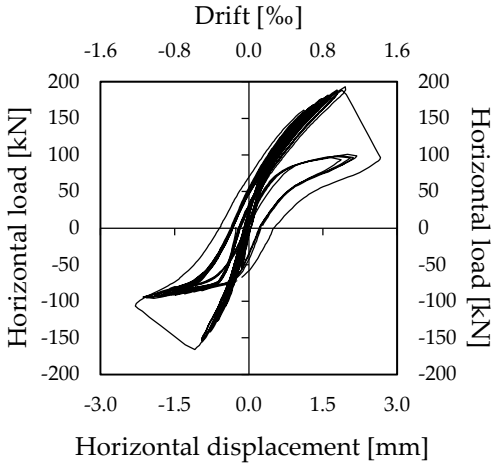

Figure 4-45: Horizontal force versus horizontal displacement of wall 3 up to collapse.

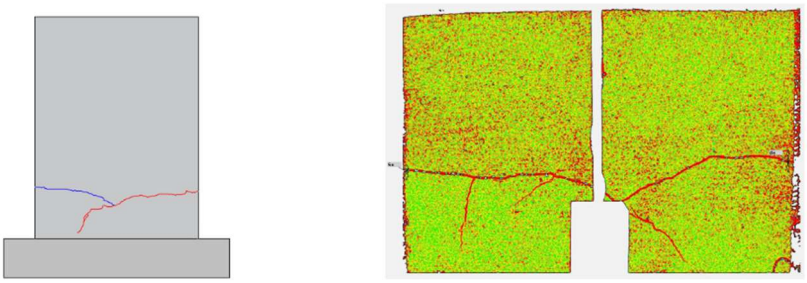

Figure 4-46: Crack pattern detected with the digital image correlation.

After the cracking the wall exhibited a rocking mechanism. The test was stopped at a drift of 1.30‰ when the load was equal to 96.73 kN (d = 2.122 mm) and to -94.51 kN (d = 2.145 mm) for the positive and negative loading direction, respectively. Figure 4-47 shows the envelope curve.

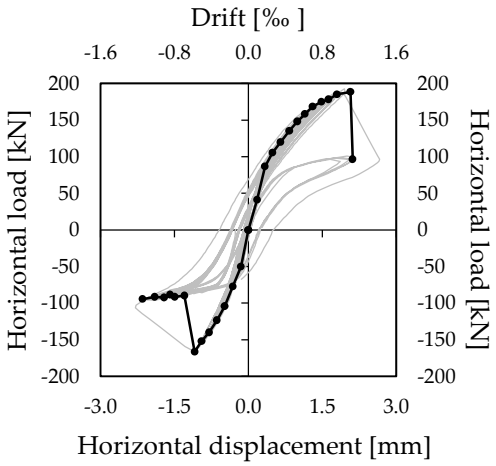

Figure 4-47: Horizontal force versus horizontal displacement: wall 3.

The performance of the structure is also described by the decrease of the in-plane stiffness (Figure 4-48) and energy dissipation capacity ξ_{eq} (Figure 4-49) over repeated cycles of increasing amplitude. Initially, the average stiffness during the first cycle (with a 0.1‰ drift) was 330.64 kN/mm. At the appearance of the first crack at 0.7‰ drift, the secant stiffness was 152.47 kN/mm a and 137.75 kN/mm for the pull and push phase, respectively. Subsequently, the secant stiffness decreased, reaching a value of 91.29 kN/mm at 1.20‰ drift when the second crack occurred and dropping to a value of 45 kN/mm at 1.20‰ drift (as shown in Figure 4-48), when the test was stopped.

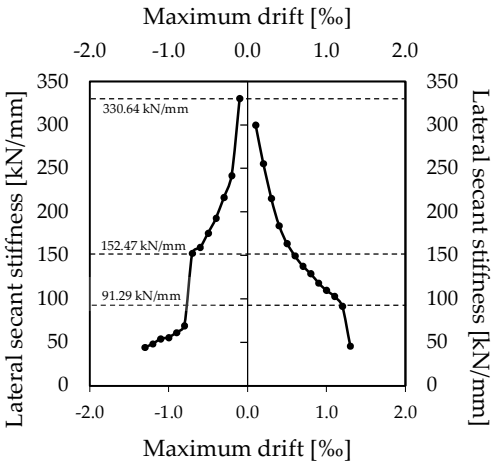

Figure 4-48: Evolution of the secant stiffness curve: wall 3.

After the first load cycles, the equivalent viscous damping coefficient (ξ_{eq}) varied from 8.2% at 0.2‰ drift to 3.0% at 0.6‰ drift. However, at 0.6‰ drift, the damping coefficient increased to 9.5% due to the occurrence of flexural failure. In the following cycles, a stable trend was observed, until the collapse occurred with a value of 10.9% at 1.2‰ drift.

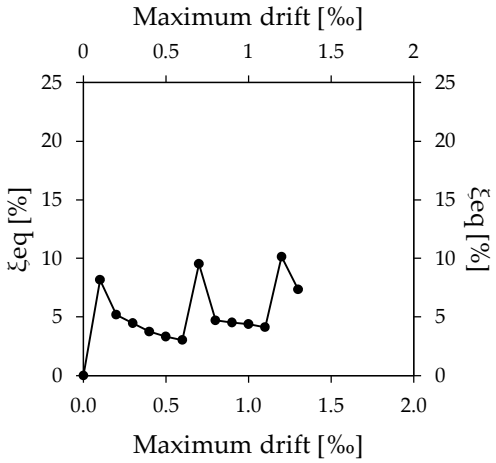

Figure 4-49: Evolution of the viscous damping coefficient: wall 3.

4.5.1.2 3DPC walls printed with material type 2

4.5.1.2.1 Unreinforced wall

Regarding the unreinforced wall, the results of the structural and thermal test are presented.

4.5.1.2.1.1 Structural test

The maximum recorded horizontal load was 202.05 kN (at a lateral displacement d = 3.191 mm) and -217.53 kN (at a lateral displacement d = -2.811 mm) for the positive and negative loading direction, respectively.
Figure 4-50 shows the initial phase of the test. The wall exhibited an initial stiffness of 299.78 kN/mm. The wall showed a bilinear elastic behaviour up to a drift of 1.4‰ (d = -2.8 mm) and a horizontal load of -217.53 kN. During this phase, the first crack (detected with the digital image correlation) appeared during the pull phase (point A- in Figure 4-53) when the load was 180.3 kN at a 0.8‰ drift (d= -1.6 mm). During the loading reversal, the crack occurred also in the push phase (point A+ in Figure 4-53) for a load of 190 kN and a drift of 1‰ (d = 2.0 mm). The crack pattern was detected thanks to the application of the digital image correlation, as shown in Figure 4-54a.

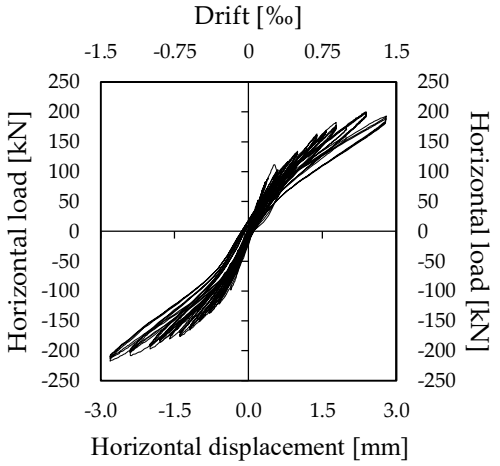

Figure 4-50: Horizontal force versus horizontal displacement of the unreinforced wall during the pre-cracking phase.

When the maximum flexural strength was reached, the wall exhibited a brittle failure at the base of the wall. Figure 4-51 shows the wall behaviour in term of applied load vs. lateral displacement in correspondence of the appearance of the flexural crack at the base of the wall, which occurred both for the pull and push direction at drift of 1.6‰ at a load of - 211.29 kN (d = -3.406) and 202.5 kN (d = 2.79), respectively (see

points B+ and B- in Figure 4-53). The crack is indicated in Figure 4-54b, it started at layer n.29 at a distance of 10 cm from the bottom corbel, then it moved downwards crossing several lower layers until layer n.19 spreading then towards the inner portion of the section parallel to the printed layer interface in correspondence of the bottom corbel.

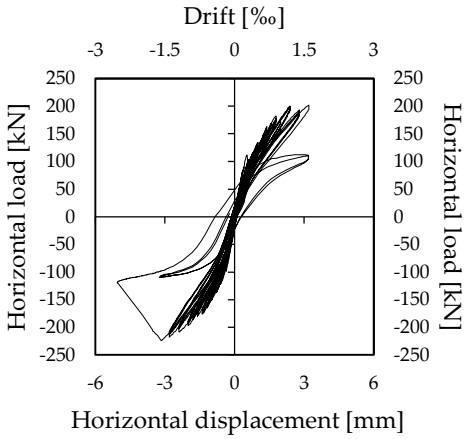

Figure 4-51: Horizontal force versus horizontal displacement of the unreinforced wall up to the formation of the flexural crack.

After the cracking the wall exhibited a rocking mechanism. The test was stopped at a drift of 5‰ when the load was equal to 98.3 kN (d = 10 mm) and to -112.9 kN (d = -9.7 mm) for the positive and negative loading direction (see points C+ and C- in Figure 4-53) , respectively (Figure 4-52). Figure 4-53 shows the envelope curve.

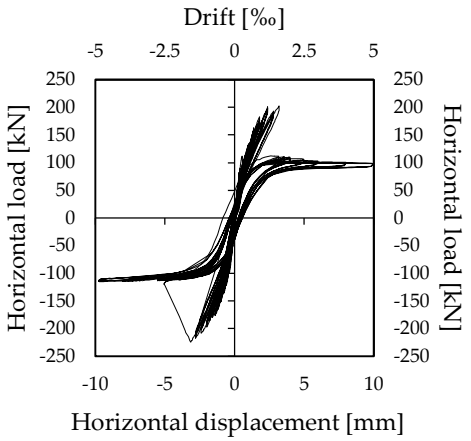

Figure 4-52: Horizontal force versus horizontal displacement of the unreinforced wall up to collapse.

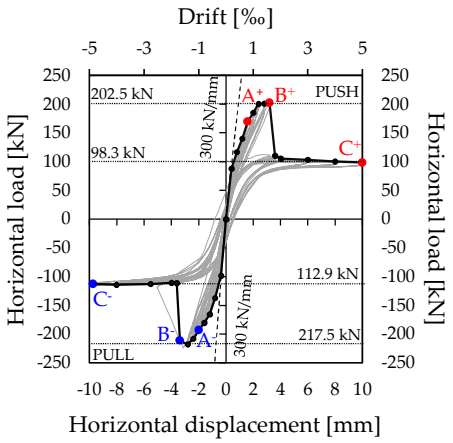

Figure 4-53: Horizontal force versus horizontal displacement: unreinforced wall.

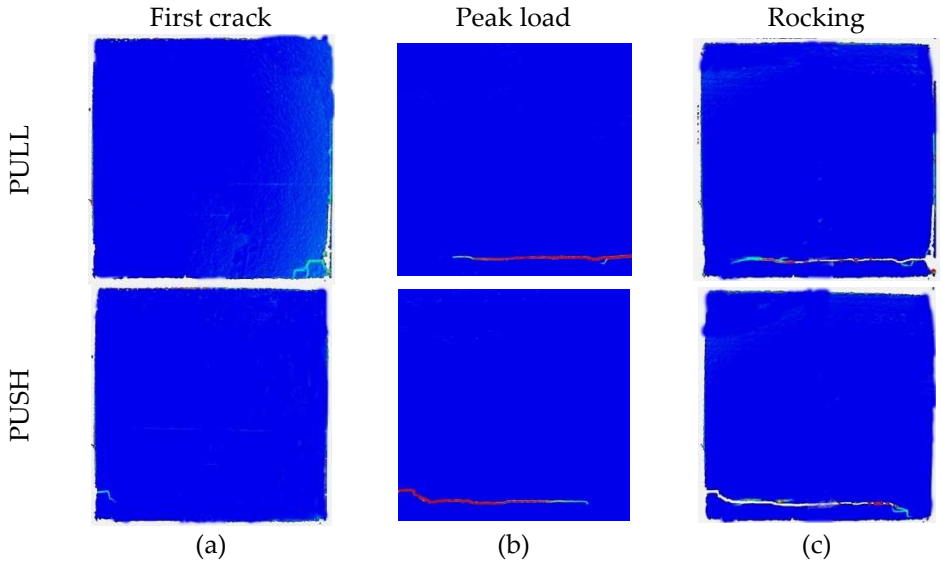

Figure 4-54: Crack pattern detected with digital image correlation: (a) first crack, (b) flexural crack at the peak load, and (c) crack pattern at the end of the test.

The performance of the structure is also described by the decrease of the in-plane stiffness (Figure 4-55) and energy dissipation capacity ξ_{eq} (Figure 4-56) over repeated cycles of increasing amplitude. Initially, the average stiffness during the first cycle (with a 0.1‰ drift) was 299.78 kN/mm. In correspondence of the first crack the secant stiffness was equal to 113.34 kN/mm at 0.8‰ drift and to 95.38 kN/mm at 1.0‰ drift for the pull and push phase, respectively. Subsequently, the secant stiffness decreased, reducing to a value of 62.67 kN/mm at 1.6‰ drift and then dropping to a

value of 11.61 kN/mm and 9.84 kN/mm at 5‰ drift when the test was stopped for the pull and push direction, respectively.

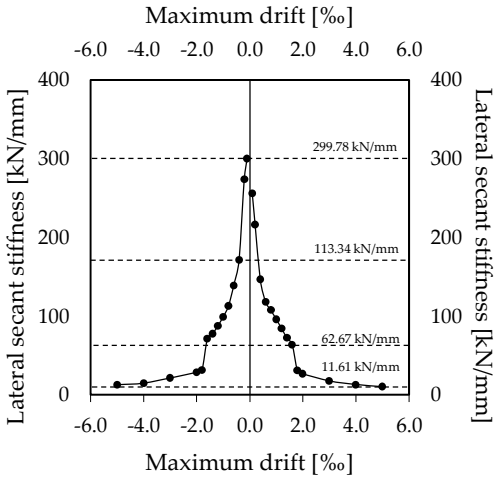

Figure 4-55: Evolution of the secant stiffness curve: unreinforced wall.

After the first load cycles, the equivalent viscous damping coefficient (ξ_{eq}) varied from 2.8% at 0.8‰ drift to 2.9% at 1.0‰ drift, displaying an overall stable behaviour. However, at 1.6‰ drift, the damping coefficient increased to 11.4% due to the occurrence of flexural failure. In the following cycles, a stable trend was observed, with a value of 5.8% at 5.0‰ drift (similarly for all repetitions of loading).

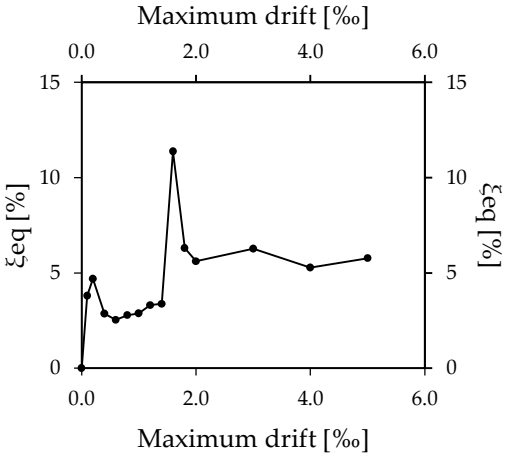

Figure 4-56: Evolution of the viscous damping coefficient: unreinforced wall.

4.5.1.2.1.2 Thermal test

Figure 4-57 shows a portion of the 3DPC unreinforced wall which was cut to be tested in a climatic chamber to assess the thermal performance [152]. The specimen had a height of 1 m, a length of 1 m and a thickness of 38.5 cm. The laboratory represents the internal environment of the building while the climatic chamber simulated the external environment. The average internal environment temperature Ti was 25°C, and the average external environment temperature Te was 60°C, with a temperature difference ΔT of 35°C. To minimize error in the flux measurement, the temperature difference was set to be as high as possible. In fact during testing, it was observed that a small temperature difference ΔT resulted in a significant error in the flux measurement. However, the difference in temperature did not impact the measurement of the thermal transmittance. To achieve one-dimensional heat flow, 10 cm of XPS insulation was placed around the specimen, and the wall cavities were sealed with plastic sheets to prevent heat loss. Four tests were conducted with different levels of insulating filling to identify the most effective (see Figure 4-58): i) no insulating material in the cavities, ii) insulating material in the external cavity, iii) insulating material in the internal triangular cavities and iv) insulating material in all the cavities. The cavities were filled with recycled cellulose fibre flakes obtained from newspapers with a thermal conductivity of 0.038 W/mK and a density of 60 kg/m^3. This material was chosen because of the low thermal conductivity and also because it is "environmental friendly" since it is derived from recycled materials. The thermal transmittance resulted to be equal to 1.58 W/m^{2}K, 0.34 W/m^{2}K, 0.32 W/m^{2}K, and 0.28 W/m^{2}K for each tested configuration, respectively.

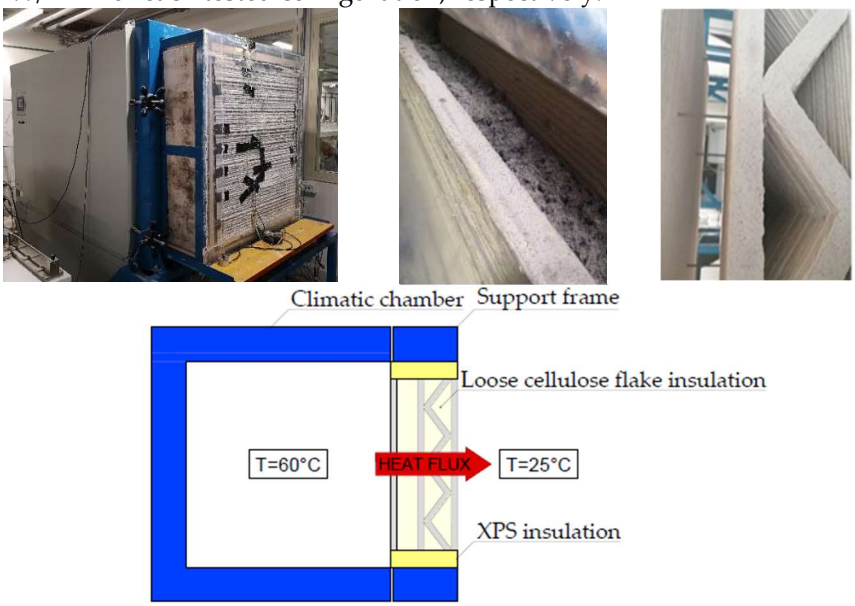

Figure 4-57: Schematic of the thermal testing.

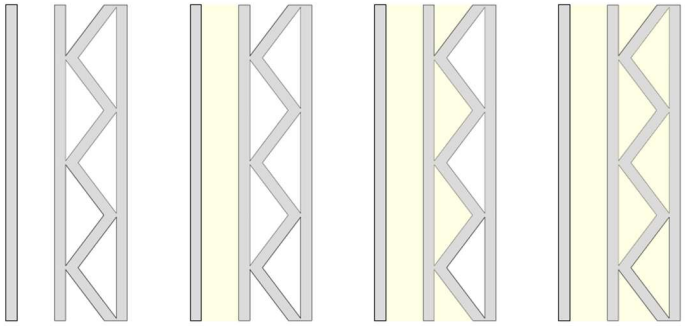

Figure 4-58: Thermal performance of 3DPC wall: tested configurations.

Considering the configuration iv) with all the cavities filled with insulating material, the experimental results were confirmed both from the analytical and numerical model proposed in section 4.2.2.1. The calculations were performed considering the scaled configuration and a thermal transmittance of 0.25 W/m²K and 0.28 W/m²K was obtained from the analytical and finite element model, respectively.
Regarding the finite element model of the thermal behaviour, the following climatic conditions were considered: indoor room temperature of 20° and outdoor room temperature of 0°. The materials used for the calculation are 3D printed concrete and cellulose flake insulation derived from newspapers. Details on the properties are provided in Table 4-2 Contour plots of thermal gradient and heat flux are shown in Figure 4-59.

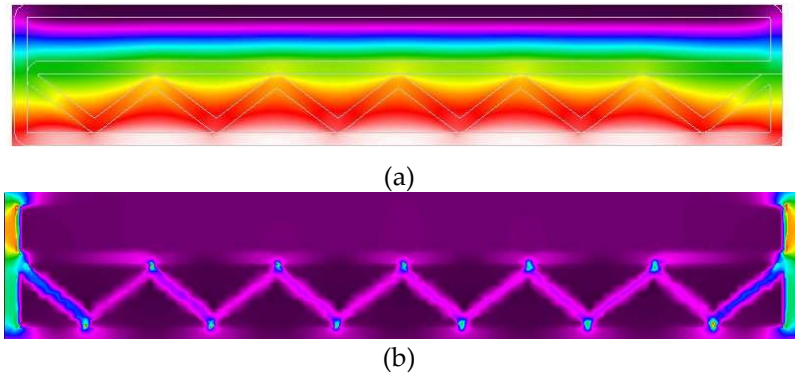

Figure 4-59: Contour plots of the FEM analysis (THERM): (a) temperature gradient and (b) heat flux.

4.5.1.2.2 Reinforced wall

The maximum recorded horizontal load was 150.48 kN (at a lateral displacement d = 1.50 mm) and -182.48 kN (at a lateral displacement d = -0.84mm) for the positive and negative loading direction, respectively.

Figure 4-60 shows the initial phase of the test. The wall exhibited an high initial stiffness of 268.98 kN/mm. The wall showed a linear elastic behaviour up to a drift of 0.25‰ (d = 0.5 mm) and a horizontal load of 134.23 kN.

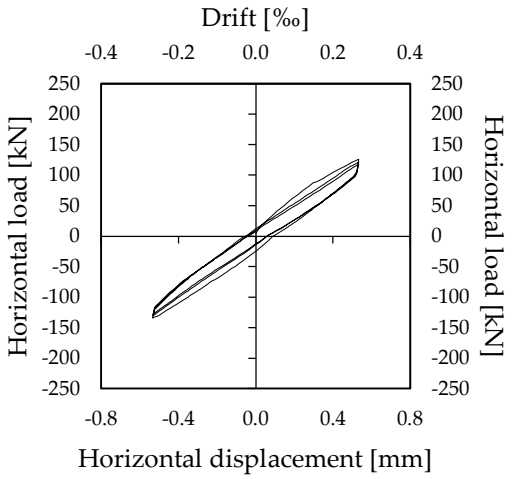

Figure 4-60: Horizontal force versus horizontal displacement of the reinforced wall during the pre-cracking phase.

Figure 4-61 shows the wall behaviour in term of applied load vs. lateral displacement in correspondence of the appearance of the crack which occurred both for the pull and push direction at drift of 0.5‰ at a load of – 182.48 kN (d = -1.49 mm) and 150.48 kN (d = 1.50 mm), respectively (see points A+ and A- in Figure 4-63). The crack pattern is shown in Figure 4-64, the crack occurred at layer 79, in correspondence of a cold joint (Figure 4-64). In fact, it has to be mentioned that during the printing process, it was necessary to stop the process due to an overheating issue for almost 45 min. The crack occurred exactly at that layer where the shear resistance was reduced by the printing interruption.

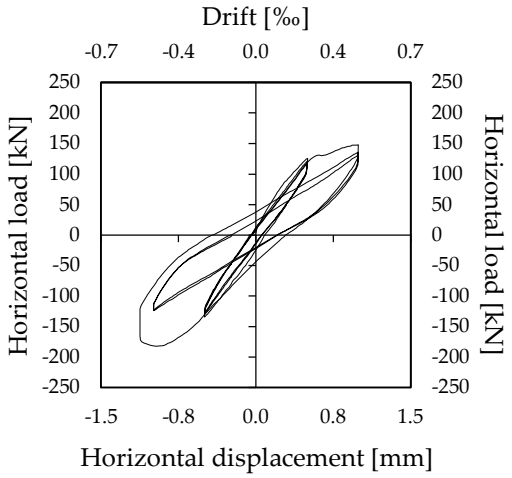

Figure 4-61: Horizontal force versus horizontal displacement of the reinforced wall up to the formation of the first crack.

After the cracking the wall exhibited a sliding mechanism along the cold joint. The test was stopped at a drift of 2‰ when the load was equal to 148.68 kN (d = 4 mm) and to -136.46 kN (d = -4 mm) for the positive and negative loading direction (see points B+ and B- in Figure 4-63) , respectively (Figure 4-62).

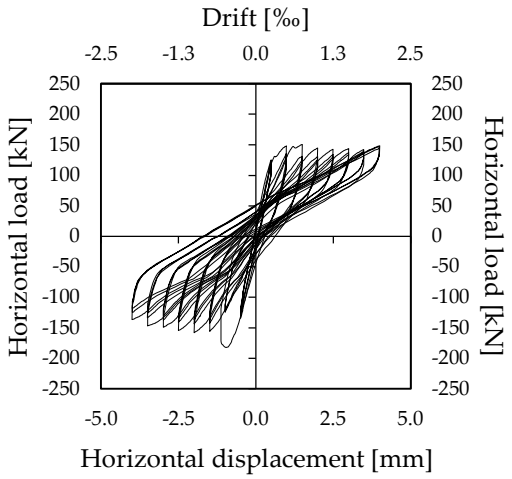

Figure 4-62: Horizontal force versus horizontal displacement of the reinforced wall up to collapse.

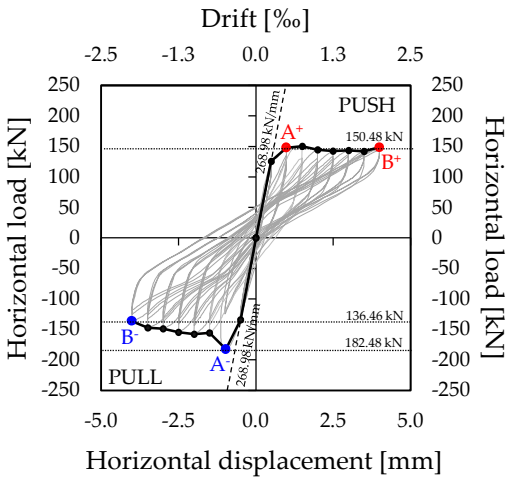

Figure 4-63: Horizontal force versus horizontal displacement: reinforced wall.

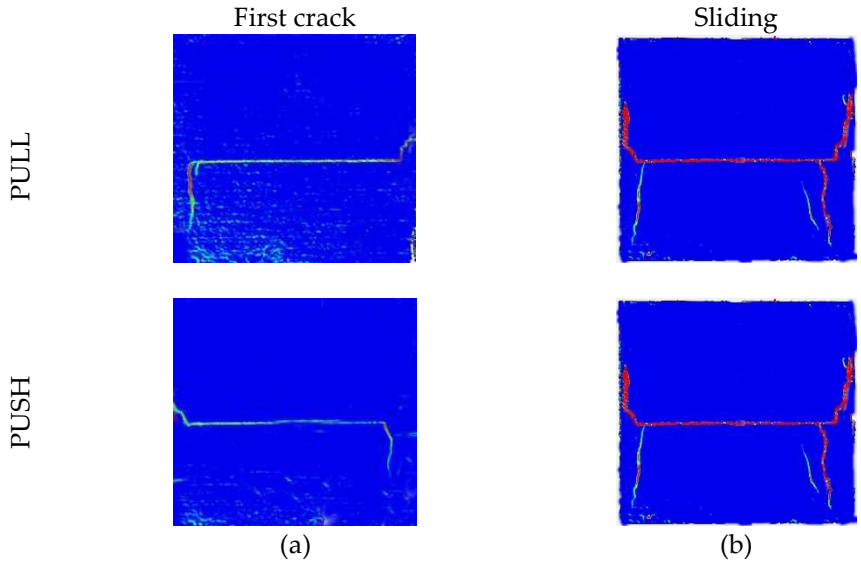

Figure 4-64: Crack pattern detected with digital image correlation: (a) first crack and (b) sliding.

The performance of the structure is also described by the decrease of the in-plane stiffness (Figure 4-65) and energy dissipation capacity ξ_{eq} (Figure 4-66) over repeated cycles of increasing amplitude. Initially, the average stiffness during the first cycle (with a 0.25‰ drift) was 268.98 kN/mm. In correspondence of the first crack the secant stiffness was equal to 188.32 kN/mm and to 148.96 kN/mm at 0.5‰ drift for the pull and push phase, respectively. Subsequently, the secant stiffness decreased,

dropping to a value of 34.11 kN/mm and 37.20 kN/mm at 2‰ drift when the test was stopped for the pull and push direction, respectively.

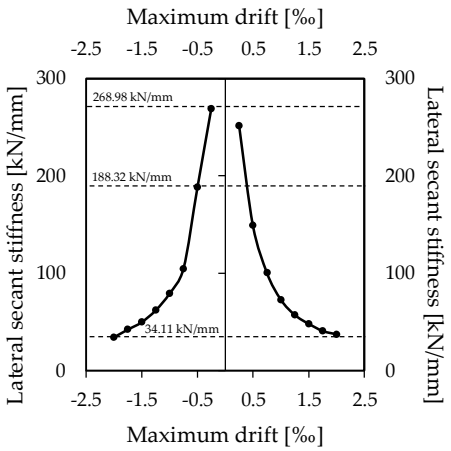

Figure 4-65: Evolution of the secant stiffness curve: reinforced wall.

After the first load cycle, the equivalent viscous damping coefficient (ξ_{eq}) was equal to 8.2% at 0.25‰. However, at 0.5‰ drift, the damping coefficient increased to 19.8% due to the occurrence of the sliding failure. In the following cycles, a stable trend was observed, with a value of 11% at 2‰ when the test was stopped.

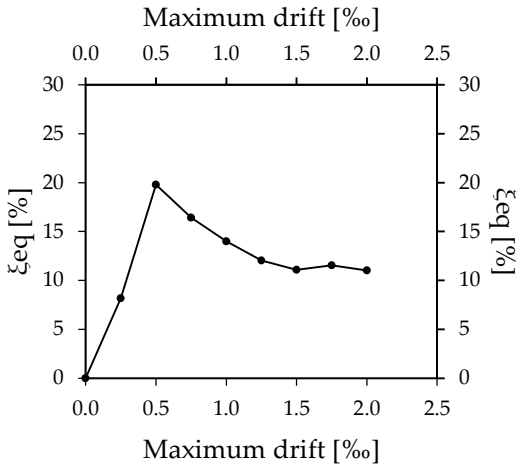

Figure 4-66: Evolution of the viscous damping coefficient: reinforced wall.

4.5.2 Analytical prediction

Analytical calculation can be used to evaluate the structural performance of 3DPC modular walls. This calculation has been validated through the experimental results presented in section 4.5.1.2.1. The model is based on simplified assumptions about the shape of the wall cross-section, using an equivalent double-T section to represent the complexity of the 3DPC wall, as illustrated in Figure 4-67 which refers to the unreinforced 3DPC wall printed with material type 2. The double-T section has a similar area and moment of inertia to the 3DPC wall cross-section; the main geometrical characteristics are given in Table 4-7.
It should be noted that in the model, the non-structural part of the wall was ignored. This is an allowable assumption since the non-structural part is connected to the structural one by two thin 3DPC concrete parts and steel connectors with low flexural stiffness. Moreover, the non-structural part is not connected to the basement foundation (see Figure 4-19). It may be expected that the outer layer does not affect the 3DPC wall structural response both in terms of strength and stiffness.

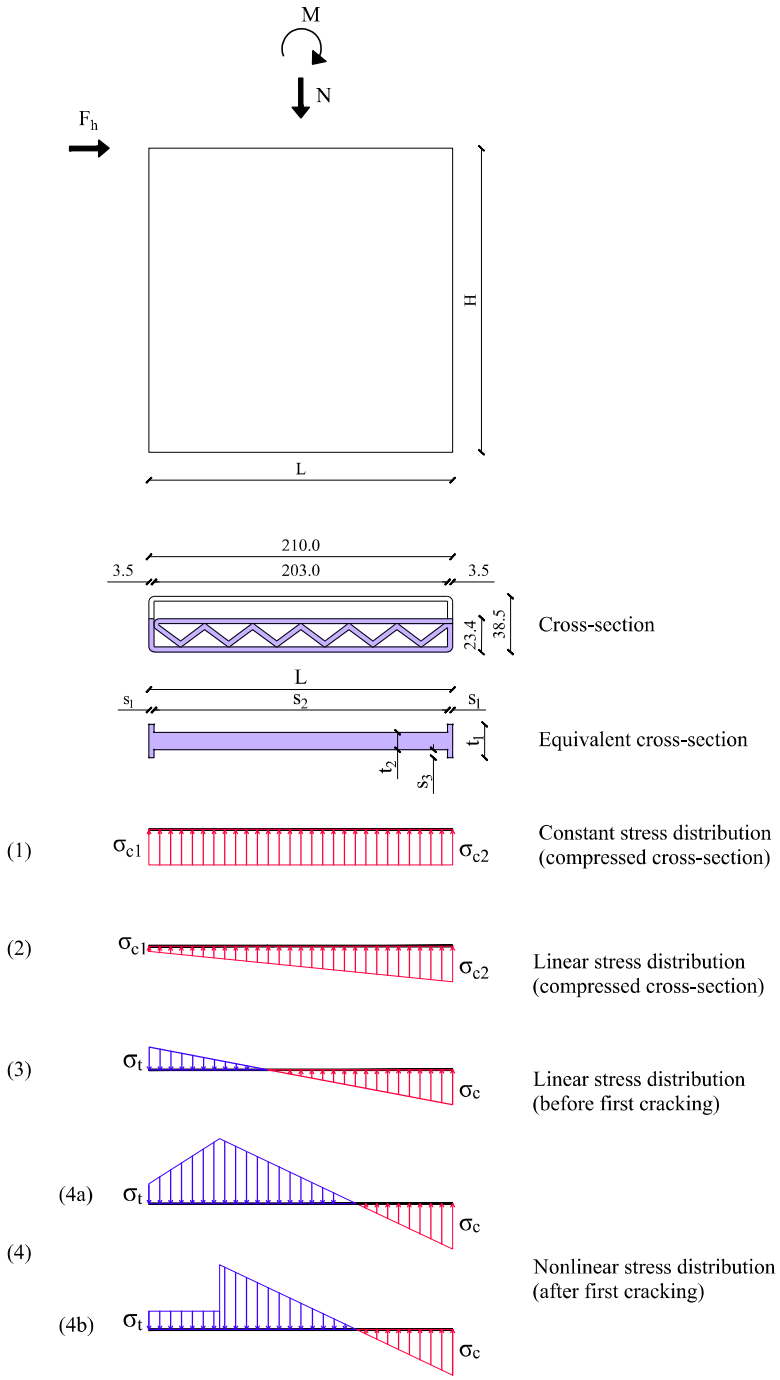

Figure 4-67: Simplified model to describe the structural performance of the 3DPC unreinforced wall.

Material	ID	L	H	t_1	t_2	s_1	s_2	A	J	$f_{cm,(90°,0°,0°)}$	$f_{ctm,(90°,0°,0°)}$
[-]	[-]	[mm]	[mm]	[mm]	[mm]	[mm]	[mm]	[mm^2]	[mm^4]	[MPa]	[MPa]
2	Unreinf	2100	2100	230	110	35	2030	239400	$9.4*10^{10}$	58	2.8
2	Reinf	2100	2100	230	110	210	1680	283000	$1.5*10^{11}$	58	2.8

Table 4-7: Geometrical properties: name of the specimen (ID), length and height of the wall (L, H), thickness of the flange (t_1), thickness of the web (t_2), length of the flange (s_1), length of the web (s_2), area of the cross-section (A), moments of inertia of the cross section (J), compressive strength of the material ($f_{cm,(90°,0°,0°)}$) and the tensile strength of the material ($f_{ctm,(90°,0°,0°)}$).

The generic section of the 3DPC wall undergoes different stresses distributions as the applied horizontal load increases, as shown in Figure 4-67. In the following, simplified stresses distributions are assumed. Initially, the stresses distribution is constant due to the application of the vertical load (configuration 1). After the application of the horizontal load, the stresses distribution is trapezoidal (configuration 2), with the entire section under compression. When the neutral axis crosses the wall cross-section, the wall is subjected to both tensile and compressive stresses with a linear distribution (configuration 3) until the maximum tensile strength $f_{ctm,(90°,0°,0°)}$ (see Table 3-21) of the 3D printed material is reached (point A Figure 4-68). Thereafter, a reduction in stiffness is observed and the stresses distribution becomes non-linear, and its configuration depends on the constitutive law adopted for the material (configuration 4). Within this study, an elasto-plastic law in compression is adopted, while in tension, a linear behaviour up to the maximum tensile strength and two post-peak alternative branches are investigated: 4a) linear and 4b) constant with reduced strength. The re-distribution of the tensile stresses continues up to the ultimate tensile strain (corresponding to the formation of a major crack) in correspondence of the maximum flexural strength (point B in Figure 4-68)). Taking into account the different stresses configurations (as shown in *Figure 4-67*and Figure 4-68)), the moment-curvature relationship of the wall cross-section can be determined by varying the deformation profile of the cross-section (the position of the neutral axis), as shown in Figure 4-68)a. Subsequently, knowing the moment profile along the height of the wall, the corresponding curvature profile can be derived using the previously evaluated moment-curvature relationship. Successively, the curvature is integrated twice (the curvature is the second order derivative of the displacement) over the height of the specimen to derive the flexural component of the top displacement. As a consequence, the force-displacement capacity curve of the wall is obtained until the maximum lateral strength of the 3DPC wall (point B), see Figure 4-68b.

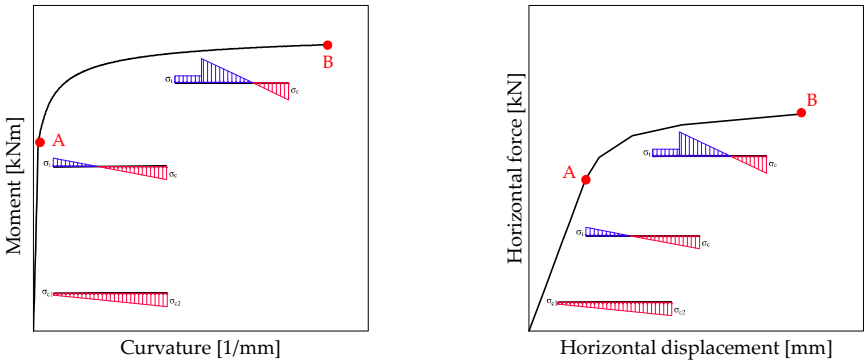

(a) (b)

Figure 4-68: Stresses configuration variation of a 3DPC unreinforced wall considering :(a) moment-curvature and (b) force-displacement.

Figure 4-69, *Figure 4-70*, *Figure 4-72* and Figure 4-74 show the stresses distribution together with the analytical calculations used to derive the moment-curvature trend of the cross-section of the wall.
Considering configuration 2, the moment- curvature trend can be derived as follows:

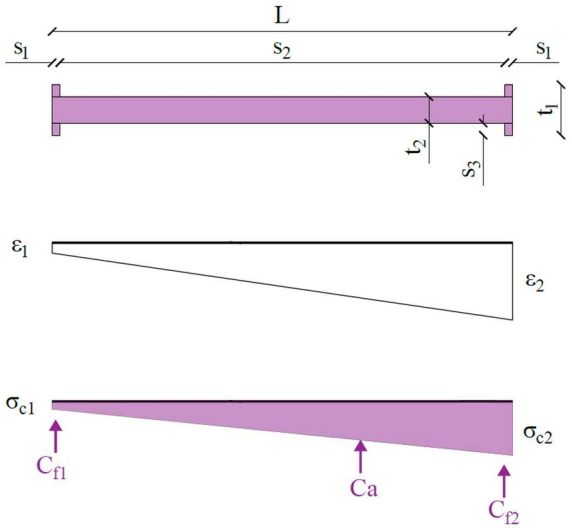

Figure 4-69: Fully compressed cross-section (configuration 2).

By varying the strain ε_1, the vertical equilibrium of the forces for a given value of the vertical load N allows to determine the value of strain ε_2:

$$N = C_a + C_{f1} + C_{f2} \quad 4\text{-}6$$

$$N = (\varepsilon_1 E L t_2 + \frac{(\varepsilon_2 - \varepsilon_1) E L t_2}{2}) + 2E\varepsilon_1 s_1 s_3 + 2E\varepsilon_2 s_1 s_3 \quad 4\text{-}7$$

Where E is the elastic modulus of the 3D printed material (see Table 3-30), L is the length and t is the thickness of the wall.
From the equation 4-7 the value of the strain ε_2 is calculated as:

$$\varepsilon_2 = \frac{2N - \varepsilon_1 E L t_2 - 4E\varepsilon_1 s_1 s_3}{E L t_2 + 4E s_1 s_3} \quad 4\text{-}8$$

By imposing the rotational equilibrium with respect to the middle of the cross-section, it is possible to derive the correspondent bending moment M:

$$M = Ne = \frac{(\varepsilon_2 - \varepsilon_1) E L t_2}{2} * \left(\frac{L}{2} - \frac{L}{3}\right) + 2E\varepsilon_1 s_1 s_3 * \left(\frac{L}{2} - \frac{s_1}{2}\right) + 2E\varepsilon_2 s_1 s_3 * \left(\frac{L}{2} - \frac{s_1}{2}\right) \quad 4\text{-}9$$

The curvature is calculated as:

$$\theta = \frac{\varepsilon_1 + \varepsilon_2}{L} \quad 4\text{-}10$$

When the neutral axis crosses the cross-section of the wall, the wall is subjected to tensile and compressive stresses with a linear distribution, as shown in *Figure 4-70*.

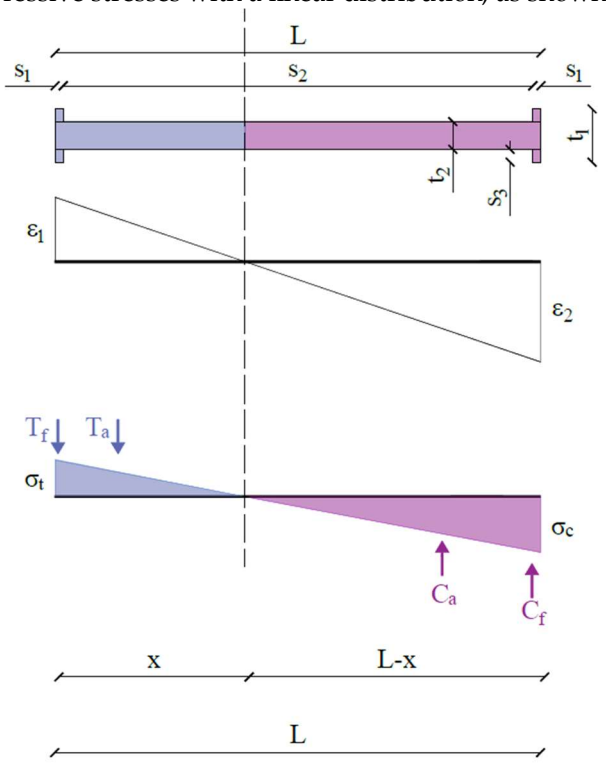

Figure 4-70: Cross section subjected to tensile and compressive stresses before the maximum tensile strength (configuration 3).

By varying the tensile strain ε_1, the vertical equilibrium of the forces for a given value of the vertical load N allows to determine the value of the compressive strain ε_2:

$$N = C - T = \left(C_a + C_f\right) - \left(T_a + T_f\right) \quad 4\text{-}11$$

$$N = \frac{\varepsilon_2 E(L-x)t_2}{2} + 2E\varepsilon_2 s_1 s_3 - \frac{\varepsilon_1 E x t_2}{2} - 2E\varepsilon_1 s_1 s_3 \quad 4\text{-}12$$

By imposing the triangle similarity, the neutral axis is calculated as:

$$\frac{\varepsilon_1}{x} = \frac{\varepsilon_2}{L-x}$$
$$x = \frac{\varepsilon_1}{\varepsilon_1 + \varepsilon_2} L \quad 4\text{-}13$$

By substituting eq.4-13 in 4-12 a second order equation is obtained to estimate the strain ε_2:

$$(ELt_2 + 4Es_1 s_3)\varepsilon_2^2 - 2N\varepsilon_2 - 2\varepsilon_1 N - ELt_2\varepsilon_1^2 - 4Es_1 s_3 \varepsilon_1^2 = 0$$
$$\Delta = (-2N)^2 - 4(ELt_2 + 4Es_1 s_3)(-2\varepsilon_1 N - ELt_2\varepsilon_1^2 - 4Es_1 s_3 \varepsilon_1^2) \quad 4\text{-}14$$
$$\varepsilon_{2a,b} = \frac{2N \pm \sqrt{\Delta}}{2(ELt_2 + 4Es_1 s_3)}$$

By imposing the rotational equilibrium with respect to the middle of the cross-section, the correspondent bending moment M is derived:

$$M = Ne = \frac{\varepsilon_2 E(L-x)t_2}{2}\left(\frac{L}{2} - \frac{L-x}{3}\right) + \frac{E\varepsilon_1 x t_2}{2}\left(\frac{L}{2} - \frac{x}{3}\right) + 2\mathrm{E}\varepsilon_1 s_1 s_3 * \left(\frac{L}{2} - \frac{s_1}{2}\right) + 2\mathrm{E}\varepsilon_2 s_1 s_3 * \left(\frac{L}{2} - \frac{s_1}{2}\right) \quad 4\text{-}15$$

The correspondent curvature can be found by applying eq.4-10.

After the maximum tensile strength $f_{ctm,(90°,0°,0°)}$ of the material is reached, the distribution of stresses becomes non-linear and it depends on the constitutive laws employed for the material (configuration 4). Firstly, a linear tensile [153] and a compressive elasto- plastic constitutive law are investigated (Figure 4-71).

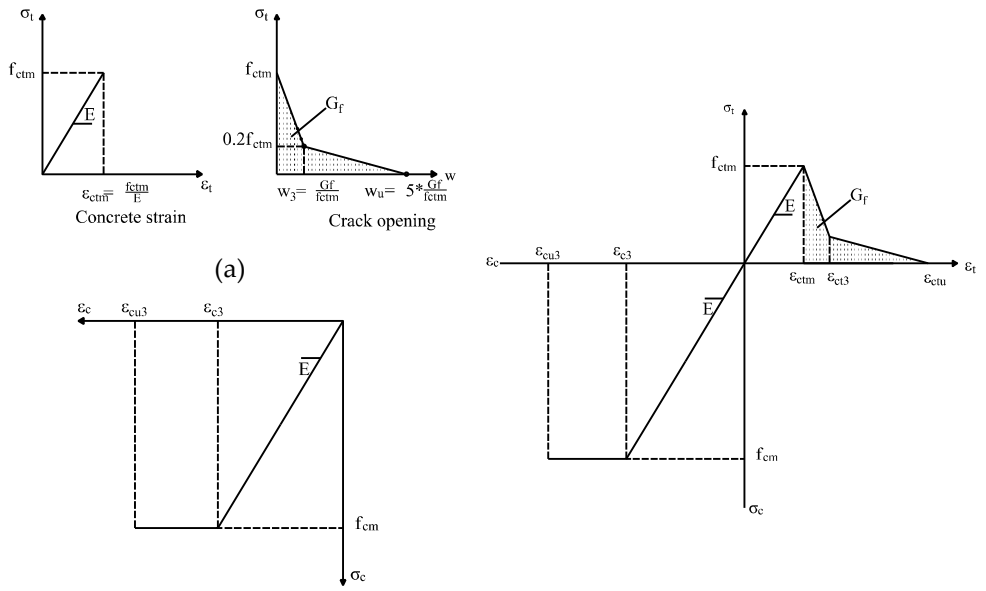

Figure 4-71: Constitutive law: (a) tensile linear constitutive law in terms of stress-strain and stress-crack opening; (b) compressive elasto-plastic constitutive law; (c) constitutive law adopted in tension and compression in terms of stress-strain.

The tensile linear constitutive law is defined as (Figure 4-71a):

$$\sigma_t = \varepsilon_1 * E \qquad \text{for } \varepsilon < \varepsilon_{ctm}$$

$$\sigma_t = f_{ctm} * (1 - 0.8\frac{w}{w_3}) \qquad \text{for } w < w_3 \qquad \text{4-16 [153]}$$

$$\sigma_t = f_{ctm} * (0.25 - 0.05\frac{w}{w_3}) \qquad \text{for } w_3 < w < w_u$$

Where σ_t is the tensile stress, f_{ctm} is the maximum tensile strength of the 3D printed material (see Table 3-21), ε_1 is the tensile strain and w is the crack opening. The crack opening is calculated as:

$$w_3 = \frac{G_f}{f_{ctm}}$$
$$w_u = 5 * \frac{G_f}{f_{ctm}} \qquad \text{4-17}$$

Where G_f is the fracture energy calculated as [153]:

$$G_f = 73 * (f_{cm})^{0.18} \qquad \text{4-18}$$

Where f_{cm} is the compressive strength of the 3D printed material (see Table 3-10).

The tensile constitutive law after the maximum tensile strength f_{ctm} is expressed in terms of stress-crack opening (Figure 4-71a). In order to express it in terms of stress-strain, the crack opening has to be divided by a structural characteristic length l_{cr}, which is assumed to be equal to the thickness of the layer, equal 10 mm considering the unreinforced 3DPC wall printed with material type 2. This is a reasonable assumption because cracks are likely to occur at the interfaces, as observed in the experimental test. So the ultimate strain ε_{ctu}, necessary to define the linear tensile constitutive law, is calculated as:

$$\varepsilon_{ctu} = \frac{w_u}{l_{cr}} \qquad 4\text{-}19$$

The compressive elasto-plastic constitutive law is defined as:

$$\sigma_c = \varepsilon_2 * E \quad \text{for } \varepsilon < \varepsilon_{c3}$$
$$\sigma_c = f_{cm} \quad \text{for } \varepsilon_{c3} < \varepsilon < \varepsilon_{cu3} \qquad 4\text{-}20$$

Where f_c is the compressive stress, f_{cm} is the compressive strength of the 3D printed material (see Table 3-10), ε_2 is the compressive strain, ε_{c3} is a concrete strain equal to 1.75‰ and ε_{cu} is the ultimate compressive strain in concrete equal to 3.5‰ (see Table 3.1 of Eurocode 2 [110]).

*Figure 4-72*a shows the stresses distribution for $w<w_3$ and *Figure 4-72*b for $w_3<w<w_u$,.

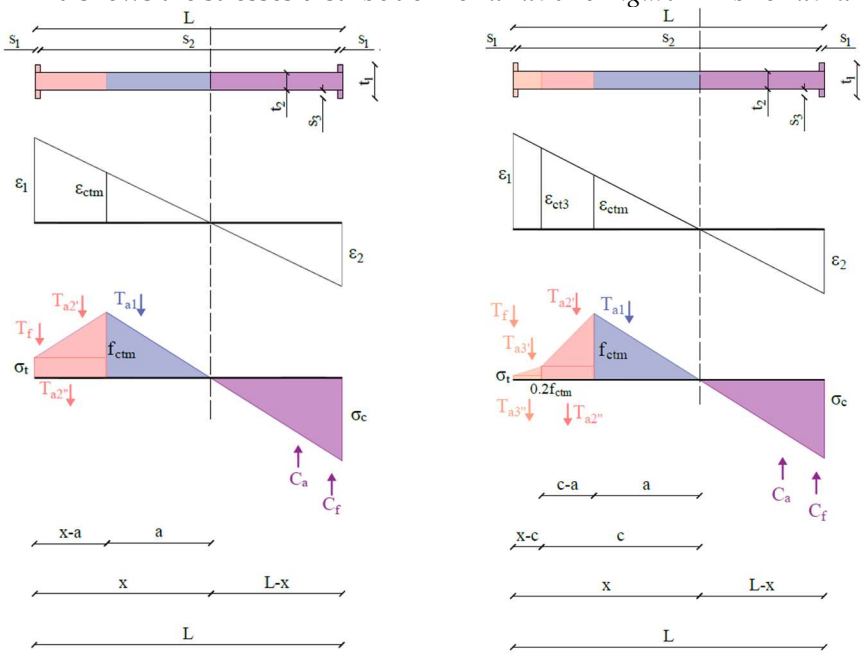

Figure 4-72: Stresses distribution of the cross-section of the wall: (a) $w<w_3$ and (b) $w_3<w<w_u$.

Considering the configuration in Figure 4-72a, by varying the tensile strain ε_1, the vertical equilibrium of the forces for a given value of the vertical load N allows to determine the value of the compressive strain ε_2:

$$N = C - T_1 - T_2 = (C_a + C_f) - T_{a1} - (T_{a2'} + T_{a2''} + T_f) \quad 4\text{-}21$$

$$N = \frac{\varepsilon_2 E(L-x)t_2}{2} + 2E\varepsilon_2 s_1 s_3 - \frac{f_{ctm} a t_2}{2} - \frac{(f_{ctm} - \sigma_t)(x-a)t_2}{2} - \sigma_t(x-a)t_2 - 2E\varepsilon_1 s_1 s_3 \quad 4\text{-}22$$

The neutral axis is obtained according to eq. 4-13 and by imposing the triangle similarity, it is possible to find the length *a:*

$$\frac{\varepsilon_{ctm}}{a} = \frac{\varepsilon_1}{x}$$
$$a = \frac{\varepsilon_{ctm}}{\varepsilon_1 + \varepsilon_2} L \quad 4\text{-}23$$

By substituting eq. 4-23 in 4-22, a second order equation to estimate the strain ε_2 is obtained:

$$(ELt_2 + 4Es_1 s_3)\varepsilon_2^2 - 2N\varepsilon_2 - 2\varepsilon_1 N - \sigma_t t_2 \varepsilon_1 L + \sigma_t t_2 \varepsilon_{ctm} L - f_{ctm} t_2 \varepsilon_1 L - 4Es_1 s_3 \varepsilon_1^2 = 0$$

$$\Delta = (-2N)^2 - 4(ELt_2 + 4Es_1 s_3)(-2\varepsilon_1 N - \sigma_t t_2 \varepsilon_1 L + \sigma_t t_2 \varepsilon_{ctm} L - f_{ctm} t_2 \varepsilon_1 L - 4Ets_1 s_3 \varepsilon_1^2) \quad 4\text{-}24$$

$$\varepsilon_{2a,b} = \frac{2N \pm \sqrt{\Delta}}{2(ELt + 4Es_1 s_3)}$$

By imposing the rotational equilibrium with respect to the middle of the cross-section the correspondent bending moment M is derived:

$$M = Ne = C_a\left(\frac{L}{2} - \frac{L-x}{3}\right) + C_f\left(\frac{L}{2} - \frac{s_1}{2}\right) + T_{a1}\left(\frac{L}{2} - (x-a) - \frac{a}{3}\right) + T_{a2'}\left(\frac{L}{2} - \frac{2}{3}(x-a)\right) + T_{a2''}\left(\frac{L}{2} - \frac{x-a}{2}\right) + T_f\left(\frac{L}{2} - \frac{s_1}{2}\right) \quad 4\text{-}25$$

The correspondent curvature can be calculated with eq.4-10.

In addition considering *Figure 4-72*b, by varying the tensile strain ε_1, the vertical equilibrium of the forces for a given value of the vertical load N allows to determine the value of the compressive strain ε_2:

$$N = C_a + C_f - T_{a1} - T_{a2'} - T_{a2''} - T_{a3'} - T_{a3''} - T_f \quad 4\text{-}26$$

$$N = \frac{\varepsilon_2 E(L-x)t_2}{2} + 2E\varepsilon_2 s_1 s_3 - \frac{f_{ctm} a t_2}{2} - \frac{(f_{ctm} - 0.2f_{ctm})(c-a)t_2}{2} - 0.2f_{ctm}(c-a)t_2 - \sigma_t(x-c)t_2 - \frac{(0.2f_{ctm} - \sigma_t)(x-c)t_2}{2} - 2E\varepsilon_1 s_1 s_3 \quad 4\text{-}27$$

By imposing the rotational equilibrium with respect to the middle of the cross-section it is possible to obtain the correspondent bending moment:

$$M = Ne = C_a\left(\frac{L}{2} - \frac{L-x}{3}\right) + C_f\left(\frac{L}{2} - \frac{s_1}{2}\right) + T_{a1}\left(\frac{L}{2} - (x-c) - (c-a) - \frac{a}{3}\right) + T_{a2'}\left(\frac{L}{2} - (x-c) - \frac{2}{3}(c-a)\right) + T_{a2''}\left(\frac{L}{2} - (x-c) - \frac{c-a}{2}\right) + T_{a3''}\left(\frac{L}{2} - \frac{x-c}{2}\right) + T_{a3'}\left(\frac{L}{2} - \frac{2}{3}(x-c) + T_f\left(\frac{L}{2} - \frac{s_1}{2}\right)\right) \quad 4\text{-}28$$

Applying the previous equations, it is possible to derive the moment-curvature relationship and the corresponding force-displacement curve of the wall (integrating the curvature twice along the height of the wall), as shown in Figure 4-73. The analytical curve (black line in Figure 4-73b) does not approximate well the experimental curve (red line in Figure 4-73b, Exp^+ refers to the envelope in the push and Exp^- in the pull direction respectively), showing an overestimation both in terms of strength and stiffness.

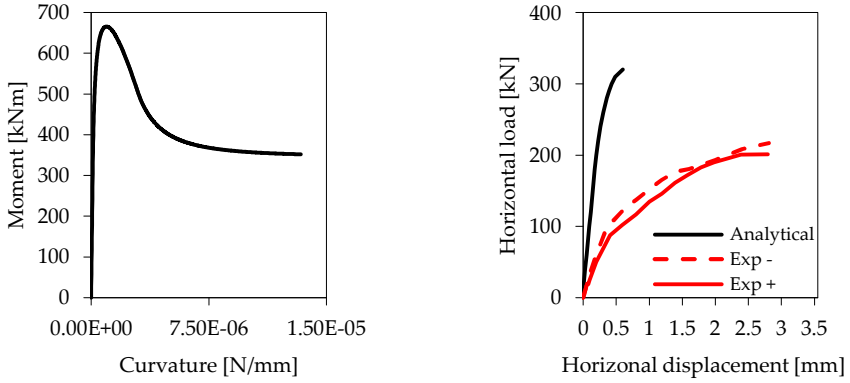

(a) (b)

Figure 4-73: Linear tensile constitutive law and compressive elasto-plastic law: (a) Moment-curvature and (b) horizontal force- horizontal displacement capacity.

Consequently, a different constitutive law is employed, which is elasto-plastic in compression and linear in tension up to the tensile strength with a constant post-peak branch, as shown in Figure 4-74.

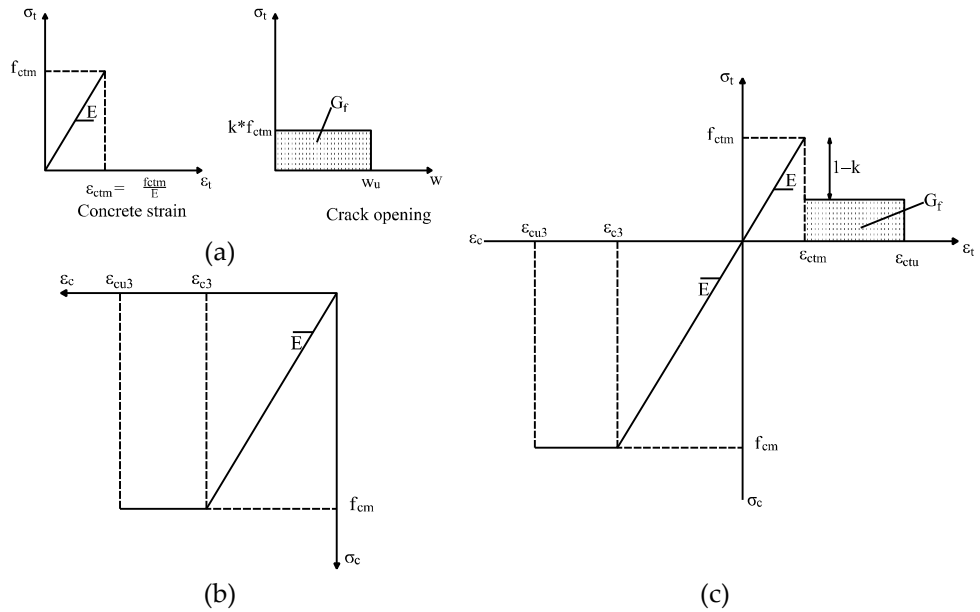

Figure 4-74: Constitutive law: (a) tensile linear constitutive law with a constant post-peak branch in terms of stress-strain and stress-crack opening; (b) compressive elasto-plastic constitutive law; (c) constitutive law adopted in tension and comperssion in terms of stress-strain.

The tensile constitutive law is defined as (Figure 4-74a):

$$\sigma_t = \varepsilon_1 * E \qquad \text{for } \varepsilon < \varepsilon_{ctm}$$
$$\sigma_t = k * f_{ctm} \qquad \text{for } w < w_u \qquad \text{4-29}$$

Where E is the elastic modulus of the 3D printed material (see Table 3-30), f_{ctm} is the tensile strength of the 3D printed material (Table 3-21), k is a reductive coefficient, ε_1 is the tensile strain, $\varepsilon_{ctm} = f_{ctm}/E$ is the strain in correspondence of the maximum tensile strength and w_u is the ultimate crack opening defined as (Figure 4-74a):

$$w_u = \frac{G_f}{k * f_{ctm}} \qquad \text{4-30}$$

Where G_f is the fracture energy calculated with equation 4-18.
In order to express the tensile constitutive law in terms of stress-strain for $\varepsilon > \varepsilon_{ct}$ the tensile ultimate strain is calculated as $\varepsilon_u = w_u/l_{cr}$, according to equation 4-24. As in the previous case the structural characteristic length l_{cr} is set equal to the thickness of the printed layer 10 mm. The compressive elasto-plastic constitutive law is defined according to equation 4-20. Figure 4-75 shows the stresses distribution.

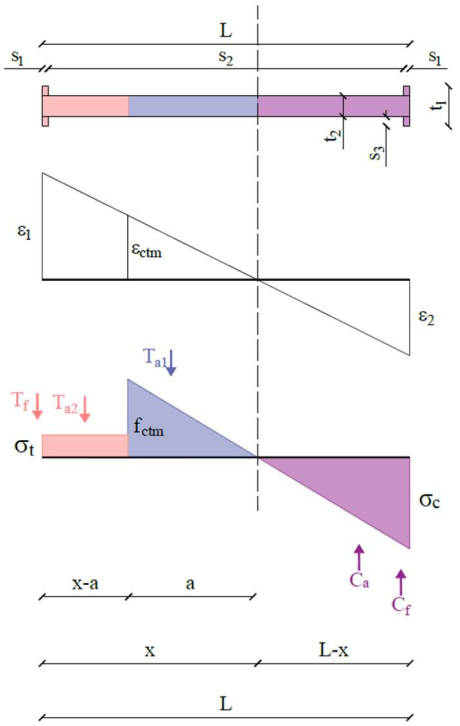

Figure 4-75: Stresses distribution of the cross-section of the wall.

By varying the tensile strain ε_1, the vertical equilibrium of the forces for a given value of the vertical load N allows to determine the value of the compressive strain ε_2:

$$N = C_a + C_f - T_{a1} - T_{a2} - T_f \quad 4\text{-}31$$

$$N = \frac{\varepsilon_2 E(L-x)t_2}{2} + 2E\varepsilon_2 s_1 s_3 - \frac{f_{ctm} a t_2}{2} - \sigma_t(x-a)t_2 - 2\sigma_t s_1 s_3 \quad 4\text{-}32$$

The neutral axis is calculated with eq. 4-13 and a with equation 4-23; by substituting in equation 4-32, a second order equation is obtained to estimate the compressive strain ε_2:

$$(ELt_2 + 4Es_1s_3)\varepsilon_2^2 + (-2N + 4\varepsilon_1 Es_1s_3 - 4\sigma_t s_1 s_3)\varepsilon_2 - 2\varepsilon_1 N - 2\sigma_t\varepsilon_1 Lt_2 + 2\sigma_t\varepsilon_{ctm}Lt_2 - \varepsilon_{ctm}^2 ELt_2 - 4\sigma_t s_1 s_3\varepsilon_1 = 0$$

$$\Delta = (-2N + 4\varepsilon_1 Es_1s_3 - 4\sigma_t s_1 s_3)^2 - 4(ELt_2 + 4Es_1s_3)(-2\varepsilon_1 N - 2\sigma_t\varepsilon_1 Lt_2 + 2\sigma_t\varepsilon_{ctm}Lt_2 - \varepsilon_{ctm}^2 ELt_2 - 4\sigma_t s_1 s_3\varepsilon_1) \quad 4\text{-}33$$

$$\varepsilon_{2a,b} = \frac{(2N - 4\varepsilon_1 Es_1s_3 + 4\sigma_t s_1 s_3) \pm \sqrt{\Delta}}{2(ELt_2 + 4\sigma_t s_1 s_3)}$$

By imposing the rotational equilibrium with respect to the middle of the cross-section, the bending moment *M* is calculated as:

$$M = Ne = C_a\left(\frac{L}{2} - \frac{L-x}{3}\right) + C_f\left(\frac{L}{2} - \frac{s_1}{2}\right)T_{a1}\left(\frac{L}{2} - (x-a) - \frac{a}{3}\right) + T_{a2}\left(\frac{L}{2} - \frac{x-a}{2}\right) + T_f\left(\frac{L}{2} - \frac{s_1}{2}\right) \quad 4\text{-}34$$

The curvature can be found by applying eq.4-10.

By applying equations from 4-31 to 4-34, the moment-curvature relationship and force-displacement curve of the wall (integrating the curvature twice along the height of the wall) can be derived, as shown in Figure 4-76a and b, respectively. A parametric study is conducted to determine the value of the reductive coefficient *k* that provides a good approximation of the maximum strength of the 3D printed wall. However, the analytical curves (indicated in black and grey in Figure 4-76b) resulted in an overestimation of the stiffness of the experimental curve (indicated in red in Figure 4-76b, Exp^+ refers to the envelope in the push and Exp^- in the pull direction respectively).

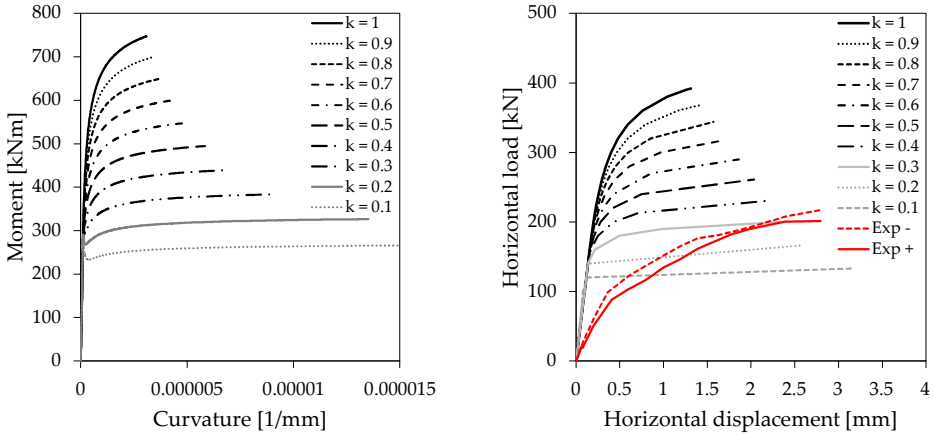

(a) (b)

Figure 4-76: Linear tensile with a constant post-peak branch and compressive elasto-plastic constitutive law: (a) moment – curvature and (b) horizontal force- horizontal displacement.

To account for reduction in stiffness, shear deformations and sliding between layers (Figure 4-77), are added to the flexural deformation.

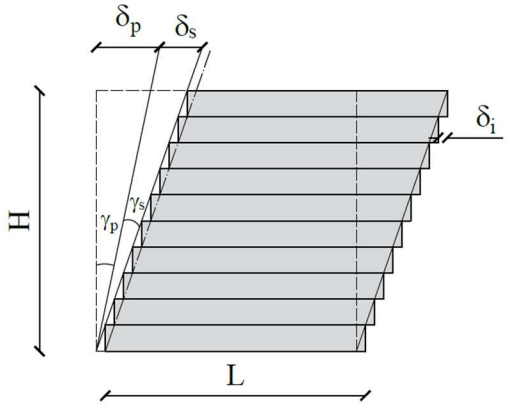

Figure 4-77: Shear deformation and sliding between the layers of the 3DPC wall.

The displacement at the top of the wall is determined by:

$$\delta_{tot} = \delta_{flexure} + \delta_{poisson} + \delta_{sliding} \quad 4\text{-}35$$

where $\delta_{flexure}$ is the displacement due to flexural deformation, $\delta_{poisson}$ is the displacement due to the shear deformation of the material and $\delta_{sliding}$ is the displacement due to the sliding between the layers.

The relative displacement between layers is estimated through the modified push-out tests on printed specimens (Figure 3-31), as discussed in Section 3-9. As mentioned in section 4.5.1.2.1, the 3DPC wall is subjected to a constant vertical load of 200 kN, corresponding to a vertical stress of about 1 MPa, and a maximum horizontal force of 220 kN, which results in a shear stress of about 0.9 MPa. Therefore, the results of the modified push-out test with 1 MPa prestress are used (Figure 3-31b). Figure 4-78a illustrates the results of the modified push-out test with application of a prestress of 1 MPa, showing that in correspondence of the maximum shear stress acting on the wall, equal to 0.9 MPa, the relative displacement between layers is equal to 0.003 mm (Figure 4-78b). From the modified push-out tests it resulted that the stiffness between the layers is about 300 kN/mm^3 ,which is the same value used to calibrate the interface between layers (of the specimens printed using material type 2) using the Finite Element software DIANA FEA, see section 5.2 (Table 5-8).

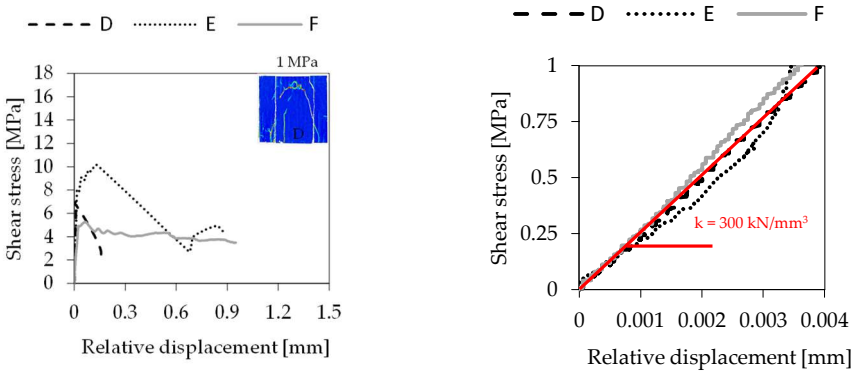

(a) (b)

Figure 4-78: (a) Shear stress versus relative displacement of the push-out test with 1 MPa lateral stress applied; (b) focus on the initial branch of the stress-strain relationship up to the maximum shear stress acting on the wall.

The wall can be represented as a system of spring in series as shown in Figure 4-79a. Multiplying the shear stress (Figure 4-78b) by the cross-sectional area of the single layer of the wall (see Table 4-7), it is possible to derive the force versus relative displacement diagram to estimate the stiffness of the single layer k_{si} (Figure 4-79b).

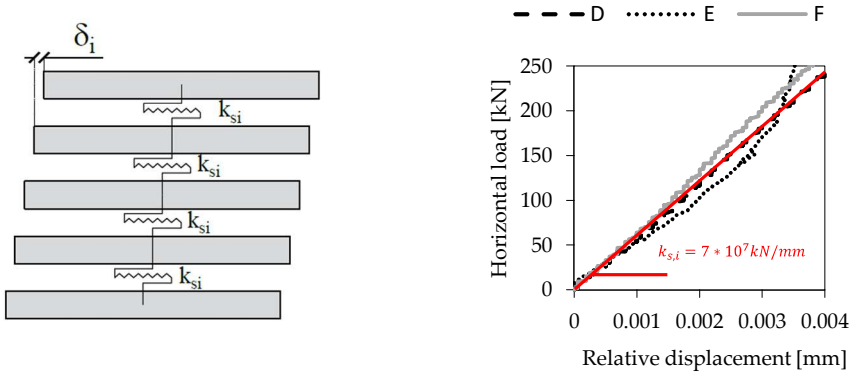

(a) (b)

Figure 4-79: (a) 3DPC wall as a system of spring in series; (b) force versus relative displacement of a single layer of the wall.

The displacement due to the shear is given by

$$\delta_{shear} = \delta_{poisson} + \delta_{sliding} = F\left(\frac{1}{k_{poisson}} + \frac{1}{k_{sliding}}\right) \quad 4\text{-}36$$

With $k_{poisson}$ and $k_{sliding}$ which are the stiffness due to the shear deformation of the material and to the sliding between the layers, estimated as:

$$k_{poisson} = \frac{G_\nu A}{\chi H} \quad 4\text{-}37$$

$$k_{sliding} = \frac{G_s A}{H} \quad 4\text{-}38$$

Where A is the area of the cross section of the wall, H is the height of the wall, $G\nu$ is the shear modulus due to the shear deformation and Gs is the shear modulus due to sliding.
The shear modulus Gν is evaluated as:

$$G_\nu = \frac{E}{2(1+\nu)} \quad 4\text{-}39$$

Where ν is the Poisson coefficient of concrete and is assumed to be equal to 0.2.
The shear modulus G_s can be estimated as:

$$\frac{F}{A} = \tau = G_s * \gamma_s \quad 4\text{-}40$$

Where γ_s is the rotation due to sliding, as consequence the previous equation can be rewritten as:

$$\frac{F}{A} = \tau = G_s * \frac{\delta_{sliding}}{H} \quad 4\text{-}41$$

Where:

$$\delta_{sliding} = n_s * \delta_i = n_s * \frac{F}{k_{s,i}} \quad 4\text{-}42$$

Where n_s is the number of layers of the wall and δ_i is the relative displacement between two layers.
By substituting equation 4-42 in 4-41 the shear modulus G_s is estimated as:

$$G_s = \frac{H\, k_{s,i}}{n_s A} = t_s \frac{k_{s,i}}{A} \quad 4\text{-}43$$

Where t_s is the thickness of the layer.
Figure 4-80 shows the force-displacement curve with the addition of the shear deformation. It can be noted that the experimental (in red in Figure 4-80, Exp^+ refers to the envelope in the push and Exp^- in the pull direction respectively) and analytical (indicated in black and grey in Figure 4-76b) stiffness are in good agreement.

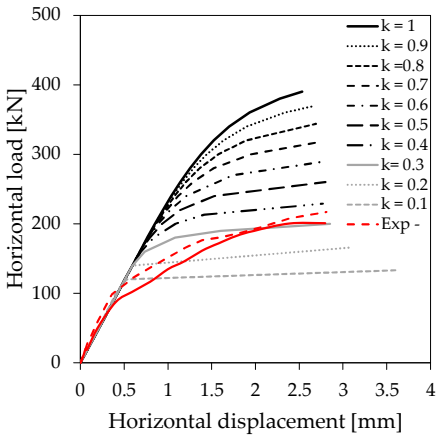

Figure 4-80: Force-displacement curve obtained using a linear tensile with constant post-peak branch and a compressive elasto-plastic constitutive law with addition of the shear deformation.

Figure 4-81 illustrates the moment-curvature and the force-displacement relationship for a reductive factor value of k = 0.3, which provides a good approximation of the experimental curve. The analytical and experimental curves show comparable stiffness and maximum strength, which is equal to 200 kN and +202.5/-217.5kN considering the analytical and experimental results, respectively. Strains and stresses are plotted at specific stages: in correspondence of point A the wall undergo both tensile and compressive stresses; at point B the maximum tensile strength, which corresponds to the first cracking, is achieved; point C represents an intermediate stage, and point D corresponds to the maximum strength. It has to be pointed out that in correspondence of point D the compressive stress σ_c is lower than the compressive strength f_{cm}.

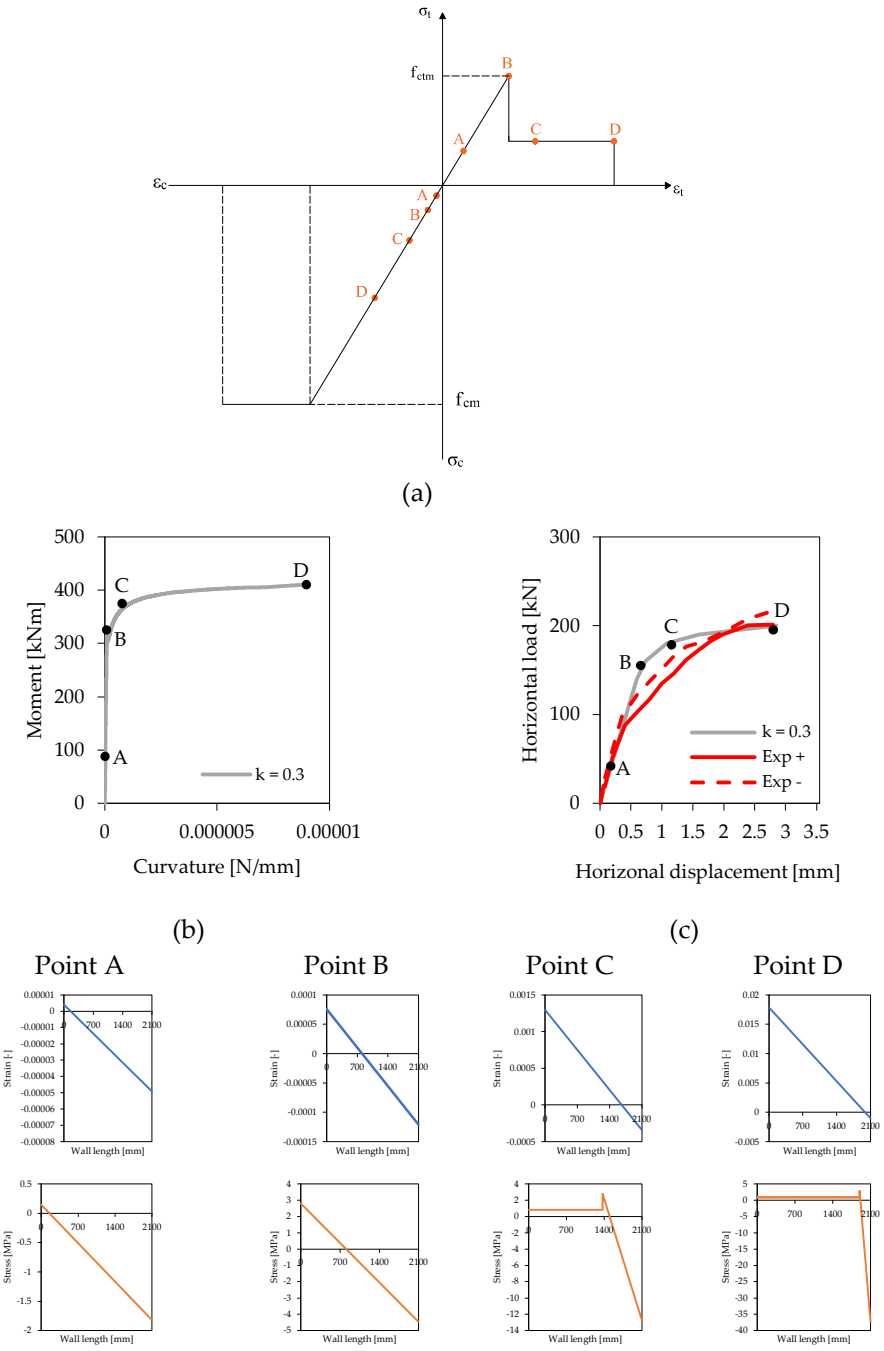

Figure 4-81: Analytical experimental curve with a reductive factor k = 0.4: (a) tensile and compressive constitutive law, (b) moment-curvature and (c) force-displacement.

Once the crack at the base of the wall is formed (in correspondence of point B in Figure 4-68b, once the maximum flexural strength is reached), it is assumed that the wall behaves as a rigid block and thus exhibits a rocking mechanism. Under the assumptions of a stress block behaviour of concrete in compression, the internal equilibrium provides the ultimate bending moment (M_u) of the wall section (Figure 4-82).

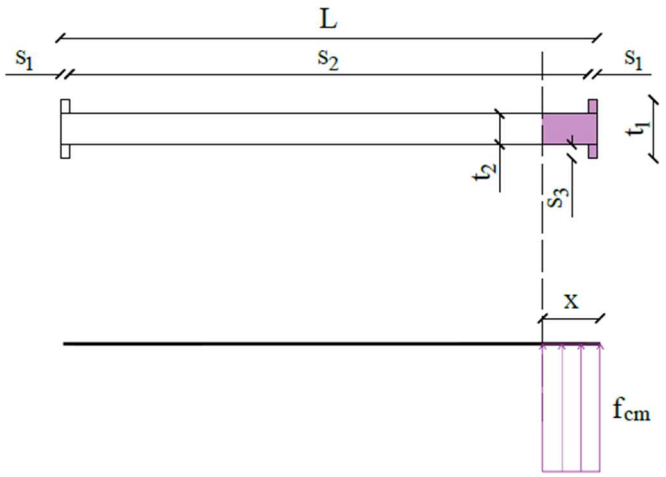

Figure 4-82: Rocking mechanism-stresses diagram.

The ultimate bending moment can be estimated using the following equation when the neutral axis passes through the flanges:

$$M_{rocking} = F_v \cdot \frac{L}{2} \cdot \left(1 - \frac{F_v}{L \cdot t_1 \cdot f_{cm}}\right) \quad 4\text{-}44$$

When the neutral axis crosses the web, the vertical force acting on the wall F_V is balanced by the sum of two forces F_{V1}, which is the sum of the vertical stress in the flange, and F_{V2}, which is the sum of the vertical stress in the web. The ultimate bending moment is calculated as follows:

$$\begin{aligned} M_{rocking} &= (F_{v1} + F_{v2}) \cdot e \\ &= t_1 \cdot s_1 \cdot f_{cm} \cdot \left(\frac{L}{2} - \frac{s_1}{2}\right) + f_{cm} t_2 \cdot (x - s_1) \cdot \left(\frac{L}{2} - \frac{x + s_1}{2}\right) \end{aligned} \quad 4\text{-}45$$

Where x is the depth of the neutral axis, which is calculated as:

$$x = \frac{F_v - t_1 \cdot s_1 \cdot f_{cm} + t_2 \cdot s_1 \cdot f_{cm}}{t_2 \cdot f_{cm}} \quad 4\text{-}46$$

The ultimate horizontal force (F_u) acting on the wall is given by:

$$F_u = \frac{M_{cr}}{H} \quad 4\text{-}47$$

Table 4-8 summarizes the results obtained from the analytical calculation and experimental test. Predicted values showed a good agreement with experimental results both for the maximum horizontal force (F_{max}) and the ultimate horizontal force (F_u).

By applying the section analysis at failure (ULS) for reinforced concrete sections, the maximum horizontal load acting on the reinforced wall can be estimated to be around 350 kN. It was decided to place three steel ribbed bars with a diameter of 16 mm in each pocket to develop an ultimate resisting moment M_u 1.5 times higher than the cracking moment M_{cr}.

Material	ID	Symbol	Unit	Analytical model prediction	Experimental test results
2	Unreinforced	F_{max}	[kN]	200	+202.5/-217.5
		F_u	[kN]	99.28	+98.3/-112.9
2	Reinforced	F_{max}	[kN]	350 kN	+150.48/-182.48

Table 4-8: Analytical model prediction and experimental test results: maximum horizontal force F_{max} and ultimate horizontal force F_u.

4.6 Summary of the results

The main findings of the structural tests on 3DPC walls are summarized.

4.6.1 3DPC walls printed with material type 1

Figure 4-83 shows the envelope curves of the three tested walls, which belonged to the 3DPC house in Milan. The three walls exhibited a similar behaviour with an initial bilinear elastic behaviour until the appearance of the first crack. The walls showed a brittle behaviour with a flexural crack at the base of the wall when the maximum flexural strength was reached. The flexural crack began in the outermost part of the cross-section and continued mainly within a layer of concrete. Approaching the innermost part of the cross-section, it moved downwards crossing several layers. At load reversal, the critical crack developed similarly from the opposite end of the cross-section and met the one created in the previous cycles. The walls were able to withstand high horizontal loads equal to 121.8 kN, 139.03 kN and 188.78 kN considering wall 1, wall 2 and wall 3, respectively. Table 4-9 summarizes the main experimental findings.

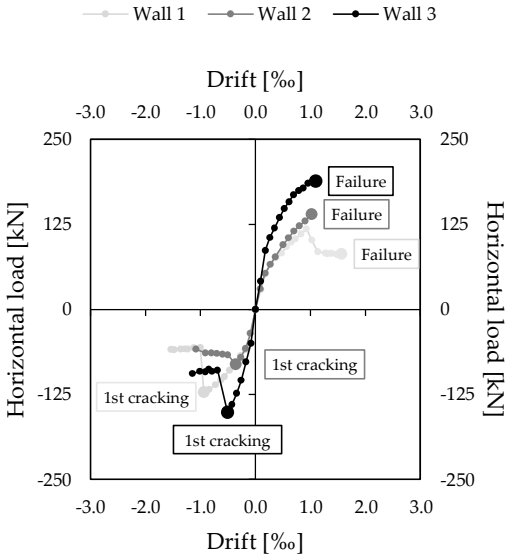

Figure 4-83: Envelope curves: wall 1 (light grey), wall 2 (dark grey), wall 3 (black).

		PULL PHASE				PUSH PHASE			
ID	V	F-	d-	Cycle-	Note	F+	d+	Cycle+	Note
[-]	[kN]	[kN]	[mm]	[-]	[-]	[kN]	[mm]	[-]	[-]
Wall 1	75+75	-122	-1.2	-1.0‰	First crack	+118	+2.2	+1.8‰	Failure
Wall 2	75+75	-81	-0.7	-0.5‰	First crack	+139	+1.4	+1.5‰	Failure
Wall 3	100+100	-166	-1.1	-0.7‰	First crack	+190	+2.0	+1.2‰	Failure

Table 4-9: Horizontal load (F), horizontal displacement (d), cycle at first crack and at failure.

The initial stiffness of the walls was similar around 300 kN/mm. However, the stiffness is characterized by a rapid degradation when the cracking occurs (Figure 4-84). The damping ratio coefficient was relatively stable, ranging from 2% to 5% before the failure. At failure, it increased to values larger than 10% (Figure 4-85).

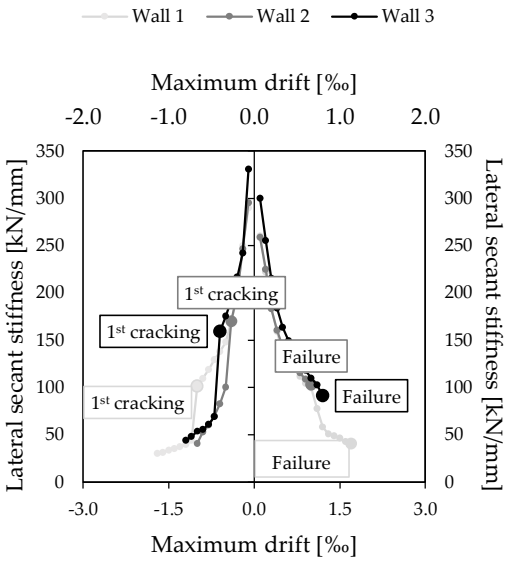

Figure 4-84: Stiffness degradation curves: wall 1 (light grey), wall 2 (dark grey), wall 3 (black).

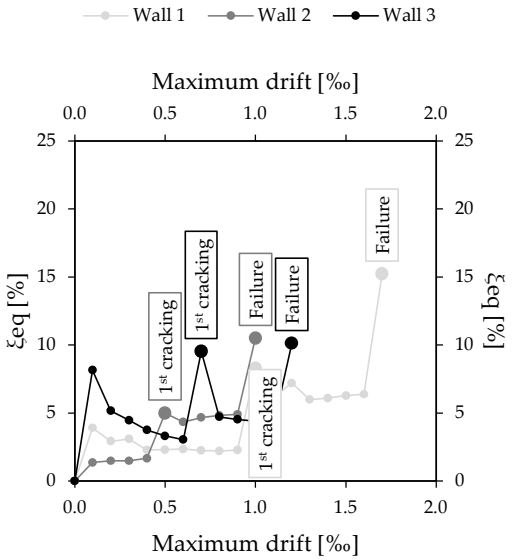

Figure 4-85: Viscous damping coefficient curves: wall 1 (light grey), wall 2 (dark grey), wall 3 (black).

4.6.2 3DPC walls printed with material type 2.

Figure 4-86 shows the envelope curves of the walls printed using material type 2. One wall was unreinforced (grey curve in Figure 4-86) and the other was reinforced (black curve in Figure 4-86) with vertical steel bars embedded in side pockets. The walls exhibited a similar behaviour with an initial elastic behaviour until the occurrence of the first crack. The unreinforced wall showed a brittle behaviour, in fact, when the maximum flexural strength was reached the wall showed a flexural crack at the base of the wall, in correspondence of the bottom corbel. The wall exhibited high resistance to horizontal load up to 220 kN. Regarding the reinforced wall, it has to be mentioned that due to overheating issue it was necessary to stop the printing process for almost 45 min. As consequence, the reinforced wall exhibited a sliding failure in correspondence of the cold-joint. This highlights an aspect inherent of the 3D printing process, in fact when a 3DPC building is printed on-site, cold joints are very likely to occur. Moreover, this result points out the importance of the layers adhesion, as discussed in Chapter 3, underlying as the bond between the layers may be reduced by long time interval gap which significantly affects the overall behaviour of the concrete element.

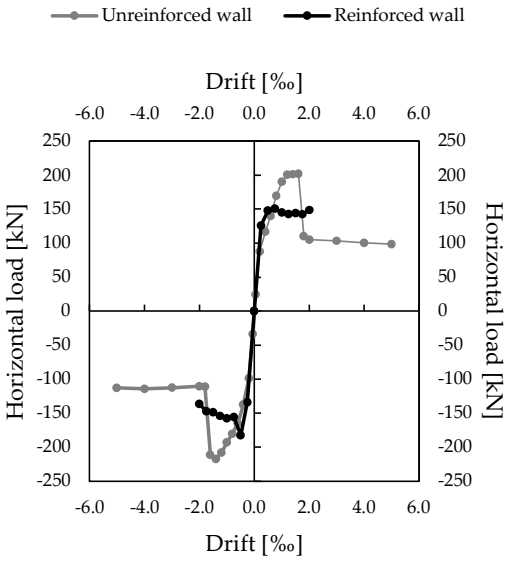

Figure 4-86: Envelope curves: unreinforced wall (dark grey), reinforced wall (black).

		PULL PHASE				PUSH PHASE			
ID [-]	V [kN]	F- [kN]	d- [mm]	Cycle- [-]	Note [-]	F+ [kN]	d+ [mm]	Cycle+ [-]	Note [-]
unreinf	100+100	-217	-2.81	1.6‰	First crack	+98	-9.72	5.00‰	Ultimate load
reinf	100+100	-183	-0.97	0.5‰	First crack	+150	4.00	2.00‰	Ultimate load

Table 4-10: Horizontal load (F), horizontal displacement (d), cycle at first crack and at failure.

The walls exhibited similarly high initial stiffness around 300 kN/mm. However, the stiffness is characterized by a rapid degradation when the cracking occurs (Figure 4-87). The damping ratio coefficient of the unreinforced wall shows a stable mechanism equal to 3% before the failure and to 6% after the failure. The dumping ratio coefficient reached a maximum value of 12% at the failure (Figure 4-88). The reinforced wall exhibited a higher damping ratio coefficient since the wall is more dissipative thanks to the presence of the reinforcement. It reached a maximum value of 19% at the failure.

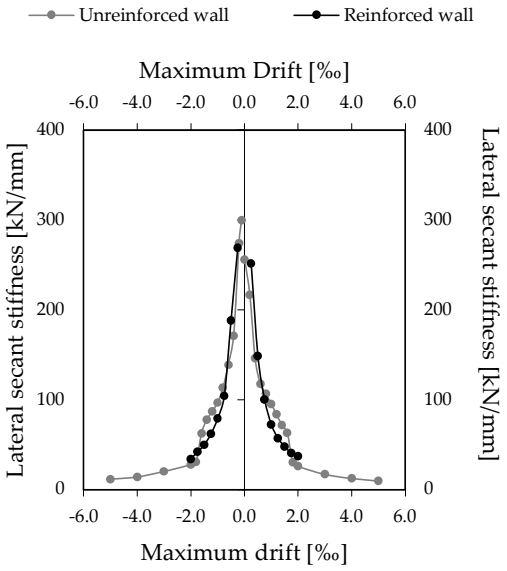

Figure 4-87: Stiffness degradation curves: unreinforced wall (dark grey), reinforced wall (black).

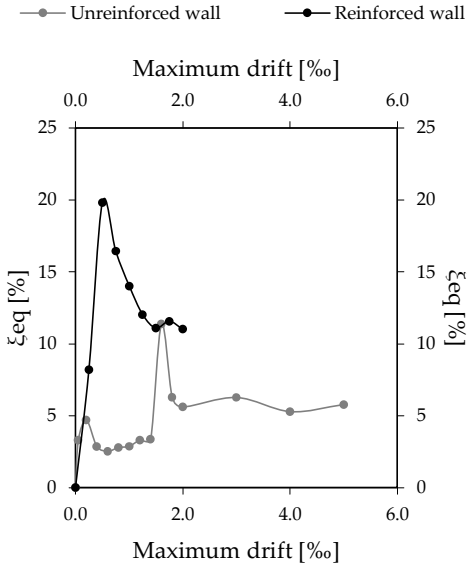

Figure 4-88: Viscous damping coefficient curves: unreinforced wall (dark grey), reinforced wall (black).

4.7 Discussion of the results

In this section the results of the experimental tests are discussed in terms of initial elastic stiffness and base shear force capacity. The results obtained from the 3DPC unreinforced wall printed with material type 2 (see section 4.5.1.2.1) are compared to other tests performed on traditional unreinforced masonry walls [134,154,155], in particular solid clay brick, hollow clay brick and AAC blocks masonry are considered. The walls have comparable dimensions, vertical load applied and boundary condition. Table 4-11 shows the geometrical characteristic of the unreinforced walls including length L, heigth H, thickness t, shear ratio H/L, vertical load N applied on the wall, and boundary condition. Table 4-12 reports the mechanical properties of the unreinforced walls including the compressive strength of the blocks $f_{c,b}$, the compressive strength of the mortar f_m, the compressive strength of the masonry $f_{c,m}$, the tensile strength of the material $f_{c,t}$, the cohesion f_{vo}, the angle of friction tgφ, the elastic modulus E and the shear modulus G.

	L [mm]	**H [mm]**	**t [mm]**	**H/L [-]**	**N [kN]**	**Boundary condition**
3DPC	2100	2100	230 (flange) 111 (web)	1	215	Cantilever
Solid clay brick [154]	2960	2710	210	0.92	223	Cantilever
Hollow clay brick [155]	2700	2600	150	0.96	235	Cantilever
AAC blocks [134]	1250	2500	300	2	150	Cantilever

Table 4-11: Geometrical characteristic of the unreinforced walls.

	$f_{c,b}$ [MPa]	**f_m [MPa]**	**$f_{c,m}$ [MPa]**	**$f_{c,t}$ [MPa]**	**f_{vo} [MPa]**	**tgφ [-]**	**E [MPa]**	**G [MPa]**
3DPC	/	/	58	2.8	6.3	1.45	37000	15416
Solid clay brick [154]	28.31	3.81	9.24	0.61	0.2	0.69	2646	1058
Hollow clay brick [155]	31.8	10.5	5.8	0.15	0.26	0.48	3495	1398
AAC blocks [134]	3.06	10	1.91	0.23	0.29	0.5	1380	357

Table 4-12: Material properties of the unreinforced walls.

4.7.1 Elastic stiffness

The initial stiffness of the wall can be predicted by the elastic stiffness k_{el} computed according to the Timoshenko beam theory

$$k_{el} = \frac{1}{\frac{H^3}{\eta EJ} + \frac{\chi H}{GA}} \quad 4\text{-}48$$

Where H is the height of the wall, η is a coefficient equal to 12 for double clumped configuration and 3 for cantilever configuration, χ is a coefficient equal to 1.2 for rectangular cross section, E is the Young modulus (Table 3-30), G is the shear modulus (calculated according equation 4-39), J and A are the moment of inertia and area of the cross-section of the wall, respectively.

When considering the 3DPC wall, it is essential also to account for the contribution resulting from the sliding between the layers, which needs to be considered for the calculation of the elastic stiffness k_{el}. Equation 4-48 can be written as follow:

$$k_{el} = \frac{1}{\frac{H^3}{\eta EJ} + \frac{\chi H}{G_{poisson}A} + \frac{H}{G_{sliding}A}} \quad 4\text{-}49$$

Where $G_{poisson}$ and $G_{sliding}$ are calculated according to equation 4-39 and 4-43.

Table 4-13 shows a comparison between the experimental $k_{exp,el}$ and theoretical elastic stiffness $k_{th,el}$. It comes out that the theoretical elastic stiffness provides a reasonable approximation of the experimental results. In particular, it underestimates the experimental results by 5% for the hollow clay brick and 20% for the 3DPC wall. On the contrary, in the case of solid clay brick masonry, the analytical calculation underestimates the experimental elastic stiffness by 41%.

Specimen	$K_{exp,el}$ [kN/mm]	$K_{th,el}$ [kN/mm]	$K_{th,el}/k_{exp,el}$ [-]
3DPC	299.8	241	0.80
Solid clay brick	162.3	95.5	0.59
Hollow clay brick	85.4	81.14	0.95
AAC block	10.00	10.02	1.002

Table 4-13: Values of the experimental elastic stiffness and theoretical elastic stiffness.

Figure 4-89 shows the theoretical elastic stiffness $k_{th,el}$ versus the shear ratio H/L, investigating how the elastic stiffness varies with the shear ratio for different wall types. A shear ratio H/L equal to 0.5 represents a squat wall, while an H/L shear ratio of 2 represents a slender wall. It can be observed that, in general, the elastic stiffness is higher for squat walls (H/L = 0.5). In addition, solid clay brick, hollow clay brick and AAC block walls have elastic stiffness values that are lower than the elastic stiffness of 3DPC walls.

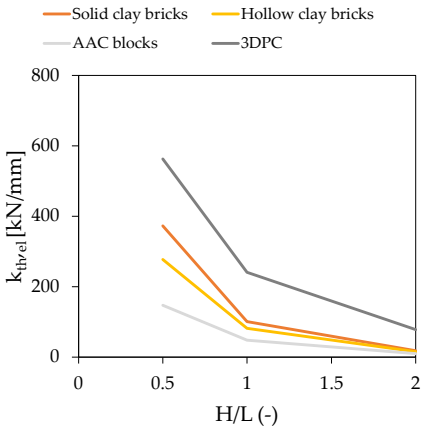

Figure 4-89: Theoretical elastic stiffness $k_{th,el}$ versus shear ratio H/L.

4.7.2 *Base shear force capacity*

Masonry piers subjected to axial and shear action are subjected to few principal failure mechanism: rocking failure, shear sliding and shear diagonal cracking.

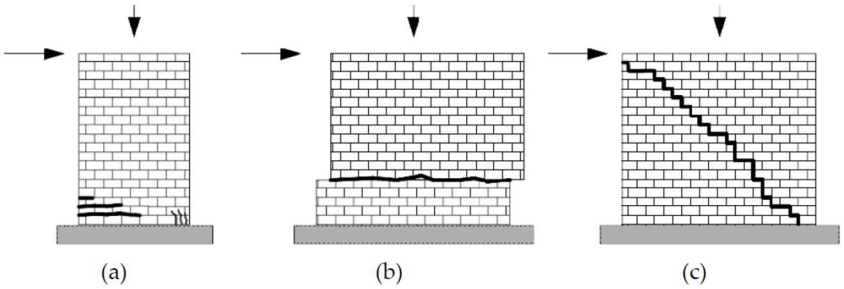

Figure 4-90: Typical masonry panel failure mechanism: (a) rocking, (b) shear sliding and (c) shear diagonal cracking [156].

Rocking failure, as shown in Figure 4-90a, occurs in two distinct phases. In the initial phase, as the horizontal load or displacement demand increases, the joints at the base of the panel undergo tensional cracking, initiating the rotation of the wall around the uncracked corner. Finally, failure occurs by crushing of the compressed corner.
Regarding the shear behaviour, two different failure modes can identified: the *shear sliding* and the *shear diagonal cracking*. The *shear sliding*, as shown in Figure 4-90b, results from the sliding of a portion of the panel along the cracked bed joints. It can occur under condition of low vertical load levels on the panel and/or when the material has low coefficients of friction. *Shear diagonal cracking* (Figure 4-90c) is identified by the formation of cracks approximately along the element diagonal. Which of those failure modes prevails depends on the geometry of the wall, the axial load, the boundary conditions and the masonry mechanical properties.

If the wall is subjected to rocking mechanism, the lateral resistance is based on the equilibrium of the wall rotating around the compressed corner and may be estimated by the following equation, which is the formulation proposed in Eurocode 8 [157] and NTC2018 [112]:

$$M_u = (L^2 t \frac{\sigma_n}{2})(1 - \frac{\sigma_n}{0.85 f_{cm}}) \quad 4\text{-}50$$

Where L and t are the length and the thickness of the wall, σ_n is the vertical stress due to the axial load acting on the wall, and f_{cm} is the masonry compressive strength.
The maximum base shear strength of a masonry wall with prevalent shear behaviour is given by the minimum between the shear sliding strength $V_{s,max}$ and the shear strength associated with diagonal cracking $V_{d,max}$:

$$V_s = \min\{V_{s,max}, V_{d,max}\} \quad 4\text{-}51$$

According to Magenes and Calvi [158], the maximum shear strength of the masonry panel due to shear sliding is given by:

$$V_{s,max} = \frac{1.5c + \mu\sigma_n}{1 + 3\frac{c\alpha_v}{\sigma_n}} * L * t \quad 4\text{-}52$$

Where L and t are the length and the thickness of the wall, c is the cohesion, μ is the coefficient of friction, σ_n is the vertical load applied and α_v is the shear ratio H/L.
The base shear force due to shear diagonal cracking is given by Turnsek and Cacovic [159] relationship and Turnsek and Sheppard [160] relationship; a diagonal shear failure occurs when the positive principal stress, evaluated at the centre of the panel, reaches the tensile strength of masonry. It is expressed as:

$$V_{d,max} = Lt\frac{f_t}{\beta}\sqrt{1 + \frac{\sigma_n}{f_t}} \quad 4\text{-}53$$

Where L and t are the length and the thickness of the wall, σ_n is the vertical stress acting on the wall, f_t is the conventional tensile strength of masonry and β is a parameter which depends on the aspect ratio H/L and accounts for the shear stress distribution at the centre of the panel. Benedetti and Tomaževic [161] estimated the value of β as 1 if the ratio H/L < 1, as H/L if the ratio 1<H/L<1.5 and as 1.5 if H/L >1.5.
For each masonry wall, an interaction diagram is derived, showing the maximum horizontal strength versus axial load for each failure mode. From Figure 4-91 to Figure 4-95 the interaction diagrams of solid clay brick masonry, hollow clay brick masonry, AAC blocks masonry and 3DPC wall are shown. In the graphs, the axes are dimensionless with respect to the ultimate load N_u to allow the comparison between different construction methods: the vertical axis refers to the horizontal strength F_h and the horizontal axis to vertical load N acting on the wall. The resistance domain

is determined (green shaded area) and is delimited by different failure line: the red curve corresponds to the rocking, the blue curve to the shear sliding strength and the yellow one to the shear strength associated with diagonal cracking. It can be observed for solid clay brick (Figure 4-91), hollow clay brick (Figure 4-92) and AAC block walls (Figure 4-93), that in slender walls (H/L = 2) and square walls (H/L = 1), the predominant mechanism is rocking. Considering squat walls (H/L = 0.5) initially shear sliding prevails, followed by diagonal cracking and rocking mechanism for high level of vertical force applied.

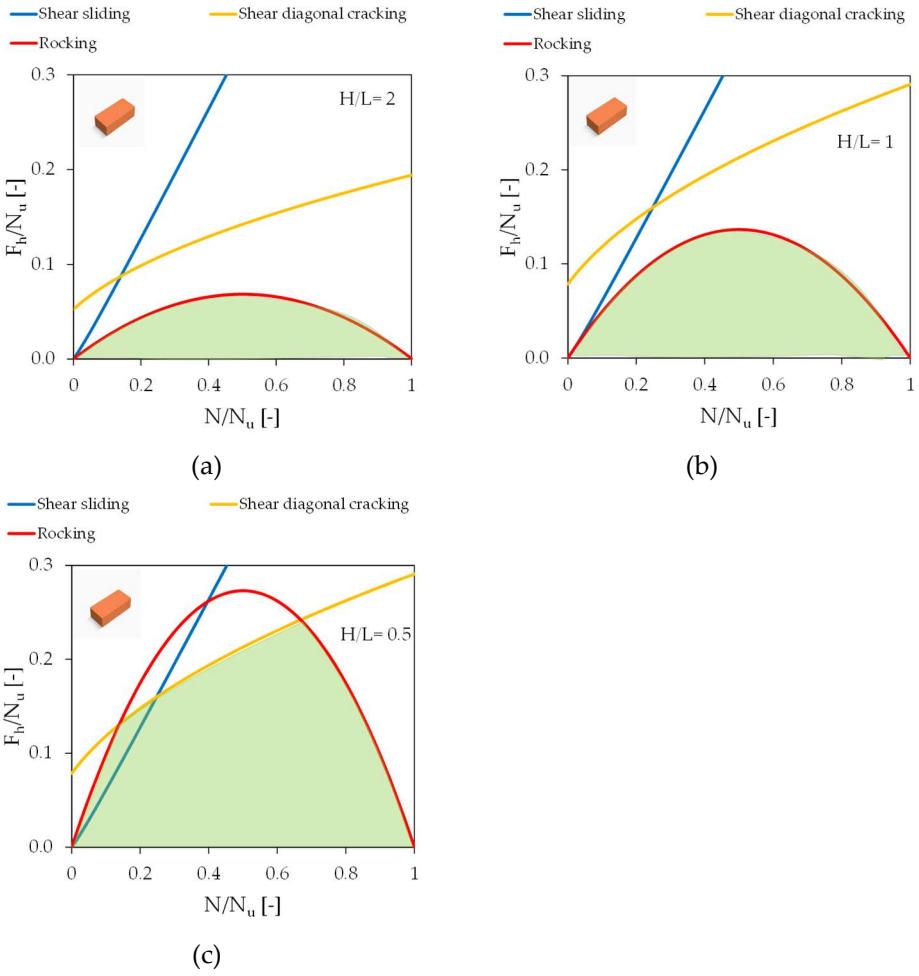

Figure 4-91: Resistance domain of solid clay masonry wall according to different shear ratio: (a) slender walls (H/L = 2); (b) square walls (H/L = 1); (c) squat walls (H/L = 0.5).

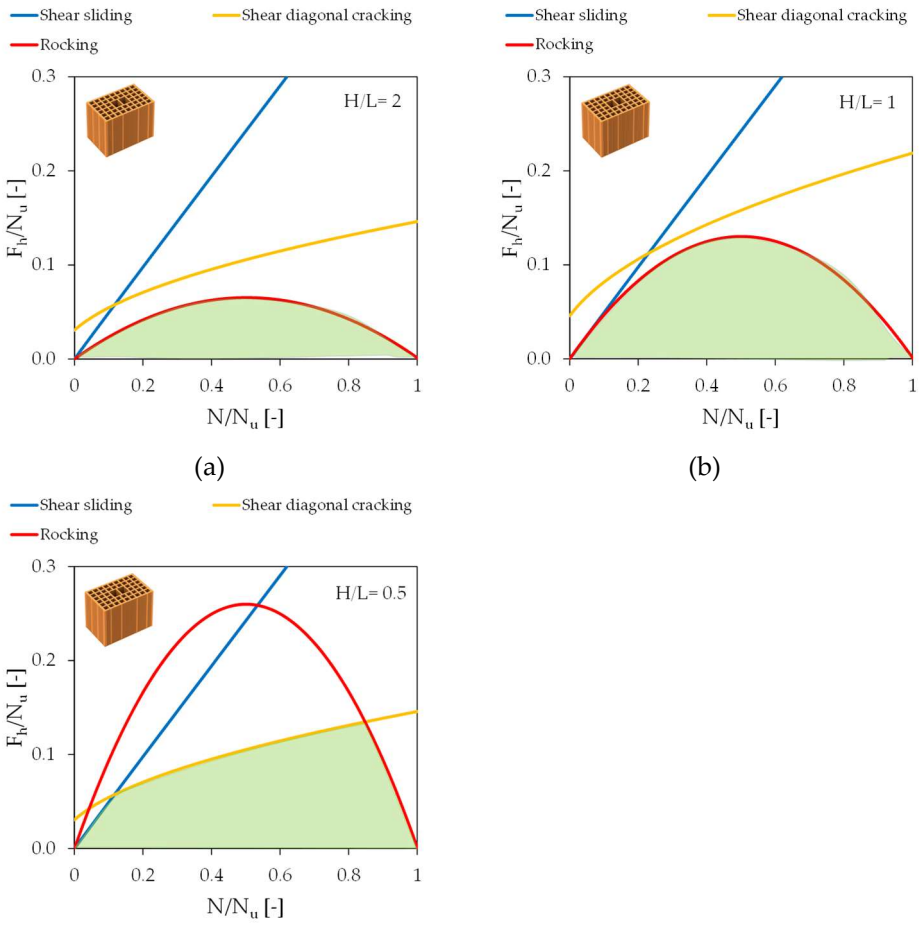

(a) (b)

(c)

Figure 4-92: Resistance domain of hollow clay masonry wall according to different shear ratio: (a) slender walls (H/L = 2); (b) square walls (H/L = 1); (c) squat walls (H/L = 0.5).

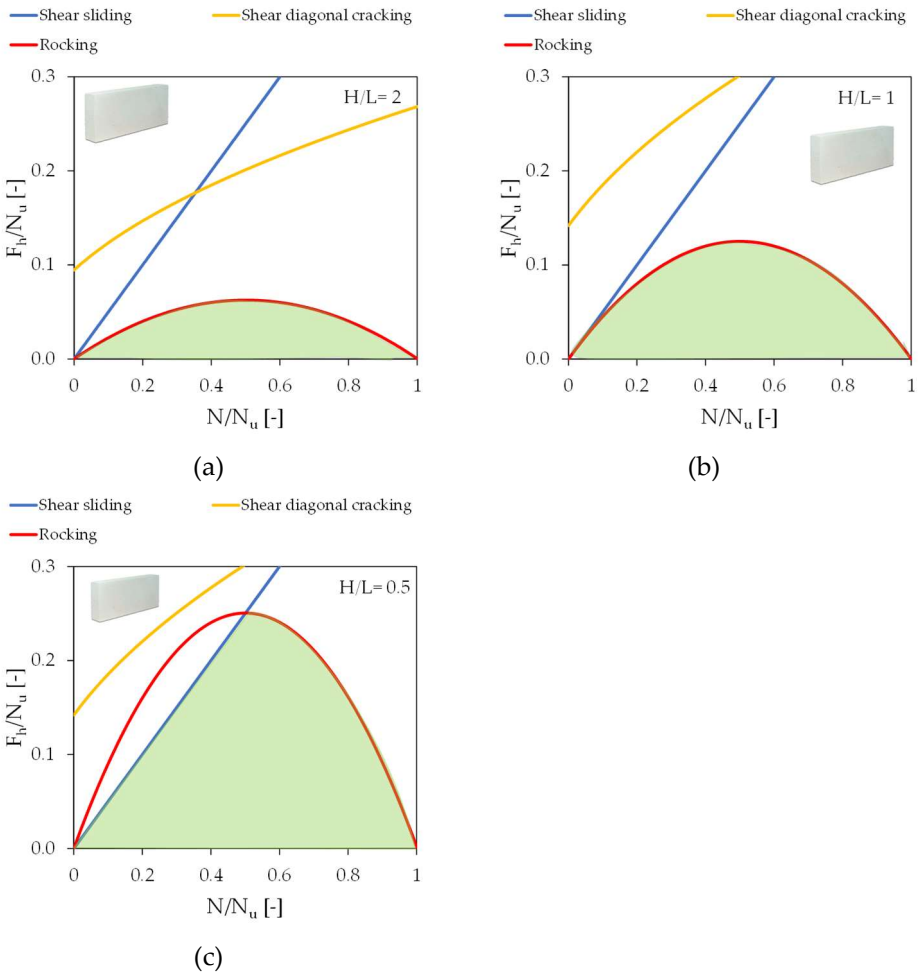

Figure 4-93: Resistance domain of AAC blocks masonry wall according to different shear ratio: (a) slender walls (H/L = 2); (b) square walls (H/L = 1); (c) squat walls (H/L = 0.5).

Regarding 3DPC wall (Figure 4-94), it has to be to noted that the capacity curve exhibits a different behaviour compared to conventional masonry (Figure 4-94a). Traditional masonry structures reach their maximum capacity in correspondence of rocking, shear sliding or shear diagonal cracking mechanisms (Figure 4-94b). On the other hand, the 3DPC wall (Figure 4-94a and c), benefiting from the tensile strength of the 3DPC material, exhibits a linear behaviour up to point A, corresponding to the achievement of the maximum tensile strength of the material, where the first cracking occur. From point A to point B, the wall continues to take advantage of its tensile strength with a re-distribution of tensile stresses, demonstrating nonlinear stresses behaviour until point B, where a major crack occurs (see Figure 4-68). As consequence, point B corresponds to the achievement of the maximum flexural strength and is identified as failure point. From point B to point C, the load decreases and the prevailing mechanism becomes rocking. Figure 4-95a-c shows the resistance domain for the 3DPC wall which is delimited by different failure lines: the light blue curve corresponds to the first cracking in correspondence of the maximum tensile strength (it is indicated as a dashed line because it is not a failure mode), the orange curve to the maximum flexural strength, the red one to the rocking (it is represented as a dashed line because in this case it is a residual strength and it can occur only after the wall has reached its maximum flexural strength), the blue one to the shear sliding strength and the yellow one to the shear strength associated with diagonal cracking. With reference to the analytical model described in section 4.5.2, the first cracking load is calculated according to equations 4-11-4-15 and the maximum flexural strength according to equations 4-31-4-34. It can be observed that for low value of the applied vertical load, the 3DPC wall failed in correspondence of the maximum lateral capacity due to the flexural failure at the base section (orange curve in Figure 4-95). As the vertical load applied to the wall increases, shear diagonal cracking mechanism becomes predominant.

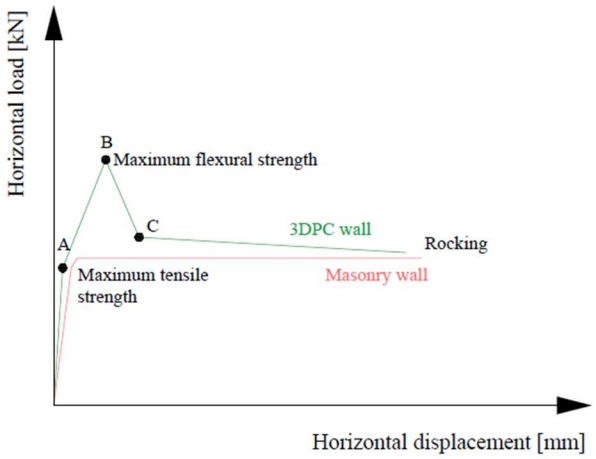

(a)

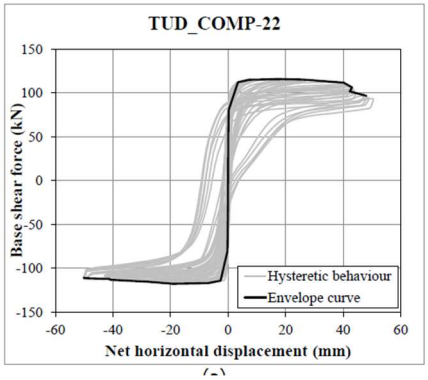

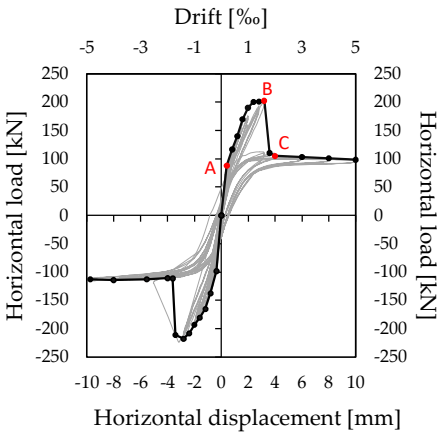

(b) (c)

Figure 4-94: Capacity curve of the unreinforced 3DPC wall versus traditional masonry wall: (a) comparison; (b) solid clay masonry wall [154] and (c) 3DPC wall.

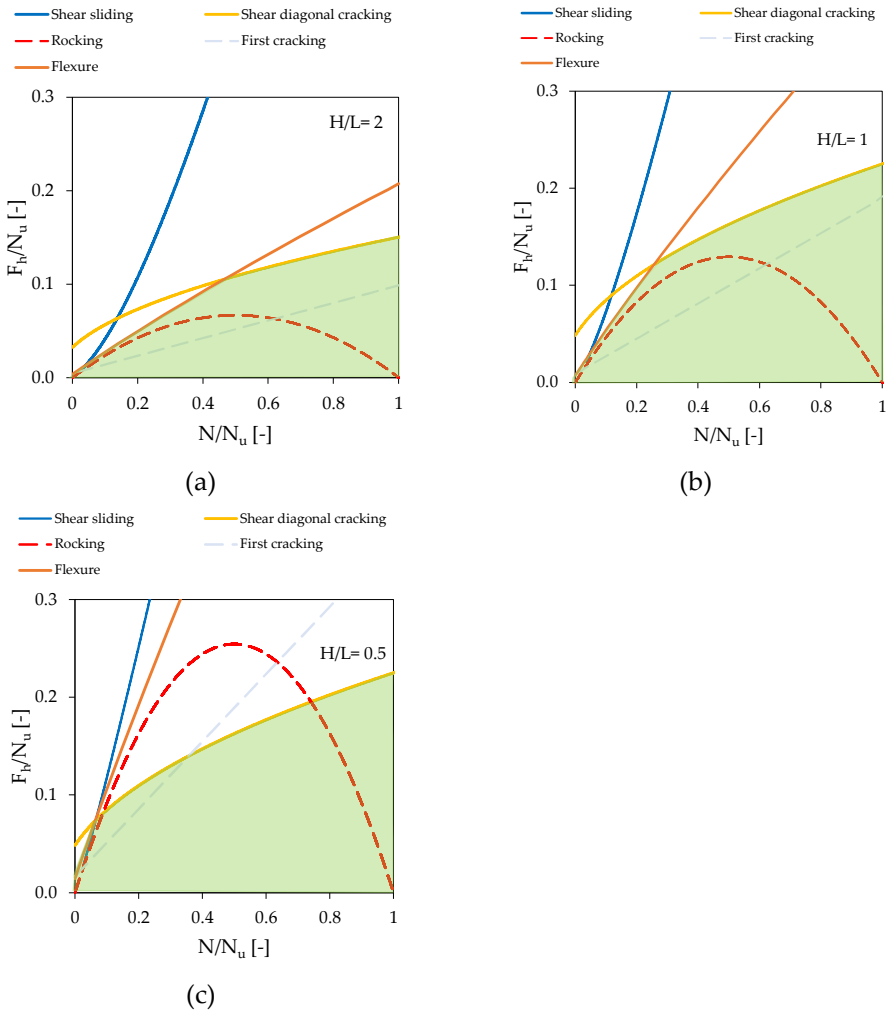

Figure 4-95: Resistance domain of 3DPC wall according to different shear ratio: (a) slender walls (H/L = 2); (b) square walls (H/L = 1); (c) squat walls (H/L = 0.5).

Figure 4-96 presents the horizontal force F_h as a function of shear ratio H/L. Figure 4-96a corresponds to a vertical load of about 200 kN applied and Figure 4-96b to a load of 360 kN, equivalent to the load of a two-story building acting on a 3 m high wall. The orange curve refers to solid clay brick, the yellow curve to hollow clay brick, the light gray curve to AAC block masonry walls, and the dark gray curve to 3DPC concrete walls. It comes out that as the shear ratio H/L decreases (from slender to squat walls), the shear force resistance of the wall increases. The 3DPC wall shows higher strength than the other construction techniques.

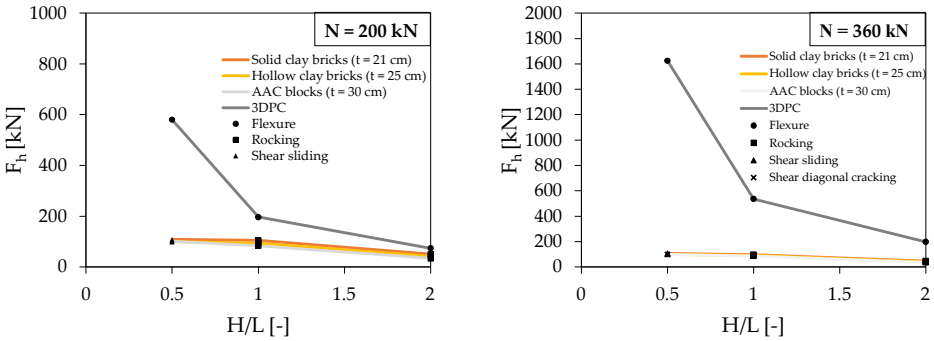

Figure 4-96: Maximum base shear force F_h versus shear ratio H/L of the unreinforced walls: (a) with 200 kN vertical load applied; (b) with 360 kN applied.

Figure 4-97 shows the failure envelope of the walls for different shear ratio (H/L = 2 refers to slender walls and H/L = 0.5 to squat walls), showing the maximum horizontal force F_h as a function of the applied vertical load N. The graphs on the left represent the failure envelope for different construction techniques, while on the right an enlarged view of the initial branch is presented, focusing on a vertical load of 200 kN, which corresponds to the vertical load applied to the walls during the experimental tests. Considering traditional masonry walls, it is evident that for both slender and square walls, rocking is the dominant mechanism, as in the experimental tests presented by Penna et al. [134], Esposito et al. [154] and Salamanpour et al. [155] (see *Figure 4-97*a2 and b2). The 3DPC wall, due to its tensile strength, shows significant overstrength for low values of vertical load applied compared to masonry walls. After the tensile strength of the material is reached (point A in Figure 4-94), the wall is subjected to a re-distribution of tensile stresses until a major crack occurs. As consequence, point B (Figure 4-94), which is the point of maximum flexural strength, is identified as failure point (*Figure 4-97*b2). In the case of squat walls (H/L = 0.5), shear mechanisms dominate, beginning with shear sliding followed by diagonal cracking (*Figure 4-97*c) for traditional masonry walls; on the other hand, 3DPC walls fails at maximum flexural strength for a low value of the applied vertical load and undergo diagonal cracking as the vertical load increases.

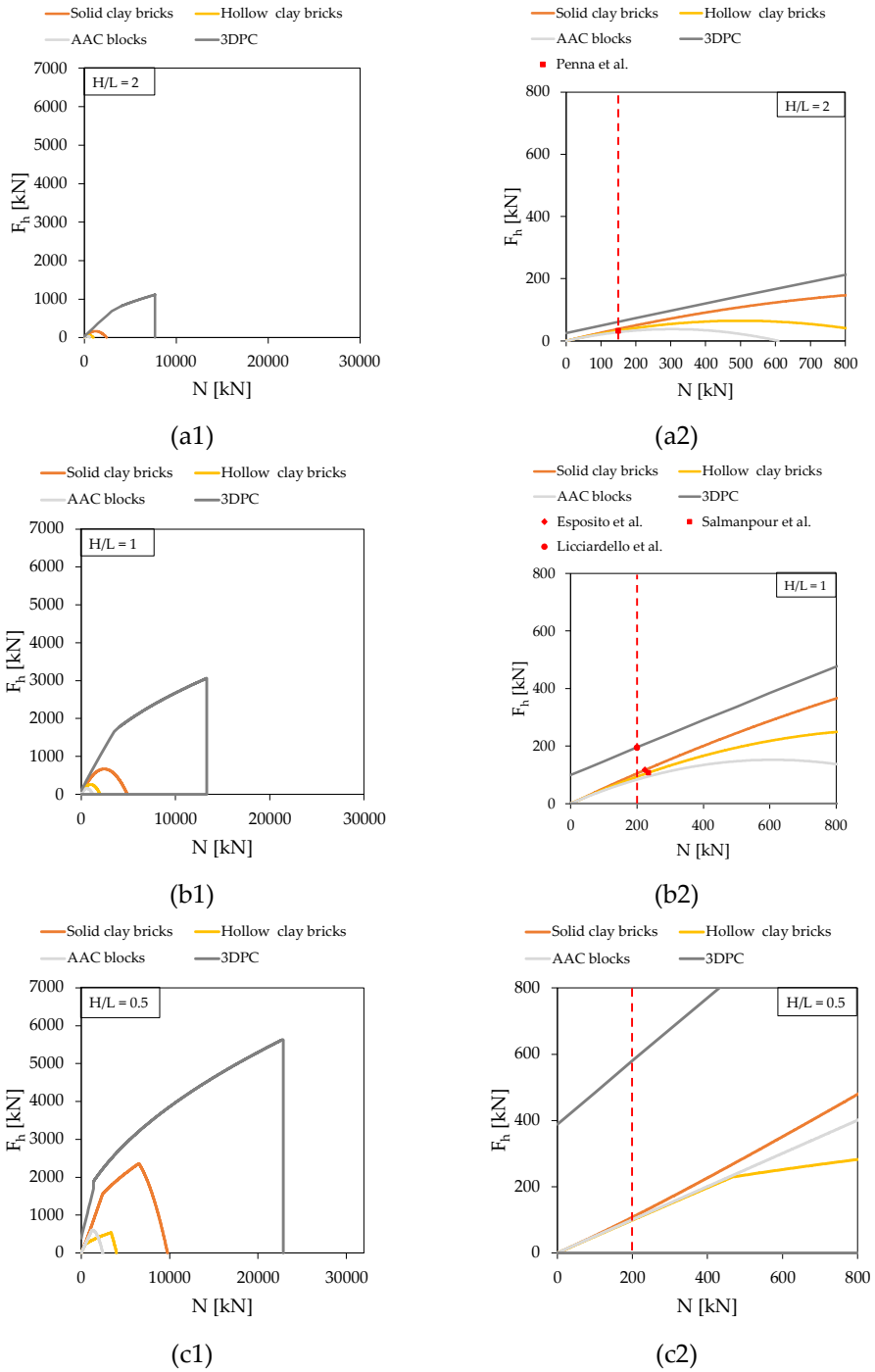

Figure 4-97: Failure envelope of the unreinforced wall: (a) slender walls; (b) square walls; (c) squat walls.

Table 4-14 reports the values of the computed and experimental strength of each wall. It can be noted that the minimum computed value of strength, associated with the dominating failure mechanism, approximates well the experimental wall lateral strength.

Specimen	$\mathbf{V_{exp}}$	$\mathbf{V_{th}}$	$\mathbf{V_{th}/V_{exp}}$
3DPC	+202.5/-217.5	200	0.98/0.92
Hollow clay brick	108	113.6	1.05
Solid clay brick	117.8	116.2	0.98
AAC block	32.18	28.26	0.88

Table 4-14: Values of the experimental and theoretical base shear force.

5 NUMERICAL ANALYSIS

5.1 Introduction

In this section, the numerical analyses conducted on 3DPC elements are presented. The finite element program DIANA FEA 10.6 was used [162].
3D printed concrete elements made using the extrusion process have certain peculiarities compared to traditional concrete structures. Whereas cast concrete can be considered an isotropic material, 3DPC material is anisotropic as it consists of several layers. A crucial aspect to be considered is the interface strength, as long time gap between layers can lead to the formation of cold joints, reducing the overall strength of the 3D printed concrete element and structure. Therefore, the development of mechanical models through numerical analysis can help to better understand the parameters affecting the structural behaviour of 3D-printed concrete elements at both small and large scale. Numerical simulation methodologies for masonry and other layered structures can serve as a reference point [163,164].
This chapter focuses firstly on the numerical analysis of the modified push-out test, which is important to understand the effect of the mechanical properties of the interface between layers on the shear behaviour of tested specimens. The modified push-out test represents the biaxial stress state acting on a wall subjected to transverse shear force and a vertical compressive load. In this test, specimens are subjected to an increasing vertical load and a constant horizontal prestress load, which represent the horizontal and vertical loads on a wall, respectively (see Chapter 3). Successively, the numerical analysis on 3DPC walls is also carried out.

5.2 Numerical analysis of the modified push-out test

5.2.1 Modelling approach

Since the 3D printing material is anisotropic, commonly used modelling approaches for masonry can be used as a reference [165,166]. In this section two different modelling approaches will be used: the smeared cracking approach and the discrete cracking approach.
With regards to the smeared cracking approach, the global behaviour of the element is simulated without distinguishing between filament layers and interface regions, considering the material as a continuum. With this model, the development of cracks

is smeared in a defined area of an element with a characteristic length (crack bandwidth). For this type of modelling different approaches are implemented in DIANA FEA like the Multi-Directional Fixed Crack Model and the Total Strain Based Crack Model. On the other hand, the discrete cracking approach analyses the behaviour of the element in more detail, considering each component individually, such in masonry structures as modelling bricks using continuum elements and joints using interface elements. Similarly, in 3DPC elements, layers are modelled using continuum elements connected by interface elements. The discrete cracking approach relies on the introduction of discontinuities in the displacement field, called fictitious cracks (discrete cracking). DIANA FEA provides various models for the interface behaviour as a discrete crack model, a *Coulomb friction model* and a *combined Cracking-Shearing-Crushing model*. For further details on the models, please refer to the DIANA 10.6 User's Guide [167].
Within this section the modelling of the modified push-out tests deals firstly with a smeared cracking approach using the Total Strain Based Crack Model which is based on the modified compression field theory [168]; subsequently a discrete modelling approach will also be implemented with specific interfaces, where the cracking is expected to occur; in this latter case the combined *Cracking-Shearing-Crushing model* [164] (also known as *composite interface model*) is assigned, while the tensile and compressive behaviour of the interlayer continuum element is described with the Total Strain Based Crack Model [167]. This is a useful tool for the modelling of 3DPC walls, which are modelled using a smeared cracking approach with an interface at the base to simulate the crack opening.

5.2.2 Geometrical properties

As described in Chapter 3 (see section 3.7.2), two different specimen configuration were considered for the modified push-out test. To exploit symmetry, only half of the test specimen was considered. The specimen made with *material type 1* was 14 cm high, 14 cm wide and 4 cm thick; the thickness of the layer was 2 cm (Figure 5-1a). The specimens made with *material type 2* had a height of 12 cm, a width of 16 cm and a thickness of 6 cm; the thickness of the layer was 1 cm (Figure 5-1b). A 2D plane stress model was chosen since a constant stress distribution over the thickness of the specimen is expected. The dimensions of the modelled specimens are shown in Figure 5-1. In addition, for both configurations, 20 mm x 40 mm steel plates were placed below the loading point and at the bottom the specimen to support it and induce failure in the specific layer.

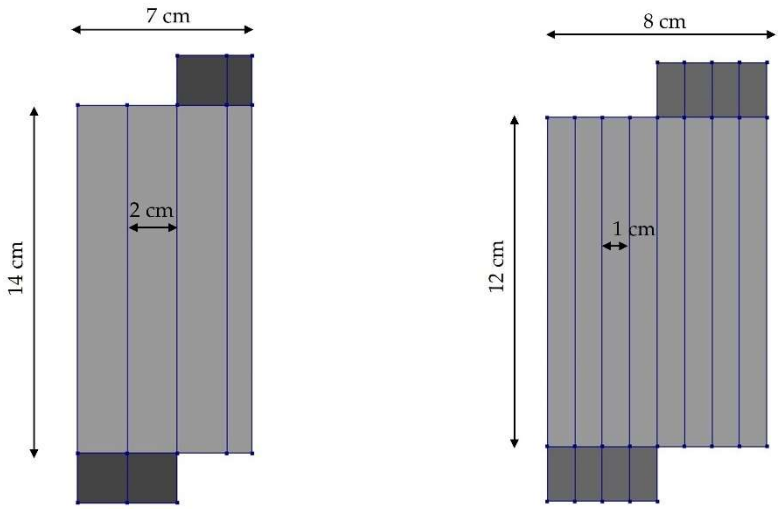

(a) (b)

Figure 5-1: Modified push-out test geometry (a) material type 1 and (b) material type 2.

5.2.3 Material properties

The specimens are made by 3D printed concrete material. Concrete is a quasi-brittle material with an appreciable compressive strength and a relatively low tensile strength. It is characterized by an elastic behaviour at the initial stage, cracking with softening in tension, crushing in compression.
Two different modelling approaches were considered: a smeared cracking approach and a discrete cracking approach.

5.2.3.1 Smeared cracking

The Total Strain Based Crack Model was used to describe the tensile and compressive behaviour of concrete. This model uses a stress-strain relationship to describe the concrete behaviour and can be either rotating or fixed, which determines whether the directions of the cracks are either fixed or continuously rotating with the principal direction of the strain vector. The crack orientation is defined as the direction of maximum principal strain when the tensile strength is reached and the principal stress-strain conditions are evaluated in an orthogonal coordinate system, which is aligned with principal strains at the integration point where the first crack occurred. The *rotating crack model* implies that the cracks reorient themselves as the test progresses with respect to their position, fixed on the basis of the stress-strain relationship, by identifying a variable orthogonal coordinate system.

In *the fixed model*, on the other hand, once this point is identified, the cracks can no longer be reoriented as a function of the strain tensor. The stress-strain relations are evaluated in a fixed coordinate system which is fixed upon cracking.
For the modeling of the modified push-out test a rotating model was chosen.
The Total Strain Based Crack Model is suitable for serviceability limit state (SLS) and for ultimate limit state (ULS) which are mainly governed by cracking or crushing. The input data for the total strain crack model consists of two parts: i) basic properties like the young's modulus, the Poisson's ratio etc and ii) the definition of the behaviour in tension, shear and compression (Table 5-1).

syntax

```
'MATERI'
1        5 6          12 13                                        80
          TOTCRK
                     FIXED
                     ROTATE
                     ROTFIX
         [EPSFIX     epsf_r ]
          ...        ...          basic properties
         [...        ... ]       tensile behaviour
         [...        ... ]       shear behaviour
         [...        ... ]       compressive behaviour
         [...        ... ]       lateral influences
```

Table 5-1: Input parameters of the Total Strain Based Crack Model

Where:

- TOTCRK specifies the type of Total Strain model to be used:
- FIXED for the total strain fixed crack model
- ROTATE for the total strain rotating crack model
- ROTFIX for the total strain crack model switching from rotated to fixed
- EPSFIX is the threshold strain switching from rotating to fixed.

The basic properties can be derived from standards [110,153] or can be based directly from laboratory test results.

5.2.3.1.1 Tensile behaviour

For the tensile behaviour of a Total Strain crack model a predefined function may be chosen or it could be customized. The common predefined tension relationship in DIANA FEA are shown in Figure 5-2.

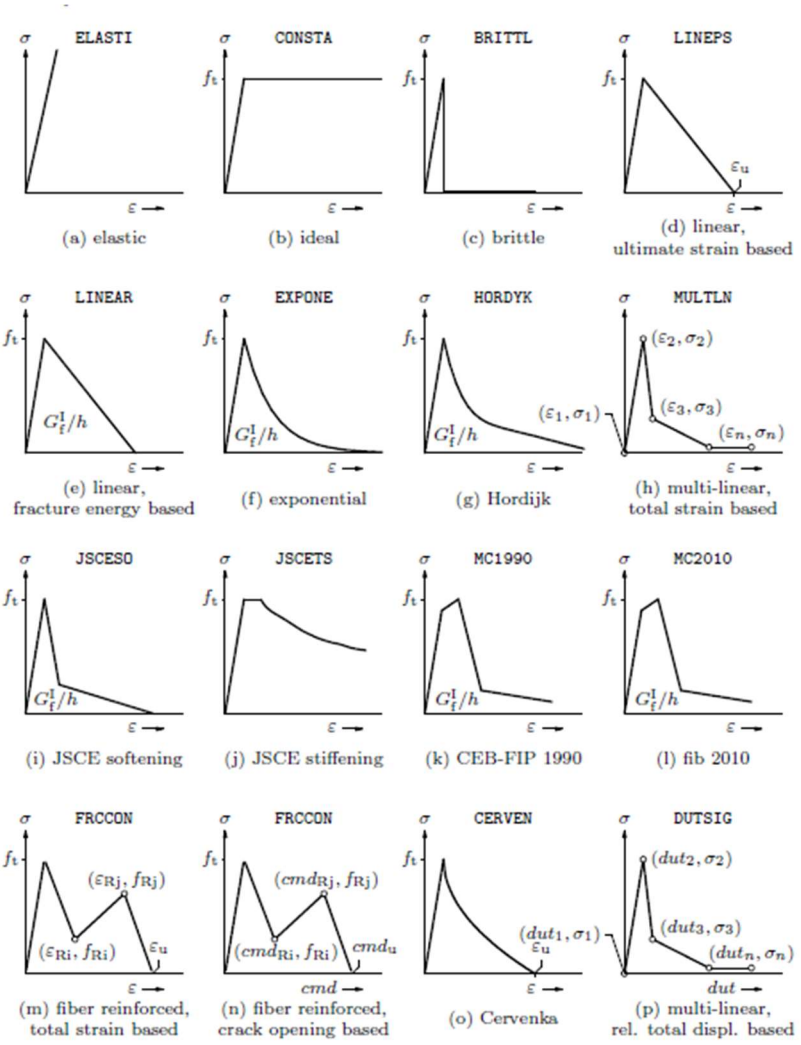

Figure 5-2: Predefined tension softening for Total Strain crack model [167].

For the modelling of the modified push-out test the multilinear model proposed from the Model Code 2010 (Figure 5-2k) was used. This constitutive law was chosen because it is one of the most used in the literature for plain concrete. Figure 5-3 shows in detail the relationship included in the Model Code 2010. The required properties are the tensile strength f_{tr}, the fracture energy g_{f1r} and the crack bendwidth h_r (Table 5-2).

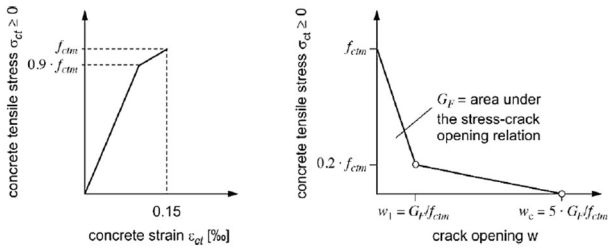

(a) (b)

Figure 5-3: (a) Stress-strain (pre-peak) and (b) stress-crack opening (post-peak) relation for uniaxial tension according to the Model Code 2010 [153].

fib Model Code for Concrete Structures 2010 *syntax*

'MATERI'

1 5	6 12	13 80
	TENCRV	MC2010
	TENSTR	ft_r
	GF1	$gf1_r$
	[CRACKB	h_r]

Table 5-2: Input parameter for the tensile relationship of the fib Model code for Concrete Structures 2010.

The mode-I fracture energy G^I_f can be calculated by using the equation proposed by the model code [153].

$$G_f = 73\,(f_{cm})^{0.18} \qquad 5\text{-}1$$

Where f_{cm} is the compressive strength of the material.
h_r is the crack bandwidth which depends on the size, the shape and the interpolation function of the used finite element. For the numerical modelling of the modified push-out test the default relationship developed by Rots was used [169].

5.2.3.1.2 Compressive behaviour

The compressive behaviour of a Total Strain Based Crack Model is in general a nonlinear function between the stress and the strain. A predefined function in DIANA FEA it might be chosen or it can be customize. The common predefined relationship for the compression behaviour in DIANA FEA are shown in Figure 5-4.

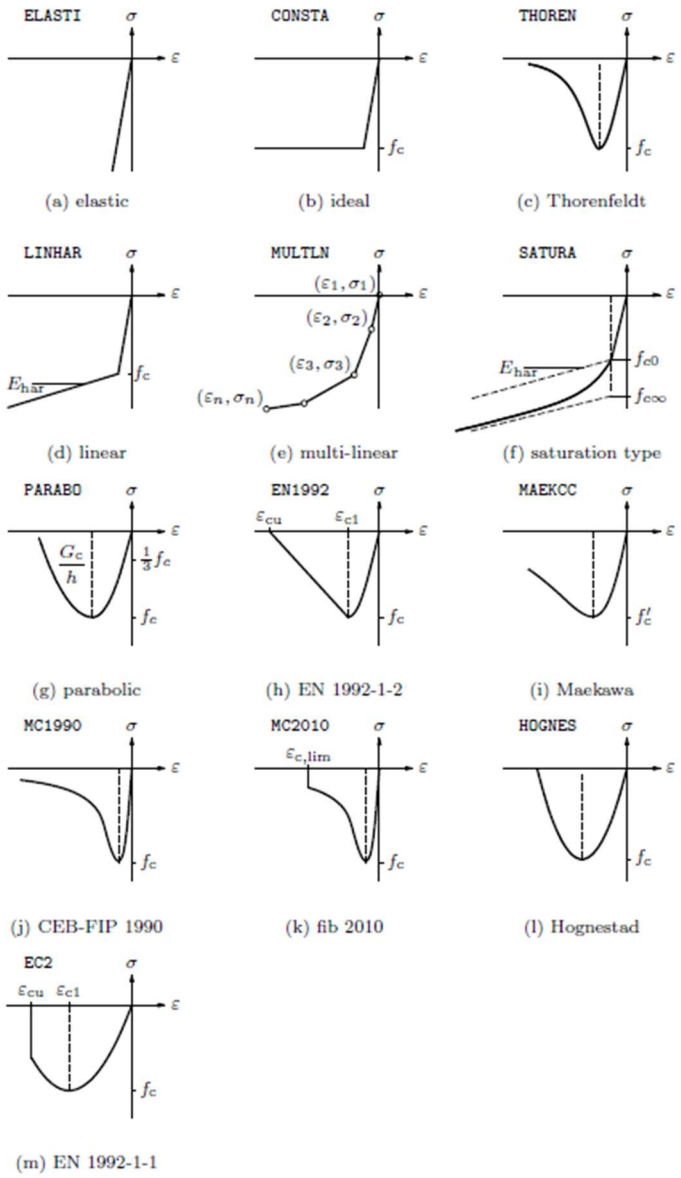

(a) elastic (b) ideal (c) Thorenfeldt

(d) linear (e) multi-linear (f) saturation type

(g) parabolic (h) EN 1992-1-2 (i) Maekawa

(j) CEB-FIP 1990 (k) fib 2010 (l) Hognestad

(m) EN 1992-1-1

Figure 5-4: Predefined compression behaviour for total strain model [167].

For the modelling of the modified push-out tests the parabolic model [170] was adopted (Figure 5-4g). The input properties of compressive parabolic relationship are summarized in Table 5-3.

Parabolic		*syntax*
'MATERI'		
1 5	6 12	13 80
	COMCRV	PARABO
	COMSTR	fc_r
	GC	gc_r
	[CRACKB	h_r]
	[RESCST	$sigres_r$]

Table 5-3: Input parameters for the compressive parabolic relationship.

Where:

- COMCRV indicates the type of function chosen for the compressive behaviour;
- COMSTR is the compressive strength of the concrete;
- GC is the compressive fracture energy, it is estimated to be 50 to 100 times the tensile fracture energy [170];
- CRACKB is the crack bandwidth;
- RESCST is the residual compressive strength, below which the compressive strength will not drop for large compressive strains.

5.2.3.2 Discrete cracking

Since the interfaces might play an important role in the overall structural behaviour of 3DPC elements, a discrete cracking approach was adopted to consider interface region and concrete layers separately.

As mentioned in section 5.2.1, to describe the compressive and the tensile behaviour of the concrete layers a *total strain model* was adopted, while for the interfaces the combined *cracking-shearing-crushing model*, also known as combined interface model, was used [164]. This model allows to take into account all the basic types of mechanisms that characterize the 3DPC material: a) interfacial cracking; b) interface shear slip; c) interlayer tensile strength; d) intralayer cracking under compression-shear e) crushing (Figure 5-5).

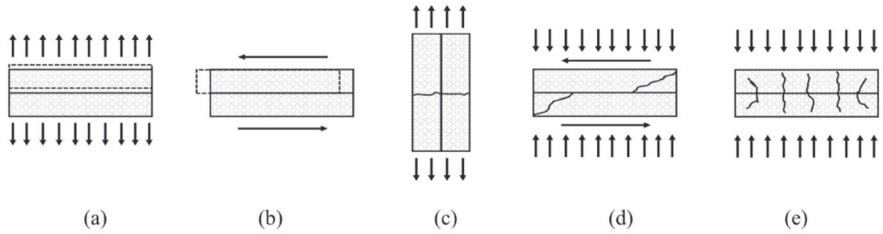

Figure 5-5: Failure mechanisms in 3DPC elements: (a) interfacial cracking (Mode I), (b) interface shear slip (Mode II), (c) interlayer tensile strength, (d) interlayer cracking under compression-shear and (e) crushing [171]

The domain is bounded by a composite yield surface that includes tension cut-off for tensile failure (Mode I), a Coulomb-friction envelope for shear (Mode II) and a cap model for compression failure (Figure 5-6).

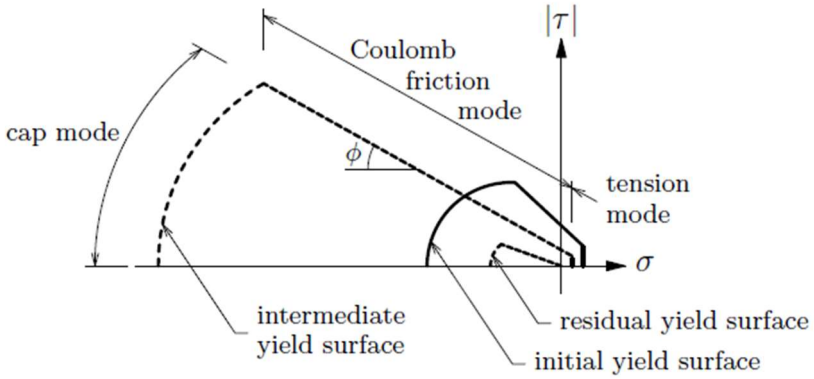

Figure 5-6: Two-dimensional composite interface model [164].

The required input parameters for the composite interface model are summarized in Table 5-4.

syntax

```
'MATERI'
1         5 6         12 13                                                80
          COMBIF
          COHESI     ch_r
          PHI        phi_r
          PSI        psi_r
         [PHIRED     phir_r
          SIGCON     sigu_r
          DEGRAD     delta_r]
          TENSTR     ft_r
          GF         gf1_r
          MO2VAL     [gf2a_r] gf2b_r
          COMSTR     fc_r
          CS         cs_r
          GC         gfc_r
          DUPEAK     kp_r
```

Table 5-4: Input parameters for the composite interface model.

Where:

- COMBIF indicated the use of the multi-surface interface yield criterion for combined cracking-shearing and crushing.
- COHESI is the cohesion c
- PHI is the angle of friction φ
- PSI is the dilatancy angle ψ
- PHIRED is the residual friction angle φ_r
- SIGCON is the confining normal stress σ_u for which the dilatancy coefficient is equal to zero [172]:

$$\tan\psi = \tan\psi_0 \left(1 - \frac{\sigma}{\sigma_u}\right) e^{-\delta v_p} \qquad 5\text{-}2$$

- Where v_p is the plastic shear displacement, ψ_0 is the dilatancy angle at zero confining stress and shear slip, σ_u is the pre-compression level at which the dilatancy goes to zero and δ is the dilatancy shear slip.
- DEGRAD is the exponential degradation coefficient δ of the dilatancy coefficient with shear-slipping displacement
- TENSTR is the tensile strength f_t
- GF is the fracture energy in tension (Mode I) G^I_f (calculated according equation 5-1, defining the area under the diagram for mode I (Figure 5-7).

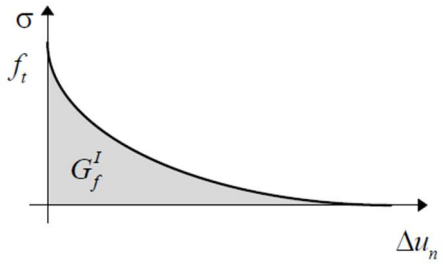

Figure 5-7: Behaviour of the model in tension (Mode I) [173].

- MO2VAL defines the Mode II fracture energy G^{II}_f (Figure 5-8) defined as:

$$G_f^{II} = a\sigma + b \quad 5\text{-}3$$

a and *b* are coefficients which can be determined from the linear regression of experimental data, if *a* is not specified it is taken as default equal to zero and the fracture energy is constant [167]. According to Lourenco [173] the Mode II fracture energy could also be assumed equal to $\frac{1}{10}c$ of the cohesion.

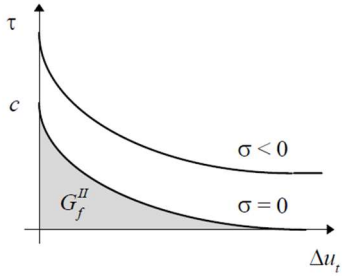

Figure 5-8: Behaviour of the model in shear (Mode II) [173].

- COMSTR is the compressive strength f_c that defines the cap criterion
- CS is a factor C_s that controls the shear traction contribution to compressive failure calculated as:

$$C_s \leq \sqrt{\frac{f_c}{c}} \quad 5\text{-}4$$

The compressive cap is described from the equation:

$$\sigma^2 + C_s\tau^2 = f_c \quad 5\text{-}5$$

Where σ and τ are the normal and the shear stress applied.

- GC is the compressive fracture energy G_{fc} estimated as according to the Model Code 1990 [174].

$$G_{fc} = 15 + 0.43\, f_c - 0.0036\, f_c^2 \quad 5\text{-}6$$

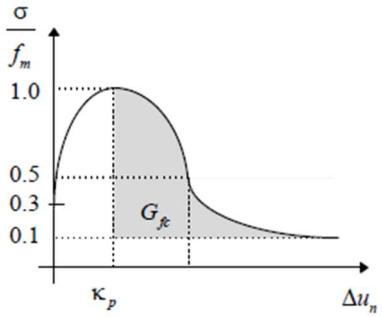

Figure 5-9: Behaviour of the model in compression [173] .

- DUPEAK is the equivalent plastic relative displacement k_p, corresponding to the peak compressive stress, which describes the compressive inelastic laws estimated
- The last two parameters to be defined are the normal stiffness modulus k_{nc} and the shear stiffness modulus k_{sn}, which is calculated as [171]:

$$k_{sc} = \frac{k_{nc}}{2 * (1 + \nu)} \qquad 5\text{-}7$$

5.2.3.3 Model parameters

In this section the materials parameters used in the model are listed. Most of them are based on the results of the experimental campaign illustrated in Chapter 3. The material parameters are presented for the smeared and discrete crack models, respectively.

5.2.3.3.1 Smeared cracking model

The material properties used for the *smeared crack model* were obtained from test results (see chapter 3) and are reported for *material type 1* (Table 5-5) and *type 2 (*Table 5-6*)*, respectively. It has to be specified that for both series of tests the steel plates were modelled using quadratic plane stress elements with a linear elastic behaviour. The elastic modulus and the Poisson coefficient were equal to 210 GPa and 0.3, respectively.

Elastic modulus	E	MPa	31000
Poisson ratio	ν	-	0.2
Crack orientation	-	-	rotating
Tensile strength	f_{ctm}	MPa	3.4
Fracture energy Mode I	G^I_f	N/mm	0.15
Compressive strength	f_{cm}	MPa	74.85
Compressive fracture energy	G_c	N/mm	10

Table 5-5: Material type 1: input parameters for the total strain based crack model.

Elastic modulus	E	MPa	35000
Poisson ratio	ν	-	0.2
Crack orientation	-	-	rotating
Tensile strength	f_{ctm}	MPa	2.8
Fracture energy Mode I	G^I_f	N/mm	0.15
Compressive strength	f_{cm}	MPa	57.67
Compressive fracture energy	G_c	N/mm	10

Table 5-6: Material type 2: input parameters for the total strain based crack model.

5.2.3.3.2 Discrete cracking model

As mentioned in section 5.2.1, to describe the compressive and the tensile behaviour of the concrete layers a *total strain model* was used (the same properties mentioned in section 5.2.3.3.1 are used), while for the interfaces the *combined interface model*, whose properties are listed in Table 5-7 and Table 5-8 for *material type 1* and *material type 2*, respectively. The tensile strength, the cohesion, the angle of friction and the compressive strength are experimental data, the other parameters are estimated using the formulations given in section 5.2.3.2.

Normal stiffness modulus	k_{nc}	N/mm^3	1000
Shear stiffness modulus	k_{sc}	N/mm^3	500
Tensile strength	f_{ctm}	MPa	3.4
Fracture energy Mode I	G^I_f	N/mm	0.15
Cohesion	c	MPa	6
Angle of friction	ϕ	°	60
Dilatancy angle	ψ	°	0
Residual friction angle	ϕ_r	°	30
Confining normal stress	σ_u	MPa	-1
Exponential degradation coefficient	δ	-	1
Fracture energy mode II	G^{II}_{fc}	N/mm	0.6
Parameter a	a	mm	0
Parameter b	b	N/mm	0.6
Compressive strength	f_{cm}	MPa	75
Factor Cs	C_s	-	3.53
Compressive fracture energy	G_c	N/mm	27.74
Equivalent plastic relative displacement	κ_p	-	0.002

Table 5-7: Material type 1: input parameters for the combined interface model.

Normal stiffness modulus	k_{nc}	N/mm³	600
Shear stiffness modulus	k_{sc}	N/mm³	300
Tensile strength	f_{ctm}	MPa	2.8
Fracture energy Mode I	G^{I}_{f}	N/mm	0.15
Cohesion	c	MPa	6
Angle of friction	ϕ	°	54
Dilatancy angle	ψ	°	0
Residual friction angle	ϕ_r	°	25
Confining normal stress	σ_u	MPa	-1
Exponential degradation coefficient	δ	-	1
Fracture energy mode II	G^{II}_{fc}	N/mm	0.6
Parameter a	a	mm	0
Parameter b	b	N/mm	0.6
Compressive strength	f_{cm}	MPa	58
Factor Cs	C_s	-	3.10
Compressive fracture energy	G_c	N/mm	27.82
Equivalent plastic relative displacement	κ_p	-	0.002

Table 5-8: Material type 2 Input parameters for the combined interface model.

5.2.4 Boundary conditions

5.2.4.1 Constraints and loads

The constraints and the applied loads are shown in Figure 5-10 The boundary conditions consist of vertical translation (y-direction) constraints at the bottom surface of the supporting steel plate and a horizontal translation (x-direction) constraint at the bottom left corner of the supporting steel plate. Due to symmetry, horizontal constraints are placed along the right-hand surface. The upper load blocks were subjected to a prescribed deformation in the negative y-direction. Moreover, as mentioned in Chapter 3 different levels of precompression (0 MPa, 1 MPa, 2 MPa, 4 MPa, and 6 MPa) were applied as a distributed load on the lateral surface of the specimen.

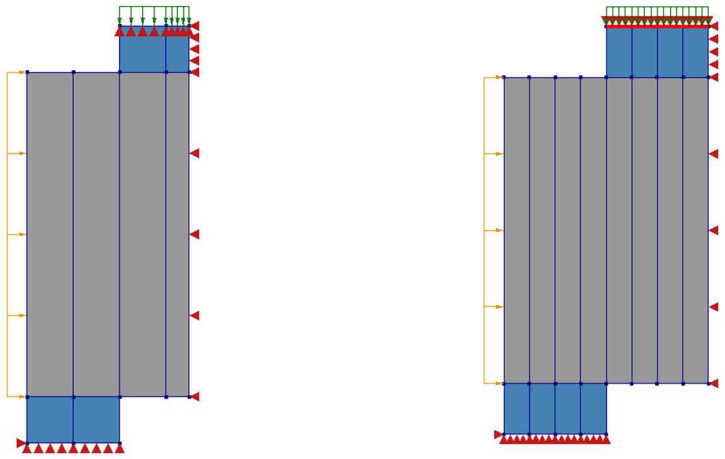

(a) (b)

Figure 5-10: Modified push-out test boundary conditions: (a) material type 1 and (b) material type 2.

5.2.4.2 Interfaces

5.2.4.2.1 Steel to concrete interface

Interface elements were used for the contact surface between the specimens and the steel support at the bottom, as shown in Figure 5-11.

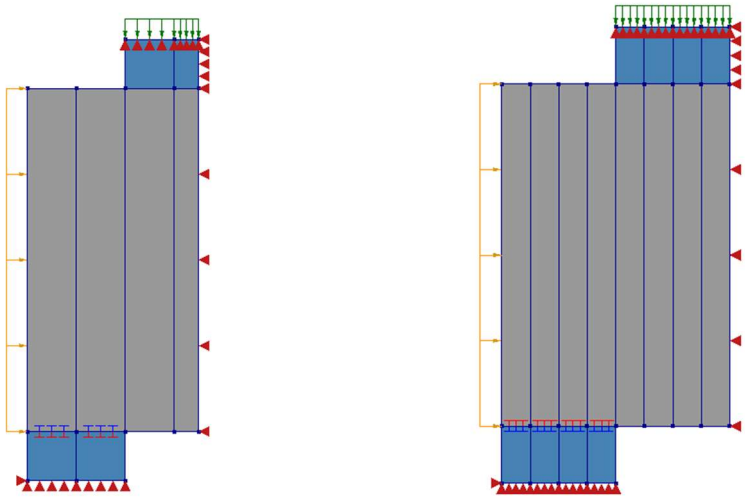

(a) (b)

Figure 5-11: Mohr-coulomb model interface between the concrete specimens and the bottom steel plate: (a) material type 1 and (b) material type 2.

A *Coulomb friction interface model* was chosen to represent a condition as much as possible realistic. In fact, when the cracking process starts, it allows sliding between the concrete and the steel plates, albeit to a minimal extent. Figure 5-12 shows the constitutive relationship and it is represented by the following equation:

$$t_t = t_n \tan\phi + c \qquad 5\text{-}8$$

Where t_t represent the shear stresses, t_n are the normal stresses, ϕ is the angle of friction and c is the cohesion.

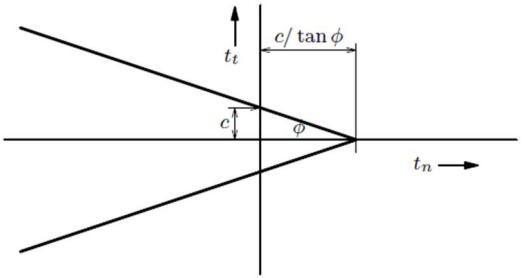

Figure 5-12: Coulomb friction criterion [167].

Table 5-9 shows the input values used for the *coulomb friction interface model* to ensure minimum adhesion between steel and concrete. A friction angle equal to 10° is a typical value between concrete and steel.

Cohesion	c	N/mm²	0
Angle of friction	ϕ	°	10
Dilatancy angle	ψ	°	0

Table 5-9: Input parameters for the Coulomb friction interface model.

Furthermore, it is necessary to specify the type of interface opening, which can either be a *gapping model* or a *tension cut-off*. The *gapping model* allows the sliding and a gap to arise if the tensile traction t_n normal to the interface exceeds a certain value. Once a gap is formed, the tensile strength immediately drops to zero, causing brittle cracking. On the other hand, the *tension cut-off* only permits sliding and is chosen in this particular case to ensure sliding between the specimen and the bottom plate. It is also required to provide the values of the normal and shear stiffness, with a high value of 10^9 N/mm³ assigned to the normal stiffness and a very low value of 10 N/mm³ assigned to the shear stiffness.

5.2.4.2.2 Discrete cracking

When using the discrete cracking approach, an interface was placed between the layers where the failure was induced to simulate the local effects between two printed layers (Figure 5-13). Table 5-7 and Table 5-8 list the properties used for the specimens printed with material type 1 (Figure 5-13a) and material type 2 (Figure 5-13b), respectively.

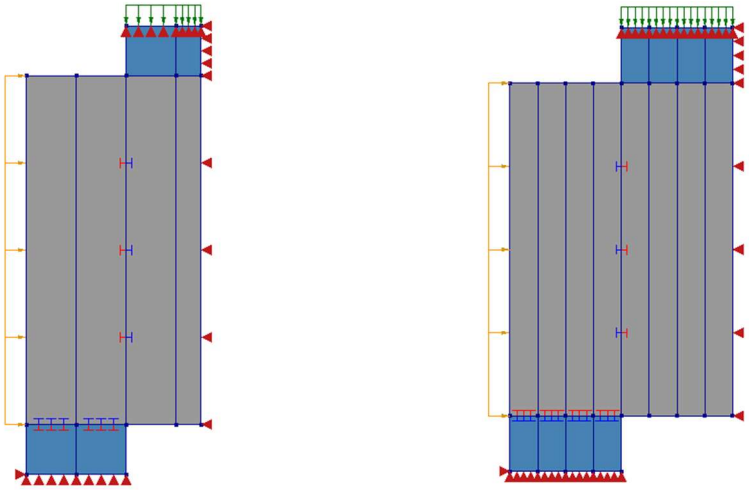

(a) (b)

Figure 5-13: Combined interface model between concrete layers: (a) material type 1 and (b) Material type 2.

5.2.4.3 Mesh

Four-node quadrilateral elements (Q8MEM) were used to simulate concrete and steel elements. Linear interface elements (L8IF) were used to simulate both the steel-concrete interface, and the interface between the concrete layers. The size of the single element was chosen to be 5 mm x 5 mm for both specimen configurations, as shown in Figure 5-14.

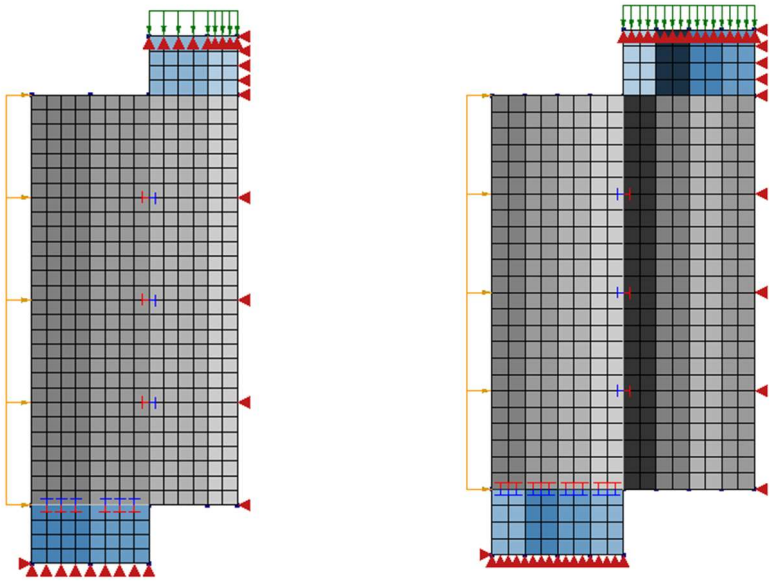

(a) (b)

Figure 5-14: Mesh size: (a) material type 1 and (b) material type 2.

The Q8MEM element is a four-node quadrilateral plane stress element. It is based on linear interpolation and Gauss integration. The program applies a 2×2 integration scheme (Figure 5-15).

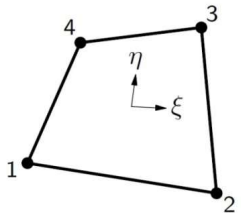

Figure 5-15: plane stress element Q8MEM [167].

The L8IF element is an interface element between two lines in a two-dimensional configuration. The local *xy* axes for the displacements are evaluated in the first node with *x* directed from node 1 to node 2. The element is based on linear interpolation (Figure 5-16).

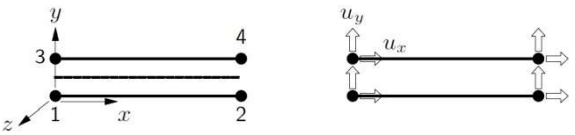

Figure 5-16: L8IF topology and displacements [167].

5.2.5 Validation of the model

The results obtained from the finite element modelling are compared with the experimental results considering both series of modified push-out tests.
The results presented in this section are the outcome of several steps. The first step was to consider a smeared cracking approach and to place a hinge in the bottom corner between the specimen and the steel plate (Figure 5-17a). In this case, the behaviour of the specimen resulted to be too stiff and exhibited concrete matrix failure below the loading point, even when prestressing was not applied. In fact, in this case, when the cracking process begins, sliding between the specimen and the bottom plate is not allowed. The next step was to modify the constraint by inserting a spring to allow relative displacement between the specimen and the bottom plate according to the stiffness of the spring (Figure 5-17b). To examine the impact of the spring stiffness on the failure mode of the specimens, different analysis were conducted to calibrate it. It was observed that with a stiffness k of less than 1000 N/mm, the specimens failed by bending at the centre of the specimen (one crack in the middle); for a stiffness between $1000<k<100000$ N/mm, the specimen failed along the interface of the concrete layer, which was the expected mechanism. However, for a stiffness k greater than 100000 N/mm, the specimens showed concrete matrix failure below the loading point. Based on these conclusions, it has been decided to introduce an interface between the concrete and the steel bottom plate using the Coulomb friction interface model, since it is more representative of the reality, with a shear stiffness of 10 kN/mm^3 (Figure 5-17c). Thus, considering an elastic stiffness k of 10000 N/mm and dividing it by the area of the steel plate (40x40 mm^2), a shear stiffness of 10 N/mm^3 is obtained (which is the value used in all the numerical analysis see section 5.2.4.2.1). Finally, a discrete cracking approach has been adopted by adding an interface between the concrete layers to investigate the local behaviour between two concrete layers and to detect any differences from a smeared cracking approach.

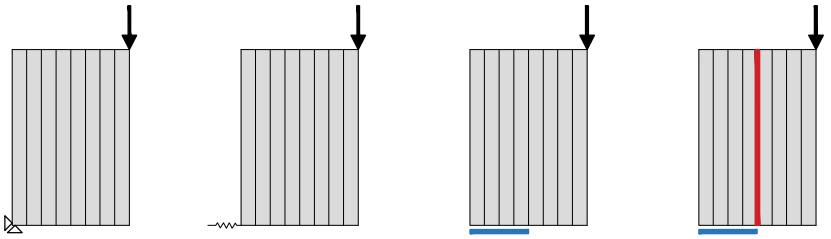

Figure 5-17: Configuration considered for the modified push-out numerical analysis: (a)-(c) smeared cracking approach with different constraints configuration between the specimen and the bottom steel plate, (d) discrete cracking approach.

5.2.5.1 Modified push-out test of specimens printed with material type 1

The FE simulation results are shown, at each pre-compression level (0 MPa, 2 MPa, 4 MPa, and 6 MPa), in terms of shear stresses versus vertical relative displacement in Figure 5-18 and Figure 5-20 for the smeared and discrete cracking approach, respectively. Moreover, the crack patterns obtained from the numerical simulation are shown in Figure 5-19 and Figure 5-21 through the crack strains considering the smeared and discrete cracking approach, respectively. It should be noted that the experimental results from this testing campaign showed scattered results (the specimens with 2 MPa precompression applied), which could be attributed to potential errors during the testing procedure, since the test setup was still being refined.

With regard to the smeared cracking approach, it is evident that the numerical results seem to be in good agreement with the experimental ones (Figure 5-18). The first linear segment branch up to the peak was well approximated for each prestressing level; the post-peak phase was accurately predicted for the specimens without confinement (Figure 5-18a) and for those with confinement of 4 MPa (Figure 5-18c). The presence of different peaks in some experimental curves may suggest that the failure did not start simultaneously in both mortar joints. However, given the symmetric nature of the modelled specimens, this aspect was not captured by the numerical analysis. As presented in Chapter 3, the specimens subjected to prestressing of 6 MPa exhibited a concrete matrix failure below the loading point. Consequently, the numerical curve also did not show post-peak behaviour (Figure 5-18d), since the failure occurred once the compressive strength of the material was reached, which occurred before the maximum shear strength. The use of the smeared cracking approach enabled the identification of the crack patterns observed during the experimental campaign. Specifically, concrete layer interface failure was detected in specimens subjected to 0 MPa, 2 MPa, and 4 MPa precompression (Figure 5-19a, b

and c). In contrast, the specimens with 6 MPa precompression exhibited concrete matrix failure under the loading point (Figure 5-19d)

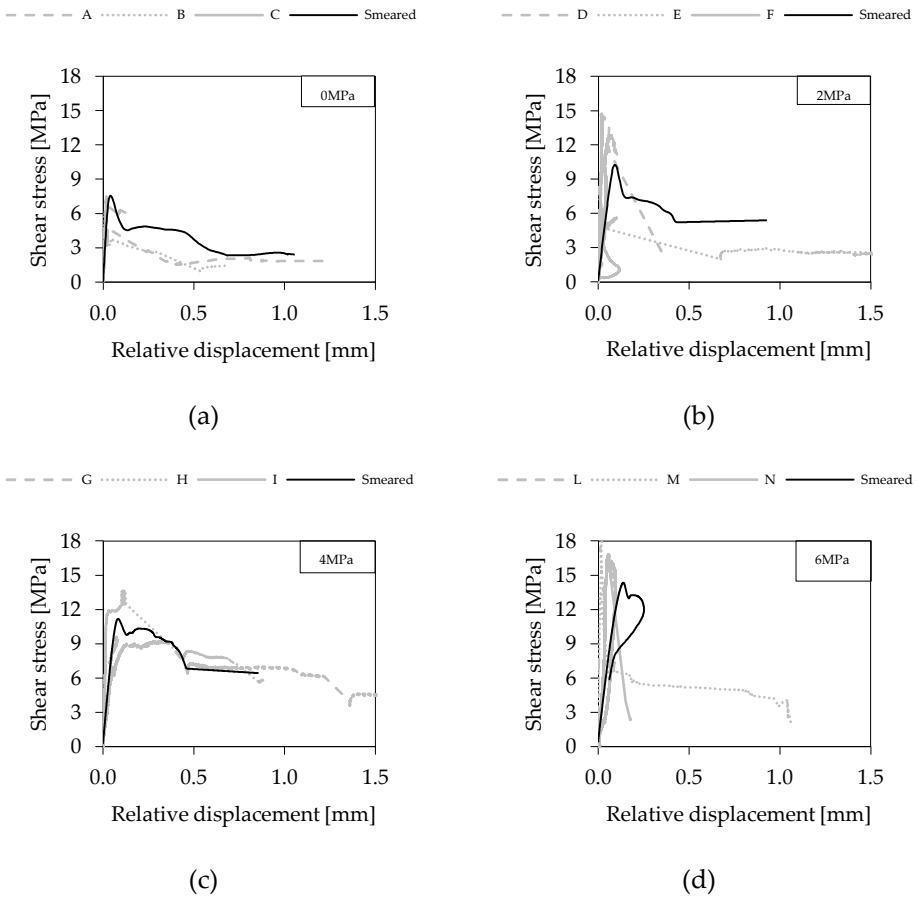

Figure 5-18: Shear stress versus relative vertical displacement with the smeared cracking approach: (a) 0 MPa, (b) 2 MPa, (c) 4 MPa and (d) 6 MPa precompression applied.

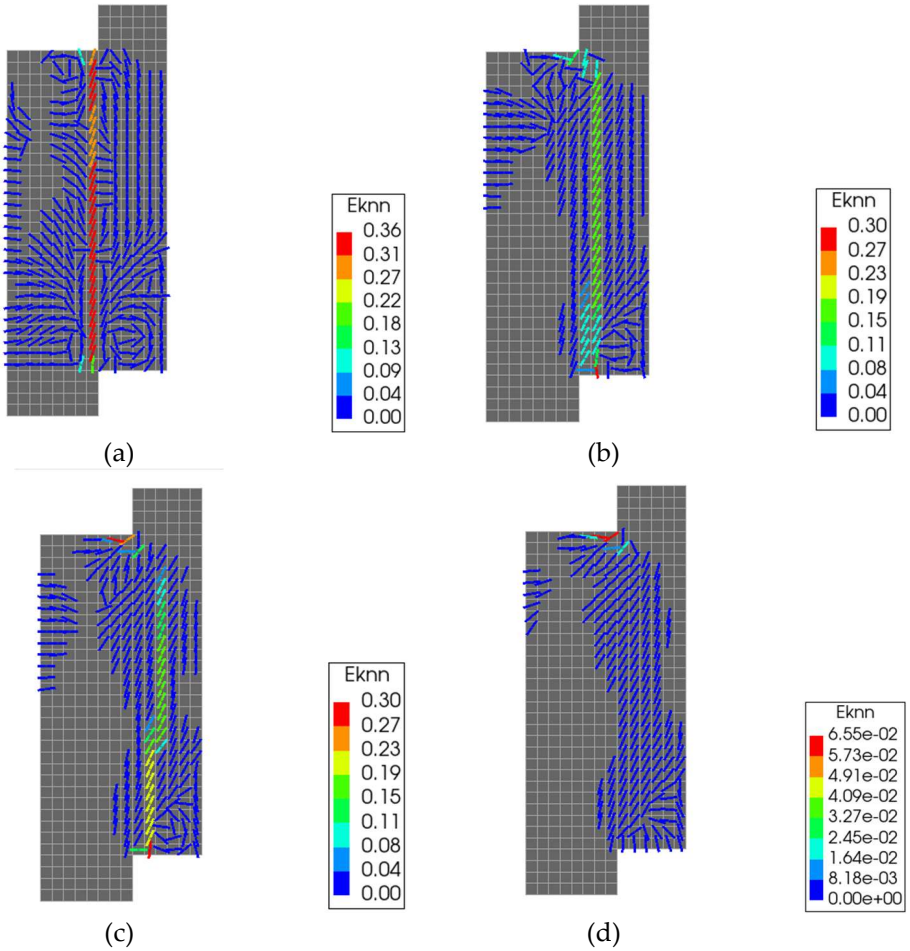

Figure 5-19: Crack patterns observed with the smeared cracking approach: (a) 0 MPa, (b) 2 MPa, (c) 4 MPa and (d) 6 MPa precompression applied.

With regard to the discrete cracking approach, the initial linear branch was accurately approximated for each prestress level (Figure 5-20). The post-peak phase was well predicted for specimens subjected to 0 MPa (Figure 5-20a) and 4 MPa prestress (Figure 5-20c). However, the post-peak behaviour was not representative for the specimens with 2 MPa prestress because, as mentioned above, the experimental results presented some inconsistencies (Figure 5-20b). In addition, this approach was not able to predict the behaviour of specimens subjected to 6 MPa prestress, since they showed concrete matrix failure below the loading point, but discrete cracking interface approach is not able to capture this failure mode since the crack is concentrated exclusively at the interface. Figure 5-21 shows the crack pattern obtained with the discrete interface model, which exhibited crack along the interface.

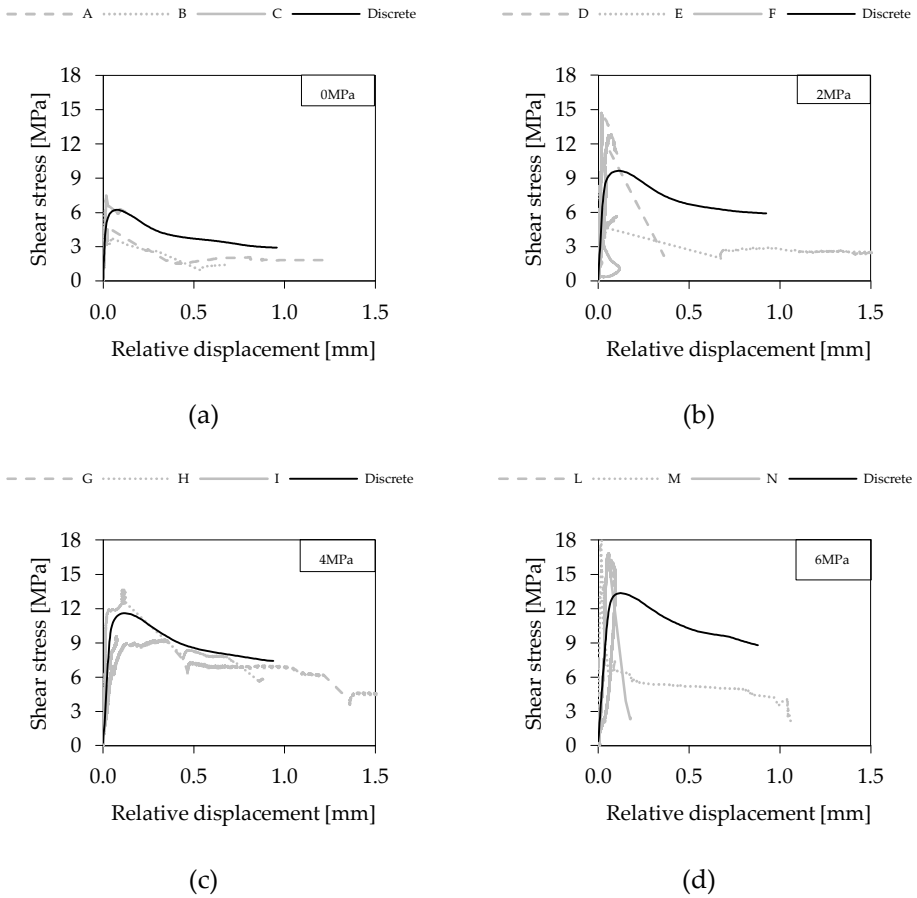

Figure 5-20: Shear stress versus relative vertical displacement with the discrete cracking approach: (a) 0 MPa, (b) 2 MPa, (c) 4 MPa and (d) 6 MPa precompression applied.

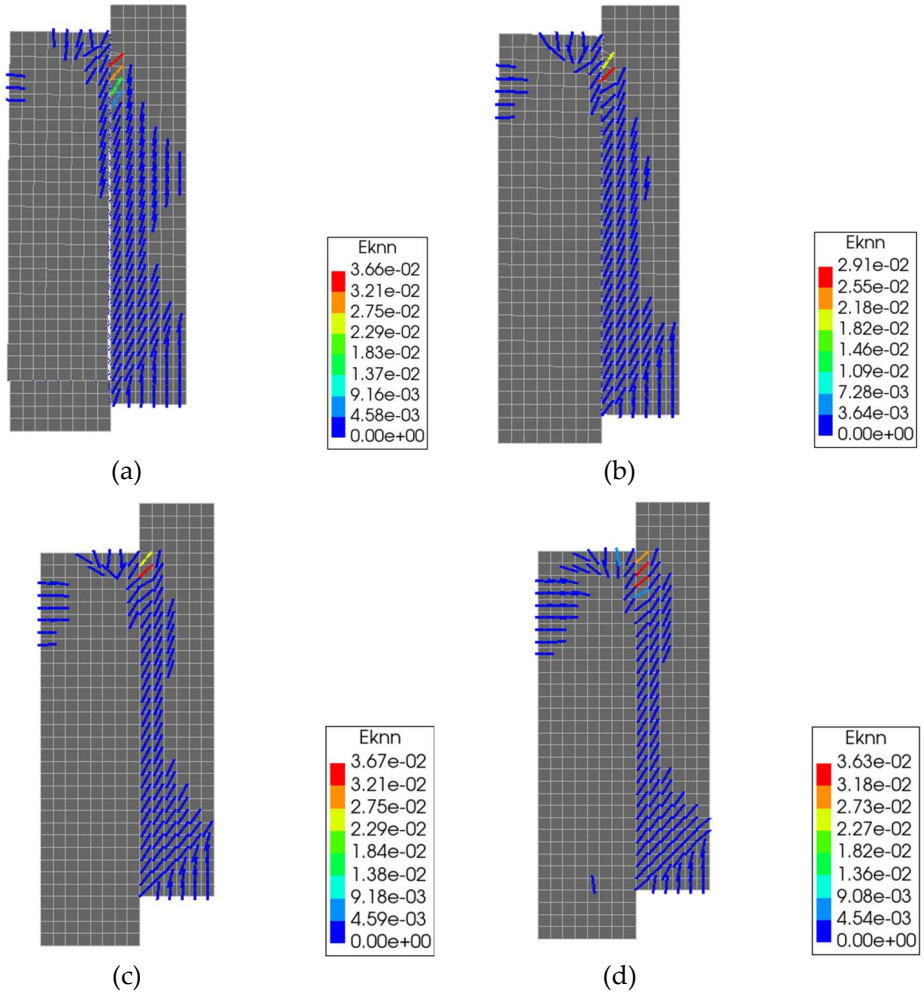

Figure 5-21: Crack patterns observed with the discrete cracking approach: (a) 0 MPa, (b) 2 MPa, (c) 4 MPa and (d) 6 MPa (not representative) precompression applied.

Comparing the two modelling approaches, it can be concluded that both predict well the behaviour of specimens subjected to modified push-out tests. The smeared cracking approach was effective in capturing concrete matrix failure under the loading point, while the discrete cracking model could be more appropriate for studying the behaviour of interfaces between layers particularly with defects, such as cold joints. Table 5-10 compares the maximum shear strength obtained from the experiments with that predicted by the smeared cracking and discrete cracking approaches. For specimens with 0 MPa and 4 MPa precompression applied, the finite element approaches overestimated/underestimated the maximum shear strength by

5%-10%, which is considered acceptable. A significant difference between the two modelling approaches was not observed. Thus, they are both considered reliable.

		Shear stress [MPa]	
Precompression	experimental	Smeared cracking	Discrete cracking
0 MPa	5.83	7.54 (+20%)	6.23 (+6%)
2 MPa	11.93	10.23 (-14%)	9.63 (-19%)
4 MPa	10.63	11.18 (+4%)	11.59 (+7%)
6 MPa	18.06	14.33 (-20%)	13.35 (-26%)

Table 5-10: Comparison between the maximum shear strength obtained from experimental results and with the smeared and discrete cracking approach.

5.2.5.2 Modified push-out test of specimens printed with material type 2

The finite element simulation results are shown, at each pre-compression level, in terms of shear stresses versus vertical relative displacement in Figure 5-22 and Figure 5-24 for the smeared and discrete cracking approach, respectively. Furthermore, the cracking patterns obtained from the numerical simulation are shown in Figure 5-23 and Figure 5-25 through the cracking strains for the smeared and discrete cracking approach, respectively. As discussed in Chapter 3, this was the second series of modified push-out test; the setup was improved and the specimens dimensions were modified accordingly to avoid concrete matrix failure below the loading point. The numerical results of the smeared cracking approach are in good agreement with the experimental ones (Figure 5-22). Up to the peak load the linear behaviour was well represented by the curve obtained from the numerical analysis. It is observed that the higher the level of prestress, the better is the approximation of post-peak behaviour by the curve obtained from the numerical analysis.

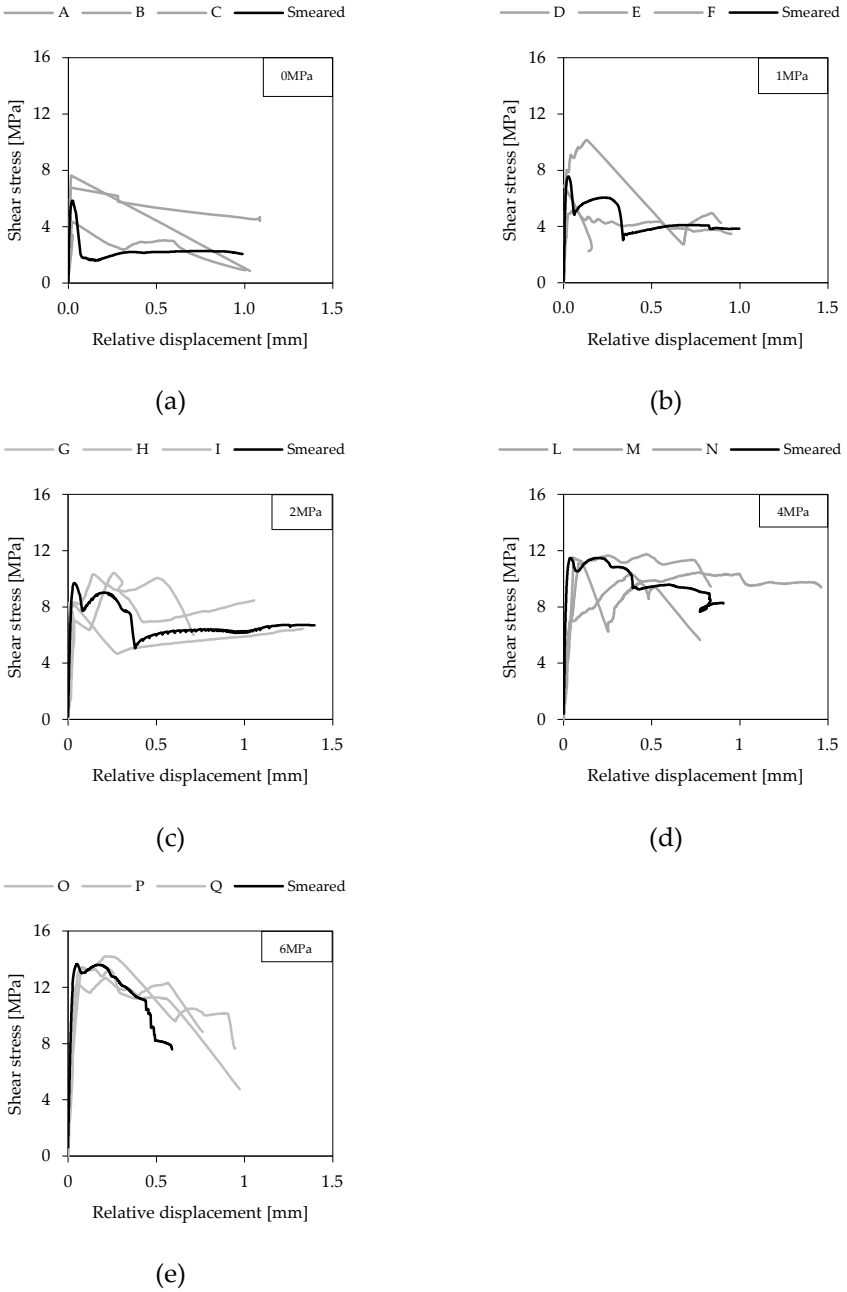

Figure 5-22: Shear stress versus relative vertical displacement with the smeared cracking approach: (a) 0 MPa, (b) 1 MPa, (c) 2 MPa, (d) 4 MPa and (e) 6 MPa precompression applied.

It should be observed that using the smeared cracking approach, it was possible to replicate the cracking patterns observed in the experimental campaign, which corresponds to concrete layer interface failure for all applied prestressing levels (Figure 5-23).

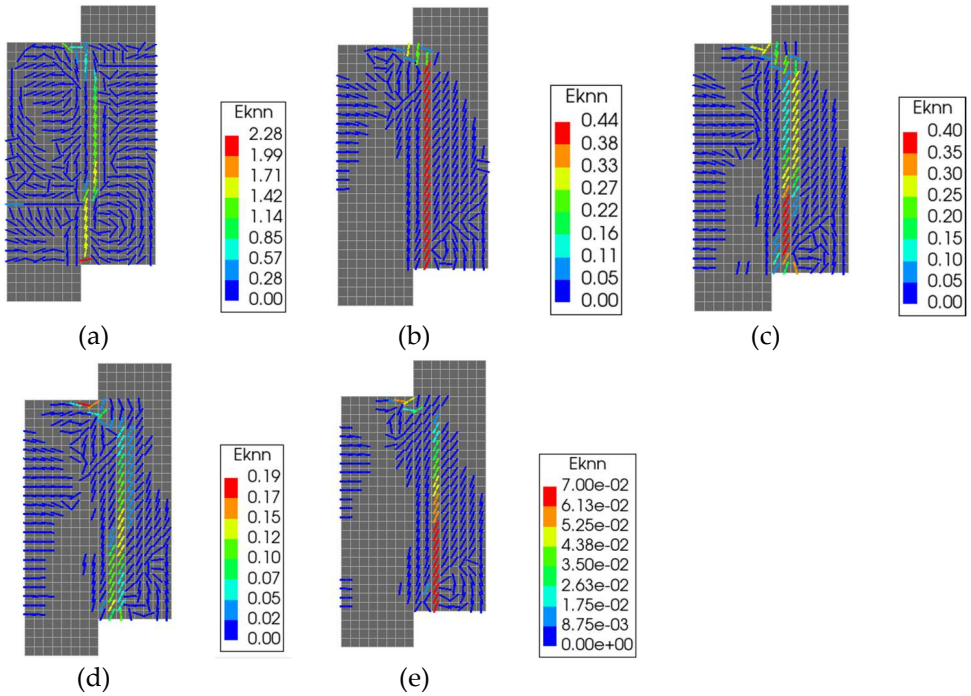

Figure 5-23: Crack patterns observed with the smeared cracking approach: (a) 0 MPa, (b) 1 MPa, (c) 2 MPa, (d) 4 MPa and (e) 6 MPa precompression applied.

With regards to the discrete cracking approach it can be observed that the up to the peak load the behaviour of all the specimens, at each precompression level was well represented by the numerical curve (Figure 5-24). The discrete cracking model was able to accurately approximate the behaviour at each prestress level. Figure 5-25 shows the cracking pattern obtained from the discrete cracking model at each prestress level, showing concrete layer interface failure along the interface.

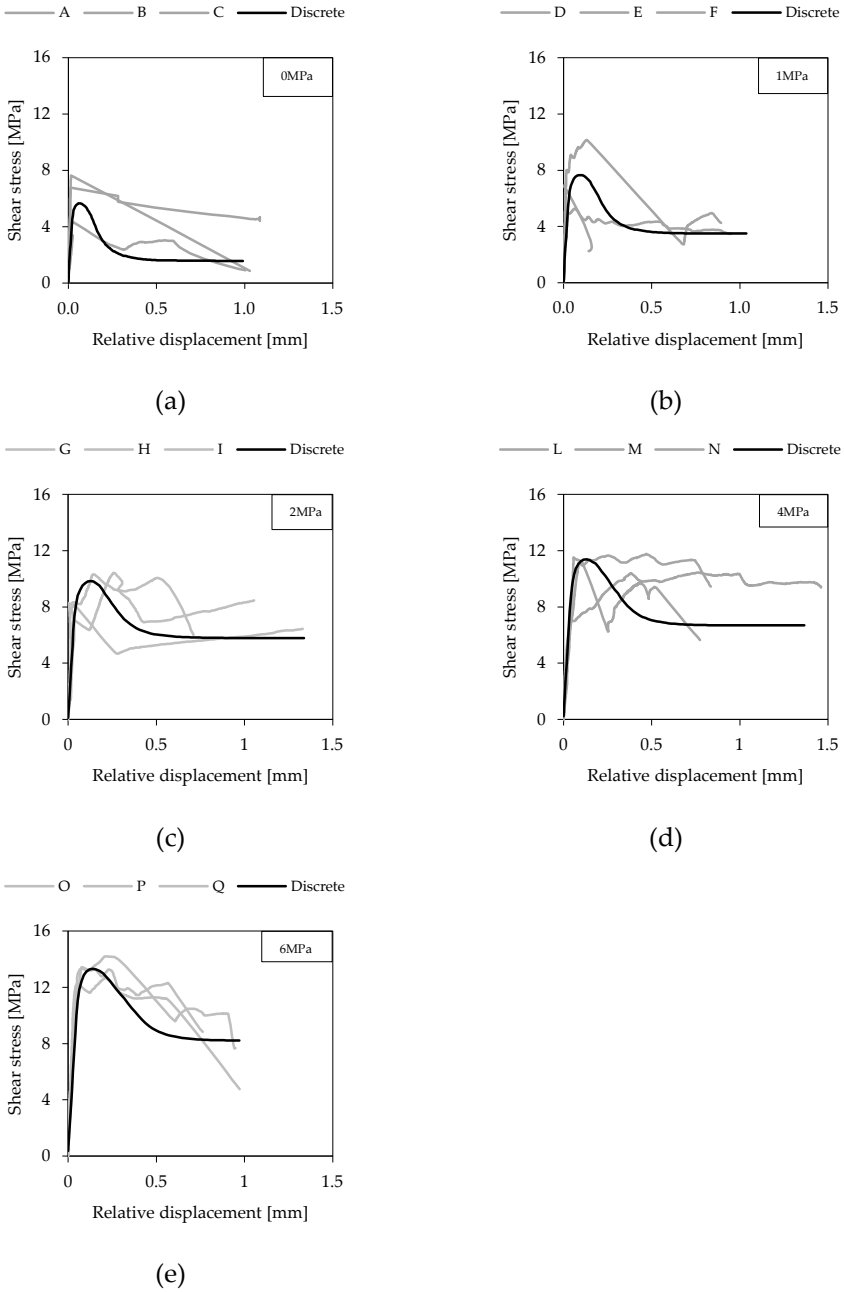

Figure 5-24: Shear stress versus relative vertical displacement with the discrete cracking approach: (a) 0 MPa, (b) 1 MPa, (c) 2 MPa, (d) 4 MPa and (e) 6 MPa precompression applied.

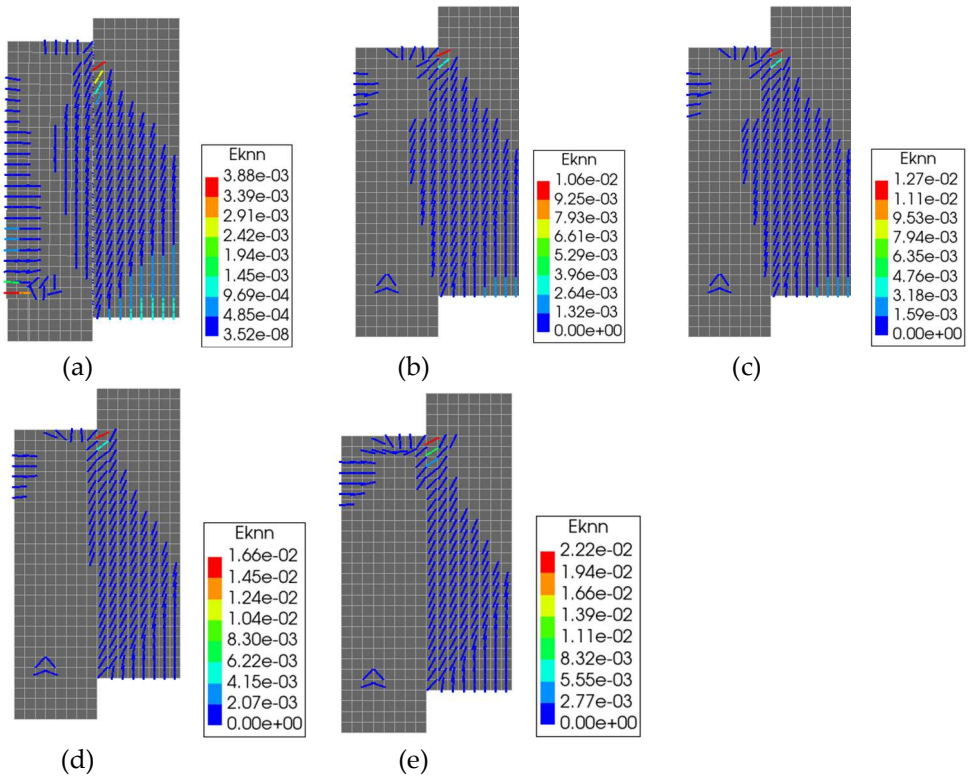

Figure 5-25: Crack patterns observed with the discrete cracking approach: (a) 0 MPa, (b) 1 MPa, (c) 2 MPa, (d) 4 MPa and (e) 6 MPa precompression applied.

Comparing the two modelling approaches, it can be concluded that both methods represent well the behaviour of specimens subjected to modified push-out tests. In fact, the approximation obtained is better than in the previous series of tests (specimens printed using material type 1), since the experimental results were less dispersive. Table 5-11 shows a comparison between the maximum shear strength obtained from the experiments and that obtained with the smeared cracking and discrete cracking approaches. It can be seen that the finite element approach overestimates or underestimates the maximum shear strength in the range of 1% to 10%, which is considered acceptable.

Precompression	Experiment	Smeared cracking	Discrete cracking
0 MPa	6.24	5.84(-6%)	5.66(-9%)
1 MPa	7.48	7.55(+1%)	7.67(+3%)
2 MPa	9.63	9.70(+1%)	9.83(+2%)
4 MPa	11.23	11.48(+3%)	11.38(+2%)
6 MPa	13.40	13.65(+2%)	13.31(-1%)

Table 5-11: Comparison between the maximum shear strength obtained from experimental results and with the smeared and discrete cracking approach.

5.2.5.3 Failure criteria

The comparison between the experimental results and the finite element results is carried out also in terms of shear stress versus normal stress. With the linear regression of the data, it is possible to obtain the shear properties: the cohesion and the angle of friction. Considering the first series of modified push-out tests (specimens printed with *material type 1*), the cohesion and the angle of friction were found to be 6.02 MPa and to 60°, respectively. The Mohr-Coulomb failure envelope derived from the experiments and finite element approaches are in good agreement. The cohesion and the angle of friction obtained with the smeared cracking approach were equal to 5.91 MPa and 59°, respectively with an underestimation of about 2% (red line in Figure 5-26a). On the other hand, the cohesion and the angle of friction obtained with the discrete cracking approach were equal to 5.68 MPa and 60°, respectively, with an underestimation of about 6% compared to the experimental results (red line in Figure 5-26b).

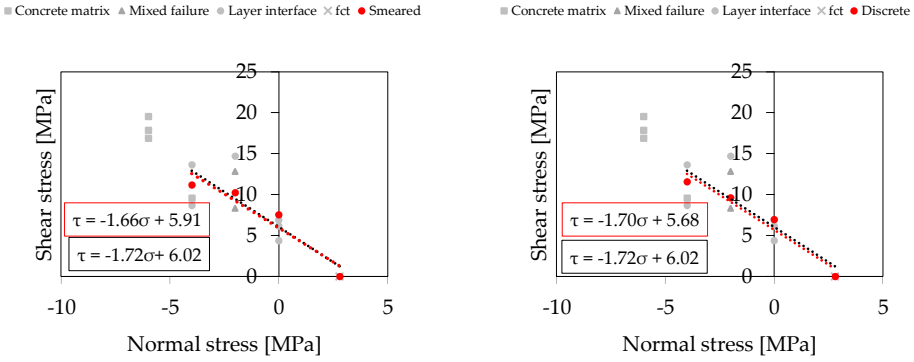

(a) (b)

Figure 5-26: Mohr-Coulomb failure envelope: specimens printed using material type 1: (a) smeared cracking approach and (b) discrete cracking approach.

In the second series of modified push-out tests (specimens printed using *material type 2*), the cohesion and angle of friction were found to be 5.95 MPa and 54°, respectively. The Mohr-Coulomb failure envelope derived from finite element approaches matches well with that found form the experimental results (red lines in Figure 5-27). Using the smeared cracking approach, the cohesion and angle of friction were found to be 5.43 MPa and 57°, respectively. Using the discrete cracking approach, the cohesion and angle of friction were found to be 5.42 MPa and 56°, respectively. The angle of friction is overestimated by 5% and 3% using the smeared cracking approach and the discrete cracking approach, respectively. The cohesion is underestimated by 8% using both the smeared and the discrete cracking approach.

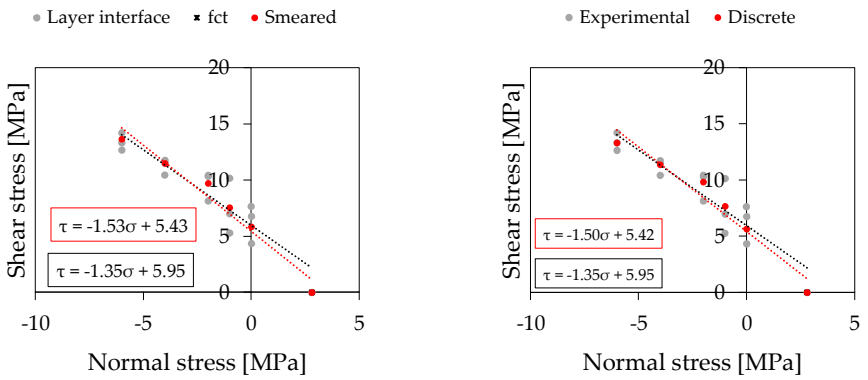

(a) (b)

Figure 5-27: Mohr-Coulomb failure envelope: specimens printed using material type 2: (a) smeared cracking approach and (b) discrete cracking approach.

5.3 Numerical analysis of 3D printed concrete walls

5.3.1 Modelling approach

Within this section, the Finite Element modelling using the software DIANA FEA of the unreinforced 3DPC wall printed with material type 2 (see section 4.2.2) is described. The wall was printed without any stops of printing process and as consequence it was decided to use a smeared cracking approach, which consider the wall as a continuum element without distinction between filament layers and interface regions. A 2D modelling approach is proposed using plane stress elements.

5.3.2 Geometrical properties

The unreinforced wall printed with *material type 2* was 210 cm high, 210 cm wide and 38.5 cm thick, it was made by 191 layers with an average thickness of 1.1 cm (see Figure 4-16). As described in section 4, the cross-section of the wall can be simplified with an equivalent double -T cross-section (Figure 5-28).

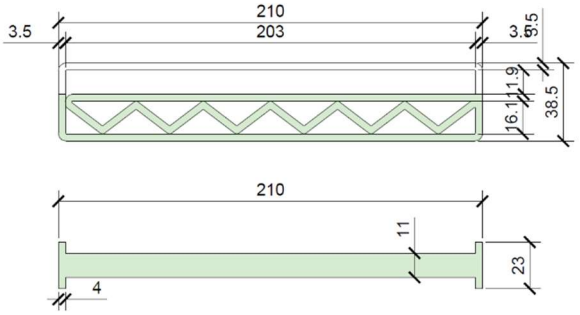

Figure 5-28: Equivalent cross-section.

Figure 5-29 shows the geometry of the 3DPC walls used for the finite element analysis. As described in Chapter 4, at the top and bottom of the walls there were two concrete corbels with a height of 20 cm and a thickness of 23 cm for the application of the horizontal load and the connection with the bottom foundation, respectively. Those corbels are represented in dark grey in Figure 5-29. The central part of the wall was represented as a double-T cross-section (Figure 5-28), the web is indicated in light grey and the flanges in dark grey. The web was 11 cm thick and the flanges were 23 cm.

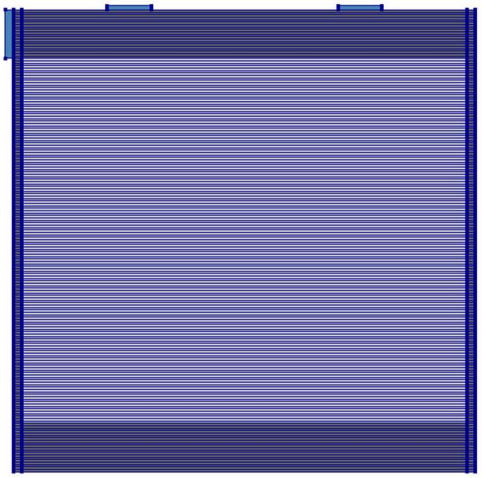

Figure 5-29: In-plane wall test geometry.

5.3.3 *Material properties*

As mentioned, the wall was modelled using a smeared rotating cracking approach. The Total Strain Base Crack Model was used to describe the behaviour of the concrete in tension and in compression. The tensile behaviour was described using the tensile constitutive law described in section 4.5.2 (see Figure 4-74), as shown in Figure 5-30.

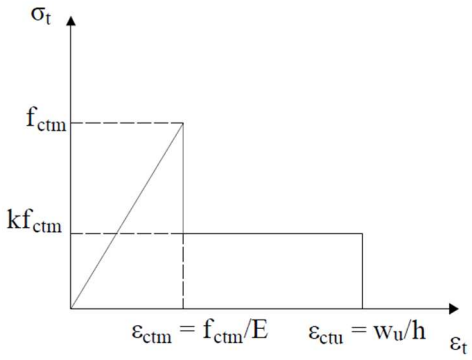

Figure 5-30:Tensile constitutive law used for the 3DPC material.

Where f_{ctm} is the maximum tensile strength, k is a reductive coefficient equal to 0.3 (see section 4.5.2), ε_{ctm} is the tensile strain in correspondence of the maximum tensile strength and ε_{ctu} is the ultimate strain calculated as the ratio between the ultimate crack opening w_u and the crack bandwidth h calculated with the formulation of Rots [169] as:

$$h = \sqrt{2A} \qquad 5\text{-}9$$

Where A is the total area of the element.

The compressive behaviour was represented with a parabolic constitutive law. The material properties used are the same of section 5.2.3 (see Table 5-6). Regarding the linear properties, an elastic modulus E equal to 37000 MPa and a Poisson's coefficient ν of 0.2 were employed. The tensile strength f_{ctm} was equal to 2.8 MPa (see Table 3-21) and the Mode I tensile fracture energy G^{I}_{f} to 0.15 N/mm (see equation 5-1).
The compressive strength f_{cm} and the compressive fracture energy G_c were equal to 58 MPa (see Table 3-10) and 10 N/mm, respectively.
To the concrete corbels were given elastic properties both in tension and in compression with an elastic modulus of 30 GPa and a Poisson's coefficient equal to 0.2. To the loading plates, for the application of the vertical and horizontal load, was given as well a linear elastic behaviour with an elastic modulus of 210 GPa and a Poisson's coefficient of 0.3.

5.3.4 Boundary conditions

5.3.4.1 Constrains and loads

The model boundary conditions comprise vertical translation (y-direction), horizontal translation (x-direction) and the rotation at the bottom of the wall (Figure 5-31). The horizontal load is applied as a monotonic prescribed deformation equal to 10 mm. The constant vertical load, which represents the load of a two-storey building, is applied on two steel plate 20 cm wide and a thickness equal to the thickness of the wall of 23 cm. The applied load is equal to 200 kN (500 N/mm), which represents the load of a two-storey building.

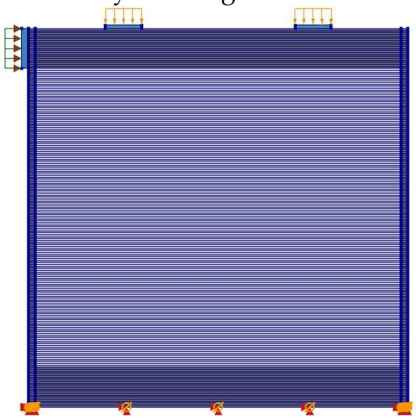

Figure 5-31: In-plane wall test boundary conditions.

5.3.4.2 Interface

It should be observed that between the bottom concrete corbel and the upper part of the wall there is a discontinuity in terms of materials and in terms of cross-section. The material used for the concrete corbel was normal strength concrete and it was

different from the 3D printed material. Moreover, the corbel has a rectangular cross-section 2.10 m long and 23 cm thick, while the cross-section of the wall is considered as a double-T shape cross-section (Figure 5-28). Therefore, an interface was inserted and modelled by a discrete interface model.

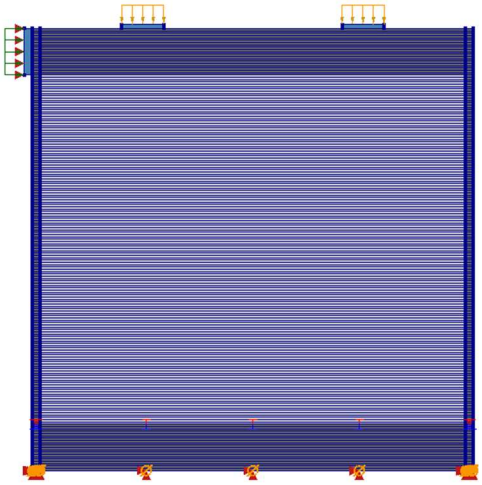

Figure 5-32:Discrete interface model between the bottom concrete corbel and the layers of the wall.

The constitutive law for discrete cracking model in DIANA FEA is based on a total deformation theory, which expresses the traction as a function of the crack width.

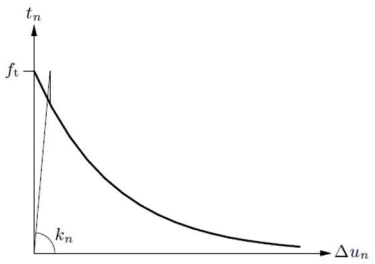

Figure 5-33: Discrete cracking [167].

It is specified as initiation, Mode I behaviour and Mode II behaviour. Table 5-12 shows the input parameters required for the discrete cracking model.

syntax

'MATERI'

1 5	6 12	13 80
	DISCRA	1
	DCRVAL	ft_r
	MODE1	$mo1_n$
	[UNLO1	$un1_n$]
	[MODE2	$mo2_n$]
	[MO2VAL	$mv2_r$]

Table 5-12: Input parameters for the discrete interface model

Where:

- DISCRA indicates a discrete crack initiation criterion of normal traction. A discrete crack arises if the normal traction t_n exceeds the tensile strength $f_{ctm.}$
- DCRVAL is the tensile strength f_{ctm}.
- MODE 1 indicates the mode I tension softening criterion. The Hordijk softening was chosen (Figure 5-34c).

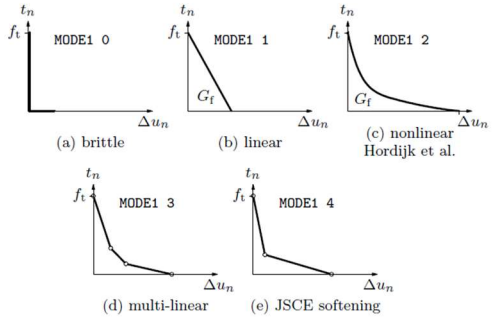

Figure 5-34: Mode I-tension softening discrete cracks.

- UNLO specifies a Mode-I unloading/reloading model, which can be secant (the chosen one) or linear elastic.
- MODE2 specifies a shear criterion to be used in the crack development stage. It can be zero shear traction and zero shear stiffness after cracking (set by default).
- MO2VAL is the value of the shear modulus to be used in the development stage of the crack. This case is only applied in case of constant shear modulus after cracking.
- Moreover, the last two parameters to be defined are the normal stiffness modulus k_{nc} and the shear stiffness modulus k_{sn}, which are set equal to $1*10^9$ N/mm^3 and 1.3 N/mm^3. The value of the shear stiffness modulus was calculated with equation 4-36, taking into account the shear deformation and the sliding between the layers (see section 4.5.2)

5.3.4.3 Mesh

Eight node quadrilateral elements (CQ16M) are used to simulate concrete and steel elements. Linear interface elements (CL12I) are used to simulate the interface between the wall and the concrete corbel. The size of the single element was chosen 11 mm x 11 mm.

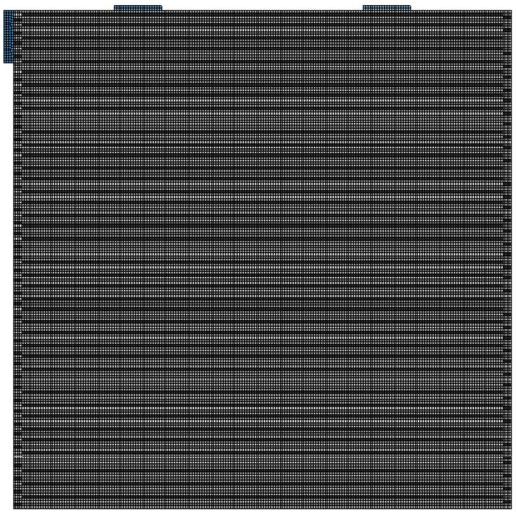

Figure 5-35: Mesh size.

5.3.5 Validation of the model

The comparison between the experimental and numerical envelope curves in terms of horizontal force versus horizontal displacement is illustrated in Figure 5-36. The black curve refers to the experiment, while the red one to the finite element analysis. At a first stage the numerical modeling was performed using the tensile constitutive law suggested by the Model Code 2010 [153] for the concrete and a mesh with dimensions of the single element equal to 11 x 50 mm. The numerical curve approximates the first linear branch of the experimental curve well, and both curves reach a maximum strength of approximately 200 kN. However, it should be noted that the experimental curve shows a stiffness reduction around 90 kN, possibly due to some microcracks that were not detected with the digital image correlation. The numerical modelling approach employed is not representative of the stiffness reduction in the second linear branch of the experimental curve. Regarding the post peak-phase, it can be observed that the numerical model overestimates the ultimate load by 20% for the push and pull loading direction, respectively. In Figure 5-37 the crack pattern obtained from the finite element analysis is shown, it occurred in correspondence of the bottom concrete corbel, as in the experimental test (see Figure 4-54).

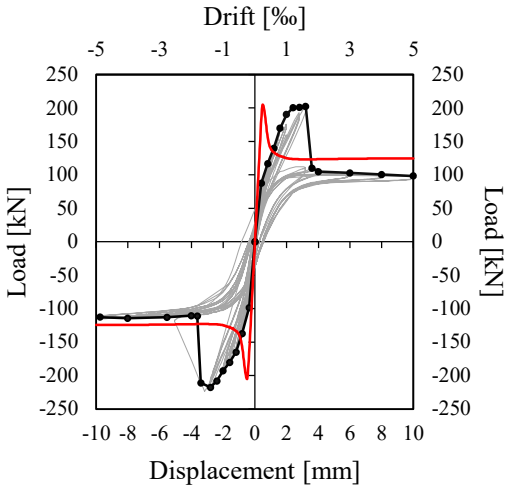

Figure 5-36: Experimental and numerical force versus horizontal displacement curves of the 3DPC wall printed with material 2.

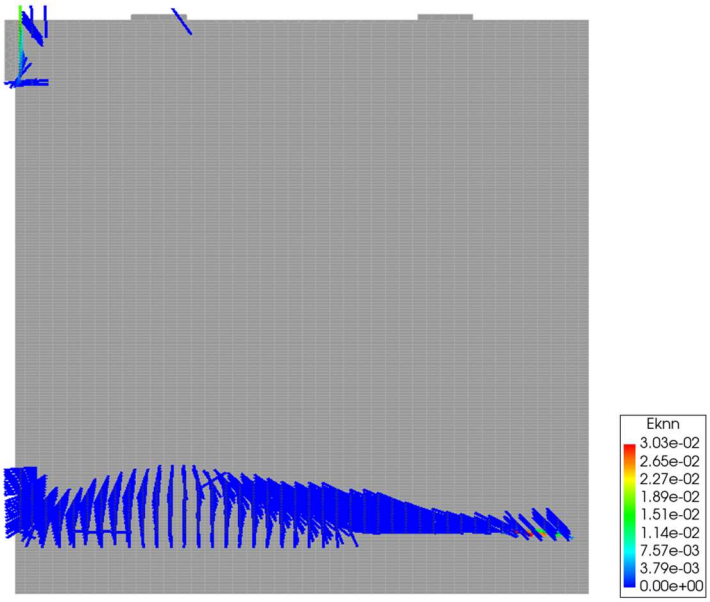

Figure 5-37: Crack pattern of the wall printed using material 2 obtained from the finite element analysis.

In a second stage, the model was improved by using a more dense mesh with dimensions 11 x 11 mm, applying the tensile constitutive law described in section 4.5.2 to 3DPC concrete (see Figure 5-30) and by using a shear stiffness modulus

calibrated taking into account the shear deformation and the sliding between the layers. The comparison between the numerical and experimental curves is shown in Figure 5-38, indicated in red and black respectively. It comes out that the dissipation energy and the first linear branch are now aligned with the experimental curve. However, the model is not representative of the stiffness reduction observed in the second linear branch of the experimental curve. Regarding the post peak-phase, it can be observed that the numerical model overestimates the ultimate load by 20% for the push and pull loading direction, respectively.

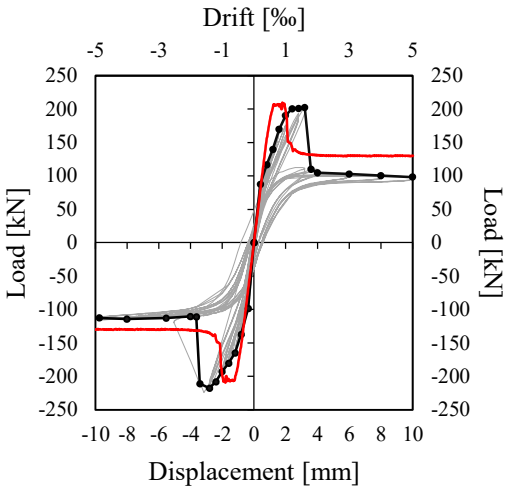

Figure 5-38: Experimental and numerical force versus horizontal displacement curves of the 3DPC wall printed with material 2.

6 CASE STUDY

In this research study it was proposed a multilevel approach to the design of 3DPC walls (see Chapter 4), that could be used in the construction of low-rise buildings with modular structural elements printed offsite. In this section, the integration of thermal, structural and sustainability design aspect of 3DCP technology is discussed with regards to a two-storey reference building [175]. The thermal performance is considered with regards to the thermal transmittance, which is a key element in containing building energy consumption. The structural performance consider its ability to support vertical and horizontal load, which is particularly relevant for structures located in earthquake-prone regions. Finally, the sustainability is considered through a simplified Life Cycle Assessment analysis (LCA), which is of particular interest to show the ability to reduce the use of materials.

6.1 Reference building

Figure 6-1 shows a two-storey building taken as a reference.

Figure 6-1: Reference building.

The 3DPC building is ideally located in north Italy, in Milan. To evaluate the risk of earthquakes in Italy, the territory is divided into four areas (1,2,3,4) with decreasing seismic hazard based on historical seismic activity, with each area assigned a specific seismic action value expressed in terms of maximum acceleration on bedrocks (zone 1 = 0.35g, zone 2 = 0.25g, zone 3 = 0.15g and zone 4 = 0.05g) [176]. Milan is located in area 3, as illustrated in Figure 6-2a. Moreover, according to [177] Italy is divided in six climate areas according to the daily degrees temperature, indicated as GG in

Figure 6-2b. The daily degrees are the sum, considering each day of the year, of the difference between the temperature of the internal environment and the daily average external environment temperature. According to this subdivision Milano is located in the area E. The building is designed to comply with the current Italian legislation (which is in compliance with the EU directive) [140], which set for new construction buildings located in area E a maximum value of the thermal transmittance for vertical walls equal to 0.26 W/m²K.

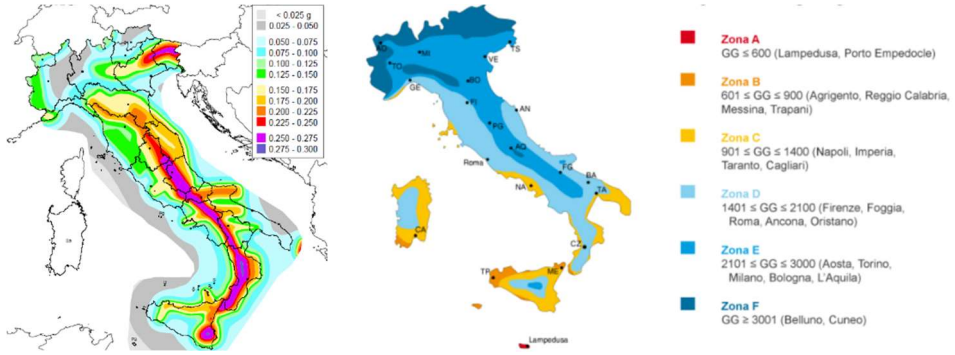

(a) (b)

Figure 6-2: Classification of the a) seismic and b) thermal areas in Italy.

The resisting shear wall considered in the following analysis is highlighted in red in Figure 6-3. Only unreinforced wall are considered, since from the experimental study it was not possible to assess the maximum capacity of a reinforced wall due to the presence of a cold joint that caused a sliding failure in its correspondence. The wall has a height of 3 m, a length of 3 m and a thickness of 55 cm and a weight of 20 kN. To estimate the vertical load acting on the wall, the following loads are assumed:

- on the floor: G_1= 4.20 kN/m²; G_2= 3.00 kN/m²; Q= 2 kN/m²
- on the roof G_1= 4.20 kN/m²; G_2= 2.30 kN/m²; Q= 1.20 kN/m²

With a tributary area of about 20 m², the vertical load is about 400 kN, for more detailed calculation see APPENDIX E.

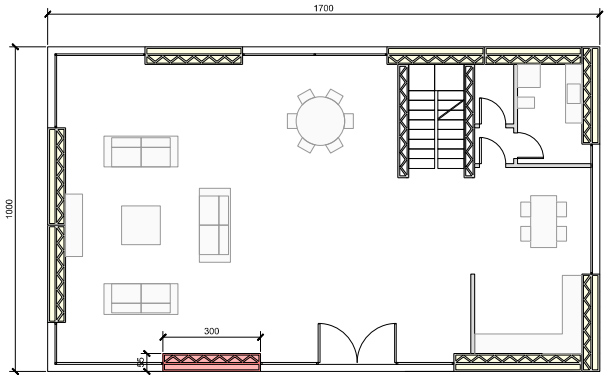

Figure 6-3: Plan view of the ground.

As illustrated in Chapter 4, the unreinforced 3DPC wall is characterized by an internal part with inclined diaphragms with a structural function (in violet in Figure 6-4), meaning it is the part that withstand the vertical and horizontal load, and an external concrete layer with just a thermal and aesthetic function (in blue in Figure 6-4). The external insulation layer was added to avoid the problem of thermal bridges at intersection point for example between walls, floor and foundation. The inclined concrete diaphragms provides stability during the printing process. The outer concrete layer is connected to the internal part of the wall with steel bars (indicated in red in Figure 6-4) with a diameter of 6 mm and a spacing of 47.5 cm in horizontal direction and 42.5 cm in the vertical one (see section 4.2.2.2), to avoid its buckling during the printing process.

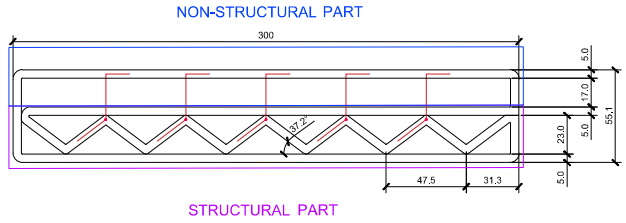

Figure 6-4: Plan view of the unreinforced 3DPC wall.

6.2 Thermal performance

Regarding the thermal design, the configuration with inclined diaphragms is one of the most common and an inclination of 37° was chosen to guarantee an integer number of internal diaphragms if a 3 m long shear wall is considered. In Chapter 4 an analytical and a finite element model were proposed to estimate the thermal transmittance [142]. In this section the 2D finite element analysis using the software THERM was replicated on the full-scale wall.

To sum up the following climate conditions are considered: temperature of the internal environment equal to 20° (paragraph 1.4 [141]), temperature of the external environment to 0°, convective air resistance of the internal environment $R_{cv,i}$ = 0.13 m²K/W, convective air resistance of the external environment 0.04 m²K/W. The material used within the calculation are 3D printable concrete and cellulose fiber (obtained from newspaper) as insulating material. The thermal conductivity of the concrete is equal to 0.963 W/mK and the thermal conductivity of the cellulose fibre is equal to 0.038 W/mK.
From the finite element calculation a value of the thermal transmittance U = 0.25 W/m²K was obtained, which is below the limit set by the standard. Figure 6-5 shows the temperature gradient and the thermal flux obtained from the finite element calculation.

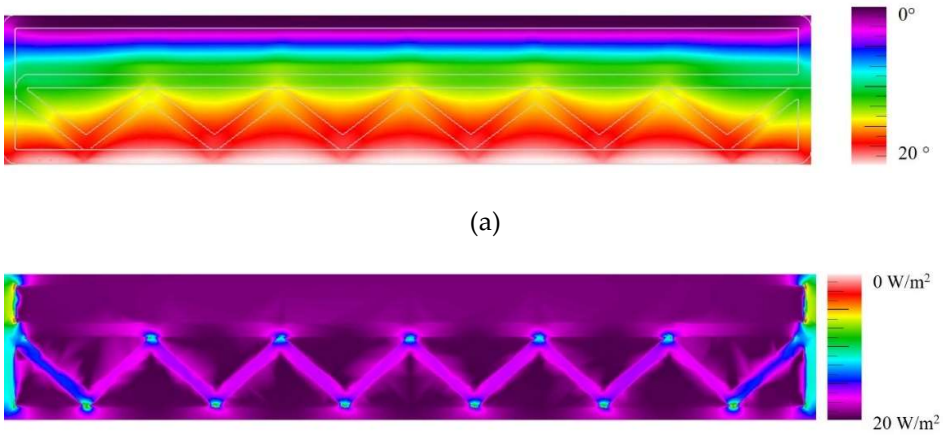

Figure 6-5: Finite element analysis using the software THERM: (a) temperature gradient; (b) thermal flux.

6.3 Structural performance

With reference to the analytical models discussed in section 4.5.2, it was possible to estimate the maximum horizontal load (F_{max}) and the ultimate horizontal load (F_u) on the 3 m high wall, of which the tested specimens are a 70% scaled representation (Table 6-1)

Performance	Symbol	Unit	70% scaled wall	100% scaled wall
Structural	F_{max}	[kN]	200	536
	F_u	[kN]	99.28	198

Table 6-1: Modeling results for the 70% and 100% scaled wall.

In addition, a linear static calculation was developed on the wall considered as reference (Figure 6-3). The building is represented as a multi degree of freedom dynamic system and the weights of the roof and of the floor are represented as lumped masses in correspondence of the intermediate floor and of the roof, respectively (Figure 6-6). The total mass of the intermediate floor is equal to m_1 = 129.5 t, the total mass of the roof is equal to m_2 = 127.5 t and the weight of the eleven walls is equal to 44 t. It results that the total mass of the intermediate floor $m_{1,tot}$ is equal to 174 t and the total mass $m_{2,tot}$ in correspondence of the roof is equal to 131 t.

Considering Milan, which as previously mentioned is located in seismic zone 3. According to the Italian Standard NTC 2018 [112], there are different categories for the subsoil (A,B,C,D,E) and for the topography (T1,T2,T3 and T4). Taking as reference Milan, it is reasonable to assume a category B (soft rocks and deposits of very thickened coarse-grained soils or very consistent fine-grained soils) for the subsoil and a category T1 (flat land, slopes and isolated elevations with average slope i ≤ 15°) for the topography. Considering these boundary conditions the maximum allowable acceleration $S_{d,slv}$ resulted equal to 0.157g. The maximum acting shear at the base of the building F_h is given by

$$F_h = m_{tot} \lambda S_{d,slv} \quad 6\text{-}1$$

Where m_{tot} is the total mass of the building and λ is a coefficient equal to 0.85 if the building has at least three floors, otherwise is equal to 1. As consequence according to equation 6-1 the maximum acting shear at the base of the building resulted equal to 478.96 kN. Considering the horizontal direction, where five wall are present, the total acting load at the base of the wall is equal to 95.79 kN. The load acting at each floor F_i is estimated as

$$F_i = F_h z_i \frac{W_i}{\sum_j z_j W_j} \quad 6\text{-}2$$

Where W_i and W_j are the weights of the mass i and j, respectively; z_i and z_j are the heights with respect to the foundation of the masses i and j, respectively.

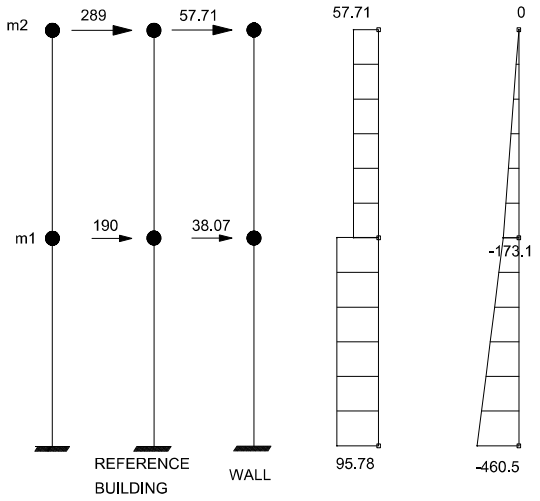

Figure 6-6: Simplified linear elastic analysis on the reference building.

From this simplified calculation it resulted that the reference wall would be subjected to a shear force lower than the maximum allowable estimated with the analytical models (600 kN) and therefore the 3DPC wall described within this section results to be suitable for construction of low-rise building in low seismic areas.

6.4 Sustainability

Also of interest is the analysis of the environmental impact of the unreinforced 3DPC wall. As part of this study, the designed 3DPC wall was compared with traditional construction solutions: brick masonry (BM) wall, reinforced concrete (RC) wall and cross laminated timber (CLT) wall, respectively. The dimensions of walls built with traditional methods were derived by imposing the same vertical load of 400 kN on all walls, which is the load of a two-story building acting on a 3 m high wall, and the same thermal transmittance of 0.2 W/m^{2}K.The walls were 3 m high and 3 m long. The thickness varied according to the type considered.
Table 6-2 summarises the main characteristics of building materials: compressive strength (f), wall thickness (t), conductive thermal resistance (λ), density (ϱ), volume (V) and weight (W).

Material	f [MPa]	t [cm]	λ [W/mK]	ϱ [kg/m³]	V [m³]	W [kg]
3DCP wall						
3d concrete	50	-	0.96	2150	0.88	1752
Insulation	-	-	0.04	60	2.8	170
Brick masonry						
Plasterboard	-	1.25	0.21	800	0.11	90
Bricks	5	20	0.23	800	1.8	1440
Insulation	-	15	0.04	30	1.35	40.5
Air	-	6	-	-	-	-
Facade cladding	-	1	1.3	1400	0.09	126
Reinforced concrete						
Plasterboard	-	0.01	0.21	800	0.11	90
Concrete	30	0.15	1.6	2500	1.35	3375
Steel bars	-	-	-	100	-	135
Insulation	-	0.18	0.04	30	1.62	48.6
Air	-	0.06	-	-	-	-
Facade cladding	-	0.01	1.3	1400	0.09	126
Cross laminated timber						
Plasterboard	-	0.01	0.21	800	0.11	90
Cross laminated timber	21	0.14	0.12	500	1.26	630
Insulation	-	0.15	0.04	30	1.35	40.5
Air	-	0.06	-	-	-	0
Facade cladding	-	0.01	1.3	1400	0.135	189

Table 6-2: Main features of the walls considered in the comparison.

The comparison was made in terms of global warming potential (GWP) with $kgCO_2eq$ as the unit of measurement. The production phase, i.e. from cradle to gate, was examined. This phase was chosen because it is the one with the highest CO_2 production. According to EN 15804 [178], the stages included in this phase are A1, A2 and A3. A1 refers to the supply of raw materials, A2 to transport to the production site and A3 to the manufacture of products and packaging. The waste produced is also included in this phase. The GWP values for each material were taken from the manufacturers' environmental product declarations (EPDs). The GWP values for each building material considered are listed in Table 6-3.

Figure:6-7 shows the comparison between the walls in terms of $kgCO_2$ equivalent. It can be seen that the wall with the largest carbon footprint is the traditional reinforced concrete wall (880 $kgCO_2$). The carbon footprint of the 3DPC wall is lower than the reinforced concrete and masonry walls. The GWP of the 3DPC wall (482 $kgCO_2$) is close to that of the timber wall (423 $kgCO_2$).

Material	Units	Value
Concrete	[kgCO_2/m^3]	300
3D concrete	[kgCO_2/m^3]	500
Brick	[kgCO_2/kg]	0.224
Cross laminated timber	[kgCO_2/m^3]	160
Plasterboard[	[kgCO_2/m^2]	2.3
Facade cladding	[kgCO_2/m^2]	17.4
Insulation	[kgCO_2/m^2]	1.22
Steel	[kgCO_2/kg]	1.8

Table 6-3: kgCO_2eq of each construction material considered.

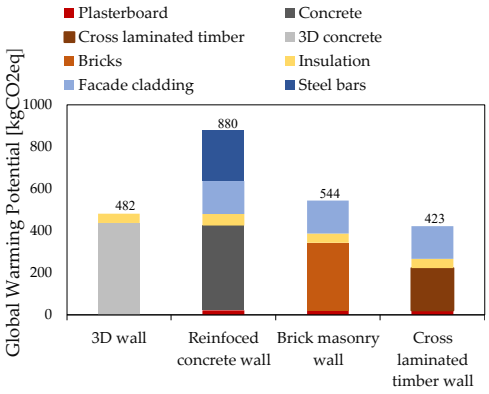

Figure:6-7: Global warming potential.

7 CONCLUSION AND RECOMMENDATIONS FOR FUTURE WORK

7.1 Conclusions

The aim of the thesis was the study on the structural behaviour of 3D printed concrete (3DPC) elements with a focus on 3DPC walls made by concrete extrusion. The primary objectives of this thesis were the development of methodologies to assess the mechanical properties of 3D printed concrete in the hardened state, by devoting special attention to the effect of the interface between layers, and the structural behaviour of 3D printed concrete walls.

As far as the assessment of the material properties in the hardened state is concerned, the compression and the flexural tensile strength were evaluated by adopting test setups commonly used for cement based mortar. Direct tensile tests were performed for interfaces subjected to tensile forces. Then, particular attention was given to the investigation on the shear behaviour at the interface between adjacent layers of 3DPC elements: modified push-out tests and modified slant shear tests were carried out. The modified push-out test, commonly used in masonry structures, consisted in the application of a vertical load parallel to the layers and a constant horizontal prestress transverse to specimen's interfaces. The modified slant shear test, typically used to determine the shear properties between traditional concrete and a repair material, was used to determine the shear properties of the 3DPC material in a combined stress state of shear and compression. Those tests provide a methodology to determine the resistance domain of 3DPC elements.

Moreover, a FE model of the push-out test was developed, which is an effective tool for the numerical modelling of large-scale elements like walls. The modified push-out test was modelled by using two approaches: a smeared cracking and a discrete cracking approach.

On a large-scale, five in-plane quasi-static cyclic tests on 3DPC walls were carried out at the University of Brescia: four unreinforced walls and a reinforced one with vertical steel bars grouted in outer small pockets. The design process of the walls focused on identifying the key thermal, geometrical and mechanical parameters. In order to assess the thermal transmittance, a simplified analytical and numerical model was proposed and eventually validated through an experimental campaign. The thermal analysis was employed to obtain a geometric configuration that allows

the wall to have a thermal transmittance in compliance with the limits imposed by the standards.

Finally, the integration of thermal, structural and sustainability design aspect of 3DCP technology is discussed with regards to a two-storey reference building. The analytical and finite element analyses were applied to a 3 m high wall identified in the case study to assess its thermal transmittance and base shear load capacity. Moreover, a simplified Life Cycle Assessment analysis was carried out on the 3DPC wall.

The following conclusions can be drawn based on the findings of this study:

- Based on the results of compression, flexure and tensile tests carried out on the 3DPC material, it is evident that the mechanical properties are influenced by the direction of the applied load with respect to the orientation of the layers. The influence of the loading direction on the compressive strength was found to be minimal, the difference of compressive strength in the different loading directions was about 5%. However, the impact on the flexural strength was more significant with a difference between 20% and 30% in the different loading directions. Higher values of the flexural tensile strength were found when the main stresses are parallel to the direction of the layers.

  The results of modified push-out and modified slant shear tests show that the inclination of the layers influences the failure mode: the specimens subjected to modified push-out test failed only at the interface, while the specimens subjected to modified slant shear test exhibited failure both at the interface and in the concrete matrix, depending on the concrete layer inclination. The modified push-out test was performed for both cast and printed specimens, that gave similar results in terms of cohesion and angle of friction, meaning that the presence of the interface (in absence of cold joint) does not affect the material properties. The failure mode was also similar between cast and printed specimens. The specimens subjected to the modified slant shear test had a cold joint due to a time gap (between layers) of 30 minutes (to investigate a certain tolerance of possible printing interruption during the production of 3D printed concrete elements), but the results (in terms of cohesion and coefficient of friction) were consistent with those found in literature, where no cold joints were present. It could be assumed that, for short time intervals (up to 30 min), the time gap does not influence on the mechanical properties.
- The results obtained from the characterization of the hardened properties of the 3D printed material were useful for the development of the numerical model of the push-out test used to study the interface behaviour between the layers. The results obtained from the finite element analysis were in good agreement with the experimental results in terms of initial linear elastic

behaviour, post-peak behaviour, maximum strength, cohesion and angle of friction. Both smeared and discrete cracking approaches gave similar results. However, when dealing with defects, such as cold joints, the discrete cracking approach provides a better approximation.

- In terms of structural response of the 3DPC walls, the unreinforced walls showed a good lateral response, both in term of initial stiffness and lateral strength. The walls exhibited a bilinear elastic behaviour until the maximum flexural strength is reached. Due to the lack of reinforcement, eventually the walls exhibited a brittle flexural failure characterised by a main crack at the base of the wall. Rocking mechanism governed the post peak behaviour since no shear damage of the wall was observed. The reinforced wall had a cold joint due to the interruption of the printing process for 45 min because of overheating of the pump. It exhibited linear elastic behaviour similar to that of the unreinforced wall until the premature collapse, if compared to the unreinforced wall, due to a shear sliding failure along the cold joint. This highlights a specific aspect of the 3D printed structural elements, as cold joints may occur during in-situ printing process, thus significantly affecting the bond resistance between the adjacent layers over long time intervals of time gap.
- On the basis of the mechanical characterization of the 3D printed material, a simple and reliable analytical model was proposed to predict the initial stiffness and the flexural strength of 3DPC walls. The model shows the significant role of the re-distribution of tensile stresses after the development of the first cracking on the wall strength, as well as the effect of interlayer shear behaviour on the wall stiffness.
- Comparing the failure domain of 3DPC unreinforced wall with the one of traditional masonry walls made by different type of bricks, it is observed that the tested 3DPC wall exhibited higher stiffness and resistance to horizontal loads. Even for low vertical stresses applied to the wall, the 3DPC tested element showed significant initial strength, attributed to the higher tensile strength of the 3D printed material as compared to traditional masonry. Consequently, unlike traditional masonry structures, which typically undergo a collapse mechanism involving rocking, shear sliding or diagonal cracking, the 3DPC tested wall failed when its maximum flexural strength was reached. The specific collapse mechanism depends on the magnitude of the applied vertical load and the shear ratio H/L.
- A proper design of the 3DPC walls allows for a good thermal performance. The designed 3DPC walls exhibited a good thermal performance in compliance with the standards.
- Considering a full-scale wall with a height of 3 m, it can be shown that the 3DPC unreinforced wall may be suitable for moderate seismic prone areas

(zone 3 in Italy). Moreover, the 3DPC wall is suitable also for buildings located in the climatic area of Norther Italy.

- Finally, the 3DPC wall was compared with traditional building systems like brickwork, reinforced concrete and cross laminated timber walls using a simplified Life Cycle Assessment analysis. The comparison was made in terms of kgCO2eq. The carbon footprint of a traditional concrete wall was the highest. The 3DPC wall showed a carbon footprint comparable to that of cross laminated timber and almost half that of traditional concrete.

7.2 Final remarks and further studies

This thesis has explored several scientific aspects and can be a valuable starting point for future research and studies. Therefore, the following suggestions and recommendations are provided:

- it is recommended to carry out further push-out and slant shear tests with a double purpose: i) define a relationship between the two test methods and ii) investigate the effect of a time gap longer than 30 minutes between the layers to examine the effect of cold joints on the structural behaviour of 3DPC elements.
- Further structural tests on 3DPC walls are required with the aim at: i) investigating different reinforcement solutions and ii) developing of specific strategies/devices/technique in presence of cold joints that enables the walls to carry the shear load and avoid localized failure.
- Experimental tests could be useful to investigate the shrinkage of the 3D printed concrete material and its influence on the structural behaviour of 3DPC walls.

8 REFERENCES

[1] Flatt RJ, Wangler T. On sustainability and digital fabrication with concrete. Cement and Concrete Research 2022;158:106837. https://doi.org/10.1016/j.cemconres.2022.106837.

[2] Agustí-Juan I, Habert G. Environmental design guidelines for digital fabrication. Journal of Cleaner Production 2017;142:2780–91. https://doi.org/10.1016/j.jclepro.2016.10.190.

[3] Agustí-Juan I, Müller F, Hack N, Wangler T, Habert G. Potential benefits of digital fabrication for complex structures: Environmental assessment of a robotically fabricated concrete wall. Journal of Cleaner Production 2017;154:330–40. https://doi.org/10.1016/j.jclepro.2017.04.002.

[4] Wolfs RJM, Bos FP, Salet TAM. Early age mechanical behaviour of 3D printed concrete: Numerical modelling and experimental testing. Cement and Concrete Research 2018;106:103–16. https://doi.org/10.1016/j.cemconres.2018.02.001.

[5] Di Carlo T, Khoshnevis B, Carlson A. Experimental and Numerical Techniques to Characterize Structural Properties of Fresh Concrete. Volume 9: Mechanics of Solids, Structures and Fluids, San Diego, California, USA: American Society of Mechanical Engineers; 2013, p. V009T10A062. https://doi.org/10.1115/IMECE2013-63993.

[6] Casagrande L, Esposito L, Menna C, Asprone D, Auricchio F. Effect of testing procedures on buildability properties of 3D-printable concrete. Construction and Building Materials 2020;245:118286. https://doi.org/10.1016/j.conbuildmat.2020.118286.

[7] Wolfs RJM, Bos FP, Salet TAM. Triaxial compression testing on early age concrete for numerical analysis of 3D concrete printing. Cement and Concrete Composites 2019;104:103344. https://doi.org/10.1016/j.cemconcomp.2019.103344.

[8] Jayathilakage R, Sanjayan J, Rajeev P. Direct shear test for the assessment of rheological parameters of concrete for 3D printing applications. Mater Struct 2019;52:12. https://doi.org/10.1617/s11527-019-1322-4.

[9] Wolfs RJM, Bos FP, Salet TAM. Hardened properties of 3D printed concrete: The influence of process parameters on interlayer adhesion. Cement and Concrete Research 2019;119:132–40. https://doi.org/10.1016/j.cemconres.2019.02.017.

[10] Panda B, Chandra Paul S, Jen Tan M. Anisotropic mechanical performance of 3D printed fiber reinforced sustainable construction material. Materials Letters 2017;209:146–9. https://doi.org/10.1016/j.matlet.2017.07.123.

[11] Marchment T, Xia M, Dodd E, Sanjayan J, Nematollahi B. Effect of Delay Time on the Mechanical Properties of Extrusion-Based 3D Printed Concrete, Taipei, Taiwan: 2017. https://doi.org/10.22260/ISARC2017/0032.

[12] van den Heever M, Bester F, Kruger J, van Zijl G. Mechanical characterisation for numerical simulation of extrusion-based 3D concrete printing. Journal of Building Engineering 2021;44:102944. https://doi.org/10.1016/j.jobe.2021.102944.

[13] Nerella VN, Hempel S, Mechtcherine V. Effects of layer-interface properties on mechanical performance of concrete elements produced by extrusion-based 3D-printing. Construction and Building Materials 2019;205:586–601. https://doi.org/10.1016/j.conbuildmat.2019.01.235.

[14] Le TT, Austin SA, Lim S, Buswell RA, Law R, Gibb AGF, et al. Hardened properties of high-performance printing concrete. Cement and Concrete Research 2012;42:558–66. https://doi.org/10.1016/j.cemconres.2011.12.003.

[15] Panda B, Paul SC, Mohamed NAN, Tay YWD, Tan MJ. Measurement of tensile bond strength of 3D printed geopolymer mortar. Measurement 2018;113:108–16. https://doi.org/10.1016/j.measurement.2017.08.051.

[16] Napolitano R, Menna C, Asprone D, Del Giudice L. Mechanical characterizatio of layer-by-layer interface in concrete elements obtained by additive manufacturing. In: Bos FP, Lucas SS, Wolfs RJM, Salet TAM, International Union of Laboratories and Experts in Construction Materials, Systems and Structures, editors. Second RILEM International Conference on Concrete and Digital Fabrication: Digital Concrete 2020, Cham: Springer; 2020.

[17] Salet TAM, Ahmed ZY, Bos FP, Laagland HLM. Design of a 3D printed concrete bridge by testing. Virtual and Physical Prototyping 2018;13:222–36. https://doi.org/10.1080/17452759.2018.1476064.

[18] Wolfs R. A framework for large-scale structural applications of 3D printed concrete 2021. https://doi.org/10.5446/56115.

[19] Weger D, Stengel T, Gehlen C, Maciejewski Y, Meyer-Brötz F. Approval for the Construction of the First 3D Printed Detached House in Germany—Significance of Large Scale Element Testing. In: Jones SZ, Kreiger EL, editors. Standards

Development for Cement and Concrete for Use in Additive Construction, 100 Barr Harbor Drive, PO Box C700, West Conshohocken, PA 19428-2959: ASTM International; 2021, p. 144–69. https://doi.org/10.1520/STP163620200119.

[20] Buswell RA, da Silva WRL, Bos FP, Schipper HR, Lowke D, Hack N, et al. A process classification framework for defining and describing Digital Fabrication with Concrete. Cement and Concrete Research 2020;134:106068. https://doi.org/10.1016/j.cemconres.2020.106068.

[21] Khoshnevis B. Automated construction by contour crafting—related robotics and information technologies. Automation in Construction 2004;13:5–19. https://doi.org/10.1016/j.autcon.2003.08.012.

[22] Khoshnevis B, Hwang D, Yao KT, Yeh Z. Mega-scale fabrication by Contour Crafting. IJISE 2006;1:301. https://doi.org/10.1504/IJISE.2006.009791.

[23] Zhang J, Khoshnevis B. Optimal machine operation planning for construction by Contour Crafting. Automation in Construction 2013;29:50–67. https://doi.org/10.1016/j.autcon.2012.08.006.

[24] E. Dini. DShape. n.d. www.d-shape.com.

[25] Lowke D, Dini E, Perrot A, Weger D, Gehlen C, Dillenburger B. Particle-bed 3D printing in concrete construction – Possibilities and challenges. Cement and Concrete Research 2018;112:50–65. https://doi.org/10.1016/j.cemconres.2018.05.018.

[26] de la Fuente A, Blanco A, Galeote E, Cavalaro S. Structural fibre-reinforced cement-based composite designed for particle bed 3D printing systems. Case study Parque de Castilla Footbridge in Madrid. Cement and Concrete Research 2022;157:106801. https://doi.org/10.1016/j.cemconres.2022.106801.

[27] Lim S, Buswell RA, Le TT, Austin SA, Gibb AGF, Thorpe T. Developments in construction-scale additive manufacturing processes. Automation in Construction 2012;21:262–8. https://doi.org/10.1016/j.autcon.2011.06.010.

[28] Lim S, Buswell RA, Valentine PJ, Piker D, Austin SA, De Kestelier X. Modelling curved-layered printing paths for fabricating large-scale construction components. Additive Manufacturing 2016;12:216–30. https://doi.org/10.1016/j.addma.2016.06.004.

[29] Salet TAM, Ahmed ZY, Bos FP, Laagland HLM. Design of a 3D printed concrete bridge by testing. Virtual and Physical Prototyping 2018;13:222–36. https://doi.org/10.1080/17452759.2018.1476064.

[30] Vantyghem G, De Corte W, Shakour E, Amir O. 3D printing of a post-tensioned concrete girder designed by topology optimization. Automation in Construction 2020;112:103084. https://doi.org/10.1016/j.autcon.2020.103084.

[31] Amir O, Shakour E. Simultaneous shape and topology optimization of prestressed concrete beams. Struct Multidisc Optim 2018;57:1831–43. https://doi.org/10.1007/s00158-017-1855-5.

[32] Ooms T, Vantyghem G, Tao Y, Bekaert M, De Schutter G, Van Tittelboom K, et al. The Production of a Topology-Optimized 3D-Printed Concrete Bridge. In: Buswell R, Blanco A, Cavalaro S, Kinnell P, editors. Third RILEM International Conference on Concrete and Digital Fabrication, vol. 37, Cham: Springer International Publishing; 2022, p. 37–42. https://doi.org/10.1007/978-3-031-06116-5_6.

[33] COBOD n.d. www.cobod.com.

[34] Kreiger E, Diggs-McGee B, Wood T, MacAllister B, Kreiger M. Field Considerations for Deploying Additive Construction. In: Bos FP, Lucas SS, Wolfs RJM, Salet TAM, editors. Second RILEM International Conference on Concrete and Digital Fabrication, vol. 28, Cham: Springer International Publishing; 2020, p. 1147–63. https://doi.org/10.1007/978-3-030-49916-7_109.

[35] Lloret E, Shahab AR, Linus M, Flatt RJ, Gramazio F, Kohler M, et al. Complex concrete structures. Computer-Aided Design 2015;60:40–9. https://doi.org/10.1016/j.cad.2014.02.011.

[36] Lloret-Fritschi E. Smart Dynamic Casting - A digital fabrication method for non-standard concrete structures. ETH Zurich, 2016. https://doi.org/10.3929/ETHZ-A-010800371.

[37] Lloret-Fritschi E, Reiter L, Wangler T, Gramazio F, Kohler M, Flatt RJ. Smart Dynamic Casting: Slipforming with Flexible Formwork - Inline Measurement and Control 2017:11 p. https://doi.org/10.3929/ETHZ-B-000219663.

[38] Lloret-Fritschi E, Scotto F, Gramazio F, Kohler M, Graser K, Wangler T, et al. Challenges of Real-Scale Production with Smart Dynamic Casting. In: Wangler T, Flatt RJ, editors. First RILEM International Conference on Concrete and Digital Fabrication – Digital Concrete 2018, vol. 19, Cham: Springer International Publishing; 2019, p. 299–310. https://doi.org/10.1007/978-3-319-99519-9_28.

[39] Dörfler K, Hack N, Sandy T, Giftthaler M, Lussi M, Walzer AN, et al. Mobile robotic fabrication beyond factory conditions: case study Mesh Mould wall of the

DFAB HOUSE. Constr Robot 2019;3:53–67. https://doi.org/10.1007/s41693-019-00020-w.

[40] Jipa M-A, Aghaei Meibodi M, Giesecke R, Shammas D, Leschok M, Bernhard M, et al. 3D-Printed Formwork for Prefabricated Concrete Slabs 2018:9 p. https://doi.org/10.3929/ETHZ-B-000507651.

[41] 3dhousing05 - Massimiliano Locatelli | CLS ARCHITETTI (n.d.), n.d. https://www.3dhousing05.com/.

[42] Apiscor n.d. www.apis-cor.com.

[43] Bos FP, Menna C, Pradena M, Kreiger E, da Silva WRL, Rehman AU, et al. The realities of additively manufactured concrete structures in practice. Cement and Concrete Research 2022;156:106746. https://doi.org/10.1016/j.cemconres.2022.106746.

[44] Mechtcherine V, Fataei S, Bos FP, Buswell RA, Silva WRL da, Keita E, et al. Digital Fabrication with Cement-Based Materials: Underlying Physics. In: Roussel N, Lowke D, editors. Digital Fabrication with Cement-Based Materials, vol. 36, Cham: Springer International Publishing; 2022, p. 49–98. https://doi.org/10.1007/978-3-030-90535-4_3.

[45] Roussel N. Rheological requirements for printable concretes. Cement and Concrete Research 2018;112:76–85. https://doi.org/10.1016/j.cemconres.2018.04.005.

[46] Reiter L, Wangler T, Roussel N, Flatt RJ. The role of early age structural build-up in digital fabrication with concrete. Cement and Concrete Research 2018;112:86–95. https://doi.org/10.1016/j.cemconres.2018.05.011.

[47] Mettler LK, Wittel FK, Flatt RJ, Herrmann HJ. Evolution of Strength and Failure of SCC during Early Hydration 2016. https://doi.org/10.48550/ARXIV.1609.02293.

[48] Wolfs RJM, Bos FP, Salet TAM. Early age mechanical behaviour of 3D printed concrete: Numerical modelling and experimental testing. Cement and Concrete Research 2018;106:103–16. https://doi.org/10.1016/j.cemconres.2018.02.001.

[49] Roussel N. Steady and transient flow behaviour of fresh cement pastes. Cement and Concrete Research 2005;35:1656–64. https://doi.org/10.1016/j.cemconres.2004.08.001.

[50] Roussel N, Ovarlez G, Garrault S, Brumaud C. The origins of thixotropy of fresh cement pastes. Cement and Concrete Research 2012;42:148–57. https://doi.org/10.1016/j.cemconres.2011.09.004.

[51] Roussel N. A thixotropy model for fresh fluid concretes: Theory, validation and applications. Cement and Concrete Research 2006;36:1797–806. https://doi.org/10.1016/j.cemconres.2006.05.025.

[52] Perrot A, Pierre A, Vitaloni S, Picandet V. Prediction of lateral form pressure exerted by concrete at low casting rates. Mater Struct 2015;48:2315–22. https://doi.org/10.1617/s11527-014-0313-8.

[53] Perrot A, Rangeard D, Pierre A. Structural built-up of cement-based materials used for 3D-printing extrusion techniques. Mater Struct 2016;49:1213–20. https://doi.org/10.1617/s11527-015-0571-0.

[54] Wangler T, Lloret E, Reiter L, Hack N, Gramazio F, Kohler M, et al. Digital concrete: opportunities and challenges. RILEM Technical Letters 2016;1:67–75. https://doi.org/10.21809/rilemtechlett.2016.16.

[55] Le TT, Austin SA, Lim S, Buswell RA, Gibb AGF, Thorpe T. Mix design and fresh properties for high-performance printing concrete. Mater Struct 2012;45:1221–32. https://doi.org/10.1617/s11527-012-9828-z.

[56] Design of Concrete Pumping Circuit. MJ 2005;102. https://doi.org/10.14359/14304.

[57] Feys D, Verhoeven R, De Schutter G. Fresh self compacting concrete, a shear thickening material. Cement and Concrete Research 2008;38:920–9. https://doi.org/10.1016/j.cemconres.2008.02.008.

[58] Mechtcherine V, Bos FP, Perrot A, da Silva WRL, Nerella VN, Fataei S, et al. Extrusion-based additive manufacturing with cement-based materials – Production steps, processes, and their underlying physics: A review. Cement and Concrete Research 2020;132:106037. https://doi.org/10.1016/j.cemconres.2020.106037.

[59] Reinold J, Nerella VN, Mechtcherine V, Meschke G. Extrusion Process Simulation and Layer Shape Prediction during 3D-Concrete-Printing Using The Particle Finite Element Method. ENGINEERING; 2020. https://doi.org/10.20944/preprints202007.0715.v1.

[60] Bos FP, Kruger PJ, Lucas SS, van Zijl GPAG. Juxtaposing fresh material characterisation methods for buildability assessment of 3D printable cementitious mortars. Cement and Concrete Composites 2021;120:104024. https://doi.org/10.1016/j.cemconcomp.2021.104024.

[61] Wolfs RJM, Bos FP, Salet TAM. Triaxial compression testing on early age concrete for numerical analysis of 3D concrete printing. Cement and Concrete Composites 2019;104:103344. https://doi.org/10.1016/j.cemconcomp.2019.103344.

[62] Suiker ASJ. Mechanical performance of wall structures in 3D printing processes: Theory, design tools and experiments. International Journal of Mechanical Sciences 2018;137:145–70. https://doi.org/10.1016/j.ijmecsci.2018.01.010.

[63] Suiker ASJ, Wolfs RJM, Lucas SM, Salet TAM. Elastic buckling and plastic collapse during 3D concrete printing. Cement and Concrete Research 2020;135:106016. https://doi.org/10.1016/j.cemconres.2020.106016.

[64] Esposito L, Menna C, Asprone D, Rossino C, Marchi M. An experimental testing procedure to assess the buildability performance of 3D printed concrete elements. Second RILEM International Conference on Concrete and Digital Fabrication: Digital Concrete 2020., Cham: Springer; 2020.

[65] Marcucci A, Kompella SK, Lo Monte F, Levi M, Ferrara L. Early Age Shear and Tensile Fracture Properties of 3D Printable Cementitious Mortar to Assess Printability Window. In: Buswell R, Blanco A, Cavalaro S, Kinnell P, editors. Third RILEM International Conference on Concrete and Digital Fabrication, vol. 37, Cham: Springer International Publishing; 2022, p. 337–42. https://doi.org/10.1007/978-3-031-06116-5_50.

[66] Bos F, Wolfs R, Ahmed Z, Salet T. Additive manufacturing of concrete in construction: potentials and challenges of 3D concrete printing. Virtual and Physical Prototyping 2016;11:209–25. https://doi.org/10.1080/17452759.2016.1209867.

[67] Mechtcherine V, Van Tittelboom K, Kazemian A, Kreiger E, Nematollahi B, Nerella VN, et al. A roadmap for quality control of hardening and hardened printed concrete. Cement and Concrete Research 2022;157:106800. https://doi.org/10.1016/j.cemconres.2022.106800.

[68] Nerella VN, Hempel S, Mechtcherine V. Effects of layer-interface properties on mechanical performance of concrete elements produced by extrusion-based 3D-printing. Construction and Building Materials 2019;205:586–601. https://doi.org/10.1016/j.conbuildmat.2019.01.235.

[69] Wolfs RJM, Bos FP, Salet TAM. Hardened properties of 3D printed concrete: The influence of process parameters on interlayer adhesion. Cement and Concrete Research 2019;119:132–40. https://doi.org/10.1016/j.cemconres.2019.02.017.

[70] Feng P, Meng X, Chen J-F, Ye L. Mechanical properties of structures 3D printed with cementitious powders. Construction and Building Materials 2015;93:486–97. https://doi.org/10.1016/j.conbuildmat.2015.05.132.

[71] Paul SC, Tay YWD, Panda B, Tan MJ. Fresh and hardened properties of 3D printable cementitious materials for building and construction. Archives of Civil and Mechanical Engineering 2018;18:311–9. https://doi.org/10.1016/j.acme.2017.02.008.

[72] van den Heever M, Bester F, Kruger J, van Zijl G. Mechanical characterisation for numerical simulation of extrusion-based 3D concrete printing. Journal of Building Engineering 2021;44:102944. https://doi.org/10.1016/j.jobe.2021.102944.

[73] van den Heever M, du Plessis A, Bester F, Kruger J, van Zijl G. A mechanistic evaluation relating microstructural morphology to a modified Mohr-Griffith compression-shear constitutive model for 3D printed concrete. Construction and Building Materials 2022;325:126743. https://doi.org/10.1016/j.conbuildmat.2022.126743.

[74] Menna C, Mata-Falcón J, Bos FP, Vantyghem G, Ferrara L, Asprone D, et al. Opportunities and challenges for structural engineering of digitally fabricated concrete. Cement and Concrete Research 2020;133:106079. https://doi.org/10.1016/j.cemconres.2020.106079.

[75] Asprone D, Menna C, Bos FP, Salet TAM, Mata-Falcón J, Kaufmann W. Rethinking reinforcement for digital fabrication with concrete. Cement and Concrete Research 2018;112:111–21. https://doi.org/10.1016/j.cemconres.2018.05.020.

[76] Mechtcherine V, Buswell R, Kloft H, Bos FP, Hack N, Wolfs R, et al. Integrating reinforcement in digital fabrication with concrete: A review and classification framework. Cement and Concrete Composites 2021;119:103964. https://doi.org/10.1016/j.cemconcomp.2021.103964.

[77] Asprone D, Auricchio F, Menna C, Mercuri V. 3D printing of reinforced concrete elements: Technology and design approach. Construction and Building Materials 2018;165:218–31. https://doi.org/10.1016/j.conbuildmat.2018.01.018.

[78] Totalkostum n.d. www.totalkostum.com.

[79] Baz B, Aouad G, Leblond P, Al-Mansouri O, D'hondt M, Remond S. Mechanical assessment of concrete – Steel bonding in 3D printed elements. Construction and Building Materials 2020;256:119457. https://doi.org/10.1016/j.conbuildmat.2020.119457.

[80] Grasser G, Pammer L, Köll H, Werner E, Bos FP. Complex Architecture in Printed Concrete: The Case of the Innsbruck University 350th Anniversary Pavilion COHESION. In: Bos FP, Lucas SS, Wolfs RJM, Salet TAM, editors. Second RILEM International Conference on Concrete and Digital Fabrication, vol. 28, Cham: Springer International Publishing; 2020, p. 1116–27. https://doi.org/10.1007/978-3-030-49916-7_106.

[81] Perrot A, Jacquet Y, Rangeard D, Courteille E, Sonebi M. Nailing of Layers: A Promising Way to Reinforce Concrete 3D Printing Structures. Materials 2020;13:1518. https://doi.org/10.3390/ma13071518.

[82] Marchment T, Sanjayan J. Bond properties of reinforcing bar penetrations in 3D concrete printing. Automation in Construction 2020;120:103394. https://doi.org/10.1016/j.autcon.2020.103394.

[83] Hass L, Bos F. Bending and Pull-Out Tests on a Novel Screw Type Reinforcement for Extrusion-Based 3D Printed Concrete. In: Bos FP, Lucas SS, Wolfs RJM, Salet TAM, editors. Second RILEM International Conference on Concrete and Digital Fabrication, vol. 28, Cham: Springer International Publishing; 2020, p. 632–45. https://doi.org/10.1007/978-3-030-49916-7_64.

[84] Hass L, Bos FP, Salet TAM. Characterizing the bond properties of automatically placed helical reinforcement in 3D printed concrete. Construction and Building Materials 2022;355:129228. https://doi.org/10.1016/j.conbuildmat.2022.129228.

[85] Bos F, Ahmed Z, Jutinov E, Salet T. Experimental Exploration of Metal Cable as Reinforcement in 3D Printed Concrete. Materials 2017;10:1314. https://doi.org/10.3390/ma10111314.

[86] Hambach M, Volkmer D. Properties of 3D-printed fiber-reinforced Portland cement paste. Cement and Concrete Composites 2017;79:62–70. https://doi.org/10.1016/j.cemconcomp.2017.02.001.

[87] Bos FP, Bosco E, Salet TAM. Ductility of 3D printed concrete reinforced with short straight steel fibers. Virtual and Physical Prototyping 2019;14:160–74. https://doi.org/10.1080/17452759.2018.1548069.

[88] Arunothayan AR, Nematollahi B, Ranade R, Bong SH, Sanjayan J. Development of 3D-printable ultra-high performance fiber-reinforced concrete for digital construction. Construction and Building Materials 2020;257:119546. https://doi.org/10.1016/j.conbuildmat.2020.119546.

[89] Ogura H, Nerella V, Mechtcherine V. Developing and Testing of Strain-Hardening Cement-Based Composites (SHCC) in the Context of 3D-Printing. Materials 2018;11:1375. https://doi.org/10.3390/ma11081375.

[90] Zhu B, Pan J, Nematollahi B, Zhou Z, Zhang Y, Sanjayan J. Development of 3D printable engineered cementitious composites with ultra-high tensile ductility for digital construction. Materials & Design 2019;181:108088. https://doi.org/10.1016/j.matdes.2019.108088.

[91] Chaves Figueiredo S, Romero Rodríguez C, Y. Ahmed Z, Bos DH, Xu Y, Salet TM, et al. Mechanical Behavior of Printed Strain Hardening Cementitious Composites. Materials 2020;13:2253. https://doi.org/10.3390/ma13102253.

[92] Li VC, Bos FP, Yu K, McGee W, Ng TY, Figueiredo SC, et al. On the emergence of 3D printable Engineered, Strain Hardening Cementitious Composites (ECC/SHCC). Cement and Concrete Research 2020;132:106038. https://doi.org/10.1016/j.cemconres.2020.106038.

[93] Soltan DG, Li VC. A self-reinforced cementitious composite for building-scale 3D printing. Cement and Concrete Composites 2018;90:1–13. https://doi.org/10.1016/j.cemconcomp.2018.03.017.

[94] Bao Y, Xu M, Soltan D, Xia T, Shih A, Clack HL, et al. Three-Dimensional Printing Multifunctional Engineered Cementitious Composites (ECC) for Structural Elements. In: Wangler T, Flatt RJ, editors. First RILEM International Conference on Concrete and Digital Fabrication – Digital Concrete 2018, vol. 19, Cham: Springer International Publishing; 2019, p. 115–28. https://doi.org/10.1007/978-3-319-99519-9_11.

[95] Yu J, Leung CKY. Impact of 3D Printing Direction on Mechanical Performance of Strain-Hardening Cementitious Composite (SHCC). In: Wangler T, Flatt RJ, editors. First RILEM International Conference on Concrete and Digital Fabrication – Digital Concrete 2018, vol. 19, Cham: Springer International Publishing; 2019, p. 255–65. https://doi.org/10.1007/978-3-319-99519-9_24.

[96] WINSUN n.d. http://www.winsun3d.com.

[97] Salet TAM, Ahmed ZY, Bos FP, Laagland HLM. Design of a 3D printed concrete bridge by testing. Virtual and Physical Prototyping 2018;13:222–36. https://doi.org/10.1080/17452759.2018.1476064.

[98] Kinomura K, Murata S, Yamamoto Y, Obi H, Hata A. Application of 3D Printed Segments Designed by Topology Optimization Analysis to a Practical Scale

Prestressed Pedestrian Bridge. In: Bos FP, Lucas SS, Wolfs RJM, Salet TAM, editors. Second RILEM International Conference on Concrete and Digital Fabrication, vol. 28, Cham: Springer International Publishing; 2020, p. 658–68. https://doi.org/10.1007/978-3-030-49916-7_66.

[99] Gebhard L, Bischof P, Anton A, Mata-Falcón J, Dillenburger B, Kaufmann W. Pre-installed Reinforcement for 3D Concrete Printing. In: Buswell R, Blanco A, Cavalaro S, Kinnell P, editors. Third RILEM International Conference on Concrete and Digital Fabrication, vol. 37, Cham: Springer International Publishing; 2022, p. 430–5. https://doi.org/10.1007/978-3-031-06116-5_64.

[100] Van der Putten J, Van Olmen A, Aerts M, Ascione E, Beneens J, Blaakmeer J, et al. 3D concrete printing on site: a novel way of building houses? In: Bos FP, Lucas SS, Wolfs RJM, Salet TAM, International Union of Laboratories and Experts in Construction Materials, Systems and Structures, editors. Second RILEM International Conference on Concrete and Digital Fabrication: Digital Concrete 2020, Cham: Springer; 2020, p. 712–9.

[101] Bos F, Wolfs R, Ahmed Z, Salet T. Large Scale Testing of Digitally Fabricated Concrete (DFC) Elements. In: Wangler T, Flatt RJ, editors. First RILEM International Conference on Concrete and Digital Fabrication – Digital Concrete 2018, vol. 19, Cham: Springer International Publishing; 2019, p. 129–47. https://doi.org/10.1007/978-3-319-99519-9_12.

[102] Sanjayan JG, Nematollahi B, Xia M, Marchment T. Effect of surface moisture on inter-layer strength of 3D printed concrete. Construction and Building Materials 2018;172:468–75. https://doi.org/10.1016/j.conbuildmat.2018.03.232.

[103] Zareiyan B, Khoshnevis B. Effects of interlocking on interlayer adhesion and strength of structures in 3D printing of concrete. Automation in Construction 2017;83:212–21. https://doi.org/10.1016/j.autcon.2017.08.019.

[104] Van Der Putten J, Deprez M, Cnudde V, De Schutter G, Van Tittelboom K. Microstructural Characterization of 3D Printed Cementitious Materials. Materials 2019;12:2993. https://doi.org/10.3390/ma12182993.

[105] Serpukhov I, Mechtcherine V. Early-Age Shrinkage of Ordinary Concrete and a Strain-Hardening Cement-Based Composite (SHCC) in the Conditions of Hot Weather Casting. CONCREEP 10, Vienna, Austria: American Society of Civil Engineers; 2015, p. 1504–13. https://doi.org/10.1061/9780784479346.176.

[106] Panda B, Paul SC, Hui LJ, Tay YWD, Tan MJ. Additive manufacturing of geopolymer for sustainable built environment. Journal of Cleaner Production 2017;167:281–8. https://doi.org/10.1016/j.jclepro.2017.08.165.

[107] Licciardello L, Giraldo Soto A, Kaufmann W, Metelli G. Determining the strength of 3D printed concrete with the Modified Slan Shear Test. Under submission to an ISI Journal. 2024.

[108] Panda B, Paul SC, Mohamed NAN, Tay YWD, Tan MJ. Measurement of tensile bond strength of 3D printed geopolymer mortar. Measurement 2018;113:108–16. https://doi.org/10.1016/j.measurement.2017.08.051.

[109] EN 1015-11 (2019). Method of test for mortar for masonry – Part 11: Determination of flexural strength of hardened mortar. 2019.

[110] EN 1992-1-1:2004, Eurocode 2: Design of concrete structures- Part 1-1: General Rules, and Rules for Buildings, European Committee for Standardization. 2004.

[111] EN 1015-11. EN 1015-11 (2019). Method of test for mortar for masonry – Part 11: Determination of flexural strength of hardened mortar. 2019.

[112] D.M 17 gennaio 2018. Norme teniche per le costruzioni 2018.

[113] EN 1992-1-1:2004, Eurocode 2: Design of concrete structures- Part 1-1: General Rules, and Rules for Buildings, European Committee for Standardization. n.d.

[114] López-Carreño R-D, Pujadas P, Cavalaro SHP, Aguado A. Bond strength of whitetoppings and bonded overlays constructed with self-compacting high-performance concrete. Construction and Building Materials 2017;153:835–45. https://doi.org/10.1016/j.conbuildmat.2017.07.136.

[115] Bi-Surface Shear Test for Evaluating Bond between Existing and New Concrete. MJ 2004;101. https://doi.org/10.14359/13045.

[116] Giraldo Soto A, Kaufmann W. Effect of Test Setups on the Shear Transfer Capacity Across Cracks in FRC. In: Serna P, Llano-Torre A, Martí-Vargas JR, Navarro-Gregori J, editors. Fibre Reinforced Concrete: Improvements and Innovations, vol. 30, Cham: Springer International Publishing; 2021, p. 163–75. https://doi.org/10.1007/978-3-030-58482-5_15.

[117] Soetens T, Matthys S. Shear-stress transfer across a crack in steel fibre-reinforced concrete. Cement and Concrete Composites 2017;82:1–13. https://doi.org/10.1016/j.cemconcomp.2017.05.010.

[118] Guan D, Liu J, Jiang C, Chen Z, Guo Z. Shear behaviour of the UHPC-NSC interface with castellated keys: Effects of castellated key dimension and dowel rebar. Structures 2021;31:172–81. https://doi.org/10.1016/j.istruc.2021.01.088.

[119] Javidmehr S, Empelmann M. Shear Bond between Ultra-High Performance Fibre Reinforced Concrete Overlays and Normal Strength Concrete Substrates. Sustainability 2021;13:8229. https://doi.org/10.3390/su13158229.

[120] Momayez A, Ehsani MR, Ramezanianpour AA, Rajaie H. Comparison of methods for evaluating bond strength between concrete substrate and repair materials. Cement and Concrete Research 2005;35:748–57. https://doi.org/10.1016/j.cemconres.2004.05.027.

[121] Zanotti C, Randl N. Are concrete-concrete bond tests comparable? Cement and Concrete Composites 2019;99:80–8. https://doi.org/10.1016/j.cemconcomp.2019.02.012.

[122] EN 1052-3 (2002).Methods of test for masonry - Part 3: Determination of initial shear strength. 2002.

[123] EN 12615 (1999): Products and systems for the protection and repair of concrete structures: test methods : determination of slant shear strength 1999.

[124] Anton A, Reiter L, Wangler T, Frangez V, Flatt RJ, Dillenburger B. A 3D concrete printing prefabrication platform for bespoke columns. Automation in Construction 2021;122:103467. https://doi.org/10.1016/j.autcon.2020.103467.

[125] Reiter L, Anton A, Wangler T, Dillenburger B, Flatt RJ. A 3D Printing Platform for Reinforced Printed-Sprayed Concrete Composites. In: Buswell R, Blanco A, Cavalaro S, Kinnell P, editors. Third RILEM International Conference on Concrete and Digital Fabrication, vol. 37, Cham: Springer International Publishing; 2022, p. 249–54. https://doi.org/10.1007/978-3-031-06116-5_37.

[126] Tor Alva - The White Tower n.d. https://sustainable-digital-construction.ethz.ch/en/tor-alva.

[127] Marti P. Theory of structures: fundamentals, framed structures, plates and shells. Berlin: Wiley, Ernst & Sohn; 2013.

[128] van den Heever M, du Plessis A, Bester F, Kruger J, van Zijl G. A mechanistic evaluation relating microstructural morphology to a modified Mohr-Griffith compression-shear constitutive model for 3D printed concrete. Construction and Building Materials 2022;325:126743. https://doi.org/10.1016/j.conbuildmat.2022.126743.

[129] Jayathilakage R, Sanjayan J, Rajeev P. Direct shear test for the assessment of rheological parameters of concrete for 3D printing applications. Mater Struct 2019;52:12. https://doi.org/10.1617/s11527-019-1322-4.

[130] EN 12390-13 (2013). Testing hardened concrete. Part 13: Determination of secant modulus of elasticity in compression. 2013.

[131] Italcementi n.d. https://www.italcementi.it/it/casa-stampata-3D.

[132] PERI n.d. https://www.peri.com/en/media/press-releases/germanys-first-printed-house-officially-openend.html.

[133] Labò S, Marini A. In-plane flexural behavior of hollow brick masonry walls with horizontal holes. Engineering Structures 2022;273:115086. https://doi.org/10.1016/j.engstruct.2022.115086.

[134] Rosti A, Penna A, Rota M, Magenes G. In-plane cyclic response of low-density AAC URM walls. Mater Struct 2016;49:4785–98. https://doi.org/10.1617/s11527-016-0825-5.

[135] Drougkas A, Licciardello L, Rots JG, Esposito R. In-plane seismic behaviour of retrofitted masonry walls subjected to subsidence-induced damage. Engineering Structures 2020;223:111192. https://doi.org/10.1016/j.engstruct.2020.111192.

[136] Gaggero MB, Korswagen PA, Esposito R, Rots JG. In-Plane Behaviour of Unreinforced Masonry Strengthened with a Structural Glass Window: A Proof of Concept. Buildings 2023;13:361. https://doi.org/10.3390/buildings13020361.

[137] Rezaee SRS, Soltani M, Nikooravesh M. Cyclic in-plane behavior of unreinforced and confined masonry walls retrofitted by shotcrete: Experimental investigation. Engineering Structures 2022;264:114432. https://doi.org/10.1016/j.engstruct.2022.114432.

[138] Ismail N, Ingham JM. In-plane and out-of-plane testing of unreinforced masonry walls strengthened using polymer textile reinforced mortar. Engineering Structures 2016;118:167–77. https://doi.org/10.1016/j.engstruct.2016.03.041.

[139] Deng M, Zhang W, Li N. In-plane cyclic loading tests of concrete hollow block masonry walls retrofitted with high ductile fiber-reinforced concrete. Construction and Building Materials 2020;238:117758. https://doi.org/10.1016/j.conbuildmat.2019.117758.

[140] D.M. n. 162/2015 Applicazione delle metodologie di calcolo delle prestazioni energetiche e defi nizione delle prescrizioni e dei requisiti minimi degli edifici. 2015.

[141] EN ISO 6946: 2017, Building components and building elements - Thermal resistance and thermal transmittance - Calculation methods 2017.

[142] Licciardello L, Reggia A, Metelli G, Plizzari GA. Investigation of the structural and thermal behaviour of 3D printed concrete walls. Symposium on Concrete and Concrete Structures, Rome: 2021.

[143] THERM n.d. https://windows.lbl.gov/tools/therm/software-download.

[144] Alkhalidi A, Hatuqay D. Energy efficient 3D printed buildings: Material and techniques selection worldwide study. Journal of Building Engineering 2020;30:101286. https://doi.org/10.1016/j.jobe.2020.101286.

[145] AlZahrani AA, Alghamdi AA, Basalah AA. Computational Optimization of 3D-Printed Concrete Walls for Improved Building Thermal Performance. Buildings 2022;12:2267. https://doi.org/10.3390/buildings12122267.

[146] Nemova D, Kotov E, Andreeva D, Khorobrov S, Olshevskiy V, Vasileva I, et al. Experimental Study on the Thermal Performance of 3D-Printed Enclosing Structures. Energies 2022;15:4230. https://doi.org/10.3390/en15124230.

[147] Sun J, Xiao J, Li Z, Feng X. Experimental study on the thermal performance of a 3D printed concrete prototype building. Energy and Buildings 2021;241:110965. https://doi.org/10.1016/j.enbuild.2021.110965.

[148] https://gelfi.unibs.it/software/telaio2d/telaio2d.htm n.d.

[149] Metelli G, Bettini N, Plizzari G. Experimental and numerical studies on the behaviour of concrete sandwich panels. European Journal of Environmental and Civil Engineering 2011;15:1465–81. https://doi.org/10.1080/19648189.2011.9723354.

[150] Guide for testing reinforced concrete structural elements under slowly applied simulated seismic loads. Farmington Hills, MI: American Concrete Institute; 2013.

[151] Morandi P, Hak S, Magenes G. Performance-based interpretation of in-plane cyclic tests on RC frames with strong masonry infills. Engineering Structures 2018;156:503–21. https://doi.org/10.1016/j.engstruct.2017.11.058.

[152] Neri M, Licciardello L, Reggia A, Pilotelli M, Lezzi AM. Improving the energy performance of a 3D-printed wall using recycled material. J Phys: Conf Ser 2024;2685:012034. https://doi.org/10.1088/1742-6596/2685/1/012034.

[153] Comité euro-international du béton, editor. Fib model code for concrete structures 2010. Berlin: Ernst & Sohn; 2013.

[154] Esposito R, Ravenshorst Geert. Quasi-static cyclic in-plane test on masonry components 2016/2017 2017.

[155] Amir Hosein Salmanpour. Displacement capacity of structural masonry n.d.

[156] Messali F. Hollow brick masonry walls: in-plane seismic response and strengthening technique with with reinforced high-performance mortar coatings n.d.

[157] EN 1998-1 (2004) Eurocode 8: design of structures for earthquake resistance. Part 1: general rules, seismic actions and rules for buildings. CEN Brussels. 2004.

[158] Magenes G, Calvi G. In--plane seismic response of brick masonry walls. Earthquake engineering & structural dynamics, 26(11) 1997.

[159] Turnsek V, Cacovic F. Some experimental results on the strength of brick masonry walls., Stoke-onTrent: Proc. of the 2nd International Brick Masonry Conference; 1971, p. 149–56.

[160] Turnsek V, Sheppard P. The shear and flexural resistance of masonry walls., Skopje: Proc. of the International Research Conference on Earthquake Engineering; 1980, p. 517–73.

[161] Benedetti D, Tomazevic M. Sulla verifica sismica di costruzioni in muratura., Ingegneria Sismica I: 1984, p. 9–16.

[162] DIANA FEA n.d. https://dianafea.com/.

[163] Lourenço PB, Rots JG, Blaauwendraad J. Continuum Model for Masonry: Parameter Estimation and Validation. J Struct Eng 1998;124:642–52. https://doi.org/10.1061/(ASCE)0733-9445(1998)124:6(642).

[164] Lourenço PB, Rots JG. Multisurface Interface Model for Analysis of Masonry Structures. J Eng Mech 1997;123:660–8. https://doi.org/10.1061/(ASCE)0733-9399(1997)123:7(660).

[165] Ferretti F, Mazzotti C, Esposito R, Rots JG. Shear-sliding behavior of masonry: Numerical micro-modeling of triplet tests. Computational Modelling of Concrete Structures. 1st ed., London: CRC Press; 2018, p. 941–51. https://doi.org/10.1201/9781315182964-109.

[166] Bompa DV, Elghazouli AY. Experimental and numerical assessment of the shear behaviour of lime mortar clay brick masonry triplets. Construction and Building Materials 2020;262:120571. https://doi.org/10.1016/j.conbuildmat.2020.120571.

[167] Manuals for DIANA FEA n.d.

[168] Vecchio FJ, Collins MP. The modified compression field theory for reinforced concrete elements subjected to shear. 1986.

[169] Rots JG. Computational modeling of concrete fracture. Doctoral thesis. TU Delft, 1988.

[170] Feenstra PH. Computational aspects of biaxial stress in plain and reinforced concrete. 1993.

[171] van den Heever M, Bester F, Kruger J, van Zijl G. Numerical modelling strategies for reinforced 3D concrete printed elements. Additive Manufacturing 2022;50:102569. https://doi.org/10.1016/j.addma.2021.102569.

[172] van Zijl GPAG. Modeling Masonry Shear-Compression: Role of Dilatancy Highlighted. J Eng Mech 2004;130:1289–96. https://doi.org/10.1061/(ASCE)0733-9399(2004)130:11(1289).

[173] Lourenco PB. A user/programmer guide for the micro-modelling of masonry structures. n.d.

[174] CEB-FIP model code 1990: design code. London: Thomas Telford; 1993.

[175] Licciardello L, Carleschi E, Massari SA, Reggia A, Metelli G, Plizzari GA. Multilevel design approach to 3D printed concrete elements, Napoli: n.d.

[176] Ordinanza del Presidente del Consiglio dei ministri 20 marzo 2003, n. 3274. Primi elementi in materia di criteri generali per la classificazione sismica del territorio nazionale e di normative tecniche per le costruzioni in zona sismica. (G.U. n. 105 del 8 maggio 2003 - S.o. n.72) n.d.

[177] D.P.R. n. 412 del 26 agosto 1993. Regolamento recante norme per la progettazione, l'installazione, l'esercizio e la manutenzione degli impianti termici degli edifici ai fini del contenimento dei consumi di energia. n.d.

[178] UNI EN 15804: 2021. Sostenibilità delle costruzioni- Dichiarazioni ambientali di prodotto - Regole quadro di sviluppo per categoria di prodotto 2021.

APPENDIX A ACCURACY OF THE PRINTED SPECIMENS

Here some specimens used to evaluate the accuracy of 3DPC specimens are shown.

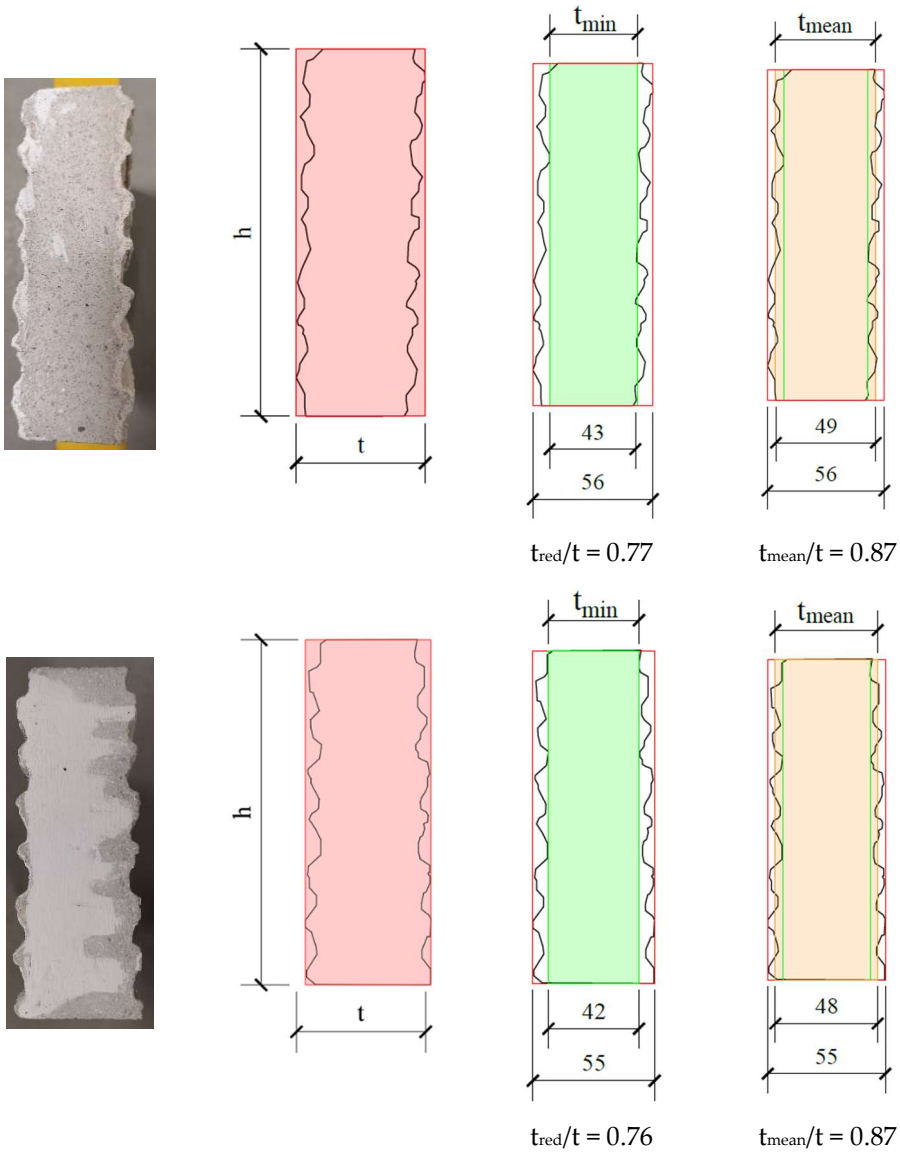

Figura A-1: Accuracy of the specimens printed with material type 1.

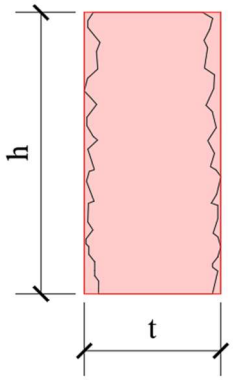

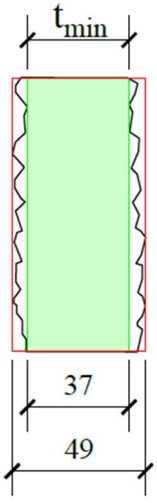

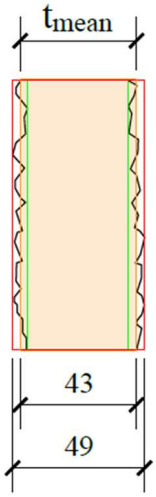

$t_{red}/t = 0.76$ $t_{mean}/t = 0.87$

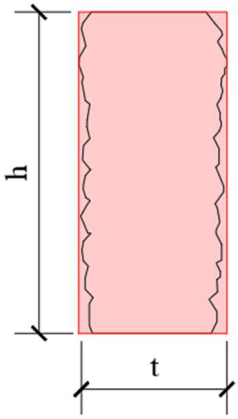

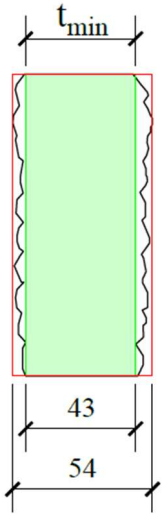

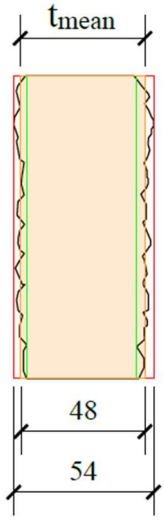

$t_{red}/t = 0.8$ $t_{mean}/t = 0.89$

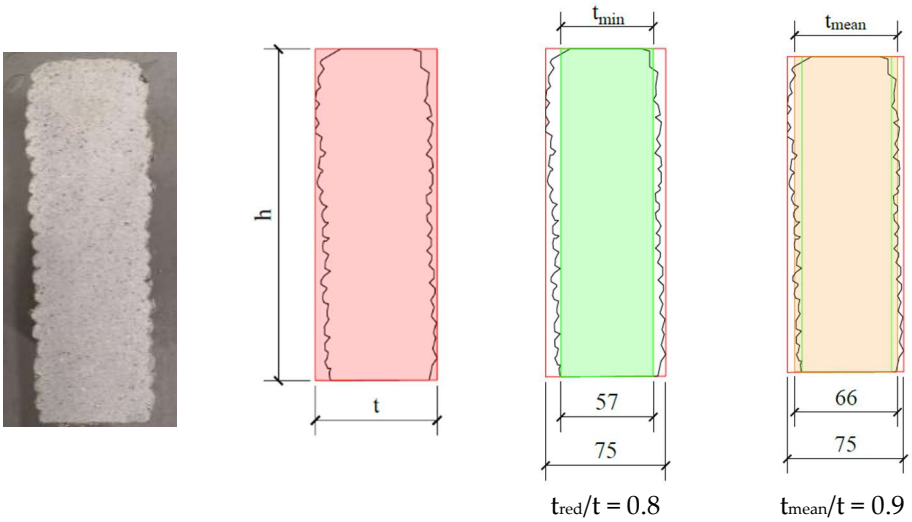

Figura A-2: Accuracy of the specimens printed with material type 2.

APPENDIX B COMPRESSION TEST

The test set-up described in section 3.6 served mainly to estimate the elastic modulus in compression. The compressive strength was measured just for material type 2, the number of tests performed is insufficient to draw conclusions with the results obtained from the compression test 1. The results are reported for completeness. Table B-1 summarizes the results obtained from the compression test type 2, which was performed just on specimens printed with material type 2. The compressive strength resulted equal to 38 MPa. As previously mentioned, on these specimens the digital image correlation was applied and as consequence it was possible to measure the strain field during the test (Figure B-1). Figure B-2 shows the specimen at the end of the test and it can be observed that the crack cross the specimen along the vertical direction.

		Orientation III			
Material	**Id**	**α**	**F_{max}**	**A**	**f_{cm}**
[-]	**[-]**	**[°]**	**[kN]**	**[mm²]**	**[MPa]**
2	3D-C-A	0	180.8	4026	44.9
2	3D-C-B	0	183.1	4224	43.34
2	3D-C-C	0	153.1	4007	38.21
2	3D-C-D	0	131	3782	34.64
2	3D-C-E	0	124.6	4198	29.68
2	3D-C-F	0	124.6	3717	33.53
2	3D-C-G	0	161.8	3776	42.84
2	3D-C-H	0	146.8	4224	34.75
Average					**37.74**
St.dev					**5.48**
C.o.V					**14%**

Table B-1: Material type 2 - Compressive strength of 3DPC specimens obtained with compression test 2.

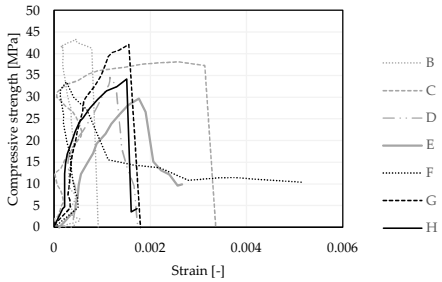

Figure B-1: Stress-strain behaviour of 3D printed concrete specimen printed with material type 2 (compression test 2).

Figure B-2: Compression test 2: failure mode.

APPENDIX C ADDITIONAL MODIFIED PUSH-OUT TEST

Additional modified push out test were conducted to decide the dimensions of the second series of tests to expand the area below the loading point and avoid concrete matrix failure. For this purpose the height of the specimens need to be determined. The tested specimens had a length of 16 cm and a height of 8 cm, 12 cm and 16 cm, respectively. The specimen with a height of 16 cm reached a maximum force of 174.95 kN (shear strength 11.76 MPa), it can be observed that it failed for sliding at the interfaces but there are many other cracks (Figura C-1a). The specimen with a height of 12 cm reached a maximum force of 130.81 kN (shear strength 12.67 MPa), it can be observed that it failed for sliding at the interfaces, there are few other cracks but is less distrubed than the previous one (Figura C-1b). The specimen with a height of 8 cm reached a maximum force of 115.07 kN (shear strength 15.98 MPa), it can be observed that it failed for sliding at the interfaces (Figura C-1c). The final choice of the specimen 12 cm was taken beacuse in the specimen 16 cm high there were other mechanims that could arise and the one 8 cm high was to small and it was difficult to place all the LVDTs.

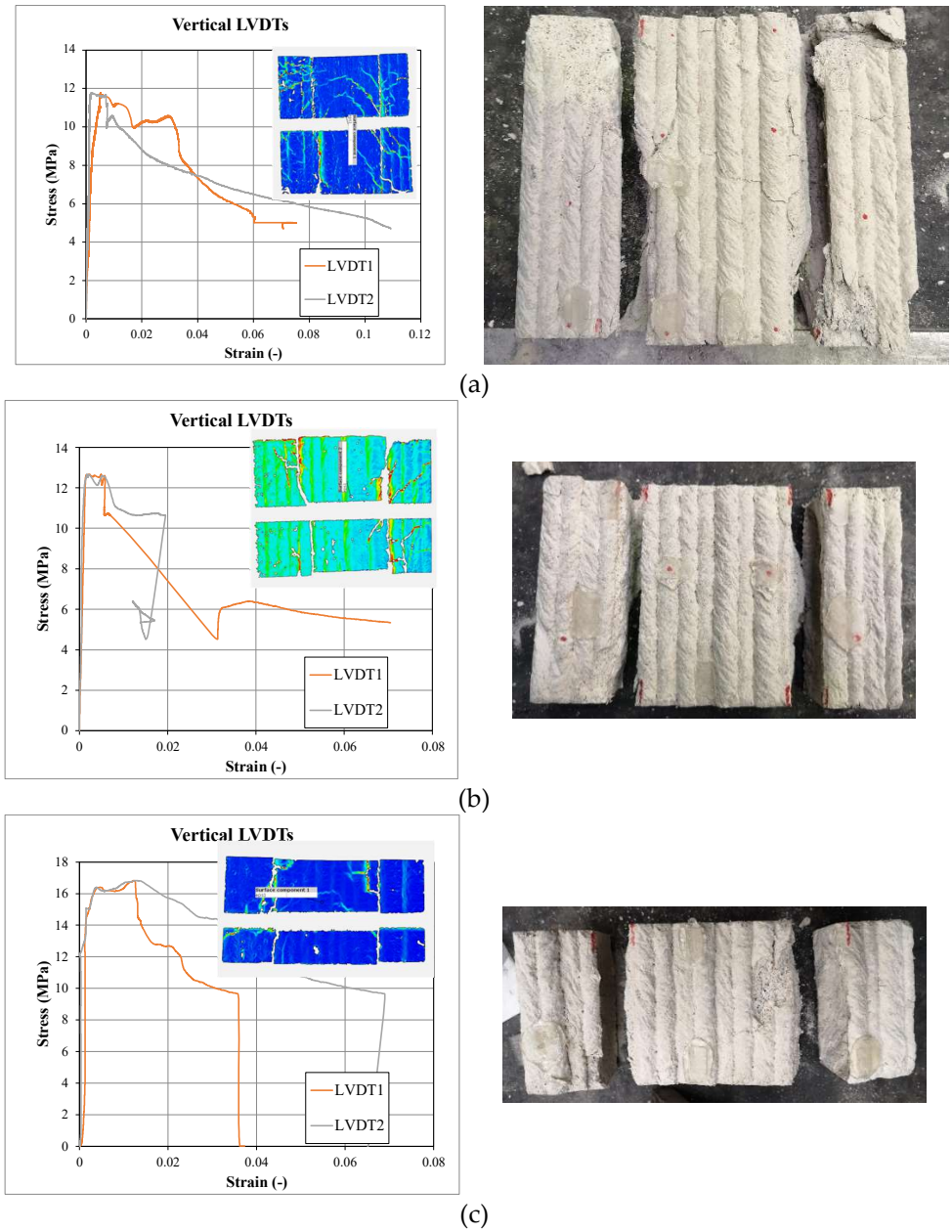

Figura C-1: Additional modified push-out test: (a) 16x16 cm, (b) 16x12 cm, and (c) 16x8 cm.

APPENDIX D ANALYTICAL METHOD FOR THE ESTIMATION OF THE THERMAL TRANSMITTANCE OF 3DPC WALLS

D.1 Wall with parallel diaphragms

D.1.1 Without insulating material in the cavities

Thermal transmittance is calculated with an analytical model using the method of the equivalent resistances to the heat fluxes, as shown in Figure D-1 Useful data for calculation are reported in Table D-1. Figure D-2 shows the areas perpendicular to the heat flux considered in the calculation.
The calculation is conducted by considering empty internal cavities.

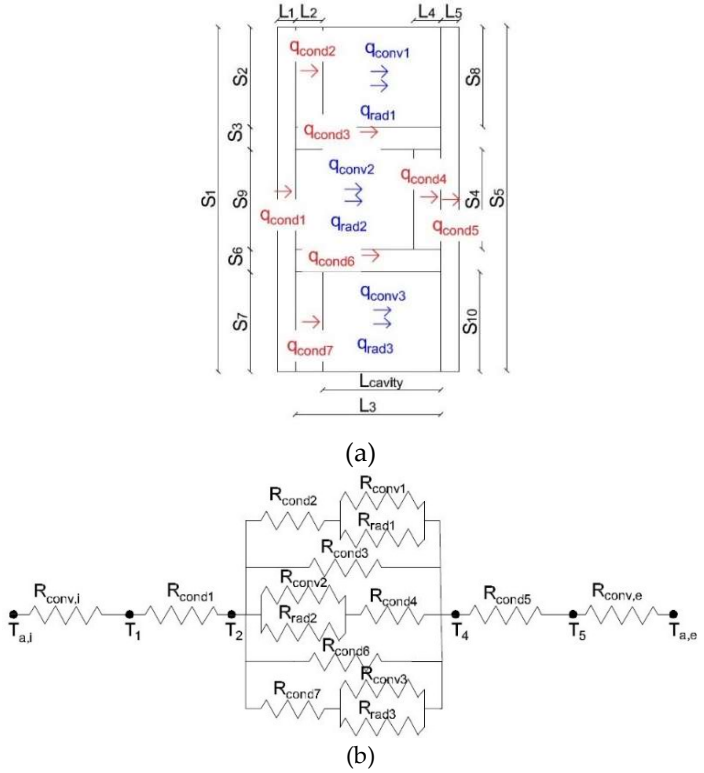

Figure D-1: 3DPC wall with parallel struts (not insulated): (a) cross section with heat flux arrows and (b) equivalent resistance scheme.

L_1=L_5	[m]	0.040
L_2=L_4	[m]	0.060
L_3	[m]	0.260
L_{cavity}	[m]	0.200
S_2=S_4 = S_7	[m]	0.200
S_8=S_9 = S_{10}	[m]	0.200
S_3=S_6	[m]	0.040
S_1=S_5	[m]	0.680
k	[W/mK]	0.979
h_i	[W/m²K]	7.69
h_e	[W/m²K]	25.000
ε*	[-]	0.900

*Standard value for concrete

Table D-1: Data used for the calculation.

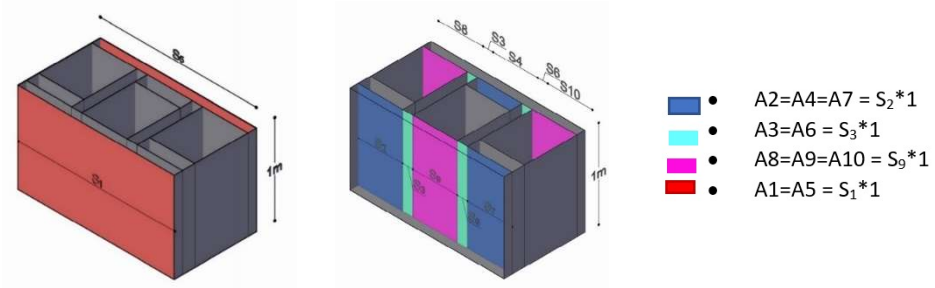

Figure D-2: Areas perpendicular to the heat flux.

The total equivalent resistance (R_{tot}) is calculated as:

$$R_{tot} = R_i + R_{cond1} + R_{mid} + R_{cond5} + R_e \quad \text{D-1}$$

where:

R_i is the convective air resistance of the internal environment;

R_{cond1} is the conductive resistance of internal wall;

R_{mid} is the resistance of the internal part of the wall including the air in the internal cavities;

R_{cond5} is the conductive resistance of the external wall; and

R_e is the convective air resistance of the external environment.

The conductive resistance ($R_{cond,i}$) is calculated as:

$$R_{cond,i} = \frac{l_i}{k_i \cdot A_i} \quad \text{D-2}$$

where:

L_i is the length traversed by the heat flux;

K_i is the thermal conductivity of the material considered; and
A_i is the area perpendicular to the heat flux.
The convective resistance ($R_{conv,i}$) is calculated as:

$$R_{conv,i} = \frac{1}{h_{conv} \cdot A_i} \quad \text{D-3}$$

where:
h_{conv} is the convective heat transfer coefficient.
The radiation resistance ($R_{rad,i}$) is calculated as:

$$R_{rad,i} = \frac{1}{h_{rad} \cdot A_i} \quad \text{D-4}$$

where:
h_{rad} is the radiation heat transfer coefficient.
The convective air resistance of internal environment (R_i) and external environment (R_e) can be calculated as:

$$R_i = \frac{1}{A_1 \cdot h_i} \quad \text{D-5}$$

$$R_e = \frac{1}{A_5 \cdot h_e} \quad \text{D-6}$$

where:
A_1 is the area of the internal wall perpendicular to the heat flux;
A_5 is the area of the external wall perpendicular to the heat flux;
h_i is the internal convective heat transfer coefficient according to EN ISO 6946:2017 [141]; and
h_e is the external convective heat transfer coefficient according to EN ISO 6946:2017 [141].
The conductive resistance of the internal wall (R_{cond1}) and external wall (R_{cond4}) can be expressed as:

$$R_{cond1} = \frac{L_1}{A_1 \cdot k} = R_{cond5} = \frac{L_5}{A_5 \cdot k} \quad \text{D-7}$$

where:
L_1 is the thickness of internal wall;
L_5 is the thickness of external wall; and
k is the thermal conductivity of the 3D printed concrete.
The global resistance of the internal part of the wall including the air cavities (R_{mid}) can be calculated, considering the scheme of resistances in series and in parallel, as follows:

$$R_{mid} = \frac{1}{\frac{1}{R_{cond2} + \frac{1}{\frac{1}{R_{conv1}} + \frac{1}{R_{rad1}}}}} + \frac{1}{R_{cond}} + \frac{1}{\frac{1}{\frac{1}{R_{conv2}} + \frac{1}{R_{rad2}}} + R_{cond4}} + \frac{1}{R_{cond6}} + \frac{1}{R_{cond7} + \frac{1}{\frac{1}{R_{cond3}} + \frac{1}{R_{rad3}}}}} \quad \text{D-8}$$

The conductivity resistances (R_{con2}, R_{cond3}, R_{cond4}, R_{cond6}, and R_{cond7}) are calculated as:

$$R_{cond2} = R_{cond4} = R_{cond7} = \frac{L_2}{A_2 \cdot k} \quad \text{D-9}$$

$$R_{cond3} = R_{cond6} = \frac{L_3}{A_3 \cdot k} \quad \text{D-10}$$

The convection resistance of the air in the cavities of the wall (R_{conv1}, R_{conv2}, and R_{conv3}) can be expressed as:

$$R_{conv1} = R_{conv2} = R_{conv3} = \frac{1}{A_8 \cdot h_{conv}} \quad \text{D-11}$$

where:

h_{conv} is the convective heat transfer coefficient of the air in the internal cavities according to EN ISO 6946:2017 [141].

The radiation heat transfer coefficient (h_{rad}) is calculated as:

$$h_{rad} = \frac{\sigma \cdot (T_i + T_e) \cdot (T_i^2 + T_e^2)}{\frac{1}{\varepsilon_1} + \frac{1}{\varepsilon_2} - 1} \quad \text{D-12}$$

where:

σ is the Stefan Boltzmann constant equal to 5.67 10-8 W/(m²K⁴);

T_i is the temperature of the internal environment (assumed equal to 22° in winter and to 25°in summer based on average summer and winter temperature in north Italy);

T_e is the temperature of the external environment (assumed equal to 0° in winter and to 30° in summer based on average summer and winter temperature in north Italy);

ε_1 is the emissivity coefficient; and

ε_2 is the emissivity coefficient.

The thermal transmittance (U) can be expressed as:

$$U = \frac{1}{R_{tot}} \quad \text{D-13}$$

D.1.2 With insulating material in the cavities

Thermal transmittance is calculated with an analytical model using the method of the equivalent resistances to the heat fluxes, as shown in Figure D-3. Useful data for calculation are reported in Table D-1. Figure D-2 shows the areas perpendicular to the heat flux considered in the calculation.
The calculation is repeated considering the internal voids filled with cellulose Fibre flakes.

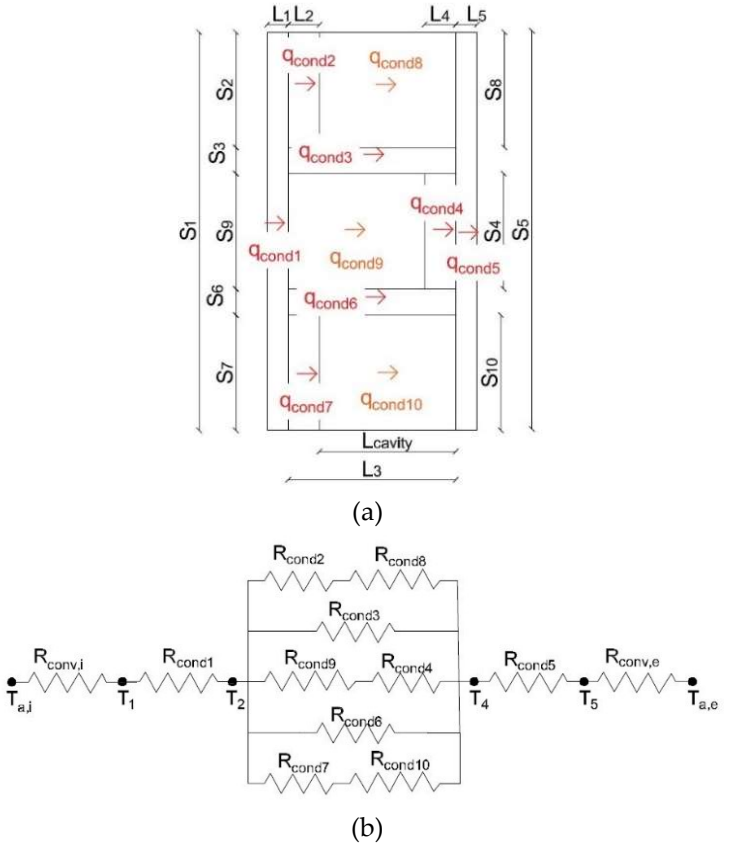

Figure D-3: 3DPC wall with parallel struts (insulated): (a) cross section with heat flux arrows and (b) equivalent resistance scheme.

The total equivalent resistance (R_{tot}) is calculated as:

$$R_{tot} = R_i + R_{cond1} + R_{mid} + R_{cond5} + R_e \qquad \text{D-14}$$

where:

$$R_{mid} = \frac{1}{\frac{1}{R_{cond2} + R_{cond8}} + \frac{1}{R_{cond3}} + \frac{1}{R_{cond9} + R_{cond4}} + \frac{1}{R_{cond6}} + \frac{1}{R_{cond7} + R_{cond10}}} \quad \text{D-15}$$

$$R_{cond8} = R_{cond9} = R_{cond10} = \frac{L_{cavity}}{A_8 \cdot k} \quad \text{D-16}$$

The thermal transmittance (U) can be expressed as:

$$U = \frac{1}{R_{tot}} \quad \text{D-17}$$

D.2 Wall with inclined diaphragms (not insulated)

D.2.1 Without insulating material in the cavities

Thermal transmittance is calculated with an analytical model using the method of the equivalent resistances to the heat fluxes, as shown in Figure D-4. Useful data for calculation are reported in Table D-2. Figure D-5 shows the areas perpendicular to the heat flux considered in the calculation.
The calculation is conducted by considering empty internal cavities.

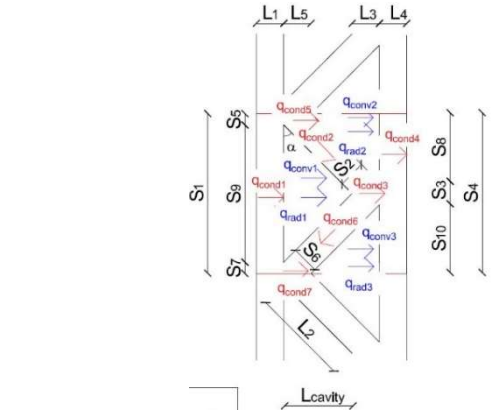

(a)

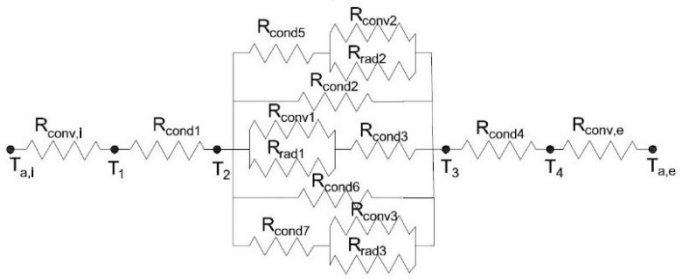

(b)

Figure D-4: 3DPC wall with inclined struts (not insulated): (a) cross section with heat flux arrows and (b) equivalent resistance scheme.

L_1	[m]	0.050
L_2	[m]	0.90
L_3	[m]	0.060
L_4	[m]	0.050
L_5	[m]	0.060
L_{cavity}	[m]	0.54
S_1=S_4	[m]	1.45
S_2=S_6	[m]	0.050
S_5=S_7	[m]	0.01
S_3	[m]	0.02
S_8=S_{10}	[m]	0.72
S_9	[m]	1.43
k	[W/mK]	0.963
h_i	[W/m²K]	7.690
h_e	[W/m²K]	25.000
h_{conv}	[W/m²K]	5.55
ε*	[-]	0.9

*Standard value for concrete

Table D-2: Data used for the calculation.

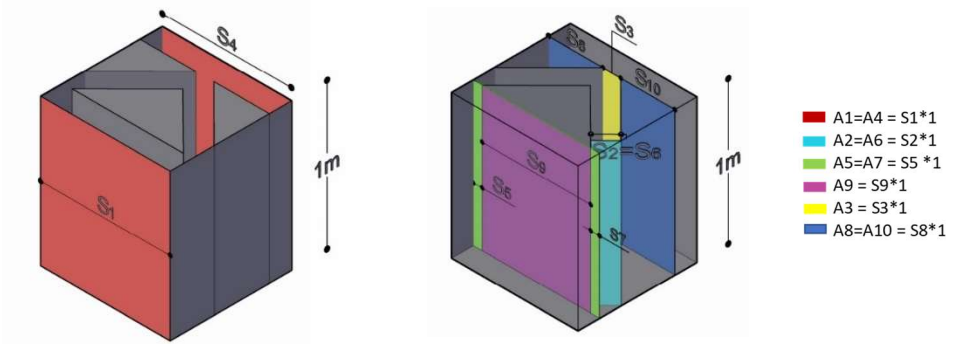

Figure D-5: Areas perpendicular to the heat flux.

The total equivalent resistance (R_{tot}) is calculated as:

$$R_{tot} = R_i + R_{cond1} + R_{mid} + R_{cond4} + R_e \quad \text{D-18}$$

where:

R_i is the convective air resistance of the internal environment;

R_{cond1} is the conductive resistance of internal wall;

R_{mid} is the resistance of the internal part of the wall including the air in the internal cavities;

R_{cond4} is the conductive resistance of the external wall; and

R_e is the convective air resistance of the external environment.

The convective air resistance of internal environment (R_i) and external environment (R_e) can be calculated as:

$$R_i = \frac{1}{A_1 h_i} \quad \text{D-19}$$

$$R_e = \frac{1}{A_4 h_e} \quad \text{D-20}$$

where:

A_1 is the area of the internal wall perpendicular to the heat flux;

A_4 is the area of the external wall perpendicular to the heat flux;

h_i is the internal convective heat transfer coefficient according to EN ISO 6946:2017 [141]; and

h_e is the external convective heat transfer coefficient according to EN ISO 6946:201 [141];

The conductive resistance of the internal wall (R_{cond1}) and external wall (R_{cond4}) can be expressed as:

$$R_{cond1} = \frac{L_1}{A_1 \cdot k} \quad \text{D-21}$$

$$R_{cond4} = \frac{L_4}{A_4 \cdot k} \quad \text{D-22}$$

where:

L_1 is the thickness of internal wall;

L_4 is the thickness of external wall; and

k is the thermal conductivity of the 3D printed concrete.

The global resistance of the internal part of the wall including the air cavities (R_{mid}) can be calculated, considering the scheme of resistances in series and in parallel, as follows:

$$R_{mid} = \frac{1}{\frac{1}{R_{cond5} + \frac{1}{\frac{1}{R_{conv2}} + \frac{1}{R_{rad2}}}} + \frac{1}{R_{cond2}} + \frac{1}{\frac{1}{\frac{1}{R_{conv1}} + \frac{1}{R_{rad1}}} + R_{cond3}} + \frac{1}{R_{cond6}} + \frac{1}{R_{cond7} + \frac{1}{\frac{1}{R_{conv3}} + \frac{1}{R_{rad3}}}}} \quad \text{D-23}$$

The conductivity resistances are calculated as:

$$R_{cond5} = \frac{L_5}{A_5 \cdot k} = R_{cond7} = \frac{L_7}{A_7 \cdot k} \quad \text{D-24}$$

$$R_{cond3} = \frac{L_3}{A_3 \cdot k} \quad \text{D-25}$$

$$R_{cond2} = \frac{L_2}{A_2 \cdot k} = R_{cond6} = \frac{L_6}{A_6 \cdot k} \quad \text{D-26}$$

where:
L_5 and L_3 are the thicknesses of the internal strut;
L_2 and L_6 are the lengths of the internal strut; and
K is the thermal conductivity of the 3D printed concrete.
The convection resistance of the air in the cavities of the wall (R_{conv1}, R_{conv2}, and R_{conv3}) can be expressed as:

$$R_{conv1} = \frac{1}{A_9 \cdot h_{conv}} \quad \text{D-27}$$

$$R_{conv2} = \frac{1}{A_8 \cdot h_{conv}} = R_{conv3} = \frac{1}{A_{10} \cdot h_{conv}} \quad \text{D-28}$$

where:
h_{conv} is the convective heat transfer coefficient of the air in the internal cavities according to EN ISO 6946:2017 [141].
The radiation resistance of the air in the internal cavities of the wall (R_{rad1} and R_{rad2}) can be calculated as:

$$R_{rad1} = \frac{1}{A_9 \cdot h_{rad}} \quad \text{D-29}$$

$$R_{rad2} = \frac{1}{A_8 h_{rad}} = R_{rad3} = \frac{1}{A_{10} h_{rad}} \quad \text{D-30}$$

The thermal transmittance (U) can be expressed as:

$$U = \frac{1}{R_{tot}} \quad \text{D-31}$$

D.2.2 With insulating material in the cavities

Thermal transmittance is calculated with an analytical model using the method of the equivalent resistances to the heat fluxes, as shown in Figure D-6. Useful data for calculation are reported in Table D-2. Figure D-5 shows the areas perpendicular to the heat flux considered in the calculation.
The calculation is repeated considering the internal voids filled with cellulose fibre flake.

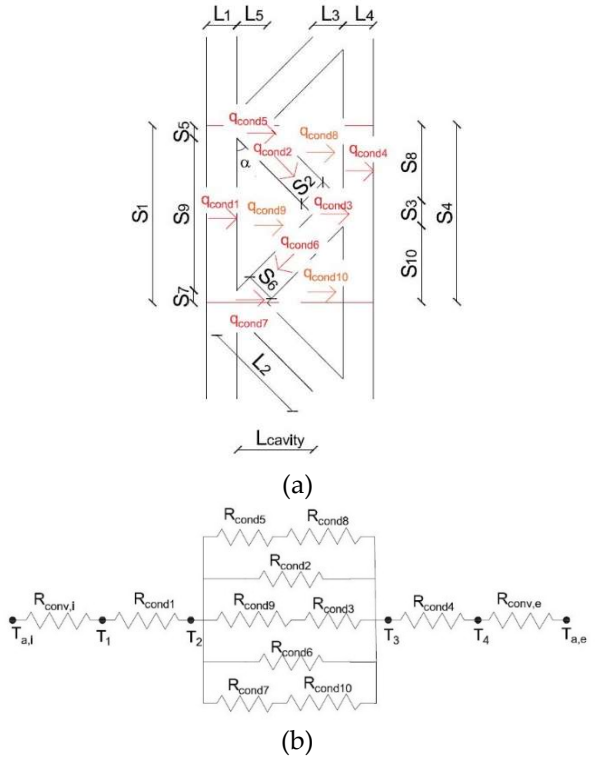

Figure D-6: 3DPC wall with inclined struts (insulated): (a) cross section with heat flux arrows and (b) equivalent resistance scheme.

The total equivalent resistance (R_{tot}) is calculated as:

$$R_{tot} = R_i + R_{cond1} + R_{mid} + R_{cond4} + R_e \quad \text{D-32}$$

$$R_{mid} = \frac{1}{\frac{1}{R_{cond5} + R_{cond8}} + \frac{1}{R_{cond2}} + \frac{1}{R_{cond9} + R_{cond3}} + \frac{1}{R_{cond6}} + \frac{1}{R_{cond7} + R_{cond10}}} \quad \text{D-33}$$

where:

R_{cond8}, R_{cond9} and R_{cond10} are the conductive resistances of the internal cavities filled with insulating material, calculated as:

$$R_{cond8} = \frac{L_{cavity}}{A_8 \cdot k} = R_{cond10} = \frac{L_{cavity}}{A_{10} \cdot k} \quad \text{D-34}$$

$$R_{cond9} = \frac{L_{cavity}}{A_9 \cdot k} \quad \text{D-35}$$

The thermal transmittance (U) can be expressed as:

$$U = \frac{1}{R_{tot}} \quad \text{D-36}$$

D.3 Wall with inclined diaphragms and outer leaf (insulated)

Thermal transmittance is calculated with an analytical model using the method of the equivalent resistances to the heat fluxes, as shown in Figure D-7. Useful data for calculation are reported in Table D-3.
The calculation is repeated considering the internal voids filled with cellulose fibre flake.

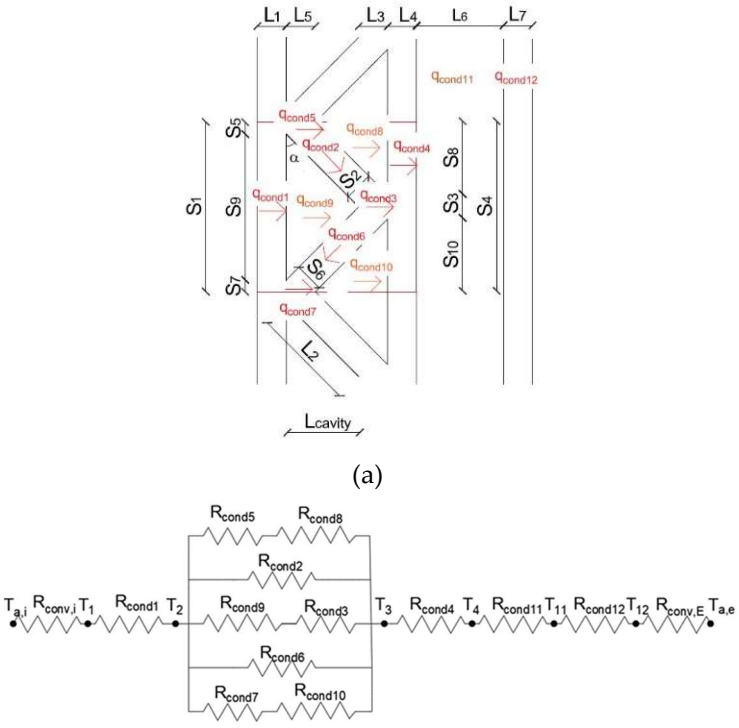

Figure D-7: 3DPC wall with inclined struts and outer leaf (insulated): (a) cross section with heat flux arrows and (b) equivalent resistance scheme.

L_1	[m]	0.050
L_2	[m]	0.300
L_3	[m]	0.060
L_4	[m]	0.050
L_5	[m]	0.060
L_6	[m]	0.170
L_7	[m]	0.050
L_{cavity}	[m]	0.170
S_1=S_4	[m]	0.500
S_2=S_6	[m]	0.050
S_5=S_7	[m]	0.010
S_3	[m]	0.020
S_8=S_{10}	[m]	0.240
S_9	[m]	0.480
k	[W/mK]	0.963
h_i	[W/m²K]	7.690
h_e	[W/m²K]	25.000
h_{conv}	[W/m²K]	5.55
ε*	[-]	0.9

*Standard value for concrete

Table D-3: Data used for the calculation.

The total equivalent resistance (R_{tot}) is calculated as:

$$R_{tot} = R_i + R_{cond1} + R_{mid} + R_{cond4} + R_{cond11} + R_{cond12} + R_e \quad \text{D-37}$$

$$R_{mid} = \frac{1}{\frac{1}{R_{cond5} + R_{cond8}} + \frac{1}{R_{cond2}} + \frac{1}{R_{cond9} + R_{cond3}} + \frac{1}{R_{cond6}} + \frac{1}{R_{cond7} + R_{cond10}}} \quad \text{D-38}$$

The thermal transmittance (U) can be expressed as:

$$U = \frac{1}{R_{tot}} \quad \text{D-39}$$

APPENDIX E CALCULATION OF THE LOAD ACTING ON A 3DPC WALL

Here the type of floor (Table E-1) and the type of roof (Table E-2) assumed to estimate the load acting on a 3DPC wall is reported.

	ϒ [kN/m³]	**s [cm]**	**q [kN/m²]**
Predalles slab floor			4.20
		tot G1	**4.20**
Layer of light-weight concrete for filling the space between heating and&or electrical system	11	12	1.32
Underfloor heating made of a layer of lightweight concrete and insulating system	-	4+4	1.2
tiles	15	2	0.30
		tot G2	**2.82**
Variable Load		**tot Q**	**2**

Table E-1: detail of the floor.

	ϒ [kN/m³]	**s [cm]**	**q [kN/m²]**
Predalles slab floor			4.20
		tot G1	**4.20**
Layer of light-weight concrete for the slope	11	10	1.10
Insulating material	0.4	12	0.05
Waterproof sheath	13.5	1	0.15
Concrete screed	11	6	0.66
tiles	15	2	0.30
		tot G2	**2.24**
Variable Load		**tot Q**	**1.20**

Table E-2: detail of the roof.

MODULO DI EMBARGO DELLA TESI
(da compilare solo se si richiede un periodo di segretazione della tesi)

Il/La sottoscritto/a…… Lucia Licciardello Nato/a il…… 15/06/1992
a (indicare anche l'eventuale paese estero)…… Brescia ……..
provincia di (ovvero sigla del paese estero)…… Brescia ……
Dottorato di Ricerca in …… Ingegneria Civile, Ambientale, della Cooperazione Internazionale e di Matematica ……
……..……

DICHIARA

- che il contenuto della tesi **non può essere immediatamente consultabile per il seguente motivo**

Dati sensibili di prove sperimentali svolte in collaborazione con ETH di Zurigo che devono prima essere pubblicati su rivista scientifica

---

La motivazione deve essere dettagliata e controfirmata obbligatoriamente dal Tutor e/o Relatore
(Brevetto, segreto industriale, motivi di priorità nella ricerca, motivi editoriali, altro)

- che il testo completo della tesi potrà essere reso consultabile dopo:

□ 6 mesi dalla data di conseguimento titolo
☑ 12 mesi dalla data di conseguimento titolo
□ 24 mesi dalla data di conseguimento titolo
□ altro periodo _____

- che sarà comunque consultabile immediatamente l'abstract della tesi, che viene caricato in Esse3, profilo studente.

Luogo e Data

Brescia, 20/04/2023

Firma del Dichiarante

Lucia Licciardello

_____

Controfirma del Tutor e/o Relatore del Dottorato
per la motivazione di embargo e il periodo.

Giovanni Metelli

_____